Angular Analysis of the $B^0 \to K^{*0}\mu^+\mu^-$ decay at the LHCb experiment

Felix Johannes Kress

High Energy Physics
Blackett Laboratory
Imperial College London

A thesis submitted to Imperial College London
for the degree of Doctor of Philosophy

July 2020

Abstract

An angular analysis of the $B^0 \to K^{*0}(\to K^+\pi^-)\mu^+\mu^-$ decay is presented in this thesis. The measurement uses a data set corresponding to an integrated luminosity of $4.7\,\text{fb}^{-1}$ of pp collision data collected with the LHCb detector during the years 2011, 2012 and 2016. Angular observables are determined in bins of the invariant dimuon mass squared using an unbinned maximum likelihood fit, in which contamination from decays with the $K^+\pi^-$ system in an S-wave configuration is taken into account. The results of the observables are the most precise to date, reducing the uncertainty with respect to the previous LHCb measurements by approximately 30%. The tension that was previously observed with the Standard Model predictions persists, and studies with the FLAVIO software package indicate a slight increase in the tension. However, the precise value depends on the choice of theory nuisance parameters.

Declaration of originality

The analysis presented in this thesis was published in Ref. [1] and is the result of the research I performed between February 2017 and March 2020, with the support of the Imperial College High Energy Physics group and members of the LHCb Collaboration. The analysis work presented in this thesis was performed by myself, with some exceptions. The selection of the analysis presented in Chpt. 5 was kept very similar to that in Ref. [2], however I contributed by making a large number of checks to ensure that the selection was correctly applied to the new data. In Chpt. 6, which outlines the mass fits to data, the values in Tab. 6.2 were calculated by Dr Christoph Michael Langenbruch. In Chpt. 7 the PID resampling corrections were performed by Dr Eluned Anne Smith, while I performed the kinematic reweighting of the simulation. The angular fit model described in Chpt. 9 was kept identical to the one in Ref. [2]. My main contribution to this chapter are the fits to the control channel detailed in Sec. 9.7 and Sec. 9.8. Half of the systematic uncertainties described in Chpt. 10 were calculated by Eluned Anne Smith, the other half by myself. In particular, my contributions to the systematic calculations are presented in Secs. 10.6–10.9.4. Chpts. 8, 11 and 12 contain the work that constitute my main contributions to the analysis. All results and figures presented in this thesis that were not the product of my own work are appropriately referenced. The figures that were taken from Ref. [1] were all produced by myself.

This thesis has not been submitted for any other qualification.

Felix Kress, July 2020

Copyright declaration

The copyright of this thesis rests with the author and is made available under a Creative Commons Attribution Non-Commercial No Derivatives licence. Researchers are free to copy, distribute or transmit the thesis on the condition that they attribute it, that they do not use it for commercial purposes and that they do not alter, transform or build upon it. For any reuse or redistribution, researchers must make clear to others the licence terms of this work.

Acknowledgements

This thesis, as the culmination of the last four years, would not have been possible without the support of those that have accompanied me on this path. First and foremost I would like to thank my supervisor Mitesh Patel, who struck the perfect balance of motivating me to pursue my work and giving me the freedom to do it at my own pace. I cannot put into words how thankful I am for all the support you provided me with in the last four years.

A big thank you to the whole $B^0 \to K^{*0}\mu^+\mu^-$ team and especially to Eluned Smith; We made it despite all obstacles!. Thank you to Thomas Blake for his help when it came to the often underrated "art of plotting" and his invaluable support during the whole analysis. I would also like to express my gratitude towards Christoph Langenbruch and his support with the FLAVIO software package. Last but not least thank you to Paula Álvarez Cartelle, Ulrik Egede and Kostas Petridis for the often spontaneous and extremely useful discussions.

I would further like to thank various members of the Imperial LHCb group; Dave, Mike, Mark, Sally, Sophie, Dan, Ryan, Matt and Matt. I always knew who I could depend on when I needed a word of advice or encountered some troublesome piece of code. Special thanks go to Thibaud, who has been supporting me far beyond his time at Imperial, welcomed me in Munich and provided me with an office space at the MPI. Thank you Malte for not only being an incredible colleague but also a good friend.

Thank you to my fellow PhD students Nellie, Toby, Rob, Artur, Albert and Sam for the various coffee breaks that were always a welcome distraction, and to Vukasin and Giacomo who always brightened up my day, both at Imperial and at CERN.

Finally I would like to thank my parents and my sister for their continued support and for always only being a call, a flight or a train journey away.

This thesis is dedicated to Susanna, my best friend and partner in everything I do.

Contents

List of figures **15**

List of tables **18**

1 Introduction **19**

I Theoretical and experimental overview **23**

2 Theory of the Standard Model and the $B^0 \to K^{*0}\mu^+\mu^-$ decay **25**

2.1 Particles and interactions in the Standard Model 25
2.2 Global and local gauge symmetries in QED 27
2.3 Spontaneous symmetry breaking 28
2.4 The Higgs mechanism and electroweak unification 29
2.4.1 Fields of the electroweak theory 30
2.4.2 The Higgs mechanism 31
2.4.3 Fermion masses 33
2.4.4 CKM mixing matrix 35
2.5 Quantum Chromodynamics 35
2.6 Summary of the SM and NP 36
2.7 Flavour changing neutral currents 37
2.8 Effective field theories 37
2.9 The $B^0 \to K^{*0}\mu^+\mu^-$ decay 40
2.9.1 Definition of the angular basis 40
2.9.2 Differential decay rate 42
2.9.3 Theory calculations and challenges 45
2.9.4 S-wave interference 46
2.10 Experimental status of $b \to s\ell^+\ell^-$ decays and global fits 47

3 The LHCb detector **53**

3.1 The Large Hadron Collider 53
3.2 Layout of the LHCb detector 53
3.3 Vertex Locator 56

3.4 Tracking and magnet . . . 57
3.5 Cherenkov detectors . . . 59
3.6 Calorimeter system . . . 60
3.7 Muon Stations . . . 61
3.8 Trigger system . . . 63
3.8.1 Low level trigger . . . 64
3.8.2 High level trigger . . . 65
3.9 Generation of simulated data . . . 67

II The angular analysis of the $B^0 \to K^{*0}\mu^+\mu^-$ decay 69

4 Analysis strategy 70
4.1 Binning in q^2 . . . 71

5 Selection 72
5.1 Stripping and pre-selection . . . 72
5.2 Peaking backgrounds . . . 73
5.2.1 Estimation of peaking background yields . . . 76
5.3 Multivariate selection . . . 76
5.4 Control channel . . . 78

6 Mass model and signal yields 80
6.1 The $K^+\pi^-\mu^+\mu^-$ invariant mass fit model . . . 80
6.2 Event yields . . . 81

7 Agreement between data and simulation 85
7.1 Resampling the particle identification variables . . . 85
7.2 Explicit reweighting . . . 86

8 Acceptance 90
8.1 Acceptance parametrisation . . . 90
8.2 q^2 reweighting at generator level . . . 92
8.3 Four-dimensional acceptance functions for the Run 1 and 2016 data . . . 93

9 Angular fit model **98**
9.1 Probability density function of the reconstructed B^0 mass and the decay angles . . . 98
9.2 S-wave and $m_{K\pi}$ distribution . . . 99
9.3 Logarithmic likelihood function . . . 101
9.4 Simultaneous fits . . . 102
9.5 Acceptance implementation in the likelihood fit . . . 103
9.6 Fit validation using pseudoexperiments . . . 105
9.6.1 Pseudoexperiments generated with SM predictions . . . 105
9.6.2 Pseudoexperiments generated with best fit values . . . 106
9.7 Fit validation on data using $B^0 \to J/\psi K^{*0}$ . . . 112
9.8 Validating the Run 1 and 2016 agreement using the $B^0 \to J/\psi K^{*0}$ decay . 114

10 Systematic uncertainties **121**
10.1 Fit bias . . . 122
10.2 Signal mass modelling . . . 122
10.3 Systematic uncertainties associated with the modelling of the $m_{K\pi}$ distribution 123
10.3.1 ISOBAR vs LASS for S-wave parameterisation . . . 123
10.3.2 Shape of the $m_{K\pi}$ background distribution . . . 123
10.3.3 Flat efficiency of the $m_{K\pi}$ distribution . . . 124
10.4 Angular background modelling . . . 124
10.5 Peaking backgrounds . . . 125
10.6 $B^+ \to K^+\mu^+\mu^-$ veto . . . 125
10.7 Higher order acceptance description . . . 127
10.8 Statistical uncertainty of the acceptance . . . 127
10.9 Agreement between data and simulation . . . 131
10.9.1 PID systematic . . . 131
10.9.2 Effects of reweighting $\chi^2_{\rm Vtx}$, $p_{\rm T}(B^0)$ and `nTracks` . . . 131
10.9.3 Kaon and pion momenta . . . 132
10.9.4 Trigger systematic . . . 132
10.10 Fixing of q^2 for four-dimensional acceptance . . . 136

11 Results **137**

12 Interpretation of results **149**

13 Conclusion and outlook **155**

References **157**

III Appendices 170

A Mass fits **171**

B Acceptance projections **173**

C Exotic charmonium states in $B^0 \to J/\psi K^+\pi^-$ **179**

D Fit validation using pseudoexperiments **181**

E Systematic uncertainties **194**

F Fit projections of the signal channel **214**

G Correlation matrices **222**

List of Figures

2.1 Feynman diagrams of the $B^0 \to K^{*0}\ell^+\ell^-$ decay . . . 38
2.2 Graphical representation of the angular basis . . . 41
2.3 Schematic of the $B \to K^{(\star)}\mu^+\mu^-$ differential branching fraction as a function of q^2. . . . 45
2.4 Theoretical challenges for calculating theory predictions . . . 46
2.5 Measurements and theory predictions of differential branching fractions of $b \to s\ell^+\ell^-$ decays . . . 48
2.6 Measurements and theory predictions of the P_5' observable . . . 49
2.7 Example of a global fit to $b \to s\ell^+\ell^-$ observables . . . 52

3.1 A cross-sectional view of the LHCb detector . . . 54
3.2 Simulated production of $b\bar{b}$ quark pairs in proton-proton collisions as a function of the opening angle . . . 55
3.3 Development of the instantaneous luminosity for ATLAS, CMS and LHCb during a representative LHC fill . . . 56
3.4 Cross sections of the VELO . . . 58
3.5 Resolutions of the PV and IP as functions of number of tracks and particle momentum . . . 58
3.6 Reconstructed Cherenkov angle as a function of track momentum . . . 60
3.7 Schematic of the calorimeter system illustrating the energy deposit of a photon, an electron and a charged hadron . . . 62
3.8 Side and front view of the muon systems . . . 63

5.1 Efficiencies and effects of the BDT . . . 78
5.2 Invariant $K^+\pi^-\mu^+\mu^-$ mass versus q^2 . . . 79

6.1 Fit to the $B^0 \to J/\psi\, K^{*0}$ control channel . . . 82
6.2 $K^+\pi^-\mu^+\mu^-$ invariant mass distribution of $B^0 \to K^{*0}\mu^+\mu^-$ candidates . . . 84

7.1 Distributions of the kaon $\mathrm{DLL}_{K\pi}$ variable . . . 86
7.2 Fit to the invariant mass of the $K^+\pi^-\mu^+\mu^-$ system for the $B^0 \to J/\psi\, K^{*0}$ control decay . . . 88
7.3 Distributions of `nTracks`, $p_{\mathrm{T}}(B^0)$ and χ^2_{Vtx} . . . 89

8.1 q^2 distributions of simulated events at generator level 93
8.2 One-dimensional projections of the four-dimensional acceptance functions . 95
8.3 Two-dimensional projections of the four-dimensional acceptance parameterisation for 2016 96

9.1 Physical region of the angular signal PDF when evaluated using the best fit values 108
9.2 Physical region of the angular signal PDF when evaluated using the SM values 109
9.3 Projections of the fitted probability density function for the $B^0 \to J/\psi K^{*0}$ decay 113
9.4 Acceptance corrected $B^0 \to J/\psi K^{*0}$ distributions 119

10.1 An example of the background fit for Run 1 and 2016 126
10.2 One-dimensional projections of the higher order acceptance functions . . . 128
10.3 Distributions of deviations of observables from pseudoexperiments generated with varied acceptances 130
10.4 Distributions of p and p_{T} for K^+ and π^- for $B^0 \to J/\psi K^{*0}$ candidates . . . 134
10.5 Correction factor for simulated events 135
10.6 Combined efficiency of the `L0Muon` and `L0DiMuon` trigger lines 135

11.1 Projections of the fitted probability density function 1 139
11.2 Projections of the fitted probability density function 2 140
11.3 Results of the fits for the *CP*-averaged angular observables 143
11.4 Results of the fits for the optimised angular observables 144
11.5 Results for the *CP*-averaged angular observables for Run 1, 2016 and the combined data set 145
11.6 Results for the optimised angular observables for Run 1, 2016 and the combined data set 146
11.7 Results for the *CP*-averaged angular observables for data sets corresponding to different magnet polarities 147
11.8 Results for the optimised angular observables for data sets corresponding to different magnet polarities 148

12.1 Likelihood scan of $\Delta\mathcal{R}e(C_9)$ 150
12.2 Fit to $\Delta\mathcal{R}e(C_9)$ and $\Delta\mathcal{R}e(C_{10})$ for different data sets 151

12.3 Fit to $\Delta\mathcal{R}e(C_9)$ and $\Delta\mathcal{R}e(C_{10})$ for different angular observables 153
12.4 Observable measurements of $F_{\rm L}$, $A_{\rm FB}$ and S_5 compared with their SM predictions and with predictions that shift $\mathcal{R}e(C_9)$ by -1.0 154

A.1 $K^+\pi^-\mu^+\mu^-$ invariant mass distribution of $B^0 \to K^{*0}\mu^+\mu^-$ candidates in the wide q^2 bins for Run 1 and 2016 171
A.2 $K^+\pi^-\mu^+\mu^-$ invariant mass distribution of $B^0 \to K^{*0}\mu^+\mu^-$ candidates in the narrow q^2 bins for Run 1 172

B.1 One-dimensional projections of the acceptance parametrisation on $\cos\theta_l$ . . 174
B.2 One-dimensional projections of the acceptance parametrisation on $\cos\theta_K$. 175
B.3 One-dimensional projections of the acceptance parametrisation on ϕ 176
B.4 Two-dimensional projections of the four-dimensional acceptance parameterisation for Run 1 177

C.1 $\cos\theta_K$ and $m(K^+\pi^-)$ distributions of toy experiments 180

F.1 Projections of the fitted probability density function on the decay angles 3 214
F.2 Projections of the fitted probability density function on the decay angles 4 215
F.3 Projections of the fitted probability density function on the decay angles 5 216
F.4 Projections of the fitted probability density function on the decay angles 6 217
F.5 Projections of the fitted probability density function on the decay angles 7 218
F.6 Projections of the fitted probability density function on the decay angles 8 219
F.7 Projections of the fitted probability density function on the decay angles 9 220
F.8 Projections of the fitted probability density function on the decay angles 10 221

List of Tables

2.1 Particle content of the Standard Model. 26
2.2 Angular observables I_i and their corresponding angular terms 43

3.1 Running conditions of the LHC and LHCb detector in the different years of data taking 55
3.2 Trigger lines 67

4.1 The q^2 binning chosen for the analysis 71

5.1 Stripping selection criteria 73
5.2 Pre-selection cuts applied to stripped candidates 74
5.3 Expected background contamination as a proportion of expected signal yield 76

6.1 Mass model parameters determined from fits to the $B^0 \to J/\psi K^{*0}$ control channel 82
6.2 Scaling factors s_σ 83
6.3 Signal and background yields 83

7.1 Data samples used for the resampling corrections 86

9.1 Fit validation 1 106
9.2 Fraction of pseudo-events with a negative signal PDF 107
9.3 Fit validation 2 111
9.4 Results of the angular fit of the $B^0 \to J/\psi K^{*0}$ decay 1 114
9.5 Results of the angular fit of the $B^0 \to J/\psi K^{*0}$ decay 2 116
9.6 Results of the angular fit of the $B^0 \to J/\psi K^{*0}$ decay 3 117
9.7 Results of the angular fit of the $B^0 \to J/\psi K^{*0}$ decay 4 118
9.8 Results of the angular fit of the $B^0 \to J/\psi K^{*0}$ decay 5 120

10.1 Summary of the different sources of systematic uncertainties 122
10.2 Results from the angular fit of the $B^0 \to J/\psi K^{*0}$ control decay using the higher order acceptance description 129

11.1 Results for the *CP*-averaged observables 141
11.2 Results for the optimised observables $P_i^{(\prime)}$ 142

C.1 Result of fitting either the angular or $m(K^+\pi^-)$ distribution of toy experiments for the S-wave fraction . . . 180

D.1 Fit validation 1 . . . 182
D.2 Fit validation 2 . . . 183
D.3 Fit validation 3 . . . 184
D.4 Fit validation 4 . . . 185
D.5 Fit validation 5 . . . 186
D.6 Fit validation 6 . . . 187
D.7 Fit validation 7 . . . 188
D.8 Fit validation 8 . . . 189
D.9 Fit validation 9 . . . 190
D.10 Fit validation 10 . . . 191
D.11 Fit validation 11 . . . 192
D.12 Fit validation 12 . . . 193

E.1 Summary of systematic uncertainties 1 . . . 194
E.2 Summary of systematic uncertainties 2 . . . 195
E.3 Summary of systematic uncertainties 3 . . . 196
E.4 Summary of systematic uncertainties 4 . . . 197
E.5 Summary of systematic uncertainties 5 . . . 198
E.6 Summary of systematic uncertainties 6 . . . 199
E.7 Summary of systematic uncertainties 7 . . . 200
E.8 Summary of systematic uncertainties 8 . . . 201
E.9 Summary of systematic uncertainties 9 . . . 202
E.10 Summary of systematic uncertainties 10 . . . 203
E.11 Summary of systematic uncertainties 11 . . . 204
E.12 Summary of systematic uncertainties 12 . . . 205
E.13 Summary of systematic uncertainties 13 . . . 206
E.14 Summary of systematic uncertainties 14 . . . 207
E.15 Summary of systematic uncertainties 15 . . . 208
E.16 Summary of systematic uncertainties 16 . . . 209
E.17 Summary of systematic uncertainties 17 . . . 210
E.18 Summary of systematic uncertainties 18 . . . 211
E.19 Summary of systematic uncertainties 19 . . . 212

E.20 Summary of systematic uncertainties 20 213

G.1 Correlation matrix 1 222
G.2 Correlation matrix 2 222
G.3 Correlation matrix 3 223
G.4 Correlation matrix 4 223
G.5 Correlation matrix 5 224
G.6 Correlation matrix 6 224
G.7 Correlation matrix 7 225
G.8 Correlation matrix 8 225
G.9 Correlation matrix 9 226
G.10 Correlation matrix 10 226
G.11 Correlation matrix 11 227
G.12 Correlation matrix 12 227
G.13 Correlation matrix 13 228
G.14 Correlation matrix 14 228
G.15 Correlation matrix 15 229
G.16 Correlation matrix 16 229
G.17 Correlation matrix 17 230
G.18 Correlation matrix 18 230
G.19 Correlation matrix 19 231
G.20 Correlation matrix 20 231

1. Introduction

The Standard Model (SM) of particle physics is unquestionably the most successful theory of the fundamental building blocks of nature and the forces that hold them together. It allows obtaining exceptionally good predictions for experimental results, which have an unprecedented accuracy. A comparison between the measurement of the anomalous magnetic moment of the electron [3] with its most recent prediction [4] illustrates this accuracy:

$$\begin{aligned} a_{\text{experiment}} &= 0.001159652180730 \pm 0.000000000000028 \\ a_{\text{theory}} &= 0.001159652181606 \pm 0.000000000000023. \end{aligned} \tag{1.1}$$

Comparing the theory prediction with the experimental measurement one observes an impressive agreement up to the 12^{th} digit.

Despite its success, the SM has several drawbacks and limitations. It does not incorporate gravity, nor does it account for Dark Matter [5] that is known to constitute up to 27% of the energy density in the universe [6]. Furthermore, the SM does not fully account for the matter-antimatter asymmetry that is observed in our cosmos [7, 8].

An intrinsic issue of the SM is its need for a substantial amount of experimental input. Many SM parameters are artificially 'fine-tuned' to experimental measurements, such as the masses of the fundamental particles, as well as the gauge couplings of the forces. This is not only theoretically unsatisfactory but it also gives rise to the 'unnaturalness' of the theory. This manifests itself in the low mass of the Higgs boson, discovered as the last piece of the SM puzzle by the ATLAS [9] and CMS [10] collaborations. The Higgs mass is measured to be $\sim 125\,\text{GeV}/c^2$, which is far too low if one makes the reasonable assumption that the SM breaks down at the Planck scale, lying at $\sim 10^{18}\,\text{GeV}$. One could therefore naively expect that the loop corrections push up the Higgs mass to the Planck scale, which is 10^{16} orders of magnitude higher than the measured mass. As this is not the case, contributions that exactly cancel the loop corrections must be present. Theoretically, this fine-tuning is difficult to motivate without introducing New Physics (NP), *i.e.* physics that lies beyond the SM.

Many extensions of the SM have proposed NP particles that are responsible for additional loop corrections, contributing with the opposite sign than those coming from the SM particles. Given the mass of the Higgs, these new particles are expected to appear

at the TeV scale. Despite the many searches performed by ATLAS and CMS, to date no evidence for NP particles has been found.

Two types of searches are typically conducted to discover NP using High Energy Physics (HEP) experiments. Direct searches aim to produce NP particles and subsequently measure them, *e.g.* via a peak in an invariant mass spectrum. One of the drawbacks of these searches is that they are limited by the energy of the beam, which produces the particles. By contrast, indirect searches have a much higher energy reach, as they take into account the possibility of virtual NP particle contributions. Indirect searches compare precisely determined predictions with their corresponding measurements and investigate their level of agreement.

Historically, indirect measurements have played an important role in the discovery of new particles, one of the most famous being the search for the $K_s \to \mu^+\mu^-$ decay performed in 1969 [11]. At the time only three of the six quarks of the SM had been discovered, the Up, the Down and the Strange quark. Using these three quarks to make predictions of the corresponding branching fraction, one would have expected a discovery of the $K_s \to \mu^+\mu^-$ decay. However, no signal was detected in the experiment. Its absence was explained by the Glashow-Iliopoulos-Maiani (GIM) mechanism [12], predicting a fourth quark interfering destructively, and thereby reducing the value of the branching fraction. The existence of the c quark was subsequently verified by the discovery of the J/ψ particle. Two research groups, one at the Brookhaven National Laboratory, lead by Samuel Ting and one at the Stanford Linear Accelerator Centre, headed by Burton Richer, accomplished this milestone of particle physics. [13, 14].

In recent years, indirect searches related to the family of rare $b \to s\ell^+\ell^-$ decays attracted great interest, as they indicate a very intriguing pattern of deviations from SM predictions. These deviations are seen in measurements that include angular observables [2, 15–21], branching fractions [21–24], as well as ratios of branching fractions between decays with different flavours of leptons [25–30]. The theoretical and experimental interest in these measurements resides in the fact that existing results can be interpreted in a coherent way in a NP framework. To be more precise, the measurements can all be explained by introducing a new vector or axial-vector particle, such as a Z' or a leptoquark [31–46].

This thesis presents the angular analysis of the $B^0 \to K^{*0}\mu^+\mu^-$ decay performed by the LHCb collaboration [1], in which observables are determined via fits to the angular distributions of the decay products. The relevant data was taken in the years 2011, 2012 and 2016, and the results of the observables are the most precise to date, reducing the

uncertainty of the previously measured observables [2] by approximately 30%. The analysis uses similar techniques to those described in Ref. [2], while also benefiting from the larger data sample that contains approximately twice as many B^0 decays, owing to the addition of the 2016 data. Moreover, one of the main systematic uncertainties has been reduced tenfold.

This thesis has three parts. Part I introduces the main theoretical concepts and subsequently gives an overview of the LHCb detector. The angular analysis of the $B^0 \to K^{*0}\mu^+\mu^-$ decay and the interpretation of its results is presented in Part II. Part III contains supplementary material. With the exception of Sec. 2.9.1 and Sec. 2.9.2, charge conjugation is implied throughout this thesis.

Part I

Theoretical and experimental overview

2. Theory of the Standard Model and the $B^0 \to K^{*0}\mu^+\mu^-$ decay

This chapter introduces the most relevant theoretical and experimental concepts needed to motivate the angular analysis of the $B^0 \to K^{*0}\mu^+\mu^-$ decay. The first part of the chapter, based on Refs. [47–49], gives an overview of the SM. The second part introduces the concept of flavour changing neutral currents, effective field theories and the theoretical description of the $B^0 \to K^{*0}\mu^+\mu^-$ decay. A short summary of the experimental status of $b \to s\ell^+\ell^-$ decays and their theoretical context in terms of global fits is given in the last section of the chapter.

2.1 Particles and interactions in the Standard Model

The SM is a Quantum Field Theory (QFT) that describes the constituents of matter and their interactions. The three fundamental forces that are present in the SM are the electromagnetic, the weak and the strong force. Each of these forces is mediated by gauge bosons of spin one. Electrically charged particles such as protons and electrons exchange photons, resulting in the electromagnetic attraction that holds atoms together. The strong force binds the quarks into nucleons and nucleons into nuclei via the exchange of gluons. The W and Z bosons are the force carriers of the weak interaction, which is responsible for particles changing their flavour.

In the SM leptons and quarks, both types of fermions with a spin of one-half, are the constituents of matter. Neutral leptons (the neutrinos) are only affected by the weak force, charged leptons feel the weak and the electromagnetic force, while quarks are sensitive to all three fundamental forces described by the SM. Both leptons and quarks come in three generations of varying mass. In order of increasing mass, the charged leptons consist of electrons (e^-), muons (μ^-) and taus (τ^-). Their corresponding neutrinos are the electron neutrino (ν_e), the muon neutrino (ν_μ) and the tau neutrino (ν_τ). Each of the three pairs has a different flavour, which is preserved in the SM. Similarly, the six types of quarks can be grouped into three generations. These are the up (u) and down (d) quark, the charm (c) and strange (s) quark, and the top (t) and bottom (b) quark. Unlike the six lepton types, each quark type has its own flavour that is not preserved. Fermions' chirality can be either right- or left-handed, which in the massless limit corresponds to the spin of the

particle being aligned or anti-aligned with its momentum.

The SM is completed by the Higgs boson, which is a spin zero particle and appears as a consequence of the Higgs mechanism that generates masses for the W and Z bosons and the fermions. The Higgs mechanism and its crucial role in the creation of mass and flavour changing processes are the main topics of the first part of this chapter.

A full list of the SM particles along with their masses and electrical charges are given in Tab. 2.1. The corresponding anti-particles have exactly the same mass but opposite physical charges. As the anti-particle of the electron, the positron has positive electrical charge and a lepton number of minus one. An electron-positron pair can therefore be created from an energetic photon, while still preserving both electrical charge and lepton number.

	Fermions			**Bosons**	
generation	1	2	3	vector	scalar
charged leptons	e	μ	τ	γ	h
$(q = +1)$	511 keV	106 MeV	1.78 GeV	0	125 GeV
neutrinos	ν_e	ν_μ	ν_τ	W^+	
$(q = 0)$	< 2 eV	< 2 eV	< 2 eV	80.4 GeV	
up-type quarks	u	c	t	Z^0	
$(q = +2/3)$	2.2 MeV	1.30 GeV	170 GeV	91.2 GeV	
down-type quarks	d	s	b	g	
$(q = -1/3)$	4.7 MeV	96 MeV	4.6 GeV	0	

Table 2.1: Particle content of the Standard Model. The mass of each particle (taken from Ref. [50]) is indicated below its symbol. Table taken from Ref [51], where the convention of $c = 1$ is used.

One of the most fascinating properties of the SM are the various symmetries that the particles and their interactions must obey. Two of these symmetries, namely electrical charge conservation and lepton number conservation, were already introduced. A different type of symmetry in the SM is given by the three discrete transformations C, T and P, where C conjugates the electrical charge, T represents time reversal and P flips the three spatial components. While the electromagnetic and strong forces respect all three symmetries, the electroweak force maximally breaks both parity and charge conjugation, as well as their combination.

One family of symmetries that is fundamental to the SM are the global and local gauge symmetries. The next section will describe gauge transformations in the context of the electromagnetic part of the SM Lagrangian, *i.e.* the Lagrangian of Quantum ElectroDynamics (QED).

2.2 Global and local gauge symmetries in QED

The motion of a free electron is described by the Dirac equation:

$$i\gamma^\mu \partial_\mu e = m_e e, \tag{2.1}$$

where e represents the electron field, m_e is the electron mass and γ^μ are the Dirac matrices. The corresponding Lagrangian can be constructed as follows:

$$\mathcal{L} = i\bar{e}\gamma^\mu \partial_\mu e - m_e \bar{e} e. \tag{2.2}$$

The Lagrangian is invariant under global gauge transformations, where the field transforms as $e \to \exp(i\theta)e$. However, when considering a local gauge transformation $e(x) \to \exp(i\theta(x))e$, where θ now depends on the position x, the Lagrangian transforms as $\mathcal{L} \to \mathcal{L} - \partial_\mu \theta(x)\bar{e}\gamma^\mu e$ and is not invariant under the transformation. Therefore, the photon field, A_μ, is introduced and set to transform as $A_\mu \to A_\mu - \partial_\mu \lambda(x)$, where $\lambda(x) = \theta(x)/g_e$ and g_e is the coupling strength between the photon field and the e field. Adding the interaction term of the photon field with the electron field results in the QED Lagrangian:

$$\mathcal{L} = i\bar{e}\gamma^\mu \partial_\mu e - m_e \bar{e} e - g_e \bar{e}\gamma^\mu e A_\mu - \frac{1}{4} F^{\mu\nu} F_{\mu\nu}, \tag{2.3}$$

which is now invariant under local gauge transformations. The term $F^{\mu\nu}F_{\mu\nu}$ has been added to account for the kinetic energy of the photon, where $F^{\mu\nu} = \partial^\mu A^\nu - \partial^\nu A^\mu$ is the electromagnetic field tensor. A mass term for the photon, given by $m_\gamma A^\mu A_\mu$, would not be invariant under local gauge transformations and does not appear in the above expression, as the photon is massless.

The QED Lagrangian can be expressed in a concise way using the covariant derivative, defined as:

$$D_\mu = \partial_\mu - i g_e A_\mu. \tag{2.4}$$

Employing this definition, the QED Lagrangian can then be re-written as

$$\mathcal{L} = \overline{e}(i\gamma^{\mu}D_{\mu} - m)e - \frac{1}{4}F^{\mu\nu}F_{\mu\nu}. \tag{2.5}$$

The introduction of an additional interaction term, which makes the theory invariant under local gauge transformations, is not only a mathematical trick, but also has fundamental physical implications. More precisely, local gauge symmetries in the SM are responsible for interaction terms and therefore for the appearance of forces between fields and particles.

In the language of group theory, QED is described as an Abelian gauge theory with symmetry group $\mathrm{U}(1)_{\mathrm{EM}}$. In the SM, the electromagnetic and the weak force are unified under a non-Abelian gauge theory with symmetry group $\mathrm{SU}(2) \times \mathrm{U}(1)$. From a model building point of view, the electroweak force is more complicated than the electromagnetic force as the charge carriers, the W and Z, are massive and as the W bosons only act on left-handed particles. The introduction of the corresponding fields is therefore not as straightforward as in the case of the photon. In order to preserve gauge invariance, the concept of spontaneous symmetry breaking needs to be employed. The next section will set the basis for the electroweak unification.

2.3 Spontaneous symmetry breaking

Spontaneous symmetry breaking is one of the most intriguing concepts in QFT. Rather than explicitly breaking a symmetry, as the weak force does with parity, spontaneous symmetry breaking preserves the invariance of the Lagrangian under the symmetry and only breaks it in the ground state. This concept can be illustrated via the following Lagrangian describing a real scalar field $\Phi(x)$:

$$\mathcal{L} = \frac{1}{2}\partial_{\mu}\Phi\partial^{\mu}\Phi - V(\Phi), \tag{2.6}$$

where the potential $V(\Phi)$ is given by:

$$V(\Phi) = \frac{1}{2}m^2\Phi^2 + \frac{\lambda}{4}\Phi^4; \lambda > 0. \tag{2.7}$$

The above Lagrangian is invariant under the discrete symmetry $\Phi \to -\Phi$. If $m^2 > 0$, *i.e.* Φ is massive, $V(\Phi)$ has a minimum at $\Phi = 0$. The symmetry for this minimum is preserved as the behaviour of the potential is the same, whether moving towards positive or negative Φ.

This picture changes if $m^2 < 0$. Completing the square and dropping the remaining constant, the potential is given by:

$$V(\Phi) = \frac{\lambda}{4}(\Phi^2 - v^2)^2, \tag{2.8}$$

where $v = \sqrt{-m^2/\lambda}$. The resulting 'double-well' potential turns V at $\Phi = 0$ into a maximum and instead has two degenerate minima at $\Phi = \pm v$, *i.e.* Φ has acquired a non-zero vacuum expectation value (VEV). The symmetry of the minima can again be analysed by moving towards the positive or negative direction of Φ. Mathematically, a perturbative expansion around $\Phi = v$[1] can be performed, replacing $\Phi(x)$ with $\Phi(x) = v + f(x)$. Using this expression and Eq. 2.8, Eq. 2.6 now reads:

$$\mathcal{L} = \frac{1}{2}\partial_\mu f \partial^\mu f - \lambda\left(v^2 f^2 + v f^3 + \frac{1}{4} f^4\right). \tag{2.9}$$

The quadratic term indicates that $f(x)$ is a scalar field representing massive excitations with $m_f^2 = 2\lambda v^2$. As the Lagrangian is not invariant under $f \to -f$, its symmetry is spontaneously broken under the minimum. However, it is not explicitly broken as the original symmetry of $\Phi \to -\Phi$ corresponding to $f \to -f - 2v$ is preserved.

2.4 The Higgs mechanism and electroweak unification

The electroweak theory, which is the unification of the electromagnetic and weak forces, is the result of the collaboration of Steven Weinberg and Abdus Salam who build on the work of Sheldon Glashow [52–54]. This gauge-invariant theory, with symmetry group $\mathrm{SU}(2) \times \mathrm{U}(1)$, is therefore also referred to as the GWS theory. The gauge symmetry of the GWS theory is spontaneously broken by the Higgs mechanism [55, 56], resulting in the weak gauge bosons becoming massive.

This section is presented in four parts: Sec. 2.4.1 lists all the relevant fields of the electroweak theory, Sec. 2.4.2 introduces the Higgs mechanism and how the W and Z bosons acquire mass, Sec. 2.4.3 gives an overview of how the fermions become massive via the Yukawa terms, and Sec. 2.4.4 discusses the CKM mixing matrix.

[1] One could have, without loss of generality, also chosen the minimum at $\Phi = -v$.

2.4.1 Fields of the electroweak theory

In the GWS theory the gauge fields corresponding to $SU(2)$ and $U(1)$ are $W^a_\mu (a = 1, 2, 3)$ and A_μ, respectively. The matter constituents of the theory are quarks and leptons, which are divided into left- and right-handed chiral fields ψ_L and ψ_R, given by:

$$\psi_L = P_L\psi = \frac{(1+\gamma^5)}{2}\psi, \tag{2.10}$$

$$\psi_R = P_R\psi = \frac{(1-\gamma^5)}{2}\psi, \tag{2.11}$$

where $\gamma^5 = i\gamma^0\gamma^1\gamma^2\gamma^3$, and P_L and P_R are operators that project out the left and right handed fields respectively. The left-handed fields are paired up in three SU(2) doublets for the leptons (L) and three SU(2) doublets for the quarks (Q):

$$\begin{aligned} L^i &= \begin{pmatrix} \nu^i \\ \ell^i \end{pmatrix}_L = \begin{pmatrix} \nu_e \\ e \end{pmatrix}_L, \begin{pmatrix} \nu_\mu \\ \mu \end{pmatrix}_L, \begin{pmatrix} \nu_\tau \\ \tau \end{pmatrix}_L \\ Q^i &= \begin{pmatrix} u^i \\ d^i \end{pmatrix}_L = \begin{pmatrix} u \\ d \end{pmatrix}_L, \begin{pmatrix} c \\ s \end{pmatrix}_L, \begin{pmatrix} t \\ b \end{pmatrix}_L, \end{aligned} \tag{2.12}$$

with $i \in \{1, 2, 3\}$. The right-handed fermions are arranged in nine singlets:

$$\begin{aligned} u^i_R &= u_R \ , \ c_R \ , \ t_R \\ d^i_R &= d_R \ , \ s_R \ , \ b_R \\ l^i_R &= e_R \ , \mu_R \ , \tau_R. \end{aligned} \tag{2.13}$$

The last component of the theory is the scalar Higgs (ϕ), given by a doublet of scalar complex fields:

$$\phi = \begin{pmatrix} \phi^+(x) \\ \phi^0(x) \end{pmatrix}. \tag{2.14}$$

The Higgs field and the fermion fields ψ transform under the local gauge transformation corresponding to SU(2) × U(1) as

$$\phi(x) \to \exp(\mathrm{i}\alpha^{\mathrm{a}}(x)\tau^a)\exp\left(\frac{\mathrm{i}\beta(x)}{2}\right)\phi(x), \tag{2.15}$$

$$\psi(x) \to \exp(\mathrm{i}\alpha^{\mathrm{a}}(x)\tau^a)\exp\left(\frac{\mathrm{i}\beta(x)}{2}\right)\psi(x), \tag{2.16}$$

where $\tau^a = \sigma^a/2$ are the three generators of SU(2) and σ^a are the Pauli matrices. Similarly as for QED (see Sec. 2.2), the corresponding covariant derivative D_μ is given by

$$D_\mu = \left(\partial_\mu + igW_\mu^a \tau^a + \frac{i}{2} g' B_\mu\right), \tag{2.17}$$

where g and g' are the couplings of the corresponding gauge bosons. One example where the covariant derivative appears in the electroweak Lagrangian are the coupling terms between the fermions and the gauge bosons:

$$\mathcal{L}^I = i\overline{Q}^i \gamma^\mu D_\mu Q^i + i\overline{u}_R^i \gamma^\mu D_\mu u_R^i + i\overline{d}_R^i \gamma^\mu D_\mu d_R^i + i\overline{L}^i \gamma^\mu D_\mu L^i + i\overline{\ell}_R^i \gamma^\mu D_\mu \ell_R^i. \tag{2.18}$$

The five terms of the interaction Lagrangian have the same structure as the interaction term in the QED Lagrangian (see Eq. 2.5).

2.4.2 The Higgs mechanism

The Higgs Lagrangian can be written as

$$\mathcal{L} = (D_\mu \phi)^\dagger (D^\mu \phi) - V(\phi), \tag{2.19}$$

where the Higgs potential $V(\phi)$ is given by

$$V(\phi) = \mu^2 \phi^\dagger \phi + \lambda (\phi^\dagger \phi)^2. \tag{2.20}$$

As in Sec. 2.3, the Higgs potential is spontaneously broken when choosing $\mu^2 < 0$. The positions of the minima are now given by $\phi^\dagger \phi = v^2/2$, where v is defined as $v^2 = -\mu^2/\lambda$. Without loss of generality the vacuum expectation value can be chosen to be

$$\phi_0 = \frac{1}{\sqrt{2}} \begin{pmatrix} 0 \\ v \end{pmatrix}. \tag{2.21}$$

Substituting this value into the first term of the Higgs Lagrangian ($(D_\mu \phi)^\dagger (D^\mu \phi)$), the following expression is obtained:

$$
\begin{aligned}
&\frac{1}{2}(0,v)\left(-igW_\mu^a\tau^a-\frac{i}{2}g'B_\mu\right)\left(igW^{a\mu}\tau^a+\frac{i}{2}g'B^\mu\right)\begin{pmatrix}0\\v\end{pmatrix}\\
=&\frac{1}{2}\frac{v^2}{4}\left[g^2(W^1)^2+g^2(W^2)^2+(-gW^3+g'B)^2\right]\\
=&\frac{1}{2}\left(m_W^2(W_\mu^+)^\dagger W^{\mu+}+m_W^2(W_\mu^-)^\dagger W^{\mu-}+m_Z^2(Z_\mu^0)^\dagger Z^{\mu 0}\right).
\end{aligned}
\tag{2.22}
$$

The last line of the above calculation introduces mass terms of the physical gauge fields W^+, W^- and Z, where

$$
\begin{aligned}
W_\mu^\pm&=\frac{1}{\sqrt{2}}(W_\mu^1\mp iW_\mu^2),\\
Z_\mu^0&=\frac{1}{\sqrt{g^2+g'^2}}(gW_\mu^3-g'B_\mu),
\end{aligned}
\tag{2.23}
$$

and the corresponding masses are $m_W=vg/2$ and $m_Z=v\sqrt{g^2+g'^2}/2$. As expected, the mass term of the physical gauge field of the photon A_μ does not appear in Eq. 2.22 due to the photon being massless. The gauge field of the photon is related to W_μ^3 and B_μ via

$$
A_\mu=\frac{1}{\sqrt{g^2+g'^2}}(g'W_\mu^3+gB_\mu). \tag{2.24}
$$

The mixing of the $SU(2)$ and $U(1)$ gauge bosons can be described in terms of the weak mixing angle θ_W, defined by

$$
\begin{pmatrix}Z^0\\A\end{pmatrix}=\begin{pmatrix}\cos\theta_W & -\sin\theta_W\\ \sin\theta_W & \cos\theta_W\end{pmatrix}\begin{pmatrix}W^3\\B\end{pmatrix}, \tag{2.25}
$$

and

$$
\cos\theta_W=\frac{g}{\sqrt{g^2+g'^2}},\ \sin\theta_W=\frac{g'}{\sqrt{g^2+g'^2}}. \tag{2.26}
$$

The weak mixing angle also links m_W and m_Z via $m_W=m_Z\cos\theta_W$ and the electromagnetic coupling g_e to the couplings g and g' via $g_e=g\sin\theta_W=g'\cos\theta_W$.

2.4.3 Fermion masses

Recalling the QED Lagrangian given in Eq. 2.3, the mass term of the electron field is given by $m\bar{e}e = m(\bar{e}_L e_R + \bar{e}_R e_L)$. Mass terms of this same form cannot appear in the electroweak Lagrangian, as the weak force is not chirally invariant, *i.e.* it couples differently to left-handed and right-handed fermions. The solution to this problem is once more the Higgs mechanism, which can be employed to give the fermions mass.

The part of the electroweak Lagrangian that is responsible for the mass of the fermions is called the Yukawa Lagrangian. To illustrate how the fermions acquire mass under spontaneous symmetry breaking it is useful to first restrict oneself to the first lepton generation. The Yukawa term can then be written as follows:

$$\mathcal{L}_{e,\phi} = -\sqrt{2}\lambda_e \left[(\overline{\nu}_e \;\; \overline{e})_L \begin{pmatrix} \phi^+ \\ \phi^0 \end{pmatrix} e_R + \overline{e}_R \left(\phi^{+*} \;\; \phi^{0*}\right) \begin{pmatrix} \nu_e \\ e \end{pmatrix}_L \right], \tag{2.27}$$

where λ_e is the Yukawa coupling. Unlike the term $m\bar{e}e$, $\mathcal{L}_{e,\phi}$ is $SU(2) \times U(1)$ invariant. Spontaneously breaking the symmetry, one can expand about the VEV of the Higgs field as was done in Sec. 2.3, *i.e.*

$$\phi(x) = \frac{1}{\sqrt{2}} \begin{pmatrix} 0 \\ v + h(x) \end{pmatrix}, \tag{2.28}$$

where the field $h(x)$ now corresponds to the physical Higgs boson. Inserting Eq. 2.28 into Eq. 2.27 results in the following term:

$$\mathcal{L}_{e,\phi} = -\lambda_e h \left(\overline{e}_L e_R + \overline{e}_R e_L\right) - \lambda_e v \left(\overline{e}_L e_R + \overline{e}_R e_L\right), \tag{2.29}$$

where the first part corresponds to the interaction between the Higgs and the electron field and the second part corresponds to the mass term of the electron. Using the Higgs mechanism, the electron acquires a mass $m_e = \lambda_e v$, while the electron neutrino stays massless. A similar approach can be used for the quarks, but in this case the top part of the doublets (the Up-type quarks) also picks up mass. The corresponding Yukawa Lagrangian therefore contains not only one term for the Down-Type, but also one for the Up-Type quarks. Similarly to the approach above, in the case of only one generation of quarks, the Yukawa Lagrangian is

$$\begin{aligned}\mathcal{L}_{q,\phi} = &-\sqrt{2}\lambda_d \left[\begin{pmatrix} \overline{u} & \overline{d} \end{pmatrix}_L \begin{pmatrix} \phi^+ \\ \phi^0 \end{pmatrix} d_R + \overline{d}_R \begin{pmatrix} \phi^{+*} & \phi^{0*} \end{pmatrix} \begin{pmatrix} u \\ d \end{pmatrix}_L \right] \\ &-\sqrt{2}\lambda_u \left[\begin{pmatrix} \overline{u} & \overline{d} \end{pmatrix}_L (i\sigma_2) \begin{pmatrix} \phi^{+*} \\ \phi^{0*} \end{pmatrix} u_R + \overline{u}_R \begin{pmatrix} \phi^0 & \phi^+ \end{pmatrix} (-i\sigma_2^\dagger) \begin{pmatrix} u \\ d \end{pmatrix}_L \right].\end{aligned} \tag{2.30}$$

Due to the introduction of the Pauli matrices in the second part of $\mathcal{L}_{q,\phi}$, spontaneous symmetry breaking leads to a mass term not only for the Down-type, but also for the Up-type quarks. The respective mass terms are given by $m_d = \lambda_d v$ and $m_u = \lambda_u v$.

Including all three generations of quarks and leptons, the mass term of the Yukawa Lagrangian, after symmetry breaking, reads

$$\mathcal{L}^{\text{Yuk}} = v \left[-\lambda^\ell_{ij} \overline{\ell}^i_L \ell^j_R - \lambda^d_{ij} \overline{d}^i_L d^j_R - \lambda^u_{ij} \overline{u}^i_L u^j_R + \text{h.c.} \right], \tag{2.31}$$

where h.c. is the hermitian conjugate of the three terms and λ^ℓ_{ij}, λ^d_{ij} and λ^u_{ij} are the entries of the 3×3 Yukawa coupling matrices. As the lepton and quark fields are in the 'flavour basis', the Yukawa matrices are allowed to contain non-zero off-diagonal terms. By rotating the fermion fields to their 'mass basis', the Yukawa matrices are diagonalised.

Considering the quarks, the Yukawa matrices are diagonalised by four unitary matrices U_u, U_d, S_u and S_d:

$$\lambda^u = U_u \Lambda^u S_u^\dagger \ , \ \lambda^d = U_d \Lambda^d S_d^\dagger, \tag{2.32}$$

where Λ^u and Λ^d are diagonal. The quark fields are then rotated by the four matrices as

$$u_L \to U_u u_L \ , \ d_L \to U_d d_L \ , \ u_R \to S_u u_R \ , \ d_R \to S_R d_R. \tag{2.33}$$

The rotation of the quark fields does not leave the rest of the electroweak Lagrangian unchanged. For example for $\mathcal{L}^I$, given in Eq. 2.18, the term $i\overline{L}^i D_\mu L^i$ is not invariant under the rotation. Specifically, the interaction parts involving quark coupling to $W^\pm$ pick up an extra factor $V_{\text{CKM}} = U_u^\dagger U_d$, where V_{CKM} is the Cabibbo-Kobayashi-Maskawa (CKM) matrix [57, 58] (see Sec. 2.4.4 for a detailed description).

Considering the leptons, only two unitary matrices are needed to diagonalise the Yukawa matrix λ^ℓ, as neutrinos do not possess a mass term. The resulting rotation therefore leaves $\mathcal{L}^I$ unchanged. The fact that the Yukawa matrix can be diagonalised while leaving $\mathcal{L}^I$ invariant means that leptons in the electroweak theory are both in their mass and their flavour basis. This gives rise to lepton number conservation.

2.4.4 CKM mixing matrix

The CKM matrix is a unitary matrix responsible for the inter-generational mixing of quarks. It has four free parameters[2] that are determined experimentally. Three of which are the quark mixing angles and one is the *CP* violating phase. The standard parameterisation of the CKM matrix for flavour mixing is [59]:

$$\begin{aligned} V_{\text{CKM}} &= \begin{pmatrix} V_{ud} & V_{us} & V_{ub} \\ V_{cd} & V_{cs} & V_{cb} \\ V_{td} & V_{ts} & V_{tb} \end{pmatrix} \\ &= \begin{pmatrix} c_{12}c_{13} & s_{12}c_{13} & s_{13}e^{-i\delta} \\ -s_{12}c_{23} - c_{12}s_{23}s_{13}e^{i\delta} & c_{12}c_{23} - s_{12}s_{23}s_{13}e^{i\delta} & s_{23}c_{13} \\ s_{12}c_{23} - c_{12}c_{23}s_{13}e^{i\delta} & -c_{12}s_{23} - s_{12}c_{23}s_{13}e^{i\delta} & c_{23}c_{13} \end{pmatrix}, \end{aligned} \tag{2.34}$$

where $s_{ij} = \sin(\theta_{ij})$, $c_{ij} = \cos(\theta_{ij})$, θ_{12}, θ_{13} and θ_{23} are the Euler angles, and δ is the phase responsible for the *CP* violation. In fact, the *CP* violating phase in the CKM matrix is the only place in the SM, which causes *CP* violation, making its determination one of the main goals of flavour physics.

Wolfenstein introduced another parameterisation that better reflects the hierarchical structure of the CKM mixing matrix [60]. This parameterisation is an expansion in terms of the parameter λ:

$$V_{\text{CKM}} = \begin{pmatrix} 1 - \lambda^2/2 & \lambda & A\lambda^3(\rho - i\eta) \\ -\lambda & 1 - \lambda^2/2 & A\lambda^2 \\ A\lambda^3(1 - \rho - i\eta) & -A\lambda^2 & 1 \end{pmatrix} + \mathcal{O}(\lambda^4), \tag{2.35}$$

where $\lambda = \sin(\theta_{12}) \approx 0.22$, $A\lambda^2 = \sin(\theta_{23})$ and $A\lambda^3(\rho - i\eta) = \sin(\theta_{13})\exp(-i\rho)$. The Wolfenstein parameterisation illustrates that the size of the coupling of quarks is smallest between the 1st and 3rd generation and biggest for quarks in the same generation.

2.5 Quantum Chromodynamics

Quantum ChromoDynamics (QCD) is the theory of the strong force, which is responsible for binding quarks in the nucleons. The symmetry group of QCD is $SU(3)$ and, unlike the

[2] A 3×3 complex matrix has 18 free parameters. Due to the unitarity condition these are reduced to 9. Another 5 can be eliminated by transforming the quark fields under $U(1)$, leaving 4 free parameters.

electroweak symmetry group, it remains unbroken. The massless gauge bosons of QCD are the eight gluons, and the conserved charge that arises out of the gauge symmetry is known as colour. Quarks are either of red, blue or green colour, while anti-quarks are of an anti-colour of the same set. In nature, quarks cannot be found on their own, but are confined to combinations of white colour: mesons consist of a quark with one colour and an anti-quark with the corresponding anti-colour, while baryons consist of three quarks of different colours (just as with real colours, red + blue + green = white).

Mathematically, the confinement of quarks is described in terms of the coupling constant of the strong force, g_S, that increases with distance (or equivalently decreases with energy). Consequently, when trying to separate quarks, an increasing amount of energy is needed the further apart they are from each other. This increase in potential energy ultimately results in the spontaneous production of further combinations of quarks that again are colourless. The quarks are said to hadronise before they can be separated.

Conversely, the closer quarks get to each other (or equivalently the higher energy scales they are at), the smaller g_S becomes, a process called 'asymptotic freedom'. From a theoretical point of view, asymptotic freedom allows for perturbative QCD calculations at high energy scales. The boundary at which the perturbative expansions break down is called the QCD scale, Λ_{QCD}, which is estimated to be at approximately 200 MeV. Below Λ_{QCD} the coupling constant takes values that are higher than one and therefore other techniques than perturbation theory have to be used to make meaningful predictions. Some of these techniques are introduced in Sec. 2.9.3, where the theoretical predictions for the $B^0 \to K^{*0}\mu^+\mu^-$ decay are described.

2.6 Summary of the SM and NP

The SM is the most established theory of particle physics. Its gauge group is the direct product of $SU(3) \times SU(2) \times U(1)$, where $SU(3)$ is the gauge group of QCD and $SU(2) \times U(1)$ is the gauge group of the electroweak theory. While the $SU(3)$ symmetry remains unbroken, the $SU(2) \times U(1)$ symmetry is spontaneously broken down to the $U(1)$ symmetry of QED by the Higgs Mechanism. The weak and electromagnetic forces are therefore only observed separately. The Higgs mechanism is also responsible for the masses of the W and Z gauge bosons, the Higgs boson and the fermions. The process through which the fermions acquire mass is of special interest in flavour Physics, as it not only results in the CKM matrix, being responsible for quark flavour mixing, but also in lepton

number conservation. The latter is the case as neutrinos in the SM are massless.

As mentioned in Chpt. 1 the SM has several drawbacks, as it cannot explain several experimental observations and is theoretically fine-tuned. The search for NP particles that could resolve some of the issues of the SM is therefore one of the central goals of modern particle physics. The following sections will introduce measurements related to the family of $b \to s\ell^+\ell^-$ decays that are currently used as some of the most promising methods to search for NP. An overview of the theoretical concepts used to analyse these decays is given, after which the discussion will turn to the $B^0 \to K^{*0}\mu^+\mu^-$ decay, one of the most prominent $b \to s\ell^+\ell^-$ decays in the current flavour landscape.

2.7 Flavour changing neutral currents

In Sec. 2.4.3 it was described how the mixing of quarks arises out of the interaction Lagrangian. The inter-generational mixing of quarks is directly related to the terms involving the $W^\pm$ gauge bosons. The rest of the interaction terms, involving the photon and Z bosons, only contain quarks of the same flavour, *i.e.* there are no flavour changing neutral current (FCNC) transitions at tree-level in the SM. Instead, FCNC decays are mediated, at lowest order, by electroweak penguin and box diagrams, as illustrated for the $B^0 \to K^{*0}\ell^+\ell^-$ transition in the two Feynman diagrams of Fig. 2.1. Due to FCNC decays only occurring at loop level, their branching fractions are suppressed. By contrast, NP contributions could already enter at tree level (see lower two diagrams of Fig. 2.1) and therefore significantly change the decay properties, making FCNC decays an excellent probe for NP. The following section introduces the theoretical framework with which these decays are analysed.

2.8 Effective field theories

When performing and analysing experiments, it is often useful to only consider the physics that is relevant at the time or length scale at which the experiment is taking place. For example, it would be a very tedious exercise to analyse the motion of a car using special relativity, when a description of classical mechanics is perfectly sufficient. There is in principle nothing wrong with applying special relativity in this example, however it is decidedly easier to use classical mechanics in the limit of small velocities. Classical mechanics is a so-called effective theory [61] of special relativity. Effective theories are

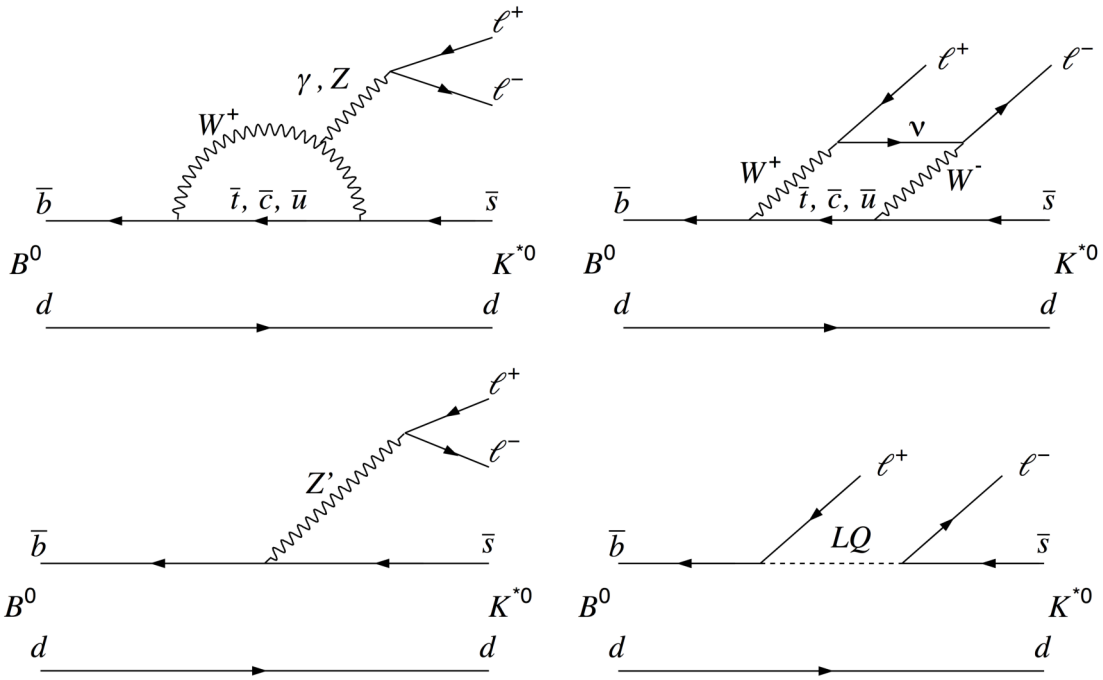


Figure 2.1: Feynman diagrams under the SM of the $B^0 \to K^{*0}\ell^+\ell^-$ decay for the electroweak penguin (top left) and box diagram (top right). Possible NP contributions: a tree-level diagram mediated by a new gauge boson Z' (bottom left) and a tree-level diagram involving a leptoquark LQ (bottom right). Figure taken from Ref. [29].

often much simpler to apply to specific problems but are limited in their application, as they are only valid for a certain time or length scale. It is, for example, not very helpful to apply classical mechanics when trying to understand the process of two proton beams colliding in the LHC.

In the case of $b \to s\ell^+\ell^-$ transitions, effective field theories allow predictions to be made that would otherwise be extremely difficult to obtain. The application of effective field theories in this context can be explained using the $B^0 \to K^{*0}\mu^+\mu^-$ decay. There are two different kinds of physics at play when analysing a decay such as $B^0 \to K^{*0}\mu^+\mu^-$. While its $b \to s\ell^+\ell^-$ transition is characterised mainly by the electroweak force, the interactions between the spectator d quark and the b quark are due to QCD effects. The energy scales of the electroweak and strong force are considerably different, as the former is characterised by the mass of the W bosons and therefore lies at approximately 80 GeV, while the latter is characterised by Λ_{QCD}, which lies at approximately 0.2 GeV. This large difference allows theorists to decouple the high energy (short distance) electroweak physics from the low energy (long distance) QCD physics, resulting in a low energy effective field theory for the

$B^0 \to K^{*0}\mu^+\mu^-$ decay.

Following the discussion presented in Ref. [62], the Hamiltonian of the effective field theory of $b \to s\ell^+\ell^-$ transitions can be written as follows:

$$\mathcal{H}_{\text{eff}} = -\frac{4G_{\text{F}}}{\sqrt{2}} V_{tb}V_{ts}^* \frac{g_e^2}{4\pi} \sum_i C_i(\mu_s)\mathcal{O}_i(\mu_s), \tag{2.36}$$

which holds for energy scales μ_s much smaller than the mass of the W bosons. In the above expression, G_{F} is the Fermi constant and C_i are the Wilson Coefficients accounting for the degrees of freedom with mass $> \mu_s$, while the operators $\mathcal{O}_i$ account for the degrees of freedom with mass $< \mu_s$. As in Fermi's effective field theory describing beta decays, the heavy degrees of freedom, such as the W and Z fields, have been integrated out into the Wilson Coefficients C_i, while the lighter fields are still present and are described by the local operators $\mathcal{O}_i$.

For the $B^0 \to K^{*0}\mu^+\mu^-$ decay the most relevant local operators are:

$$\begin{aligned}
\mathcal{O}_7 &= \tfrac{m_b}{g_e}\bar{s}\sigma^{\mu\nu}b_R F_{\mu\nu}\,, & \mathcal{O}'_7 &= \tfrac{m_b}{g_e}\bar{s}\sigma^{\mu\nu}b_L F_{\mu\nu}\,,\\
\mathcal{O}_9 &= \bar{s}\gamma_\mu b_L\,\bar{\ell}\gamma^\mu\ell\,, & \mathcal{O}'_9 &= \bar{s}\gamma_\mu b_R\,\bar{\ell}\gamma^\mu\ell\,,\\
\mathcal{O}_{10} &= \bar{s}\gamma_\mu b_L\,\bar{\ell}\gamma^\mu\gamma_5\ell\,, & \mathcal{O}'_{10} &= \bar{s}\gamma_\mu b_R\,\bar{\ell}\gamma^\mu\gamma_5\ell\,.
\end{aligned} \tag{2.37}$$

In the above expressions m_b is the mass of the b quark and $\sigma^{\mu\nu} = \frac{i}{2}[\gamma^\mu, \gamma^\nu]$. The operators describe the upper two Feynman diagrams of Fig. 2.1: $\mathcal{O}_7^{(\prime)}$ corresponds to the electroweak penguin diagram including a photon, while $\mathcal{O}_9^{(\prime)}$ and $\mathcal{O}_{10}^{(\prime)}$ are the semi-leptonic vector and axial-vector operators that correspond to the electroweak penguin diagram including a Z boson and the box diagram. In the SM the Wilson coefficients C_i' corresponding to the primed operators are suppressed by $\mathcal{O}(\frac{m_s}{m_b})$, as the W bosons only couple to left handed fermions. The ratio of the two masses is the result of the chirality flip of the right handed b and s quarks via the Higgs interaction.

At $\mu_s = m_b$, the values of the Wilson coefficients in the SM are

$$C_7^{\text{SM}} = -0.3\,, \quad C_9^{\text{SM}} = +4.2\,, \quad C_{10}^{\text{SM}} = -4.2\,. \tag{2.38}$$

The Wilson coefficients take the same values for other $b \to s\ell^+\ell^-$ decays, such as $B^0 \to K^{*0}e^+e^-$, $B^+ \to K^+\mu^+\mu^-$ and $B_s^0 \to \mu^+\mu^-$, as the short distance physics is the same for all of them. Introducing NP particles could modify the values of the Wilson coefficients, *i.e.* $C_i^{(\prime)} = C_i^{(\prime)\,\text{SM}} + C_i^{(\prime)\,\text{NP}}$. The advantage of the effective field theory approach therefore does not only lie in the feasibility of calculations, but also in the model independent context it provides. This approach enables extraction of the Wilson coefficients via a fit to several measurements, which is also known as performing a global fit (see Sec. 2.10).

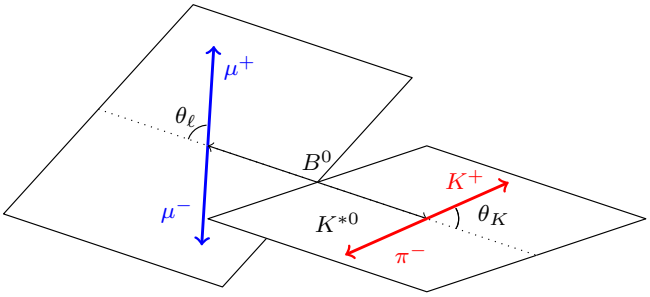
2.9 The $B^0 \to K^{*0}\mu^+\mu^-$ decay

The $B^0 \to K^{*0}\mu^+\mu^-$ decay is a key channel for understanding $b \to s\ell^+\ell^-$ transitions and the corresponding Wilson coefficients. It is of particular interest, as the K^{*0} is a short lived vector particle that decays into a kaon and a pion, giving access to its polarisation states. In terms of Wilson coefficients, the $B^0 \to K^{*0}\mu^+\mu^-$ decay provides information about C_7, C_9 and C_{10}. Experimentally, the $B^0 \to K^{*0}\mu^+\mu^-$ decay is preferable to the $B^0 \to K^{*0}e^+e^-$ decay, as the two muons, in comparison with the two electrons, give a much cleaner detector signature and can be triggered more efficiently at the LHCb experiment (see Sec. 3.7 and Sec. 3.8). Due to its non-trivial structure, the $B^0 \to K^{*0}\mu^+\mu^-$ decay provides various observables of interest: the differential branching fraction [22], *CP* asymmetries [63], isospin asymmetries [24], and angular observables that are related to the angular distribution of the daughter particles [2, 15–18]. Measuring these angular observables is the main aim of this thesis.

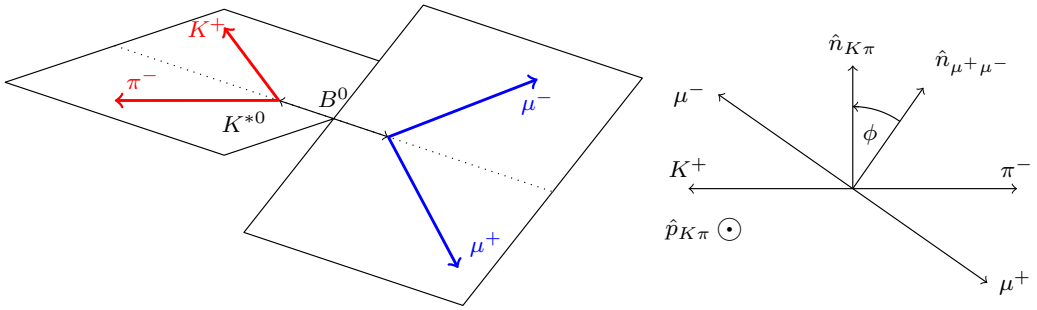
2.9.1 Definition of the angular basis

The angular distribution of the $B^0 \to K^{*0}\mu^+\mu^-$ decay can be expressed in terms of the square of the invariant mass of the dimuon system q^2, and the three decay angles θ_l, θ_K and ϕ, commonly abbreviated as $\vec{\Omega} = (\cos\theta_l, \cos\theta_K, \phi)$. Different angular conventions are typically used by experimentalists and theorists. The angular convention chosen by the majority of theorists is defined in Refs. [64, 65]. This thesis adopts the experimental convention that is also used in the previous LHCb publications [2, 66, 67].

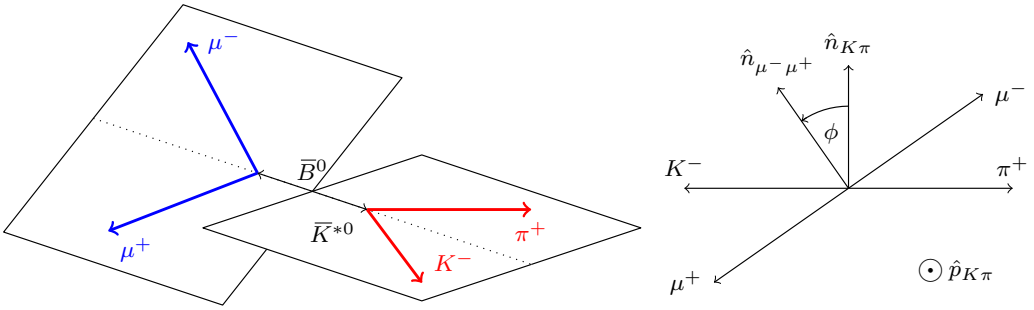
The definition of the angles, used in this thesis, is illustrated in Fig. 2.2. The angle θ_l is the angle between the direction of the μ^+ (μ^-) and the direction opposite to that of the B^0 ($\overline{B}^0$) in the rest frame of the dimuon system. The angle θ_K lies between the direction of the K^+ (K^-) and the direction of the B^0 ($\overline{B}^0$) in the rest frame of the K^{*0} ($\overline{K}^{*0}$). The angle ϕ lies between the plane defined by the muon pair and the plane defined by the kaon and pion in the B^0 ($\overline{B}^0$) rest frame. The angles are defined so that the angular definition of the $\overline{B}^0$ decay is a *CP* transformation of that of the B^0 decay.



(a) θ_K and θ_ℓ definitions for the B^0 decay



(b) ϕ definition for the B^0 decay



(c) ϕ definition for the $\overline{B}^0$ decay

Figure 2.2: Graphical representation of the angular basis used for $B^0 \to K^{*0}\mu^+\mu^-$ and $\overline{B}^0 \to \overline{K}^{*0}\mu^+\mu^-$ decays in this paper. The notation $\hat{n}_{ab}$ is used to represent the normal to the plane containing particles a and b in the B^0 (or $\overline{B}^0$) rest frame.

2.9.2 Differential decay rate

The differential decay rates of $\overline{B}^0 \to \overline{K}^{*0}\mu^+\mu^-$ and $B^0 \to K^{*0}\mu^+\mu^-$ as functions of q^2 and the three decay angles are given by

$$\frac{\mathrm{d}^4\Gamma[\overline{B}^0 \to \overline{K}^{*0}\mu^+\mu^-]}{\mathrm{d}q^2\mathrm{d}\vec{\Omega}} = \sum_i I_i(q^2) f_i(\vec{\Omega}) \text{ and} \tag{2.39}$$

$$\frac{\mathrm{d}^4\bar{\Gamma}[B^0 \to K^{*0}\mu^+\mu^-]}{\mathrm{d}q^2\mathrm{d}\vec{\Omega}} = \sum_i \bar{I}_i(q^2) f_i(\vec{\Omega}) \ , \tag{2.40}$$

where the $f_i(\vec{\Omega})$ are formed from combinations of spherical harmonics, which are in turn functions of the angles. The I_i ($\bar{I}_i$) are q^2-dependent angular observables, which can be expressed as combinations of the six complex decay amplitudes, $\mathcal{A}^{\mathrm{L,R}}_{0,\parallel,\perp}$, corresponding to the different transversity states of the K^{*0} meson and the different (left- and right-handed) chiralities of the dimuon system. Tab. 2.2 gives a full list of the angular observables as a function of the complex decay amplitudes, as well as their corresponding angular terms. The relations in Tab. 2.2 only hold for the limiting case of muons being massless, an approximation used in the analysis presented in this thesis. In this limit $I_{1s} = 3I_{2s}$ and $I_{1c} = -2I_{2c}$, which reduces the number of independent angular observables from eleven to nine. Furthermore it is useful to define the q^2-dependent *CP* averages, S_i, in terms of the angular observables I_i and $\bar{I}_i$:

$$S_i = (I_i + \bar{I}_i) / \left(\frac{\mathrm{d}\Gamma}{\mathrm{d}q^2} + \frac{\mathrm{d}\bar{\Gamma}}{\mathrm{d}q^2} \right) \ . \tag{2.41}$$

The number of independent S_i observables is reduced from nine to eight due to the following relation $\frac{3}{4}(2S_{1s} + S_{1c}) - \frac{1}{4}(\frac{2}{3}S_{1s} + \frac{1}{2}S_{1c}) = 1$. In addition, the *CP* averaged observables are related to the longitudinal polarisation of the K^{*0} meson, denoted as F_{L}, and the forward-backward asymmetry of the dimuon system A_{FB}:

$$\begin{aligned} F_{\mathrm{L}} &= 1 - \frac{4}{3} S_{1s}, \\ A_{\mathrm{FB}} &= \frac{3}{4} S_{6s}. \end{aligned} \tag{2.42}$$

i	I_i	f_i
$1s$	$\frac{3}{4}\left[\lvert\mathcal{A}_\parallel^{\rm L}\rvert^2+\lvert\mathcal{A}_\perp^{\rm L}\rvert^2+\lvert\mathcal{A}_\parallel^{\rm R}\rvert^2+\lvert\mathcal{A}_\perp^{\rm R}\rvert^2\right]$	$\sin^2\theta_K$
$1c$	$\lvert\mathcal{A}_0^{\rm L}\rvert^2+\lvert\mathcal{A}_0^{\rm R}\rvert^2$	$\cos^2\theta_K$
$2s$	$\frac{1}{4}\left[\lvert\mathcal{A}_\parallel^{\rm L}\rvert^2+\lvert\mathcal{A}_\perp^{\rm L}\rvert^2+\lvert\mathcal{A}_\parallel^{\rm R}\rvert^2+\lvert\mathcal{A}_\perp^{\rm R}\rvert^2\right]$	$\sin^2\theta_K\cos 2\theta_l$
$2c$	$-\lvert\mathcal{A}_0^{\rm L}\rvert^2-\lvert\mathcal{A}_0^{\rm R}\rvert^2$	$\cos^2\theta_K\cos 2\theta_l$
3	$\frac{1}{2}\left[\lvert\mathcal{A}_\perp^{\rm L}\rvert^2-\lvert\mathcal{A}_\parallel^{\rm L}\rvert^2+\lvert\mathcal{A}_\perp^{\rm R}\rvert^2-\lvert\mathcal{A}_\parallel^{\rm R}\rvert^2\right]$	$\sin^2\theta_K\sin^2\theta_l\cos 2\phi$
4	$\sqrt{\frac{1}{2}}\mathrm{Re}(\mathcal{A}_0^{\rm L}\mathcal{A}_\parallel^{\rm L*}+\mathcal{A}_0^{\rm R}\mathcal{A}_\parallel^{\rm R*})$	$\sin 2\theta_K\sin 2\theta_l\cos\phi$
5	$\sqrt{2}\mathrm{Re}(\mathcal{A}_0^{\rm L}\mathcal{A}_\perp^{\rm L*}-\mathcal{A}_0^{\rm R}\mathcal{A}_\perp^{\rm R*})$	$\sin 2\theta_K\sin\theta_l\cos\phi$
$6s$	$2\mathrm{Re}(\mathcal{A}_\parallel^{\rm L}\mathcal{A}_\perp^{\rm L*}-\mathcal{A}_\parallel^{\rm R}\mathcal{A}_\perp^{\rm R*})$	$\sin^2\theta_K\cos\theta_l$
7	$\sqrt{2}\mathrm{Im}(\mathcal{A}_0^{\rm L}\mathcal{A}_\parallel^{\rm L*}-\mathcal{A}_0^{\rm R}\mathcal{A}_\parallel^{\rm R*})$	$\sin 2\theta_K\sin\theta_l\sin\phi$
8	$\sqrt{\frac{1}{2}}\mathrm{Im}(\mathcal{A}_0^{\rm L}\mathcal{A}_\perp^{\rm L*}+\mathcal{A}_0^{\rm R}\mathcal{A}_\perp^{\rm R*})$	$\sin 2\theta_K\sin 2\theta_l\sin\phi$
9	$\mathrm{Im}(\mathcal{A}_\parallel^{\rm L*}\mathcal{A}_\perp^{\rm L}+\mathcal{A}_\parallel^{\rm R*}\mathcal{A}_\perp^{\rm R})$	$\sin^2\theta_K\sin^2\theta_l\sin 2\phi$
10	$\frac{1}{3}\left[\lvert\mathcal{A}_{\rm S}^{\rm L}\rvert^2+\lvert\mathcal{A}_{\rm S}^{\rm R}\rvert^2\right]$	1
11	$\sqrt{\frac{4}{3}}\mathrm{Re}(\mathcal{A}_{\rm S}^{\rm L}\mathcal{A}_0^{\rm L*}+\mathcal{A}_{\rm S}^{\rm R}\mathcal{A}_0^{\rm R*})$	$\cos\theta_K$
12	$-\frac{1}{3}\left[\lvert\mathcal{A}_{\rm S}^{\rm L}\rvert^2+\lvert\mathcal{A}_{\rm S}^{\rm R}\rvert^2\right]$	$\cos 2\theta_l$
13	$-\sqrt{\frac{4}{3}}\mathrm{Re}(\mathcal{A}_{\rm S}^{\rm L}\mathcal{A}_0^{\rm L*}+\mathcal{A}_{\rm S}^{\rm R}\mathcal{A}_0^{\rm R*})$	$\cos\theta_K\cos 2\theta_l$
14	$\sqrt{\frac{2}{3}}\mathrm{Re}(\mathcal{A}_{\rm S}^{\rm L}\mathcal{A}_\parallel^{\rm L*}+\mathcal{A}_{\rm S}^{\rm R}\mathcal{A}_\parallel^{\rm R*})$	$\sin\theta_K\sin 2\theta_l\cos\phi$
15	$\sqrt{\frac{8}{3}}\mathrm{Re}(\mathcal{A}_{\rm S}^{\rm L}\mathcal{A}_\perp^{\rm L*}-\mathcal{A}_{\rm S}^{\rm R}\mathcal{A}_\perp^{\rm R*})$	$\sin\theta_K\sin\theta_l\cos\phi$
16	$\sqrt{\frac{8}{3}}\mathrm{Im}(\mathcal{A}_{\rm S}^{\rm L}\mathcal{A}_\parallel^{\rm L*}-\mathcal{A}_{\rm S}^{\rm R}\mathcal{A}_\perp^{\rm R*})$	$\sin\theta_K\sin\theta_l\sin\phi$
17	$\sqrt{\frac{2}{3}}\mathrm{Im}(\mathcal{A}_{\rm S}^{\rm L}\mathcal{A}_\perp^{\rm L*}+\mathcal{A}_{\rm S}^{\rm R}\mathcal{A}_\perp^{\rm R*})$	$\sin\theta_K\sin 2\theta_l\sin\phi$

Table 2.2: Angular observables I_i and their corresponding angular terms in the limit of the muon mass being zero. The terms in the lower part of the table arise from the $K^+\pi^-$ S-wave contribution to the $K^+\pi^-\mu^+\mu^-$ final state. The $\bar{I}_i$ coefficients are obtained by making the substitution $\mathcal{A}\to\bar{\mathcal{A}}$. Table taken from Ref. [2].

Using the above definitions, the *CP*-averaged angular distribution of the $B^0 \to K^{*0}\mu^+\mu^-$ decay can therefore be written as

$$\begin{aligned}\frac{1}{\mathrm{d}(\Gamma+\bar{\Gamma})/\mathrm{d}q^2}\frac{\mathrm{d}^4(\Gamma+\bar{\Gamma})}{\mathrm{d}q^2\mathrm{d}\vec{\Omega}} = \frac{9}{32\pi}[&\frac{3}{4}(1-F_\mathrm{L})\sin^2\theta_K + F_\mathrm{L}\cos^2\theta_K \\ &+\frac{1}{4}(1-F_\mathrm{L})\sin^2\theta_K\cos 2\theta_l \\ &-F_\mathrm{L}\cos^2\theta_K\cos 2\theta_l + S_3\sin^2\theta_K\sin^2\theta_l\cos 2\phi \\ &+S_4\sin 2\theta_K\sin 2\theta_l\cos\phi + S_5\sin 2\theta_K\sin\theta_l\cos\phi \\ &+\frac{4}{3}A_\mathrm{FB}\sin^2\theta_K\cos\theta_l + S_7\sin 2\theta_K\sin\theta_l\sin\phi \\ &+S_8\sin 2\theta_K\sin 2\theta_l\sin\phi + S_9\sin^2\theta_K\sin^2\theta_l\sin 2\phi]\ .\end{aligned} \tag{2.43}$$

The above expression of the decay rate can be re-expressed using the 'optimised' observables $P_i^{(\prime)}$ [68]. In this basis some of the observables, such as P_5', have a smaller theory uncertainty related to form factors (see Sec. 2.9.3). This can be advantageous when comparing the measurement and the theory prediction of a specific observable[3]. The optimised observables are defined as

$$\begin{aligned}P_1 &= \frac{2S_3}{(1-F_\mathrm{L})}, \\ P_2 &= \frac{2}{3}\frac{A_\mathrm{FB}}{(1-F_\mathrm{L})}, \\ P_3 &= \frac{-S_9}{(1-F_\mathrm{L})}, \\ P'_{4,5,8} &= \frac{S_{4,5,8}}{\sqrt{F_\mathrm{L}(1-F_\mathrm{L})}}, \\ P'_6 &= \frac{S_7}{\sqrt{F_\mathrm{L}(1-F_\mathrm{L})}}.\end{aligned} \tag{2.44}$$

[3]When fitting the full set of observables and taking into account their correlations, there is no advantage in using either the $P_i^{(\prime)}$ or S_i basis.

2.9.3 Theory calculations and challenges

In the previous section the differential decay rate was expressed in terms of the angular observables. These observables can be measured by fitting to the angular distributions of the daughter particles. Theoretically, they are related to the decay amplitudes, which themselves depend on the Wilson coefficients. The calculations of the decay amplitudes depend on the q^2 region, as different assumptions are valid at low and high q^2. In addition, decays that include intermediate resonances and have the same final state as the $B^0 \to K^{*0}\mu^+\mu^-$ decay start appearing when increasing q^2. This phenomenon is illustrated using Fig. 2.3, a sketch of the differential $B^0 \to K^{*0}\mu^+\mu^-$ branching fraction, which also includes the contributions of the charmonium resonances. In the low q^2 region ($1 < q^2 < 8\,\mathrm{GeV}^2/c^4$), the contribution to the blue line is dominated by the $B^0 \to K^{*0}\mu^+\mu^-$ decay. In the medium q^2 region of $8 < q^2 < 15\,\mathrm{GeV}^2/c^4$, the two peaks are attributable to the $B^0 \to J/\psi\, K^{*0}$ and $B^0 \to \psi(2S)K^{*0}$ decays, which proceed via tree-level $b \to c\bar{c}s$ transitions. The high q^2 region ($15 < q^2 < 19\,\mathrm{GeV}^2/c^4$) is characterised by the interference between the $B^0 \to K^{*0}\mu^+\mu^-$ decay and decays including broad charmonium resonances.

In the low q^2 region, theoretical predictions can be obtained using the method of QCD factorisation [69], while at high q^2 the heavy quark effective field theory is employed [70].

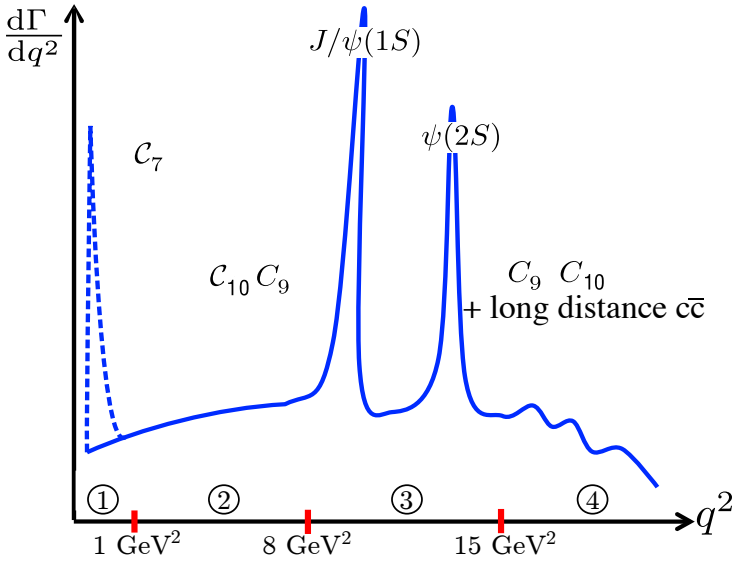


Figure 2.3: Schematic of the sum of the $B \to K^{(\star)}\mu^+\mu^-$ differential branching fraction and the differential branching fractions of decays with the same final state as a function of q^2. The radiative pole in the very low q^2 region, shown with the dashed line, does not appear for scalar K. Figure taken from Ref. [51].

Part of the corresponding theoretical uncertainties are encoded in the form factors that in the former case are obtained via the principle of light cone sum rules [71] and in the latter case are approximated using lattice QCD calculations [72]. The form factors, which describe the transition of the B meson to a K^{*0} meson (see the interaction of the $\overline{b}$ and $\overline{s}$ quarks with the spectator d quark in Fig. 2.4), are difficult to calculate due to their non-perturbative nature and are generally responsible for the largest theory uncertainties. However, there are additional hadronic uncertainties, such as those coming from charm-loops [71,73–76]. As mentioned in Sec. 2.8, the factorisation of the electroweak and the QCD scales allows for the use of the effective field theory approach. This 'naïve factorisation' [69] partially breaks down when considering long distance contributions, such as those illustrated in Fig. 2.4, where a charm loop exchanges gluons with the $\overline{b}$ and $\overline{s}$ quarks. The presence of the virtual photon points to the charm loop being related to a vector-like coupling, which is also the case for the coupling described by the C_9 Wilson coefficient. This is alarming as therefore potential NP effects could be mimicked. The study of the additional non-factorisable hadronic effects is thus of crucial importance and has been the topic of intense discussions among the theory community.

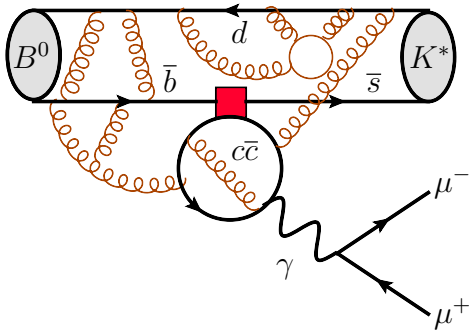


Figure 2.4: Theoretical challenges for calculating theory predictions: the effect of gluons in the interaction of the $\overline{b}$ and $\overline{s}$ quarks with the spectator d quark result in form factor uncertainties, while the charm loop exchanging gluons with the $\overline{b}$ and $\overline{s}$ quarks causes further non-factorisable hadronic uncertainties.

2.9.4 S-wave interference

In addition to the theoretical challenges that the $B^0 \to K^{*0}\mu^+\mu^-$ decay poses, there exists an experimental difficulty related to the state of the K^{*0} meson. The differential decay rate presented in Eq. 2.43 only includes the terms that are necessary to describe the $K^{*0}(892)$ resonance, which is in a P-wave configuration. However, the K^{*0} meson can also

be in an S-wave configuration, as is the case with the $K_0^*(1430)$ resonance, for example. Additional terms have to therefore be added to the differential decay rate to account for the S-wave contribution, which can be as large as 10% in the low q^2 region [22]. The S-wave observables and their relation to the two complex amplitudes $\mathcal{A}_{\rm S}^{\rm L,R}$ are given in the lower part of Tab. 2.2. The angular distribution becomes

$$\begin{aligned}\frac{1}{\mathrm{d}(\Gamma+\bar{\Gamma})/\mathrm{d}q^2}\left.\frac{\mathrm{d}^4(\Gamma+\bar{\Gamma})}{\mathrm{d}q^2\,\mathrm{d}\vec{\Omega}}\right|_{\rm S+P} &= (1-F_{\rm S})\,\frac{1}{\mathrm{d}(\Gamma+\bar{\Gamma})/\mathrm{d}q^2}\left.\frac{\mathrm{d}^4(\Gamma+\bar{\Gamma})}{\mathrm{d}q^2\,\mathrm{d}\vec{\Omega}}\right|_{\rm P} \\ &\quad + \frac{3}{16\pi}F_{\rm S}\sin^2\theta_l \\ &\quad + \frac{9}{32\pi}S_{\rm S1}\sin^2\theta_l\cos\theta_K \\ &\quad + \frac{9}{32\pi}(S_{\rm S2}\cos\phi + S_{\rm S5}\sin\phi)\sin 2\theta_l\sin\theta_K \\ &\quad + \frac{9}{32\pi}(S_{\rm S3}\cos\phi + S_{\rm S4}\sin\phi)\sin\theta_l\sin\theta_K\,,\end{aligned} \tag{2.45}$$

where $F_{\rm S}$ denotes the S-wave fraction,

$$F_{\rm S} = \frac{|\mathcal{A}_{\rm S}^{\rm L}|^2 + |\mathcal{A}_{\rm S}^{\rm R}|^2}{|\mathcal{A}_{\rm S}^{\rm L}|^2 + |\mathcal{A}_{\rm S}^{\rm R}|^2 + |\mathcal{A}_0^{\rm L}|^2 + |\mathcal{A}_0^{\rm R}|^2 + |\mathcal{A}_\parallel^{\rm L}|^2 + |\mathcal{A}_\parallel^{\rm R}|^2 + |\mathcal{A}_\perp^{\rm L}|^2 + |\mathcal{A}_\perp^{\rm R}|^2}\,, \tag{2.46}$$

and the terms $S_{\rm S1}$–$S_{\rm S5}$ arise from interference between the S- and P-wave amplitudes.

2.10 Experimental status of $b \to s\ell^+\ell^-$ decays and global fits

There are three common measurements relating to $b\to s\ell^+\ell^-$ decays, each with a different level of theory uncertainty:

1. Predictions of **branching fractions** are theoretically very challenging, as described in Sec. 2.9.3. This results in large form factor uncertainties. In addition, there are contributions from hadronic uncertainties that are related to non-factorisable effects.

2. **Angular observables** are constructed in such a way that form factor uncertainties are considerably reduced; *e.g.* in the calculation of the P_5' variable, the form factors cancel to first order. However, non-factorisable hadronic effects play a role also in the predictions of the angular observables.

3. **Lepton flavour universality ratios** are especially useful, as form factor and non-factorisable hadronic uncertainties cancel completely in their predictions. The reason for this is that in the SM the coupling of gauge bosons to leptons is universal and therefore independent of lepton flavour. Hence, the predictions of the branching fractions of *e.g.* $B^0 \to K^{*0}\mu^+\mu^-$ and $B^0 \to K^{*0}e^+e^-$ are identical apart from a factor that accounts for the difference in radiative corrections and the difference in mass between muons and electrons.

Measurements of differential branching fractions of several $b \to s\ell^+\ell^-$ decays and their corresponding theoretical SM predictions are shown in Fig. 2.5. For most of the decays the measurements in the lowest q^2 bins lie below their relevant predictions.

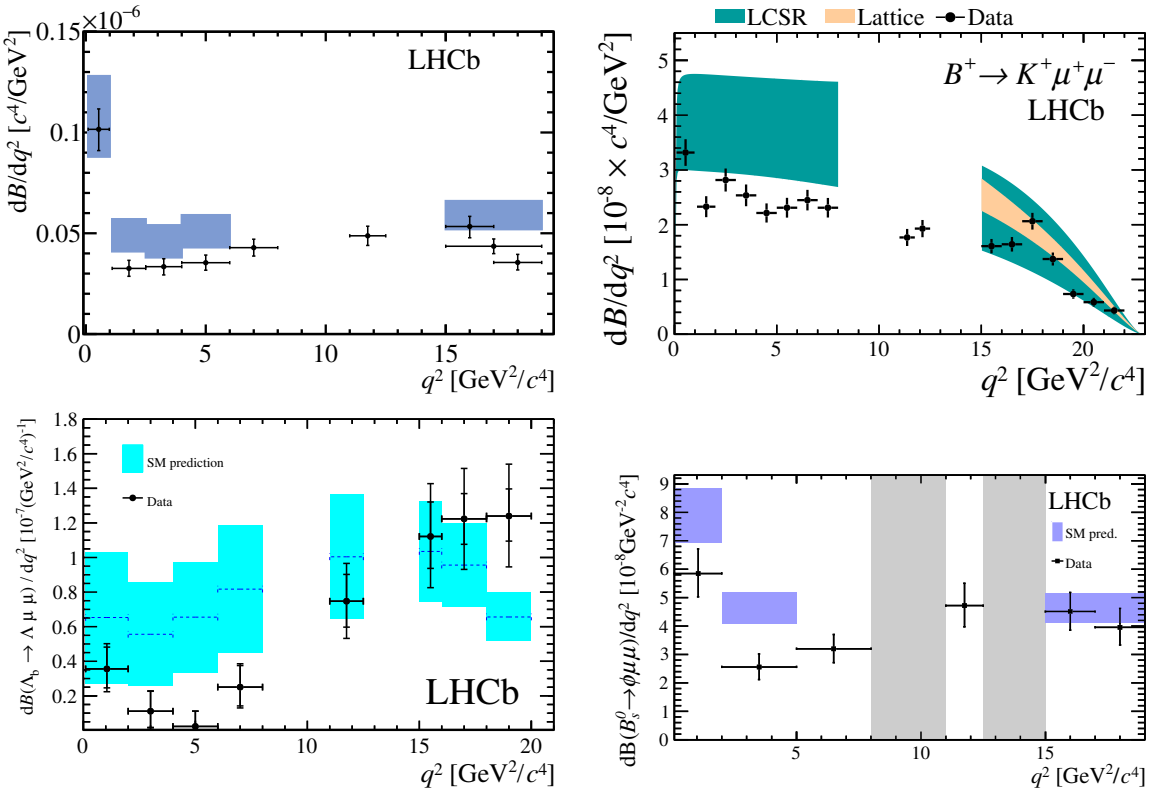


Figure 2.5: Measurements and theory predictions of the differential branching factions of the $B^0 \to K^{*0}\mu^+\mu^-$ [22] (top left), $B^+ \to K^+\mu^+\mu^-$ [24] (top right), $\Lambda_b^0 \to \Lambda\mu^+\mu^-$ [23] (bottom left) and $B_s^0 \to \phi(1020)\mu^+\mu^-$ [21] (bottom right) decays.

With respect to angular analyses, the P_5' variable has attracted most attention in the recent years. Fig. 2.6 shows P_5' as a function of q^2. The measurements have been performed by the LHCb, CMS, Belle and ATLAS collaborations [2,15–17], while the theory

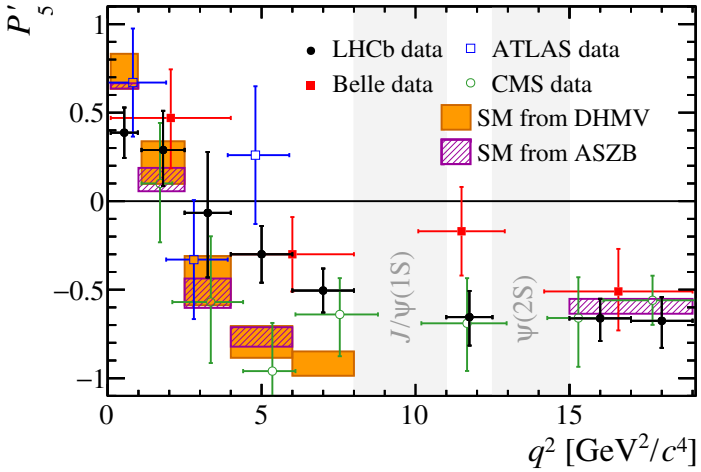


Figure 2.6: Measurements and theory predictions of the P'_5 observable. The experimental results were presented by the LHCb, CMS, Belle and ATLAS collaborations, the theory predictions were made by S. Descotes-Genon *et al.* (DHMV) [77] and W. Altmannshofer *et al.* (ASZB) [78].

predictions are based on the papers of S. Descotes-Genon *et al.* [77] and W. Altmannshofer *et al.* [78]. Most striking are the discrepancies between the measurements and the theory predictions in the range $4.0 < q^2 < 8.0\,\text{GeV}^2/c^4$. The LHCb collaboration measurements are the most precise and show the largest tension with the SM prediction. The data analysed to obtain this result were recorded in 2011 and 2012, at centre-of-mass energies of 7 and 8 TeV respectively and correspond to an integrated luminosity of $3.0\,\text{fb}^{-1}$ of pp collisions. The analysis presented in this thesis adds the data recorded in 2016 at a centre-of-mass energy of 13 TeV and an integrated luminosity of $1.7\,\text{fb}^{-1}$. This approximately doubles the number of B^0 decays as the $b\bar{b}$ production cross-section increases by roughly a factor of two between the Run 1 and 2016 datasets [79] (see also Sec. 3.2).

Due to their theoretically clean nature, lepton flavour universality ratios have been an extremely useful tool for probing $b \to s\ell^+\ell^-$ decays for NP. The ratios R_K and R_{K^*} have played a particularly important role and are defined as

$$R_K = \frac{\int_{q^2_{\text{min}}}^{q^2_{\text{max}}} \frac{\text{d}\mathcal{B}\left(B^+ \to K^+\mu^+\mu^-\right)}{\text{d}q^2}\text{d}q^2}{\int_{q^2_{\text{min}}}^{q^2_{\text{max}}} \frac{\text{d}\mathcal{B}(B^+ \to K^+e^+e^-)}{\text{d}q^2}\text{d}q^2}, \tag{2.47}$$

$$R_{K^*} = \frac{\int_{q^2_{\text{min}}}^{q^2_{\text{max}}} \frac{\text{d}\mathcal{B}\left(B^0 \to K^{*0}\mu^+\mu^-\right)}{\text{d}q^2}\text{d}q^2}{\int_{q^2_{\text{min}}}^{q^2_{\text{max}}} \frac{\text{d}\mathcal{B}(B^0 \to K^{*0}e^+e^-)}{\text{d}q^2}\text{d}q^2}. \tag{2.48}$$

The SM predictions for these ratios can deviate from unity as each lepton family interacts with the electromagnetic field surrounding the decay in a different manner, and as each family has a different mass. However, the uncertainty on these predictions is only of $\mathcal{O}(1\%)$ [80]. The LHCb collaboration has determined R_K in the di-lepton invariant mass range $1.1 < q^2 < 6\,\mathrm{GeV}^2/c^4$ [26]:

$$R_K{}^{[1.1,6]} = 0.846\ ^{+0.060}_{-0.054}\ (\mathrm{stat.})\ ^{+0.016}_{-0.014}\ (\mathrm{syst.}), \tag{2.49}$$

and also presented results for R_{K^*} [29],

$$R_{K^*}{}^{[0.045,1.1]} = 0.66\ ^{+0.11}_{-0.07}\ (\mathrm{stat.})\ \pm 0.03\ (\mathrm{syst.}), \tag{2.50}$$

$$R_{K^*}{}^{[1.1,6]} = 0.69\ ^{+0.11}_{-0.07}\ (\mathrm{stat.})\ \pm 0.05\ (\mathrm{syst.}), \tag{2.51}$$

where the superscripts indicate the di-lepton invariant mass bin in GeV^2/c^4. The measurements for both R_K and R_{K^*} lie below the SM predictions, and are in mild tension with the predictions at a level of 2.5 standard deviations (σ).

The presented discrepancies can be analysed in the framework of effective field theories (see Sec. 2.8). Under this approach global fits to several $b \to s\ell^+\ell^-$ observables are performed by varying one or multiple Wilson coefficients. Aebischer *et al.* [32] performed such global fits and can explain the discrepancies by shifting the values of the muonic $C_9 = -C_{10}$ ($C_9^{bs\mu\mu} = -C_{10}^{bs\mu\mu}$) Wilson coefficients. Alternatively, shifting only the muonic C_9 ($C_9^{bs\mu\mu}$) value gives a good fit to the experimental observables. The discrepancies with the SM are in both cases at the level of 6σ, while the best fit points for the two scenarios lie at $C_9^{bs\mu\mu} = -C_{10}^{bs\mu\mu} = -0.53$ and $C_9^{bs\mu\mu} = -0.97$. Algueró *et al.* [31] obtain similar results. In their fits, the discrepancies with the SM lie at the level of 5.5σ and the best fit points are $C_9^{bs\mu\mu} = -C_{10}^{bs\mu\mu} = -0.46$ and $C_9^{bs\mu\mu} = -0.98$.

In addition to a shift of the Wilson coefficients in the muonic sector, both papers analyse a scenario in which there is an additional universal shift to C_9 ($C_9^{\mathrm{univ.}}$) that affects all lepton flavours. In this case, the NP Wilson coefficients are given by:

$$C_9^{bs\mu\mu} = \Delta C_9^{bs\mu\mu} + C_9^{\mathrm{univ.}}\,, \tag{2.52}$$

$$C_9^{bsee} = C_9^{bs\tau\tau} = C_9^{\mathrm{univ.}}\,, \tag{2.53}$$

$$C_{10}^{bs\mu\mu} = -\Delta C_9^{bs\mu\mu}\,, \tag{2.54}$$

$$C_{10}^{bsee} = C_{10}^{bs\tau\tau} = 0\,. \tag{2.55}$$

Fig. 2.7 shows the 2D likelihood contours of neutral current lepton flavour universality (NCLFU) observables, $b \to s\mu^+\mu^-$ branching fraction and angular observables, and the combination of the two (global). The likelihood contours are obtained from fits to $C_9^{\text{univ.}}$ and $\Delta C_9^{bs\mu\mu} = -C_{10}^{bs\mu\mu}$. It can be observed that there is good agreement between the $b \to s\mu^+\mu^-$ and the NCLFU observables. The centre of the global contour lies at $(C_9^{\text{univ.}} = -0.49; \Delta C_9^{bs\mu\mu} = -0.44)$ and the discrepancy with the SM is at a level of 6.5σ.

The global fits show that the tensions between measurements and theory predictions within the $b \to s\ell^+\ell^-$ sector can all be explained by shifts of the vector and axial-vector Wilson coefficients C_9 and C_{10}. Even though the tensions are above 5σ, NP has not yet been claimed because of the outstanding issues related to the non-factorisable hadronic effects that could potentially increase the theory uncertainties. In addition, the scenarios presented only consider a shift in one or two Wilson coefficients, while keeping the rest fixed to their respective SM values.

There have been several proposals of new particles and interactions that could explain the tensions with the SM predictions with NP. The main difficulty in introducing new particles is that they have to obey many experimental constraints, such as those coming from direct searches of decays that violate lepton flavour universality [81–86], the lifetime of the proton [50], B_s^0 and B^0 mixing [87–89] and direct searches that could have already discovered the proposed particles [90, 91]. Nonetheless, several theorists have been able to construct complete models that include Z's and/or leptoquarks [31–46], which can couple to both quarks and leptons (see Fig. 2.1). Crivellin *et al.* [44] propose two scalar leptoquarks to explain both the $b \to s\ell^+\ell^-$ anomalies and the anomaly seen in the R_D and R_{D^*} lepton flavour universality ratios that are defined as

$$R_D = \frac{\mathcal{B}(B \to D\tau^+\nu_\tau)}{\mathcal{B}(B \to D\mu^+\nu_\mu)}, \qquad R_{D^*} = \frac{\mathcal{B}(B \to D^*\tau^+\nu_\tau)}{\mathcal{B}(B \to D^*\mu^+\nu_\mu)}, \tag{2.56}$$

where the B or $D^{(*)}$ denote either a charged or neutral meson. The decays analysed in these ratios are mediated by tree-level $b \to c\ell\nu$ transitions and are therefore theoretically challenging to explain, as the NP contributions have to be large. Combining the measurements of R_D and R_{D^*} performed with the Belle [92–95], LHCb [96, 97] and BaBar [98, 99] detectors results in a discrepancy with the SM prediction at the level of 3σ.

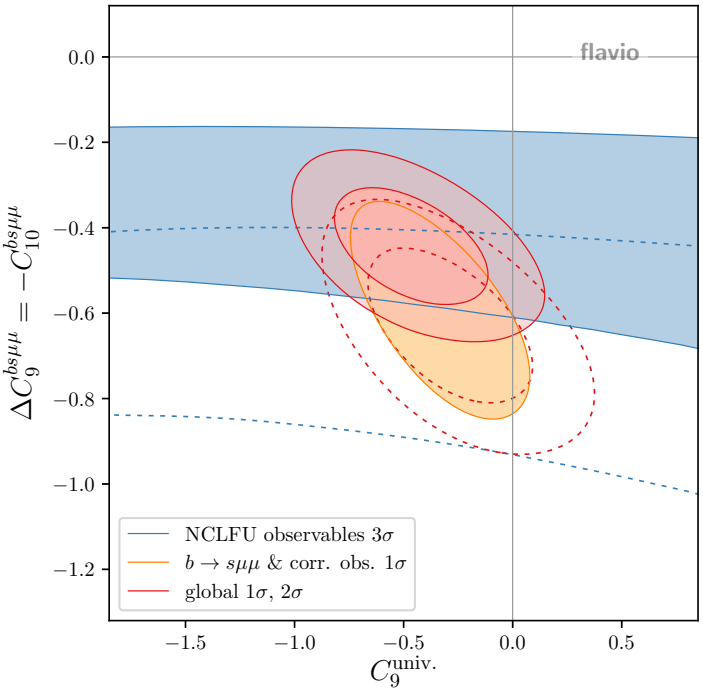


Figure 2.7: Likelihood contours of NCLFU observables, $b \to s\mu^+\mu^-$ branching fraction and angular observables ($b \to s\mu^+\mu^-$), and the combination of the two (global). The likelihood contours are obtained from fits to $C_9^{\text{univ.}}$ and $\Delta C_9^{bs\mu\mu} = -C_{10}^{bs\mu\mu}$. Solid (dashed) contours include (exclude) the Moriond-2019 results for R_K and R_{K^*} [26, 27, 30]. Figure taken from Ref. [32].

3. The LHCb detector

The B mesons used to perform the angular analysis of $B^0 \to K^{*0}\mu^+\mu^-$, presented in this thesis, are produced in proton-proton collisions at the Large Hadron Collider and recorded with the LHCb detector. This section gives a short description of the former and a more detailed summary of the latter.

3.1 The Large Hadron Collider

The Large Hadron Collider (LHC) [100] at the European Organisation for Nuclear Research (CERN) is the largest particle collider ever constructed. It is designed to collide protons at an unprecedented centre-of-mass energy of 14 TeV and is also used to accelerate and collide heavy ions. The LHC is a circular collider with a circumference of 27 km that is situated 50–157 m below the ground spanning the French-Swiss border. Before being injected into the LHC, protons are accelerated to an energy of up to 450 GeV using a chain of several boosters and synchrotrons. The proton beams are then further accelerated by 16 radio frequency chambers and are kept in their trajectories using 1232 superconducting dipole magnets. Moreover, 392 superconducting quadrupole magnets squeeze and collimate the proton beams. Once the desired beam energies are reached, the two proton beams are collided at four different points along the accelerator ring. Four main particle detectors are located at these collision points.

Two of them, CMS [101] and ATLAS [102] are general purpose detectors, while ALICE [103] studies heavy ion collisions and LHCb [104] is dedicated to heavy flavour physics.

3.2 Layout of the LHCb detector

The LHCb detector, shown in Fig. 3.1, is dedicated to the study of flavour particles containing b or c quarks. Its design is strongly motivated by this physics goal. Most strikingly, unlike the general purpose detectors CMS [101] and ATLAS [102], it covers the azimuthal beam angle range $10 < \theta < 250$ mrad or equivalently, the pseudorapidity[a] range $2 < \eta < 5$. It is therefore often referred to as a single-arm forward spectrometer;

[a] Defined as $\eta = -\ln(\tan(\theta/2))$.

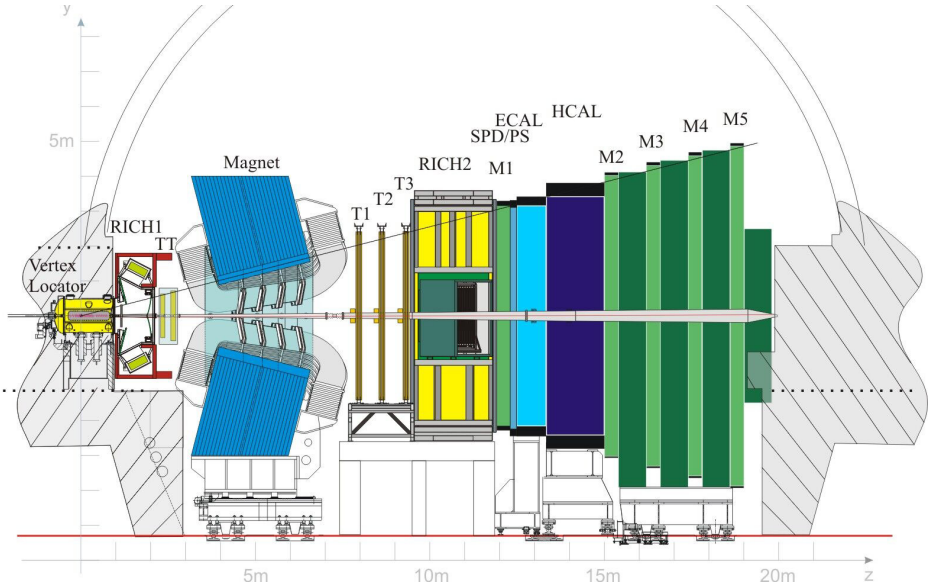


Figure 3.1: A cross-sectional view of the LHCb detector in the y–z plane, where the z axis points along the beamline. The x axis points into the paper. Figure taken from Ref. [104].

single-arm as the detector is only situated at positive θ and forward since the detector is built along the direction of the beamline. The motivation for this layout stems from the large forward production of b and c hadrons at the LHC. In particular, as shown in Fig. 3.2, the production of $b\bar{b}$ quark pairs is concentrated around $\theta = 0$. The production cross-section of $pp \to b\bar{b}X$ in the acceptance of the detector is measured to be $\sigma(pp \to b\bar{b}X) = 75.3 \pm 5.4 \pm 13.0\,\text{mb}$ [105] and $\sigma(pp \to b\bar{b}X) = 144.3 \pm 1 \pm 21\,\text{mb}$ [106] at 7 TeV and 13 TeV respectively, where the first uncertainty is statistical and the second systematic. Hence, the production cross-sections scale approximately linearly with the centre-of-mass energy. Data were recorded with the LHCb detector in 2011 and 2012 (Run 1), as well as between 2015 and 2018 (Run 2). A full summary of the running conditions can be found in Tab. 3.1. The data used to perform the analysis presented in this thesis was taken in the years 2011, 2012 and 2016. Approximately twice as many B mesons were produced for a given integrated luminosity in the 2016 data in comparison with Run 1. This is due to the increase in the centre-of-mass energy for Run 2.

A crucial limitation of hadron collider experiments is the large background originating from inelastic processes. These mainly come from soft QCD processes that are in turn related to the amount of visible pp interactions. Therefore the LHCb detector operates at a luminosity of $\sim 4 \times 10^{32}\,\text{cm}^{-2}\,\text{s}^{-1}$. At this luminosity, the probability to have one to two pp interactions per collision is the highest. To tune the beams to achieve this

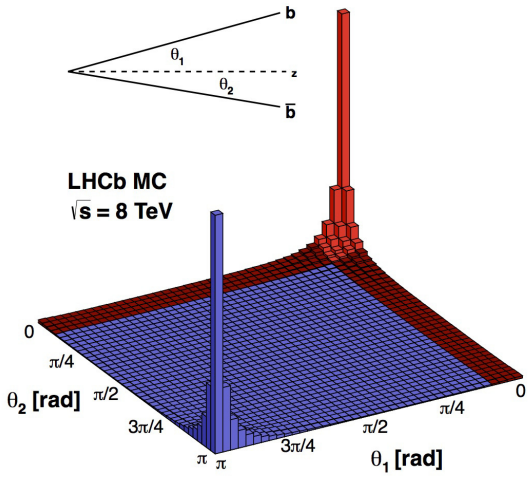


Figure 3.2: The simulated production of $b\bar{b}$ quark pairs in proton-proton collisions as a function of the opening angle, θ_1 (θ_2) of the $b-$ ($\bar{b}-$) quark, shown in the inlay. The red coloured section shows the acceptance of the LHCb detector. Figure taken from Ref. [107].

	Run 1		**Run 2**			
Year	2011	2012	2015	2016	2017	2018
$\sqrt{s}$ [TeV]	7	8	13	13	13	13
$\mathcal{L}$ [$\times 10^{32}\,\mathrm{cm}^{-2}\,\mathrm{s}^{-1}$]	~ 3.5	~ 4.0	~ 4.0	~ 4.0	~ 4.0	~ 4.5
$\int \mathcal{L}\,\mathrm{d}t$ [fb^{-1}]	1.0	2.0	0.3	1.7	1.7	2.1

Table 3.1: Running conditions of the LHC and LHCb detector in the different years of data taking.

luminosity, a technique called luminosity levelling is employed, in which the two colliding proton beams are slightly offset from each other. This method has the additional benefit of providing a uniform instantaneous luminosity to the LHCb detector. The evolution of the instantaneous luminosities for ATLAS, CMS and LHCb during one example fill are shown in Fig. 3.3. While the instantaneous luminosities for ATLAS and CMS decrease with time, LHCb's luminosity is kept stable within a range of 5% by changing the beam overlap accordingly.

The following sections give a brief overview of the different subdetectors shown in Fig. 3.1. The tracking of the particles is performed by the Vertex Locator and the

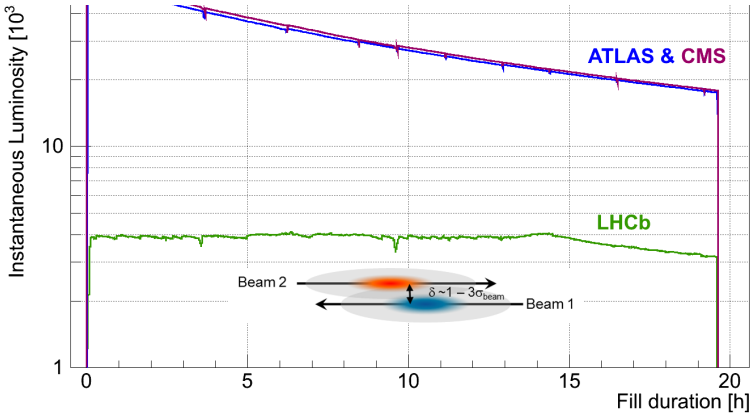


Figure 3.3: Development of the instantaneous luminosity for ATLAS, CMS and LHCb during a representative LHC fill. After ramping to the desired value of $\sim 4 \times 10^{32}\,\mathrm{cm}^{-2}\,\mathrm{s}^{-1}$ for LHCb, the luminosity is kept stable within a range of 5% for approximately 15 hours by adjusting the transversal beam overlap. The difference in luminosity towards the end of the fill between ATLAS, CMS and LHCb is due to the difference in the final focusing at the collision points. Figure taken from Ref. [108].

tracking stations, as outlined in Sec. 3.3 and Sec. 3.4 respectively. The different particle species are identified using Cherenkov detectors, calorimeters and muon systems, as described in Sec. 3.5, Sec. 3.6 and Sec. 3.7. The following paragraph describes some of the definitions that will be used in these sections.

An 'event' occurs when the two proton beams collide in the LHCb detector. Each particle that is created in an event and traverses the detector leaves energy deposits in the detector material. When these deposits are made in the active detector material, 'hits' are identified. A 'track' is formed by associating these hits with the trajectory of a particle. A 'candidate' B hadron is produced by forming n-track combinations in a given event. For example, a $B^0 \to K^{*0}\mu^+\mu^-$ candidate with $K^{*0} \to K^+\pi^-$ is constructed by combining a K^+, π^- and two oppositely charged muon tracks.

3.3 Vertex Locator

The subdetector closest to the interaction point in Fig. 3.1 is the VErtex LOcator (VELO). Its main purpose is to separate primary vertices resulting from pp interactions from secondary vertices that originate from beauty or charmed mesons. In the case of $B^0 \to K^{*0}\mu^+\mu^-$ decays, the B meson originates from pp collisions in the primary vertex (PV) and subsequently flies a short distance, before decaying into its daughter particles in

the secondary vertex.

The VELO subdetector, illustrated in Fig. 3.4, consists of two parts that are to the left and to the right of the beam respectively. Each of them contain 21 silicon modules in the shape of semi circles. The modules themselves are made up of two silicon strip sensors, one to provide radial information (R) and one to provide azimuthal (ϕ[b]) information. In order to protect them against radiation damage, the sensors that are positioned 8 mm from the beam line during stable beam conditions are moved to around 3 cm when the beam is injected. The two positions are illustrated in Fig. 3.4. The distance between the strips, called the strip pitch, ranges from 38 µm to 102 µm to keep the hit occupancy along the module approximately equal. The two VELO parts are kept in separate aluminium boxes to protect them from the rapidly-varying magnetic field that is created by the proton beams. These boxes have their own vacuum, which is separated from the LHC vacuum.

The hit resolution of the VELO varies between approximately 4 and 40 µm. This results in a very good impact parameter (IP[c]) resolution and an excellent PV resolution. The dependence of the two resolutions with respect to momentum and number of tracks is shown in Fig. 3.5.

3.4 Tracking and magnet

The LHCb detector uses tracking stations to determine the trajectories of particles, and a warm dipole magnet that is positioned between the stations to bend charged particles. The momentum of the charged particles is inferred from the deviation of their trajectories in the magnetic field.

The magnet produces a magnetic field along the y axis and has a bending power of about 4 Tm. Its maximal magnetic field, which sits at the centre of the magnet, is approximately 1.1 T. To reduce the effects of asymmetries that are induced by the magnet bending opposite charged particles in opposite directions, the polarity of the magnet is reversed periodically. This results in approximately half of the data being taken when the magnetic field points in the positive y direction, and the other half being taken when the field points in the negative y direction.

The tracking system consists of the Tracker Turicensis (TT) [110], placed upstream of the magnet, and three further tracking stations labelled T1, T2 and T3 located downstream

[b] In this chapter ϕ denotes the azimuthal angle. For all other chapters ϕ is defined in Sec. 2.9.1.

[c] The minimum distance of a track to a PV.

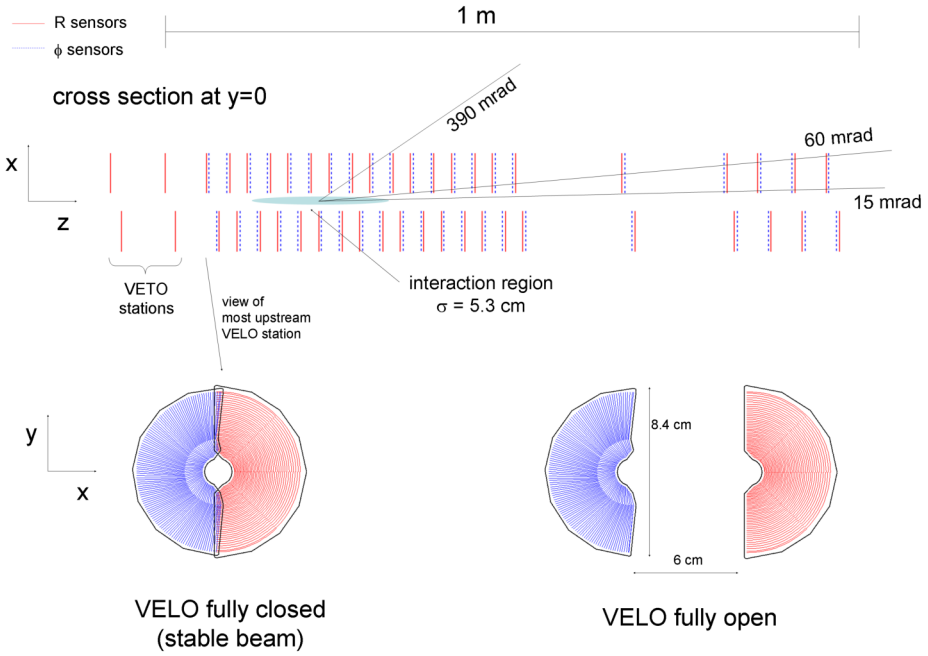


Figure 3.4: The top part of the plot illustrates the cross section of the VELO in the x–z plane at $y = 0$ during stable beam conditions. The lower left (right) shows the front of the first module in the closed (open) positions. Figure taken from Ref. [104].

of the magnet. The two technologies used in the tracking systems take into account the density of tracks, which is typically higher the closer one gets to the beam. Silicon strip

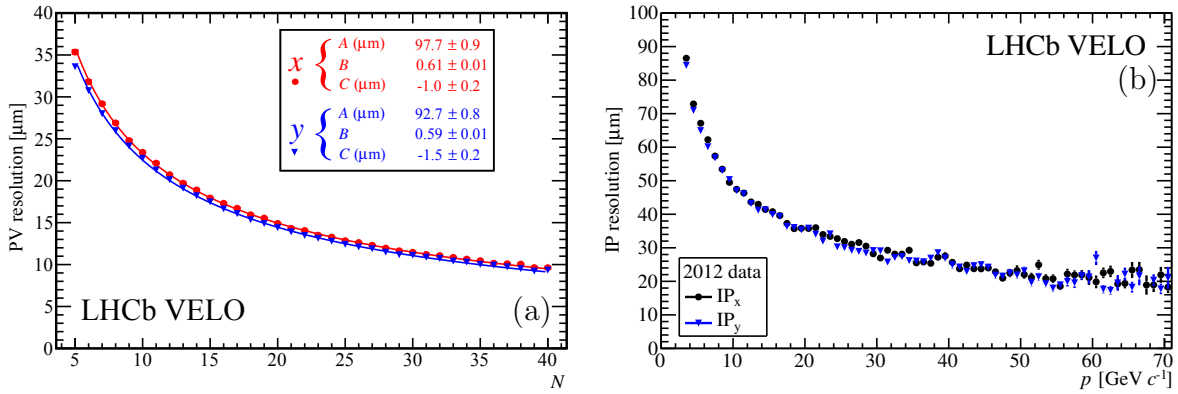


Figure 3.5: Resolutions of the PV and IP as a function of the number of tracks forming the PV, N, and particle momentum, p, in (a) and (b) respectively. Figures taken from Ref. [109].

detectors are used for the Inner Tracker (IT) that consists of the TT and the central regions of T1, T2 and T3. Straw tubes are used for the Outer Tracker (OT), which is made up of the outer part of T1, T2 and T3.

Most charged particles leave hits in one or more of the tracking stations, as well as in the VELO. A Kalman filter algorithm [111, 112] is used to fit tracks of particles corresponding to these hits. This algorithm also takes into account the energy losses caused by ionisation, as well as multiple scattering attributable to the material of the detector. As the input of the Kalman filter algorithm naturally contains statistical noise and measurement inaccuracies, the algorithm may find tracks that are not physical. These fake tracks, mainly consisting of fake hits or hits that were produced by other particles, are called *ghost tracks*. The presence of *ghost tracks* in data sets can be strongly suppressed, as these tracks usually have larger χ^2 values and leave fewer hits. A ghost probability, $\text{prob}_{\text{ghost}}$, can be estimated combining information of the track fit [113, 114].

The performance of the tracking system of the LHCb detector is excellent. For example, muon tracks with $p_{\text{T}} > 2.5$ GeV have a tracking efficiency above 95% and a momentum resolution below 0.5% [115].

3.5 Cherenkov detectors

Two Ring Imaging Cherenkov (RICH) detectors [116] play a vital role in particle identification (PID) at the LHCb experiment. The first, RICH1, is located upstream of the magnet and the second, RICH2, downstream of the magnet.

The RICH detector technology is based on the phenomenon of Cherenkov radiation. This radiation occurs when charged particles travel through a medium at a speed faster than the speed of light in that medium. The emitted light cone forms an angle, θ_c, with respect to the particle's trajectory. Using θ_c and the momentum, p, of the particle, obtained from the tracking system, the mass of the particle can be determined via the following equation:

$$\cos\theta_c = \frac{\sqrt{m^2c^2 + p^2}}{pn}, \tag{3.1}$$

where n is the refractive index of the medium. Taking advantage of the fact that different refractive indices will result in different momentum ranges, the two RICH detectors are filled with different gases. While RICH1 contains C_4F_{10} with $n \sim 1.0018$, providing PID in the momentum range $1 < p < 60\,\text{GeV}$, RICH2 contains CF_4 with $n = 1.0005$, providing

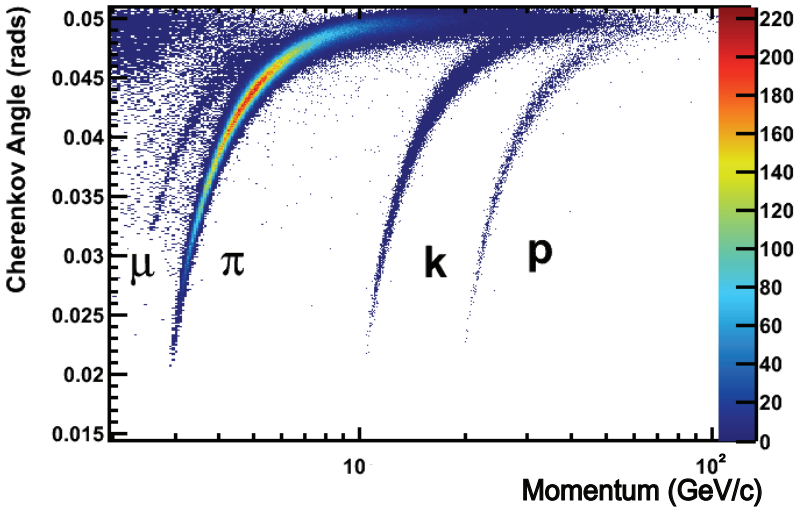


Figure 3.6: Reconstructed Cherenkov angle as a function of track momentum in the C_4F_{10} radiator. Figure taken from Ref. [109].

PID in the momentum range $15 < p < 100\,\text{GeV}$. The Cherenkov angle as a function of momentum for different particle species can be seen in Fig. 3.6. Good discrimination of particle species is observed at all but high and low momentum values. At high momenta the saturation point is reached and at low momenta the particles are not producing any Cherenkov light.

The information of the RICH detectors is combined with that of the tracking in order to associate each track with a mass hypothesis. The result of this process provides variables that quantify the difference in log-likelihood, DLL, between two mass hypotheses for a given particle. For example, the definition of the DLL between the kaon and the pion hypothesis is given in the following equation:

$$\text{DLL}_{K\pi} = \log(\mathcal{L}_K) - \log(\mathcal{L}_\pi), \tag{3.2}$$

where $\mathcal{L}_K(\mathcal{L}_\pi)$ is the likelihood for the kaon (pion) hypothesis. The DLL variables play a crucial role in reducing peaking backgrounds of $B^0 \to K^{*0}\mu^+\mu^-$, as described in Sec. 5.2.

3.6 Calorimeter system

The calorimeters at the LHCb experiment provide information on the energy, PID, as well as on the position of hadrons, electrons and photons. They consists of three detectors:

the scintillating pad (SPD) and pre-shower detector (PS), the electromagnetic calorimeter (ECAL), and the hadronic calorimeter (HCAL). All three detectors operate on the same principle. When particles pass through them their energy is absorbed and re-emitted as light. This light is then guided to photomultiplier tubes by wavelength shifting fibres.

The SPD and PS are mainly used to discriminate between electrons, photons and hadrons. Both the SPD and PS are made out of scintillator pads with a 15 mm thick lead wall separating them. The SPD distinguishes between electrons and photons, as it detects the emitted light of charged particles only. After traversing the SPD, the particles encounter the lead barrier, which has a radiation length of 2.5. When photons meet the barrier an electromagnetic shower is initiated, whereby they convert to electron-positron pairs. These in turn are detected by the PS. In this way the PS can differentiate between photons and hadrons. To differentiate between photons and neutral pions that decay into a pair of photons, multivariate classifiers are used. These are trained on the information extracted from the complete calorimetry and tracking systems [117].

Both the ECAL and HCAL consist of several layers of scintillator material separated by layers of absorbing material. In the case of the ECAL the absorber is made out of lead, while in the case of the HCAL the absorber is made out of iron. The ECAL has a thickness equivalent to 25 radiation lengths and can therefore contain all of the electromagnetic showers. Consequently, the ECAL is able to provide an energy resolution of $\frac{\sigma_E}{E} = \frac{10\%}{E} \oplus 1\%$, where E is measured in GeV. By contrast, the HCAL has a thickness corresponding to 5.6 interaction lengths, achieving a resolution of $\frac{\sigma_E}{E} = \frac{70\%}{E} \oplus 10\%$. However, this resolution is still good enough to fulfil its main purpose, which is to provide information for the hadron trigger, as detailed in Sec. 3.8. Fig. 3.7 gives an overview of the calorimeter system and indicates where the different particle species leave traces in the subdetectors.

The calorimeter systems and especially the ECAL play a minor role in the angular analysis of $B^0 \to K^{*0}\mu^+\mu^-$. However, they are still being used in PID and also in the systematic uncertainty calculations of the trigger as outlined in Sec. 10.9.4.

3.7 Muon Stations

The muon stations are of fundamental importance for correctly identifying $B^0 \to K^{*0}\mu^+\mu^-$ candidates and hence for the angular analysis presented in this thesis. As muons are highly penetrating particles the muon stations are placed at the end of the LHCb detector.

The muon system shown in Fig. 3.7(a) consists of five stations. The first station,

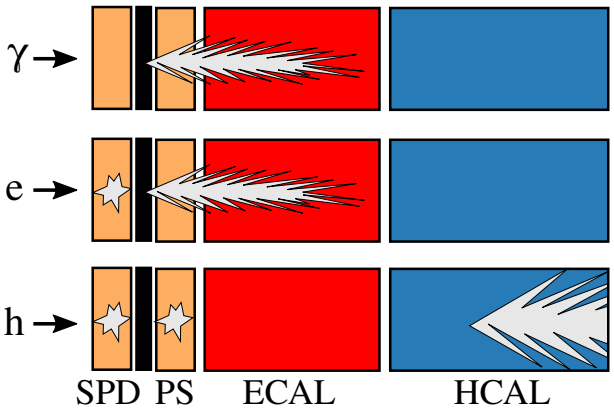


Figure 3.7: Schematic of the calorimeter system illustrating the energy deposit of a photon (γ), an electron (e), and a charged hadron (h). Figure taken from Ref. [51].

M1, is located between RICH2 and SPD, and its main purpose is to give an improved measurement of the muon p_{T}. The remaining stations, M2–M5, are placed after the HCAL and are interleaved with 80 cm-thick iron walls to stop particles other than muons from traversing the muon system. Together with the calorimeter these iron walls cover approximately 21 interaction lengths, creating an excellent stopping target for all particles apart from muons with momenta higher than 6 GeV/c.

The muon stations are made up of 276 multi-wire proportional chambers (MWPC) [118] that are filled with an Ar, CO_2, CF_4 mixture designed to detect charged tracks. An exception is M1, which consists of 12 triple-gas electron multiplier (triple-GEM) detectors and 264 MPWCs. The triple-GEM detectors are closest to the beam pipe because the high occupancy results in an increased risk of radiation damage.

Fig. 3.7(b) shows that each muon station consists of four increasingly large regions, labelled R1–4. These regions are constructed to take into account the track occupancy of the beam. Each region is separated into logical pads, which define the partial resolution of the muon system.

The muon stations provide two main functions. The first is the triggering of events with high muon p_{T} (see also Sec. 3.8), while the second is the determination of PID information. There are two important PID variables that make use of the muon stations. The binary isMuon variable takes the value TRUE if a muon leaves hits in two (if $p < 6$ GeV), three (if $p < 10\,\mathrm{GeV}$) or four (if $p > 10\,\mathrm{GeV}$) stations among M2 to M5. The isMuon variable has an excellent performance, identifying true muons with an efficiency of 95–100% and misidentifying protons, pions or kaons as muons with a probability of less than 2%.

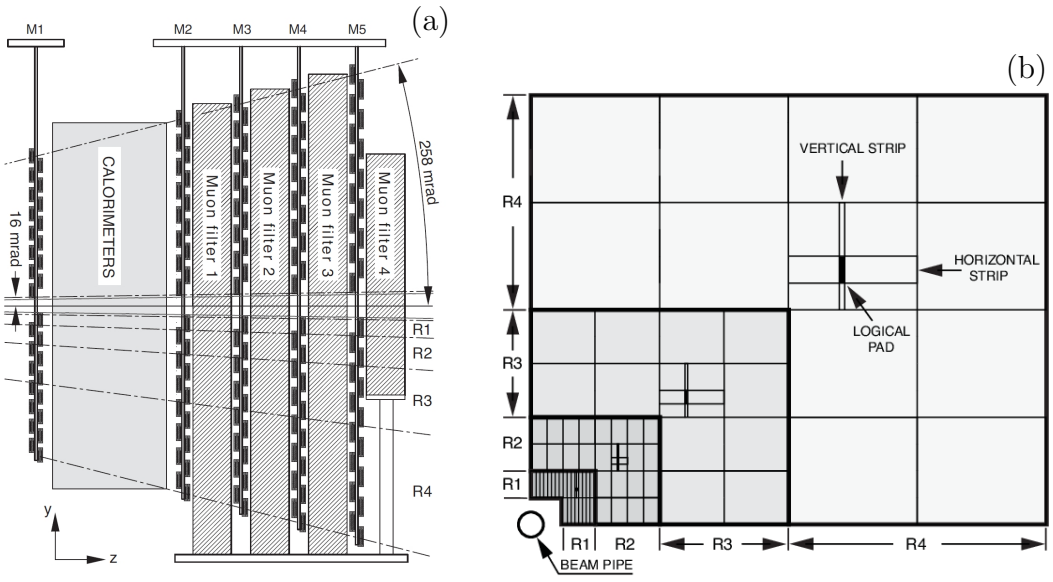


Figure 3.8: Side view of the muon system (a) and front view of one quadrant of stations M2 and M3 showing the partitioning into sectors (b). Figure (b) shows the different regions R1-4 with decreasing mean occupancy. Each region in black depicts a logical pad. Figures taken from Ref. [104].

The second PID variable is a DLL variable that is defined in a similar way as $\mathrm{DLL}_{K\pi}$ in equation Eq. 3.2:

$$\mathrm{DLL}_{\mu\pi} = \log(\mathcal{L}(\theta_c, p, D^2|\mu)) - \log(\mathcal{L}(\theta_c, p, D^2|\pi)), \tag{3.3}$$

where θ_c is the Cherenkov angle provided by the RICH, p is the particle momentum and D^2 is the average squared distance significance of hits in M1 – M5 with respect to the extrapolated position of the tracks from the tracking systems.

3.8 Trigger system

The bunch crossing rate at the LHCb detector is approximately 20 MHz, which results in a large amount of visible events. These events cannot all be processed at the same time, nor can they be all stored on tape. The trigger system [119] is designed to select those events that are of most interest. At the LHCb experiment, the trigger is divided into the first level trigger (L0) and the high level trigger (HLT). While the L0 trigger is based on hardware, the HLT is software-based. The process of reducing the rate of 20 MHz to 5 kHz and 12.5 kHz using these two triggers in Run 1 and Run 2 respectively is described

in the sections below.

3.8.1 Low level trigger

The L0 trigger reduces the data rate from 20 MHz to approximately 1 MHz by using five different trigger lines. These lines base their decisions on information from the muon and calorimeter systems. Two of them, `L0Muon` and `L0DiMuon`, search for muon and dimuon systems that have high p_{T}. The remaining lines, `L0Electron`, `L0Photon` and `L0Hadron`, make decisions based on the transverse energy (E_{T}) recorded by the calorimeter system. The `L0Electron`, `L0Photon` and `L0Hadron` trigger lines differentiate between electrons, photons and hadrons by using the technique illustrated in Fig. 3.7. Events are saved if their E_{T} recorded by the ECAL (HCAL) is measured to be above 2.5–3.0 GeV (3.5–4.0 GeV), with the threshold changing depending on the data taking conditions. The L0 trigger selection for $B^0 \to K^{*0}\mu^+\mu^-$ decays is based solely on the `L0Muon` and `L0DiMuon` trigger lines, and these are explained in more detail in the following paragraph.

The `L0Muon` and `L0DiMuon` trigger algorithms use information from the five muon stations to detect tracks that are formed by aligned hits. An approximate estimate of the p_{T} of each track can be obtained from the spatial coordinates of the corresponding hits. The two tracks with the largest p_{T} are then used to make the trigger decision. The `L0Muon` trigger saves events if the larger p_{T} of the two is above a certain threshold, while in the case of the `L0DiMuon` trigger requirements are imposed on the product of the two largest p_{T} tracks. The thresholds are approximately 1.5–1.8 GeV and 1.0–2.3 GeV^2 for the `L0Muon` and `L0DiMuon` trigger lines respectively, varying with the data-taking conditions.

To take advantage of all the trigger lines, *e.g.* when calculating efficiencies and systematic uncertainties, the trigger decisions have to be categorised into groups. The three main categories are TOS, TIS and TISTOS. An event is categorised as a Trigger On Signal (TOS) event if its signal candidate causes the trigger to fire. It is categorised as a Trigger Independent of Signal (TIS) event if the trigger is fired by a particle that does not belong to the signal candidate. Due to the possibility that a trigger can be fired by both the signal candidate and a non-signal particle there is a third category that combines the other two, *i.e.* TISTOS = TIS & TOS.

To illustrate these categories the following example can be considered. A $B^0 \to K^{*0}\mu^+\mu^-$ signal candidate is triggered by one of its muons that has a p_{T} of 3 GeV. This is a clear TOS candidate for the `L0Muon` trigger. In the same event there is an independent muon that does not belong to the signal candidate, which has a p_{T} of 1.8 GeV.

The L0Muon trigger is therefore triggered again, but in this case the event is categorised as a TIS event. Since the event is triggered by both the signal candidate and a muon that does not belong to the signal, it is also a TISTOS event.

3.8.2 High level trigger

Events that pass the L0 trigger stage are subsequently processed by the software-based HLT. The HLT further reduces the output rate from 1 MHz to 5 kHz and 12.5 kHz in Run 1 and Run 2 respectively. Events that pass also the HLT are recorded in long-term storage. The HLT consists of two successive algorithms, the HLT1 and HLT2.

The first-level software trigger

The HLT1 trigger algorithm focuses on a fast reconstruction of tracks in events and selects those that most likely contain interesting flavour physics. It starts by performing a full reconstruction of tracks in the VELO, after which two different algorithms are employed in order to determine whether an event qualifies to be tested against the final requirements of the trigger.

The first of these short algorithms selects muon candidates. VELO tracks that also leave a hit in a defined search window of M3 pass the first stage of this algorithm. The search window is determined by extrapolating the VELO tracks by assuming that they correspond to a muon of at least 6 GeV. Those tracks that pass this first stage are then recalculated by combining the information from the VELO with the information from the M3 hit(s). The second stage subsequently searches for hits of these tracks in the M2, M4 and M5 stations. If at least one is found, the tracks are tagged as provisional muon candidates. By performing a linear fit of these tracks in the horizontal plane, their quality can be assessed by using the fits' χ^2 divided by the number of degrees of freedom (χ^2/ndf). The provisional muon candidate tracks are fitted until at least one fulfils the requirement of $\chi^2/\text{ndf} < 25$, at which point the algorithm stops. The second algorithm simply selects those tracks that have a sufficiently large IP with respect to any PV.

The next stage of the HLT1 is called 'forward tracking'. Those tracks that pass one or both of the two short algorithms are used to define search windows in the T1–T3 stations. Requirements are imposed on the momenta of the tracks in order to reduce the size of these search windows and therefore the processing time. Those hits that are found in the tracking stations are then combined with the information from the tracks by refitting the tracks using a Kalman [111, 112] filter.

The HLT1 trigger lines, used for the Run 1 data in this analysis, are called `Hlt1TrackAllL0` and `Hlt1TrackMuon` triggers. The `Hlt1TrackAllL0` trigger line selects all events with a track candidate with a $p_{\mathrm{T}} > 1.6$ GeV, while the `Hlt1TrackMuon` trigger line selects all events with a track candidate with a $p_{\mathrm{T}} > 1$ GeV and where the isMuon condition is satisfied. In addition, both lines require a minimum IP from the PV.

For the Run 2 period, the `Hlt1TrackAllL0` trigger line was replaced by the `Hlt1TrackMVA` and `Hlt1TwoTrackMVA` trigger lines. These two trigger lines are based on multivariate analysis (MVA) techniques[d], which increase the selection efficiencies.

The second-level software trigger

The HLT2 algorithm uses the information from all the sub-detectors to perform a complete reconstruction of all tracks in a given event. It then selects events using both inclusive and exclusive criteria. Exclusive HLT2 trigger lines are dedicated to specifically selected decays, while inclusive HLT2 trigger lines select decays that exhibit a certain topology. When selecting potential $B^0 \to K^{*0}\mu^+\mu^-$ candidates, two exclusive muon as well as six topological trigger lines are used.

The two exclusive muon algorithms used in the presented analysis are the `Hlt2SingleMuon` and the `Hlt2DiMuonDetached` trigger lines. An event passes the `Hlt2SingleMuon` line if one or both of the following criteria are satisfied: either a muon candidate within an event has a $p_{\mathrm{T}} > 10$ GeV, or the event has a muon track with a minimum p_{T} of 1.3 GeV, a very low χ^2/ndf and a significant IP. The `Hlt2DiMuonDetached` algorithm on the other hand requires two muon candidate tracks with low χ^2/ndf that originate from the same vertex and where both tracks have a significant IP with respect to the PV. Finally, the dimuon invariant mass of the tracks need to be above 1 GeV and the dimuon p_{T} has to be above 1.5 GeV.

The topological trigger lines exploit MVA techniques that use the vertex and track information of the event candidates. There are topological triggers for 2-, 3- and 4-body decays that contain at least one muon (`Hlt2TopoMu[2,3,4]Body`) and three equivalent trigger lines for multi-body decays that do not necessarily contain a muon (`Hlt2Topo[2,3,4]Body`). All six trigger lines require that the tracks come from a displaced B-hadron decay. In addition, the MVA classifier uses the IP of the tracks and the individual combined momenta and masses as input parameters.

The full list of trigger lines used for the analysis and for the different data sets can

[d]See Sec. 5.3 for more details on MVA techniques.

Stage	Triggers Run 1	Triggers 2016
L0	`L0Muon`	`L0Muon` or `L0DiMuon`
HLT 1	`Hlt1TrackAllL0` or `Hlt1TrackMuon`	`Hlt1TrackMVA`, `Hlt1TrackMuon` or `Hlt1TwoTrackMVA`
HLT 2	`Hlt2Topo[2,3,4]BodyBBDT`, `Hlt2TopoMu[2,3,4]BodyBBDT`, `Hlt2SingleMuon` or `Hlt2DiMuonDetached`	`Hlt2Topo[2,3,4]Body`, `Hlt2TopoMu[2,3,4]Body` or `Hlt2SingleMuon`

Table 3.2: Candidate events from 2011 and 2012 data (Run 1) and 2016 data are required to pass the below trigger lines. The trigger lines in this table correspond to TOS lines, *i.e.* they only select TOS events.

be found in Tab. 3.2. The `L0DiMuon` line is introduced in the selection applied to the 2016 data set, as it adds an additional $\sim 2.5\%$ of signal events. The `Hlt2DiMuonDetached` is however dropped, as it contains several inaccuracies that are difficult to correct. The number of signal candidates lost due to this decision is negligible.

3.9 Generation of simulated data

Simulated events are used in several places in the angular analysis of $B^0 \to K^{*0}\mu^+\mu^-$. Most importantly, simulated signal events are used to determine the distortion of the detector geometry, trigger, reconstruction and candidate selection of the angular distribution of the signal. This will be described in detail in Chpt. 8.

The analysis presented in this thesis makes use of two types of simulation. A decay's PHase SPace (PHSP) simulation only takes into account the kinematic constraints of the particles and does not depend on any input from theoretical models. On the contrary, physics simulations are based on theoretical models that dictate the physics of the particles within the decay. The physics simulations that are used in this thesis are generated according to the SM.

Events are simulated by generating pp collisions using Pythia [120,121] with a specific LHCb configuration [122]. The EvtGen software [123] is subsequently used to describe the decays of the hadronic particles. The final-state radiation is generated using Photos [124].

The GEANT4 [125] toolkit subsequently models the interaction of the simulated particles with the LHCb detector. To correct for data simulation differences all simulated samples are PID resampled, as well as reweighted in some of their variables as described in Sec. 7.2.

Part II

The angular analysis of the $B^0 \to K^{*0}\mu^+\mu^-$ decay

4. Analysis strategy

In this chapter the strategy for the angular analysis of $B^0 \to K^{*0}\mu^+\mu^-$ at LHCb is presented. The central objective of this analysis is to measure angular observables, in bins of q^2, using a maximum likelihood fit. The selection and the fit model closely follow those of the analysis of the LHCb collaboration presented in 2015 [2], where only the Run 1 data set was studied. The analysis presented here adds the 2016 data set, which approximately doubles the number of signal decays.

The first step of the analysis is to select the signal decay $B^0 \to K^{*0}(\to K^+\pi^-)\mu^+\mu^-$, as described in Chpt. 5. The selection consists of a cut-based approach, as well as a multivariate classifier to reduce background. The tree-level decays $B^0 \to \phi(1020)(\to \mu^+\mu^-)K^{*0}(\to K^+\pi^-)$, $B^0 \to J/\psi\,(\to \mu^+\mu^-)K^{*0}(\to K^+\pi^-)$ and $B^0 \to \psi(2S)(\to \mu^+\mu^-)K^{*0}(\to K^+\pi^-)$ with the same final state are rejected in the selection using vetoes of the q^2-regions $0.98 < q^2 < 1.1\,\mathrm{GeV}^2/c^4$, $8.0 < q^2 < 11.0\,\mathrm{GeV}^2/c^4$ and $12.5 < q^2 < 15.0\,\mathrm{GeV}^2/c^4$. However, the candidates of the $B^0 \to J/\psi\,K^{*0}$ are retained as they constitute the events of the control mode, enabling the validation of the angular fit. The control mode is also used for the training of the multivariate selection and to make sure that the simulation correctly describes the data. While the selection for the Run 1 data set is unchanged, there are slight differences between the selection for the Run 1 and the 2016 data set. These differences are emphasised in Chpt. 5.

The angular analysis is performed using a maximum likelihood fit of the reconstructed B mass, and the three decay angles $\vec{\Omega} = (\cos\theta_l, \cos\theta_K, \phi)$ defined in Sec. 2.9.1. The distribution of the invariant $K\pi$ mass, $m(K^+\pi^-)$, is fitted simultaneously to constrain contributions to the final state that do not arise from a decay of the K^{*0}-meson, the so-called S-wave, where K^+ and π^- are in a spin 0 configuration. The eight CP-averaged P-wave observables that describe the $B^0 \to K^{*0}\mu^+\mu^-$ decay are defined in Sec. 2.9.2. The observables are determined in bins of q^2, defined in Sec. 4.1, for both the S_i and the $P_i^{(\prime)}$ bases. The additional angular observables describing the S-wave and interference terms are fitted but treated as nuisance parameters.

The distributions of the decay angles and q^2 are distorted by the reconstruction and selection. This acceptance effect is accounted for by using an 'acceptance function' that is obtained from simulation, as described in Chpt. 8. The angular fit is performed simultaneously for the Run 1 and 2016 data samples, sharing the angular observables and using the appropriate acceptance corrections. Further details on the unbinned maximum-

likelihood fit are given in Chpt. 9. The systematic uncertainties that arise are presented in Chpt. 10 and the measurements of the angular observables are presented in Chpt. 11. A fit to these measurements using the FLAVIO software package is described in Chpt. 12.

4.1 Binning in q^2

The chosen q^2 binning is given in Tab. 4.1. It consists of two wide q^2 bins $1.1 < q^2 < 6.0\,\mathrm{GeV}^2/c^4$ and $15.0 < q^2 < 19.0\,\mathrm{GeV}^2/c^4$ and eight narrow bins of an approximate width of $2\,\mathrm{GeV}^2/c^4$.

Bin	q^2 range $[\,\mathrm{GeV}^2/c^4]$
1	$[0.1, 0.98]$
2	$[1.1, 2.5]$
3	$[2.5, 4.0]$
4	$[4.0, 6.0]$
5	$[6.0, 8.0]$
6	$[11.0, 12.5]$
7	$[15.0, 17.0]$
8	$[17.0, 19.0]$
9	$[1.1, 6.0]$
10	$[15.0, 19.0]$

Table 4.1: The q^2-binning chosen for the analysis presented in this thesis.

5. Selection

This chapter describes the process by which the events that pass the trigger are further selected in order to minimise the amount of background, while maximising the number of signal events. The first step in performing the selection is to form $B^0 \to K^{*0}(\to K^+\pi^-)\mu^+\mu^-$ signal candidates. This is achieved by combining a K^+, π^- and two oppositely charged muon tracks. However, not all of the signal candidates that are constructed in this way correspond to true signal decays. There are two major sources of backgrounds. In so-called peaking backgrounds some of the final-state particles have been misidentified, while in combinatorial backgrounds the particle tracks originate from multiple b-hadron decay modes. The following sections describe how these backgrounds can be reduced, starting with a cut-based selection that includes the stripping and pre-selection presented in Sec. 5.1, as well as the vetoes for specific peaking backgrounds described in Sec. 5.2. The combinatorial background is further reduced by a multivariate technique presented in Sec. 5.3. In the last part of the selection, described in Sec. 5.4, the tree level decays $B^0 \to \phi(1020)(\to \mu^+\mu^-)K^{*0}$, $B^0 \to J/\psi(\to \mu^+\mu^-)K^{*0}$ and $B^0 \to \psi(2S)(\to \mu^+\mu^-)K^{*0}$ with the same final state as the $B^0 \to K^{*0}\mu^+\mu^-$ decay are separated from the signal.

5.1 Stripping and pre-selection

The complete LHCb dataset cannot be made continuously available to the whole LHCb collaboration, as there are only finite computing resources available. A process known as stripping is therefore run over the dataset. This is an additional selection process that reduces the size of the dataset by approximately an order of magnitude, while having an above 90% efficiency on signal candidates. Several stripping 'lines' are defined that all consist of a different selection process and therefore have a different physics focus. Two very slightly differing versions of the `B2XMuMu` stripping line are used for the Run 1 and 2016 data. Both versions require the four tracks of the final-state particles to have significant IP with respect to all PVs in the event. In addition, the IP of the B^0 candidate has to be small with respect to the best PV. The angle between the reconstructed B^0 momentum and the line connecting this PV to the secondary vertex, the DIRA angle, is also required to be small. The secondary vertex has to be significantly displaced from the same PV. A full list of the stripping requirements is given in Tab. 5.1.

The candidates that pass the stripping line are required to satisfy some additional cri-

Candidate	Stripping Run 1	Stripping 2016
B meson	IP $\chi^2 < 16$ (best PV)	IP $\chi^2 < 16$ (best PV)
B meson	$4800\,\text{MeV}/c^2 < M < 7100\,\text{MeV}/c^2$	$4800\,\text{MeV}/c^2 < M < 7100\,\text{MeV}/c^2$
B meson	DIRA angle $< 14\,\text{mrad}$	DIRA angle $< 14\,\text{mrad}$
B meson	flight distance $\chi^2 > 121$	flight distance $\chi^2 > 121$
B meson	vertex $\chi^2/\text{ndf} < 8$	vertex $\chi^2/\text{ndf} < 8$
$\mu^+\mu^-$	$m(\mu^+\mu^-) < 7100\,\text{MeV}/c^2$	$m(\mu^+\mu^-) < 7100\,\text{MeV}/c^2$
$\mu^+\mu^-$	vertex $\chi^2/\text{ndf} < 9$	vertex $\chi^2/\text{ndf} < 9$
K^{*0}	$m(K^+\pi^-) < 6200\,\text{MeV}/c^2$	$m(K^+\pi^-) < 6200\,\text{MeV}/c^2$
K^{*0}	vertex $\chi^2/\text{ndf} < 9$	vertex $\chi^2/\text{ndf} < 8$
K^{*0}	flight distance $\chi^2 > 9$	flight distance $\chi^2 > 16$
tracks	$\text{prob}_{\text{ghost}} < 0.4$	$\text{prob}_{\text{ghost}} < 0.5$
hadron	min IP $\chi^2 > 9$	min IP $\chi^2 > 6$
muon	min IP $\chi^2 > 9$	min IP $\chi^2 > 9$
muon	isMuon	isMuon
muon	$\text{DLL}_{\mu\pi} > -3$	$\text{DLL}_{\mu\pi} > -3$

Table 5.1: Stripping selection criteria for the Run 1 and 2016 data.

teria, referred to as pre-selection criteria, which are designed to reject obvious backgrounds while retaining high signal efficiency. Two of these conditions are: to restrict the opening angle between every pair of tracks to be larger than 1 mrad, and to only accept pion and kaon track candidates that have been detected in the RICH. The former is enforced to avoid the same track being used to construct more than one of the final state particles. In addition, candidates are required to have $5170 < m(K^+\pi^-\mu^+\mu^-) < 5700\,\text{MeV}/c^2$ and $795.9 < m(K^+\pi^-) < 995.9\,\text{MeV}/c^2$. Tab. 5.2 gives a full list of all pre-selection requirements.

5.2 Peaking backgrounds

Several vetoes are applied to reject backgrounds from misidentified decays, also referred to as peaking backgrounds, as they are typically clustered in the reconstructed $m(K^+\pi^-\mu^+\mu^-)$ mass. Peaking backgrounds from $B_s^0 \to \phi(1020)\mu^+\mu^-$, $\Lambda_b^0 \to pK^-\mu^+\mu^-$, $B^0 \to J/\psi\, K^{*0}$, $B^0 \to \psi(2S)K^{*0}$, $B^+ \to K^+\mu^+\mu^-$ and $\overline{B}^0 \to \overline{K}^{*0}\mu^+\mu^-$ decays are considered. Vetoes

Candidates	Selection
Track	$0 < \theta < 400$ mrad
Track Pairs	$\theta_{pair} > 1$ mrad
K	`hasRich` True
K	$\mathrm{DLL}_{K\pi} >$ -5
π	`hasRich` True
π	$\mathrm{DLL}_{K\pi} < 25$
hadron	min IP $\chi^2 > 9$
B^0	$5170 < m(K^+\pi^-\mu^+\mu^-) < 5700\,\mathrm{MeV}/c^2$
K^{*0}	$795.9 < m(K^+\pi^-) < 995.9\,\mathrm{MeV}/c^2$

Table 5.2: Pre-selection cuts applied to stripped candidates. In this table θ is the angle relative to the beamline and θ_{pair} denotes the opening angle between two track pairs.

using PID and mass information are formed to reject these backgrounds. A detailed description of each veto is given below.

To reject background from $K \leftrightarrow \pi$ misidentification due to misreconstructed $\overline{B}^0 \to \overline{K}^{*0}\mu^+\mu^-$ signal decays the cut $\mathrm{DLL}_{K\pi}(K) > \mathrm{DLL}_{K\pi}(\pi)$ is applied. This cut also rejects background from $\Lambda_b^0 \to pK^-\mu^+\mu^-$ decays where the proton is misidentified as a pion. Furthermore, two dedicated vetos against $\Lambda_b^0 \to pK^-\mu^+\mu^-$ decays are applied. To reject candidates where the proton is misidentified as pion, candidates with

$$\begin{aligned} \mathrm{DLL}_{p\pi}(\pi) > 0 \text{ and} \\ m_{K(\pi\to p)\mu\mu} \in [5575, 5665]\,\mathrm{MeV}/c^2 \end{aligned} \tag{5.1}$$

are vetoed. The Λ_b^0 decays can also mimic the signal decays if the proton is misidentified as a kaon and the kaon as a pion. As a further veto, candidates with

$$\begin{aligned} \mathrm{DLL}_{K\pi}(\pi) > 0 \text{ and} \\ m_{(K\to p)(\pi\to K)\mu\mu} \in [5575, 5665]\,\mathrm{MeV}/c^2 \end{aligned} \tag{5.2}$$

are therefore rejected.

Another potential source of peaking backgrounds are the tree-level charmonium decays $B^0 \to J/\psi(\to \mu^+\mu^-)K^{*0}(\to K^+\pi^-)$ and $B^0 \to \psi(2S)(\to \mu^+\mu^-)K^{*0}(\to K^+\pi^-)$. If the μ^- is misidentified as π^- and the π^- as μ^- (or the μ^+ as K^+ and the K^+ as μ^+) this decay can escape the charmonium vetoes (*i.e.* the q^2 regions $[8.0, 11.0]\,\mathrm{GeV}^2/c^4$ and

$[12.5, 15.0]\,\mathrm{GeV}^2/c^4$) and can be misreconstructed as signal. This background is vetoed by rejecting events with

$$m_{(\pi\to\mu)\mu} \in [3036, 3156]\,\mathrm{MeV}/c^2 \text{ and} \quad \mathrm{DLL}_{\mu\pi}(\pi) > 5.0 \text{ or } \mathrm{isMuon}(\pi) \tag{5.3}$$

as well as

$$m_{(K\to\mu)\mu} \in [3036, 3156]\,\mathrm{MeV}/c^2 \text{ and} \quad \mathrm{DLL}_{\mu\pi}(K) > 5.0 \text{ or } \mathrm{isMuon}(K). \tag{5.4}$$

To reject the potential contribution from $\psi(2S)$ decays, candidates with

$$m_{(\pi\to\mu)\mu} \in [3626, 3746]\,\mathrm{MeV}/c^2 \text{ and} \quad \mathrm{DLL}_{\mu\pi}(\pi) > 5.0 \text{ or } \mathrm{isMuon}(\pi) \tag{5.5}$$

and

$$m_{(K\to\mu)\mu} \in [3626, 3746]\,\mathrm{MeV}/c^2 \text{ and} \quad \mathrm{DLL}_{\mu\pi}(K) > 5.0 \text{ or } \mathrm{isMuon}(K) \tag{5.6}$$

are vetoed.

The rare $B^0_s \to \phi(1020)(\to K^+K^-)\mu^+\mu^-$ decay can be misreconstructed as signal if a kaon is misreconstructed as a pion. This background is removed by rejecting candidates with

$$m_{K(\pi\to K)\mu\mu} \in [5321, 5411]\,\mathrm{MeV}/c^2 \tag{5.7}$$

and

$$m_{K(\pi\to K)} \in [1010, 1030]\,\mathrm{MeV}/c^2 \text{ and } \mathrm{DLL}_{K\pi}(\pi) > -10 \text{ or} \quad m_{K(\pi\to K)} \in [1030, 1075]\,\mathrm{MeV}/c^2 \text{ and } \mathrm{DLL}_{K\pi}(\pi) > +10. \tag{5.8}$$

The first tighter window captures the majority of the $B^0_s \to \phi(1020)(\to K^+K^-)\mu^+\mu^-$ events, while the looser window captures the upper ϕ tail and some of the KK S-wave contribution. Finally, the rare decay $B^+ \to K^+\mu^+\mu^-$ can be a source of background if a random slow pion from the rest of the event is added to the final state. As the random pion carries additional momentum, this background is located in the upper mass sideband. It is removed by rejecting candidates with

$$m_{K\pi\mu\mu} > 5380\,\mathrm{MeV}/c^2 \text{ and} \quad m_{K\mu\mu} \in [5220, 5340]\,\mathrm{MeV}/c^2. \tag{5.9}$$

Decay	Total eff.(%)	Eff rel. to sig.(%)	Yield rel. to sig.(%)
$B^0 \to K^{*0}\mu^+\mu^-$	0.7280± 0.0028	100	-
$B^0 \to J/\psi\, K^{*0}$	0.0087± 0.0023	1.20	0.11± 0.21
$\overline{B}^0 \to \overline{K}^{*0}\mu^+\mu^-$	0.0162± 0.0004	2.23	0.65±0.02
$\Lambda_b^0 \to pK^-\mu^+\mu^-$	0.0018± 0.0002	0.25	0.06±0.02
$B_s^0 \to \phi(1020)\mu^+\mu^-$	0.0093± 0.0004	1.28	0.21±0.03
$B^+ \to K^+\mu^+\mu^-$	0.0009± 0.0001	0.13	0.09±0.01

Table 5.3: Expected background contamination as a proportion of expected signal yield.

5.2.1 Estimation of peaking background yields

The background yields that remain after the full selection are estimated using simulated events and are summarised in Tab. 5.3. The largest residual backgrounds are from $\overline{B}^0 \to \overline{K}^{*0}\mu^+\mu^-$ and $B_s^0 \to \phi(1020)(\to K^+K^-)\mu^+\mu^-$ decays, with contributions of $(0.65 \pm 0.02)\%$ and $(0.21 \pm 0.03)\%$ of the signal yield respectively. The background levels are small enough so that they can be neglected in the final angular fit. A systematic uncertainty that arises as a byproduct is assigned and described in Sec. 10.5. Furthermore, the $B^+ \to K^+\mu^+\mu^-$ veto has an effect on the angular distribution of the background and therefore an additional systematic uncertainty is assigned (see Sec. 10.6).

5.3 Multivariate selection

Most of the combinatorial background is reduced by Boosted Decision Trees (BDTs) [126]. This MVA approach gives a value for each event that lies between -1 and 1, with 1 being most signal-like and -1 being most background-like. A BDT is constructed out of many individual decision trees that classify the event either as signal or background, depending on given input variables (*e.g.* the p_{T} of the B^0). The final result of the BDT is obtained by forming a weighted combination of the individual decision trees. The separation power that BDTs provide can be more powerful than purely cut-based analysis approaches when the combination of decision trees is chosen well, the main reason being that a BDT efficiently exploits the correlation between its input variables.

The analysis presented here uses two BDTs, one for the Run 1 data selection and another for the 2016 data selection. The BDTs are trained on data, using $B^0 \to J/\psi\, K^{*0}$ events as signal proxy, and the upper mass sideband of $B^0 \to K^{*0}\mu^+\mu^-$

decays ($m(K^+\pi^-\mu^+\mu^-)$ in $[5350, 7000]\,\mathrm{MeV}/c^2$) as background proxy. In order to remove the background in the data sample, the *sPlot* [127] technique is employed. This statistically removes the background contribution by providing each event with an *sWeight*. Using these *sWeights* the distributions can be considered to only consist of $B^0 \to J/\psi\, K^{*0}$ signal events. The variable used to obtain the *sPlot* is the $K^+\pi^-\mu^+\mu^-$ invariant mass.

The BDTs are trained with the AdaBoost algorithm [128] provided by the Toolkit for Multivariate Analysis [129]. In order to use all events for training and testing without introducing any bias, the *k-fold* technique with ten folds is used [130]. The events are first split into ten equal parts. The BDTs are then trained on nine of these parts before being tested on the tenth part. This can be done ten times without running into statistical dependencies of train- and test-samples.

The input variables used in the BDTs are:

- the B^0 candidate lifetime;
- the B^0 momentum and p_T;
- the B^0 DIRA angle;
- the $K^+\pi^-\mu^+\mu^-$ vertex χ^2;
- the $\mathrm{DLL}_{K\pi}$ of the kaon and pion;
- the $\mathrm{DLL}_{\mu\pi}$ of the muons;
- the isolation variables of the four final state particles.

The isolation variables are a measure of the spatial separation between muons and hadrons and the other particles in the event. Only the muon isolation variables are used for the BDT of the 2016 data (BDT_{2016}), as the hadron isolation variables used in Run 1 were not available for the 2016 stripping. All of the above variables show a good separation power between signal and background.

The input variables of the BDTs were chosen in such a way that they are only weakly correlated to q^2, the $K^+\pi^-\mu^+\mu^-$ invariant mass and the angular distribution of the final state particles. The efficiency of the BDT_{2016} as a function of the angles is shown in Fig. 5.1(a)-(c). Fig. 5.1(d) illustrates the effect of the BDT_{2016} on the $B^0 \to J/\psi\, K^{*0}$ control channel. While the background is clearly reduced by applying the BDT selection, the signal peak remains nearly unchanged. The efficiency on the signal channel is obtained

by using simulation. The BDT requirement rejects more than 97% of the remaining combinatorial background and retains more than 85% of the signal.

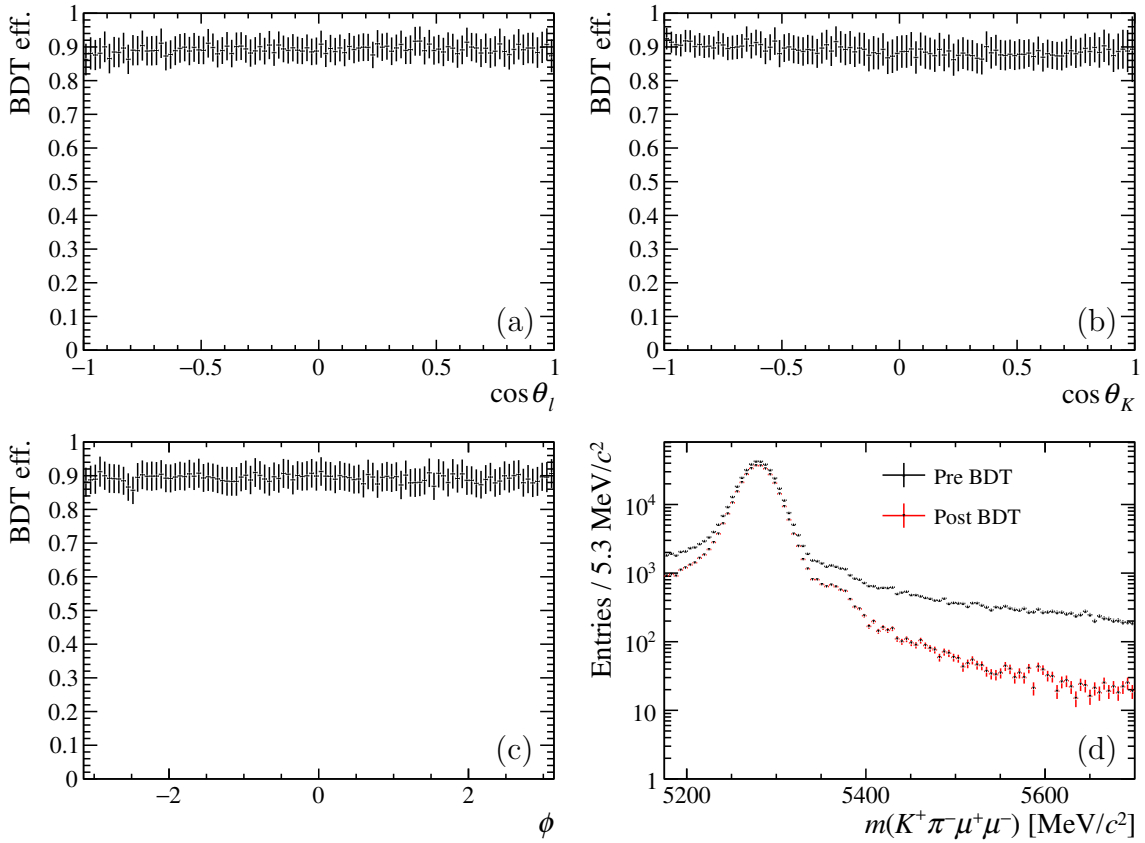


Figure 5.1: The efficiencies of the BDT cut across the angles as calculated on $B^0 \to J/\psi K^{*0}$ physics simulation are shown in (a)-(c). Plot (d) illustrates the effect of the BDT on the 2016 data set. It shows the $K^+\pi^-\mu^+\mu^-$ invariant mass distribution of the $B^0 \to J/\psi K^{*0}$ control channel before and after the BDT selection has been applied. The $B_s^0 \to J/\psi K^{*0}$ channel can be seen to the right of the mass peak (see Chpt. 6).

5.4 Control channel

The $B^0 \to K^{*0}\mu^+\mu^-$ signal decay can be separated from the $B^0 \to J/\psi K^{*0}$ control channel and the $B^0 \to \psi(2S)K^{*0}$ decay by applying a cut on q^2. Fig. 5.2 shows the 2D plots of the $K^+\pi^-\mu^+\mu^-$ invariant mass versus q^2 for candidates that pass the full selection for both the Run 1 and 2016 data. The vertical band in both plots corresponds to $B^0 \to K^{*0}\mu^+\mu^-$ signal candidates, while the contributions from the $B^0 \to J/\psi K^{*0}$ and $B^0 \to \psi(2S)K^{*0}$

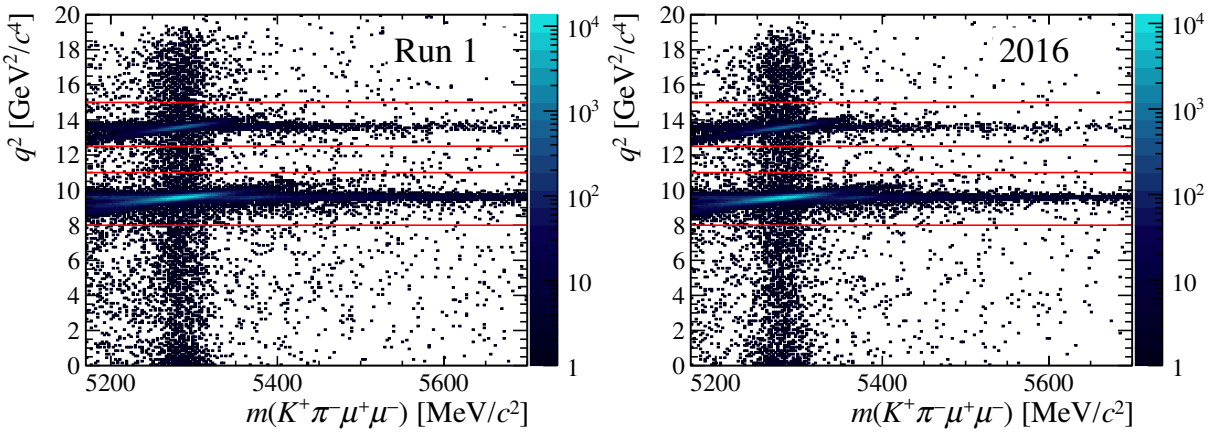


Figure 5.2: The invariant $K^+\pi^-\mu^+\mu^-$ mass versus q^2. The horizontal bands correspond to the J/ψ and $\psi(2S)$ resonances respectively. These resonances are removed for the measurement of the angular observables in the signal channel. The corresponding vetoes are illustrated by the red lines. The vertical band corresponds to the $B^0 \to K^{*0}\mu^+\mu^-$ signal decay.

decays can clearly be seen in the horizontal bands around the nominal B^0 mass. The $B^0 \to J/\psi\, K^{*0}$ and $B^0 \to \psi(2S)K^{*0}$ decays both proceed via a tree-level $b \to c\bar{c}s$ transition and therefore dominate the flavour changing neutral current transition of $B^0 \to K^{*0}\mu^+\mu^-$. Hence the q^2 regions of the J/ψ and $\psi(2S)$ resonances, $8.0 < q^2 < 11.0\,\mathrm{GeV}^2/c^4$ and $12.5 < q^2 < 15.0\,\mathrm{GeV}^2/c^4$, are excluded from the analysis of the signal decay. Although a much smaller contribution, $B^0 \to \phi(1020)K^{*0}$ decays are also rejected using a veto of $0.98 < q^2 < 1.1\,\mathrm{GeV}^2/c^4$.

While the $B^0 \to \psi(2S)K^{*0}$ and $B^0 \to \phi(1020)K^{*0}$ events are rejected, the candidates of the $B^0 \to J/\psi\, K^{*0}$ are retained as they constitute the events of the control mode, which are used to validate the angular fit (see Sec. 9.7). In Sec. 7.2 the control mode is further used to correct for data and simulation differences.

6. Mass model and signal yields

Fits to the $K^+\pi^-\mu^+\mu^-$ invariant mass distribution play a central role in the angular analysis of $B^0 \to K^{*0}\mu^+\mu^-$. Most importantly, they allow signal and background candidates to be differentiated, which is essential for the angular fit (see Chpt. 9) and for the correction of simulation data differences (see Sec. 7.2). The following two sections describe the mass model used in the analysis, and report the signal and background yields in both the control and signal channel.

6.1 The $K^+\pi^-\mu^+\mu^-$ invariant mass fit model

Two effects must be taken into account when designing the fit model for the $K^+\pi^-\mu^+\mu^-$ invariant mass distribution: the resolution of the detector and the bremsstrahlung of the final state particles. While the former results in the mass distribution taking a Gaussian shape, the latter can influence the tails of the mass distribution. The bremsstrahlung of the final state particles results in the $K^+\pi^-\mu^+\mu^-$ mass being systematically too small, as softly radiated photons are not considered in the reconstruction algorithm of the detector.

To parameterise both these effects, the Crystal Ball function is used, which is a combination of a Gaussian and a power law tail. Its shape is given by

$$\mathcal{P}_{\mathrm{CB}}(m|\mu,\sigma,\alpha,n) = \begin{cases} e^{-\frac{1}{2}\left(\frac{m-\mu}{\sigma}\right)^2} & \frac{m-\mu}{\sigma} > -|\alpha| \\ \frac{a}{\left(b-\left(\frac{m-\mu}{\sigma}\right)\right)^n} & \frac{m-\mu}{\sigma} \leq -|\alpha| \end{cases}, \tag{6.1}$$

where m is the invariant mass, μ the mean of the former and n the tail parameter. The parameter α is used to separate the shape into a Gaussian and a power law tail. The parameters a and b in the power law tail description are given by

$$\begin{aligned} a =& \left(\frac{n}{|\alpha|}\right)^n e^{-\frac{1}{2}\alpha^2} \text{ and} \\ b =& \frac{n}{|\alpha|} - |\alpha| \ . \end{aligned} \tag{6.2}$$

The signal part of the $K^+\pi^-\mu^+\mu^-$ invariant mass distribution of the $B^0 \to K^{*0}\mu^+\mu^-$ and $B^0 \to J/\psi\, K^{*0}$ decays is best described by the sum of two Crystal Ball functions with a common μ, α and n, but different σ (σ_1 and σ_2). Explicitly, the reconstructed B^0 mass

is parameterised as

$$\mathcal{P}_{\text{sig}}(m|\vec{\lambda}) = f_{\text{core}}\mathcal{P}_{\text{CB}}(m|\mu,\sigma_1,\alpha,n) + (1-f_{\text{core}})\mathcal{P}_{\text{CB}}(m|\mu,\sigma_2,\alpha,n), \tag{6.3}$$

where f_{core} is the fraction of the first Crystal Ball function and $(1-f_{\text{core}})$ the fraction of the second. The background of the invariant mass distribution is described by an exponential distribution with the decay constant τ_{m}.

The fit to the $B^0 \to J/\psi K^{*0}$ control decay includes an additional signal component to account for $B_s^0 \to J/\psi K^{*0}$ events. The component is expressed with the same signal parameterisation as the control channel, but includes a shift of the mean μ by $\Delta m = m(B_s^0) - m(B^0)$. The results of the fits to the Run 1 and 2016 data are shown in Fig. 6.1. The slight inaccuracies at 5425 MeV/c^2 and above 5500 MeV/c^2 are due to residual $\Lambda_b^0 \to J/\psi p\pi^-$ background decays and the $B^+ \to K^+\mu^+\mu^-$ veto, respectively. While the remaining background of the $\Lambda_b^0 \to J/\psi p\pi^-$ decay is negligible when fitting for the $B^0 \to K^{*0}\mu^+\mu^-$ signal, the effect of the $B^+ \to K^+\mu^+\mu^-$ veto results in a small systematic uncertainty (see Sec. 10.6). The fit yields for the $B^0 \to J/\psi K^{*0}$ channel for the Run 1 and 2016 data are $347\,350 \pm 830$ and $324\,970 \pm 760$ respectively. The mass parameters of the fits are given in Tab. 6.1.

The values of the parameters describing the $B^0 \to K^{*0}\mu^+\mu^-$ signal mass shape are the same as those obtained by the fit to the control channel. However, to account for possible changes of the signal mass shape with q^2, a scaling factor s_σ is determined from fits to simulated $B^0 \to K^{*0}\mu^+\mu^-$ signal events. This scaling factor is multiplied by the widths of the Crystal Ball functions to obtain the correct widths for the signal channel, *i.e.* $\sigma'_{1,2} = s_\sigma \cdot \sigma_{1,2}$. The scaling factors for the two data taking periods are given in Tab. 6.2.

6.2 Event yields

The fits to the $K^+\pi^-\mu^+\mu^-$ invariant mass distribution of $B^0 \to K^{*0}\mu^+\mu^-$ candidates for the narrow q^2 bins are shown in Fig. 6.2 for the 2016 data. The equivalent distributions and fits for the Run 1 data, as well as the fits for the wide bins for both data taking periods can be found in Fig. A.1 and Fig. A.2 of Appendix A. The $B^0 \to K^{*0}\mu^+\mu^-$ yield, integrated over the q^2 ranges $0.10 < q^2 < 0.98\,\text{GeV}^2/c^4$, $1.1 < q^2 < 8.0\,\text{GeV}^2/c^4$, $11 < q^2 < 12.5\,\text{GeV}^2/c^4$ and $15.0 < q^2 < 19.0\,\text{GeV}^2/c^4$, is determined to be 2398 ± 57 for the Run 1 data, and 2187 ± 53 for the 2016 data. The full list of the signal and background yields in each q^2 bin for the two data taking periods are given in Tab. 6.3.

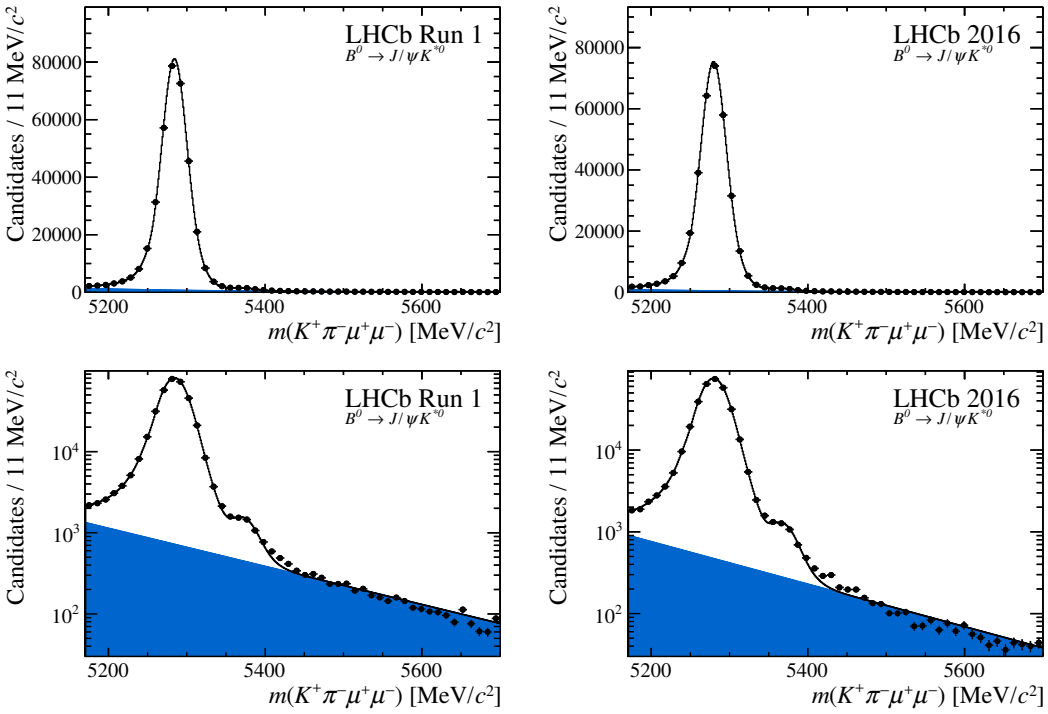


Figure 6.1: Fit to the $B^0 \to J/\psi K^{*0}$ control channel in the Run 1 and 2016 data. The background is indicated by the shaded region. Figure taken from Ref. [1].

Parameter	Run 1	2016
f_{sig}	0.9262 ± 0.0017	0.9436 ± 0.0018
$m_{B^0}(\mu)[\,\text{MeV}/c]$	5284.357 ± 0.044	5279.713 ± 0.045
f_{core}	0.707 ± 0.025	0.722 ± 0.026
$\sigma_1[\,\text{MeV}/c]$	15.36 ± 0.16	15.66 ± 0.17
$\sigma_2[\,\text{MeV}/c]$	25.87 ± 0.60	26.41 ± 0.68
α	1.499 ± 0.034	1.568 ± 0.041
n	5.16 ± 0.87	5.2 ± 1.1
$\tau_{\text{m}}[s^{-1}]$	154.3 ± 2.5	132.2 ± 2.5
$f_{B_s^0}$	0.01195 ± 0.00037	0.01153 ± 0.00038
$\Delta m[\,\text{MeV}/c]$	90.68 ± 0.86	88.17 ± 0.86

Table 6.1: Mass model parameters determined from fits to the $B^0 \to J/\psi K^{*0}$ control channel in the Run 1 and 2016 data. The parameter f_{sig} refers to the fraction of events that are signal candidates. The discrepancy in m_{B^0} between the different data taking periods originates from the fact that no momentum rescaling has been applied in Run 1.

$q^2[\,\mathrm{GeV}^2]$	s_σ Run 1	s_σ 2016
$[0.1, 0.98]$	0.982	0.960
$[1.1, 2.5]$	0.996	0.977
$[2.5, 4.0]$	0.992	0.989
$[4.0, 6.0]$	0.996	0.992
$[6.0, 8.0]$	1.000	0.994
$[11.0, 12.5]$	1.007	1.008
$[15.0, 17.0]$	1.049	1.051
$[17.0, 19.0]$	1.074	1.062
$[1.1, 6.0]$	0.995	0.987
$[15.0, 19.0]$	1.059	1.056

Table 6.2: Scaling factors s_σ to correct for the Crystal ball widths in the $B^0 \to K^{*0}\mu^+\mu^-$ channel for the Run 1 and 2016 data.

	Run 1		2016	
$q^2[\,\mathrm{GeV}^2]$	signal yield	background yield	signal yield	background yield
$[0.1, 0.98]$	337.7 ± 19.6	57.8 ± 10.2	289.6 ± 18.2	59.9 ± 10.1
$[1.1, 2.5]$	179.4 ± 15.4	120.1 ± 13.3	185.1 ± 15.7	113.4 ± 13.2
$[2.5, 4.0]$	164.6 ± 15.8	200.9 ± 16.9	166.7 ± 15.1	126.8 ± 13.7
$[4.0, 6.0]$	278.6 ± 20.1	290.9 ± 20.4	244.9 ± 18.0	161.6 ± 15.5
$[6.0, 8.0]$	343.6 ± 22.1	337.9 ± 21.9	339.3 ± 21.3	189.1 ± 17.4
$[11.0, 12.5]$	329.7 ± 21.0	206.8 ± 17.8	296.9 ± 19.5	130.6 ± 14.6
$[15.0, 17.0]$	448.3 ± 23.8	185.2 ± 17.4	408.8 ± 22.3	120.7 ± 14.5
$[17.0, 19.0]$	300.1 ± 19.8	139.4 ± 15.2	255.6 ± 17.6	71.9 ± 11.2
$[1.1, 6.0]$	623.5 ± 29.9	612.0 ± 29.7	597.3 ± 28.3	402.2 ± 24.6
$[15.0, 19.0]$	748.6 ± 30.9	324.9 ± 23.1	664.8 ± 28.5	192.7 ± 18.5
$[0.1, 19.0]$	2392.7 ± 56.5	1578.8 ± 48.7	2187.3 ± 53.3	979.2 ± 39.9

Table 6.3: Signal and background yields in bins of q^2 for the Run 1 and 2016 data.

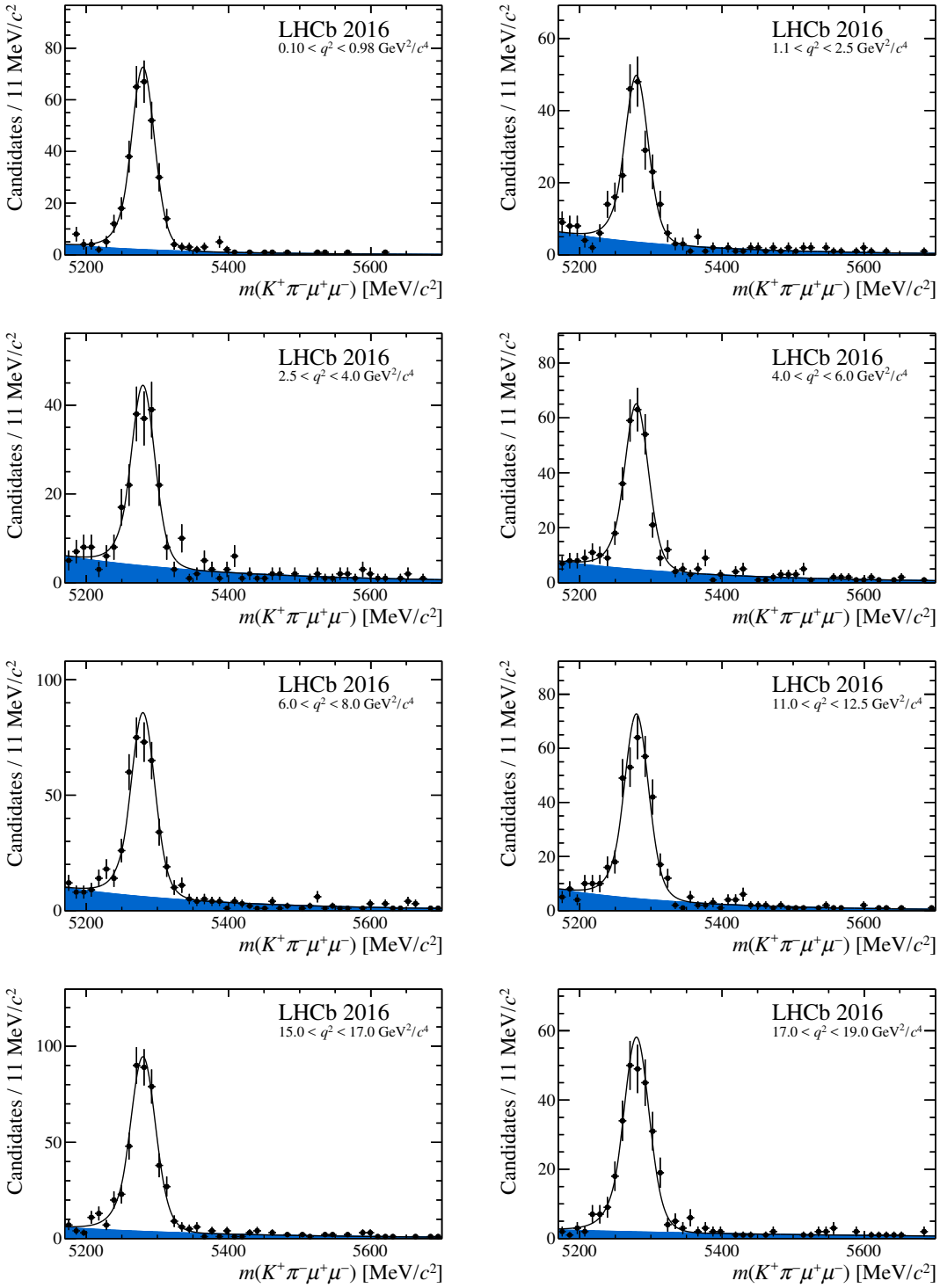


Figure 6.2: The $K^+\pi^-\mu^+\mu^-$ invariant mass distribution of $B^0 \to K^{*0}\mu^+\mu^-$ candidates in the narrow q^2 bins for the 2016 data. Figure taken from Ref. [1].

7. Agreement between data and simulation

Good agreement between data and simulated events is vital for the reliable calculation of acceptance effects. To improve this agreement, data-driven corrections are employed in two steps. First, the PID variables are resampled, as described in Sec. 7.1. Secondly, remaining differences are corrected by explicitly re-weighting distributions of kinematic variables, as outlined in Sec. 7.2.

7.1 Resampling the particle identification variables

Specific criteria are applied to PID variables to reduce the amount of peaking background events in the data sample (see Sec. 5.2). As the same peaking background selection is applied to simulation, the agreement between the PID variable distributions in simulation and data is crucial. However, the presence of large numbers of incorrectly modelled low energy photons in the RICH detectors result in the PID variables in simulation being poorly reproduced. To correct for their values in simulation, all PID variables are resampled using clean high statistics control samples selected from the data. These samples are listed in Tab. 7.1.

For Run 1, histograms of the PID variables are produced in bins of η, track multiplicity (`nTracks`) and p_{T} using the data control samples. For a given simulated track, the PID variables are then randomly sampled from the corresponding calibration histogram, which is chosen using the track's η and p_{T}, as well as the number of tracks in the event.

A more sophisticated method that was not available for the Run 1 data is used for the 2016 data. The distributions of the four relevant variables (PID, `nTracks`, p_{T}, η) in the applicable high statistics data sample are approximated with a kernel density estimation (KDE) technique. The PID variables in simulation are then sampled from the resulting kernels that describe the distribution. The kernels are calculated following the method outlined in Ref. [131]. The advantages of the KDE technique, in comparison with the usual histogram resampling method, include a reduced dependency on the binning choice and increased ability to capture finer features in the distributions.

The validation of the PID resampling is performed by comparing the *sWeighted* [127]

Particle	Sample
K	$D^{*+} \to D^0(\to K^+\pi^-)\pi^+$
π	$D^{*+} \to D^0(\to K^+\pi^-)\pi^+$
μ	$J/\psi \to \mu^+\mu^-$

Table 7.1: High statistics data samples used for the Run 1 and 2016 resampling corrections.

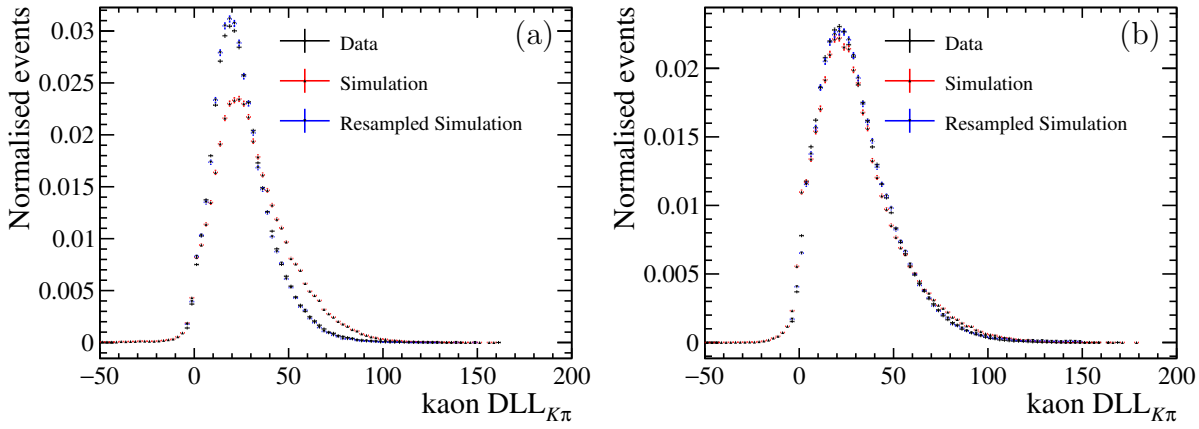


Figure 7.1: Distributions of the kaon DLL$_{K\pi}$ variable for *sWeighted* $B^0 \to J/\psi K^{*0}$ data and (resampled) $B^0 \to J/\psi K^{*0}$ simulation for Run 1 in (a) and 2016 in (b).

$B^0 \to J/\psi K^{*0}$ data with $B^0 \to J/\psi K^{*0}$ physics simulation, where the simulation has been resampled and reweighted as per the reweighting procedure outlined in Sec. 7.2. Fig. 7.1 shows the distributions for the DLL$_{K\pi}$ variable for the kaons in the Run 1 and 2016 data, as well as their respective simulations. The PID resampling does not perfectly replicate the DLL distributions from data in simulation, and a systematic uncertainty is therefore assigned (see Sec. 10.9.1).

7.2 Explicit reweighting

The remaining differences between simulation and data are corrected by explicitly reweighting the distributions of the number of tracks in the event (`nTracks`), the vertex fit quality of the signal candidate (χ^2_{Vtx}), and the B^0 candidate's transverse momentum $p_{\text{T}}(B^0)$. These variables need to be corrected for simulation data discrepancies as the vertex fit quality and the B^0 transverse momentum are used in the BDT. In addition, the number

of tracks in the event are poorly modelled in simulation, and have a strong impact on the particle identification performance.

The event weights for all simulated samples are calculated by comparing distributions of $B^0 \to J/\psi K^{*0}$ control channel events in data to the corresponding distributions from simulated events. In order to remove the background in the data sample the *sPlot* [127] technique is employed. The fit model used to determine the *sWeights* is described in Chpt. 6 and the result of the fit to the 2016 data can be seen in Fig. 7.2. Using the *sWeighted* data and the corresponding simulated distributions of `nTracks`, χ^2_{Vtx} and the candidate's p_{T}, the weights that correct for data simulation discrepancies can be determined. These weights are derived sequentially, with the $(N-1)^{\text{th}}$ weight being applied before deriving the N^{th} weight: first, an event weight is derived for `nTracks`, which is then applied before deriving the weight for $p_{\text{T}}(B^0)$. The product of the event weights for `nTracks` and $p_{\text{T}}(B^0)$ is then applied before deriving the weight for χ^2_{Vtx}. The event weights are stored in histograms, which are subsequently used to weight all simulated samples.

The effect of this procedure for the 2016 data and simulation is shown in Fig. 7.3. The BDT selection is not performed on the data that is used for the re-weighting calculation, as the BDT uses two of the re-weighted variables as input. The data are fitted in the invariant mass range of $5170 < m(K^+\pi^-\mu^+\mu^-) < 5800\,\text{MeV}/c^2$ and integrated over a q^2 range of $8.0 < q^2 < 11.0\,\text{GeV}^2/c^4$. The re-weighting procedure for the simulated Run 1 samples is performed in an equivalent way.

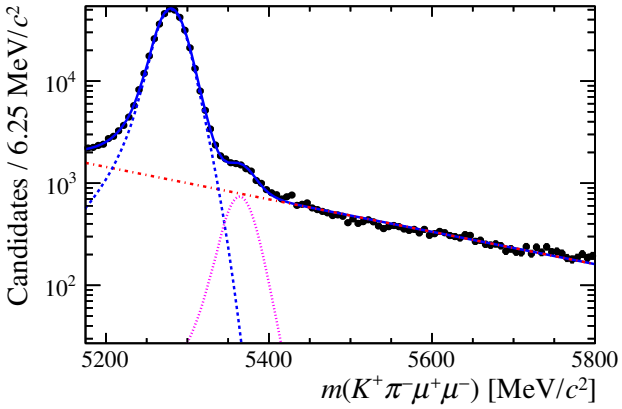


Figure 7.2: Fit to the invariant mass of the $K^+\pi^-\mu^+\mu^-$ system for the $B^0 \to J/\psi\, K^{*0}$ control decay for the 2016 data. The black dots correspond to data points, the solid blue line to the complete fit model, the dashed blue line to the signal component, the dotted magenta line to the $B_s^0 \to J/\psi\, K^{*0}$ model and the red dashed line to the background component.

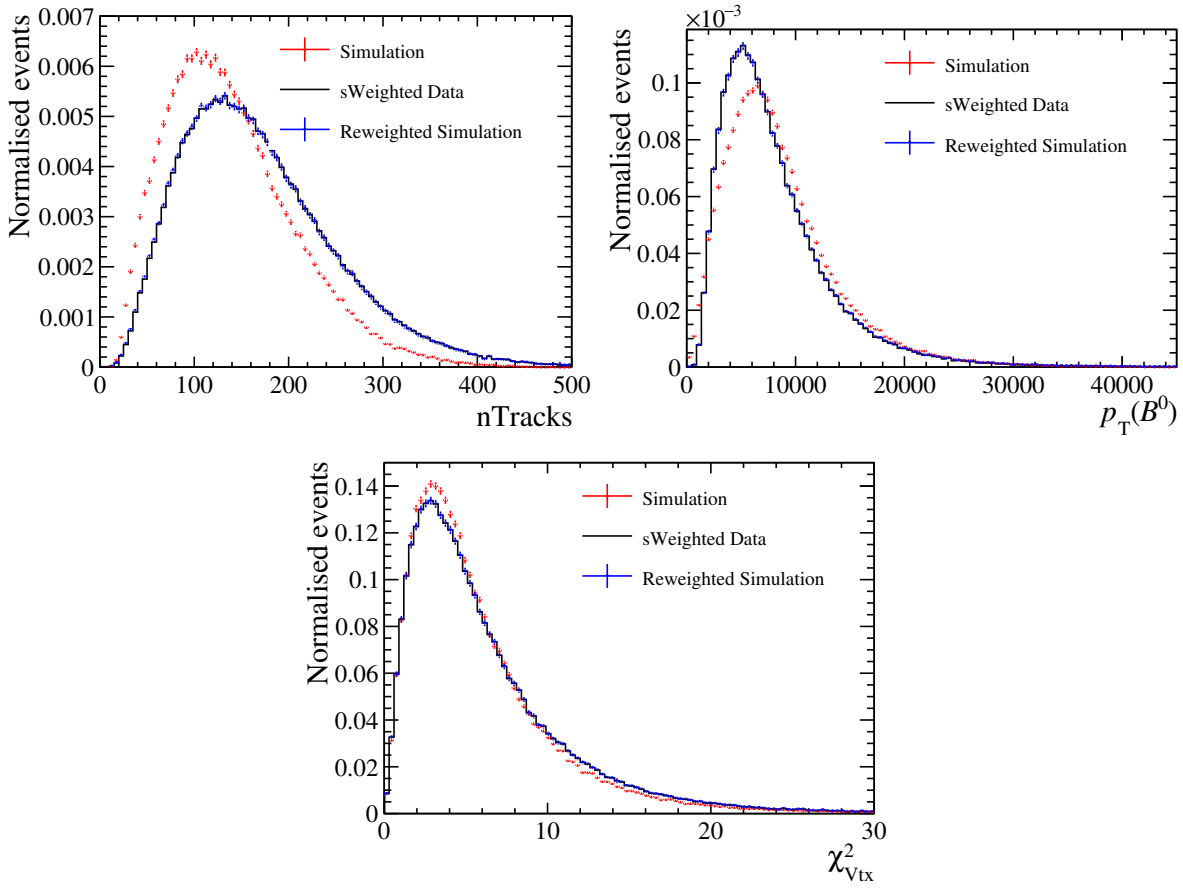


Figure 7.3: The distributions of `nTracks`, $p_T(B^0)$ and χ^2_{Vtx} are shown for the 2016 $B^0 \to J/\psi K^{*0}$ simulation and the corresponding *sWeighted* data. After the re-weighting procedure, the simulated distributions agree with the *sWeighted* data distributions.

8. Acceptance

The reconstruction and selection of the signal decay distorts the distributions of the decay angles and q^2, resulting in a so-called acceptance effect. This effect is modelled using $B^0 \to K^{*0}\mu^+\mu^-$ PHSP simulation that has been generated by the procedure outlined in Sec. 3.9. The distortion created by reconstructing and selecting the simulated events is accounted for by an acceptance function that is parameterised using a method of moments approach, whereby the angular and q^2 distributions of the simulated events are described using Legendre polynomials. This chapter explains in detail how this function is determined, introduces the necessary reweighting of the simulation and gives the results of the acceptance functions for the Run 1 and 2016 data.

8.1 Acceptance parametrisation

The acceptance functions for the Run 1 and 2016 data are parameterised in the three decay angles $\cos\theta_l$, $\cos\theta_K$ and ϕ, as well as in q^2, without assuming factorisation. This results in the expression

$$\varepsilon(\cos\theta_l, \cos\theta_K, \phi, q^2) = \sum_{ijmn} c_{ijmn} L_i(\cos\theta_l) L_j(\cos\theta_K) L_m(\phi) L_n(q^2), \tag{8.1}$$

where $L_h(x)$ are Legendre polynomials of order h and the observables q^2, $\cos\theta_K$, $\cos\theta_l$ and ϕ are rescaled to the range $-1 < x < +1$ when evaluating the polynomial. The coefficients c_{ijmn} are obtained using simulated signal events. An expression for the coefficients can be calculated using Monte Carlo integration and the intrinsic orthogonality property of the Legendre polynomials, where the latter is given by

$$\int_{-1}^{+1} L_{i'}(x) L_i(x) \mathrm{d}x = \frac{2}{2i+1} \delta_{ii'}. \tag{8.2}$$

For the sake of clarity, the derivation of the coefficients is illustrated only for $\cos\theta_l$. The same method can easily be extended to also include $\cos\theta_K$, q^2 and ϕ, where the latter two variables are rescaled linearly to the range $-1 < x < +1$ before calculating the coefficients. Reducing Eq. 8.1 by excluding all but the $\cos\theta_l$ terms results in the following expression for the acceptance function:

$$\varepsilon(\cos\theta_l) = \sum_i c_i L_i(\cos\theta_l). \tag{8.3}$$

As a first step in the derivation, Eq. 8.3 is multiplied by $L_i'(\cos\theta_l)$ and integrated over $\cos\theta_l$ to give

$$\int_{-1}^{+1} L_{i'}(\cos\theta_l)\varepsilon(\cos\theta_l)\mathrm{d}\cos\theta_l = \sum_i \int_{-1}^{+1} L_{i'}(\cos\theta_l)c_i L_i(\cos\theta_l)\mathrm{d}\cos\theta_l. \tag{8.4}$$

Pairing up the matching Legendre polynomial and using the orthogonality property given by Eq. 8.2, the following is obtained:

$$\int_{-1}^{+1} L_{i'}(\cos\theta_l)\varepsilon(\cos\theta_l)\mathrm{d}\cos\theta_l = \sum_i c_i \frac{2}{2i+1}\delta_{ii'}. \tag{8.5}$$

Hence

$$c_i = \int_{-1}^{+1} \left(\frac{2i+1}{2}\right) L_i(\cos\theta_l)\varepsilon(\cos\theta_l)\mathrm{d}\cos\theta_l, \tag{8.6}$$

where the prime has been dropped. At this stage the Monte Carlo integration approximation is implemented. It is given by

$$\varepsilon(\cos\theta_l) \approx \frac{1}{N}\sum_{e=1}^{N}\delta(\cos\theta_l - \cos\theta_{l,e}), \tag{8.7}$$

where e is the index of the simulated signal event and N is the number of all the signal events in the simulation. Inserting the above expression into Eq. 8.6 and evaluating the delta function results in the coefficients being given by the following

$$c_i = \frac{1}{N}\sum_{e=1}^{N}\left(\frac{2i+1}{2}\right) L_i(\cos\theta_{l,e}). \tag{8.8}$$

Generalising Eq. 8.8 to also include the $\cos\theta_K$, ϕ and q^2 terms results in the expression

$$\begin{aligned} c_{ijmn} = \frac{1}{N}\sum_{e=1}^{N}&\left(\frac{2i+1}{2}\right)\left(\frac{2j+1}{2}\right)\left(\frac{2m+1}{2}\right)\left(\frac{2n+1}{2}\right) \\ &L_i(\cos\theta_{l,e})L_j(\cos\theta_{K,e})L_m(\phi_e)L_n(q_e^2), \end{aligned} \tag{8.9}$$

As a last step, weights (denoted by w_e) are introduced in order to correct for the non-flat distribution of events in q^2 (see Sec. 8.2) and to account for data-driven corrections (see Sec. 7.2). Accounting for these weights, Eq. 8.8 becomes

$$c_{ijmn} = \frac{1}{N'} \sum_{e=1}^{N} w_e \left(\frac{2i+1}{2}\right) \left(\frac{2j+1}{2}\right) \left(\frac{2m+1}{2}\right) \left(\frac{2n+1}{2}\right) \\ L_i(\cos\theta_{l,e}) L_j(\cos\theta_{K,e}) L_m(\phi_e) L_n(q^2_e). \tag{8.10}$$

In addition to introducing the weights, the above formula also accounts for the change in normalisation by replacing N by N', where

$$N' = \sum_{e=1}^{N} w_e. \tag{8.11}$$

The following section will describe how the non-flat distributions of events in q^2 have been corrected for, in both the Run 1 and 2016 data.

8.2 q^2 reweighting at generator level

The simulated events are generated using a PHSP model (see Sec. 3.9). This is very convenient, as it ensures that the distribution of the events is flat in $\cos\theta_l$, $\cos\theta_K$ and ϕ. Any subsequent change in the shape can thus be interpreted as the efficiency distribution of the variable in question. However, generating the simulation with a pure PHSP model means that the q^2 distribution is non-flat, as there is a reduced probability of generating muon pairs at high q^2. To account for this, weights are derived at generator level to force the q^2 distribution to be flat. In this section, the procedure used to calculate these so-called q^2 weights, for both the Run 1 and 2016 simulations, is outlined.

To obtain the q^2 weights, the q^2 distribution of events at generator level has to be simulated. The results of the generator level q^2 distributions for both the pure PHSP simulation used in Run 1, as well as for the FLATQ2 model used to generate the simulation for 2016, can be seen in Fig. 8.1. It can be observed that the distribution of the pure PHSP simulation decreases faster in q^2 than that of the distribution of the FLATQ2 model. Despite its name the FLATQ2 model does not produce a perfectly flat distribution in q^2. This is because the finite width of the K^{*0} resonance leads to different $K\pi$ masses and thus results in different PHSP constraints for the dimuon pair. If the K^{*0} were a narrow

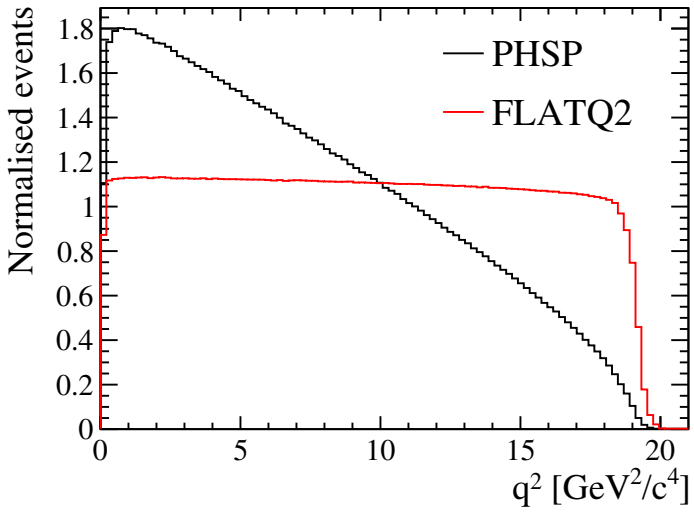


Figure 8.1: The q^2 distributions of simulated events at the generator level using the PHSP model and the FLATQ2 model.

resonance, this distribution would appear completely flat. Weights must therefore be applied also for the FLATQ2 model to force the q^2 distribution to be flat. The weights for the Run 1 and 2016 simulations are determined by taking the inverse of the corresponding distribution shown in Fig. 8.1.

8.3 Four-dimensional acceptance functions for the Run 1 and 2016 data

The two acceptance functions for the Run 1 and 2016 data are modelled using Legendre polynomials of the lowest order that are sufficient to describe the simulation accurately[a]. For q^2, Legendre polynomials of fifth and lower orders are used. For the decay angles, polynomials of fourth and lower orders are used for $\cos\theta_l$, fifth and lower orders for $\cos\theta_K$ and sixth and lower orders for the angle ϕ. This results in a total of 1260 coefficients that are determined using 1.406 M (7.657 M) reconstructed and selected simulated signal events in the Run 1 (2016) data. The number of events for both simulation samples is

[a]The order of the Legendre polynomials is determined by comparing the one- and two-dimensional projections of the acceptance function with the corresponding simulation. In addition, high orders are avoided, as they result in the appearance of oscillations at the borders of the distributions (Runge phenomenon [132]).

sufficiently large to obtain an accurate description of the acceptance effects. In particular, the systematic uncertainty associated with the limited statistics of the simulation samples is small compared to most of the other systematic uncertainties (see Sec. 10.8).

The one-dimensional projections of the acceptance functions on q^2 and on the three decay angles are given in Fig. 8.2. Good agreement is seen between these projections and the distributions of the corresponding simulations, with the exception of those in q^2. In this case, the acceptance functions do not describe the corresponding simulation well at low q^2. Higher order q^2 polynomials of the acceptance functions successfully capture the features that are poorly modelled, and a small systematic uncertainty is assigned in Sec. 10.7 by using a higher order parameterisation. This higher order parameterisation is not used as the nominal, as the proponents of the analysis decided not to change the Run 1 acceptance from that in Ref. [2]. This decision is well motivated, as the systematic uncertainty due to using the lower order parameterisation is small compared to the other systematic uncertainties and negligible compared to the statistical uncertainty. Fig. B.1, Fig. B.2 and Fig. B.3 in Appendix B show the one-dimensional projections of the acceptance functions and simulations on $\cos\theta_l$, $\cos\theta_K$ and ϕ, in bins of q^2. Again, the four dimensional parameterisations describe the distribution of the simulations very well. In addition, Fig. 8.3 gives the two-dimensional projections of the 2016 acceptance parameterisation, and the corresponding two-dimensional efficiency determined from simulation. The equivalent figure for Run 1, Fig. B.4, can be found in Appendix B. The difference between the Run 1 and 2016 acceptance functions are due to the changes in the trigger and the BDT (see Chpt. 5).

A few general comments can be made about the shape of the projections of the acceptance functions in Fig. 8.2. The distributions of $\cos\theta_l$ and ϕ both appear to be symmetric about the y-axis. This symmetry arises naturally from the definition of the two angles. While the symmetry in ϕ is forced in the acceptance parametrisations, the same is not true of $\cos\theta_l$; a small misalignment of the detector could namely lead to a bias, resulting in positively charged muons being treated differently than their negative counterparts. An asymmetry could therefore arise in $\cos\theta_l$. In contrast, $\cos\theta_K$ is naturally asymmetric because of the different masses of the pion and the kaon.

When comparing the differences in the error bars of the Run 1 and 2016 simulations it can be observed that those of the 2016 simulation are generally smaller, as more simulated events are available. The difference is particularly prominent in the high q^2 bins of Fig. B.1, Fig. B.2 and Fig. B.3. This is not only because there are more simulated events

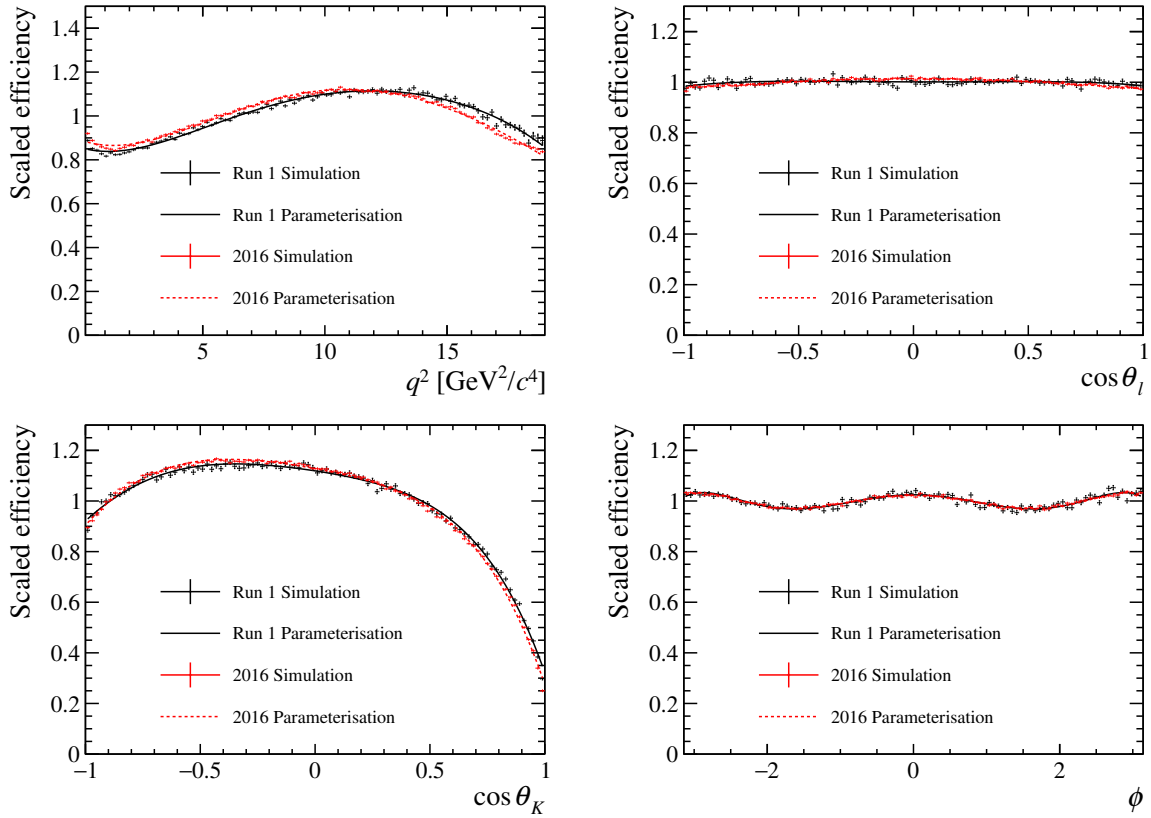


Figure 8.2: Distributions of the Run 1 and 2016 acceptance simulations in q^2, $\cos\theta_l$, $\cos\theta_K$, and ϕ. Corresponding one-dimensional projections of the four-dimensional acceptance functions on q^2, $\cos\theta_l$, $\cos\theta_K$, and ϕ are also shown.

available in 2016, but also because the FlatQ2 model provides many more events at high q^2 than the PHSP model (see Fig. 8.1).

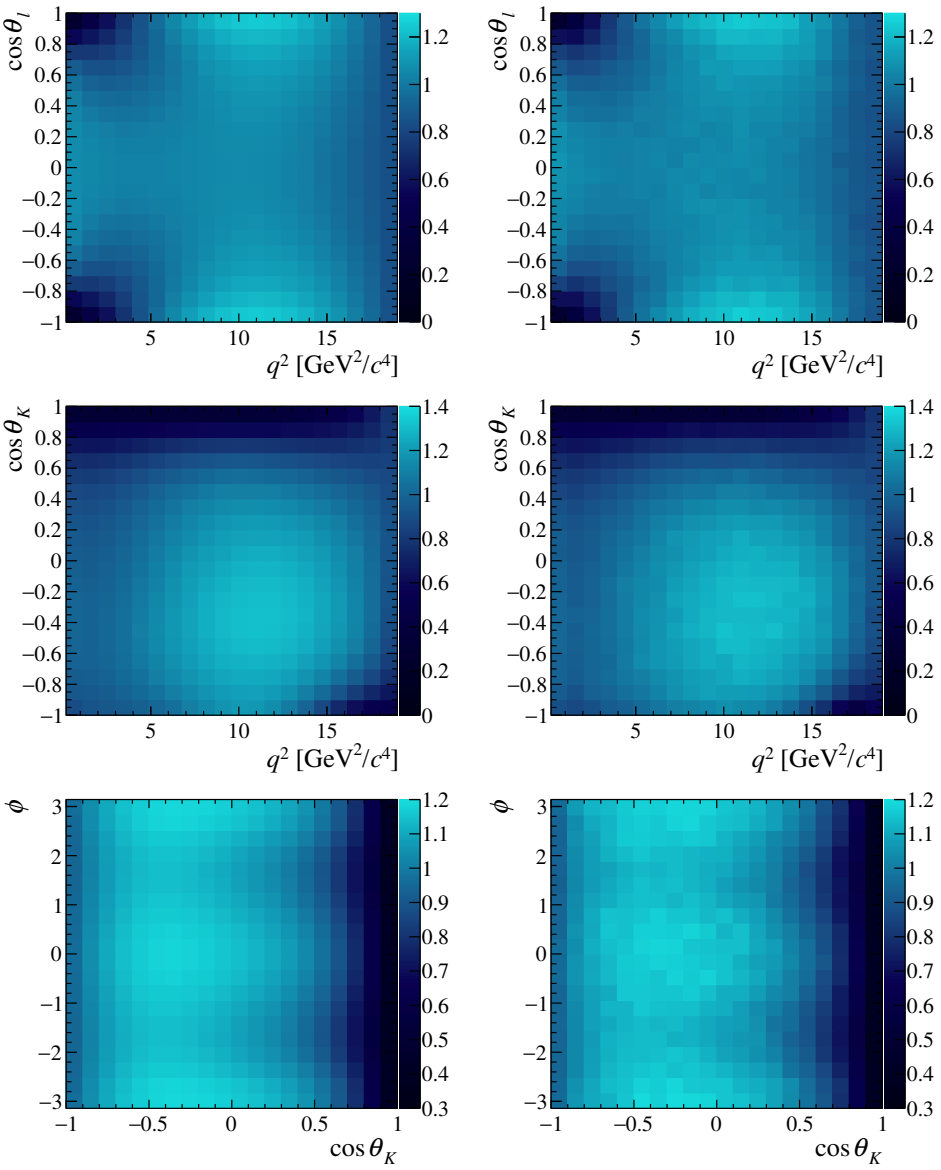


Figure 8.3: Two-dimensional projections of the four-dimensional acceptance parameterisation on q^2, $\cos\theta_l$, $\cos\theta_K$, and ϕ for 2016 (left), compared with the corresponding efficiency projection determined from the simulation histograms (right).

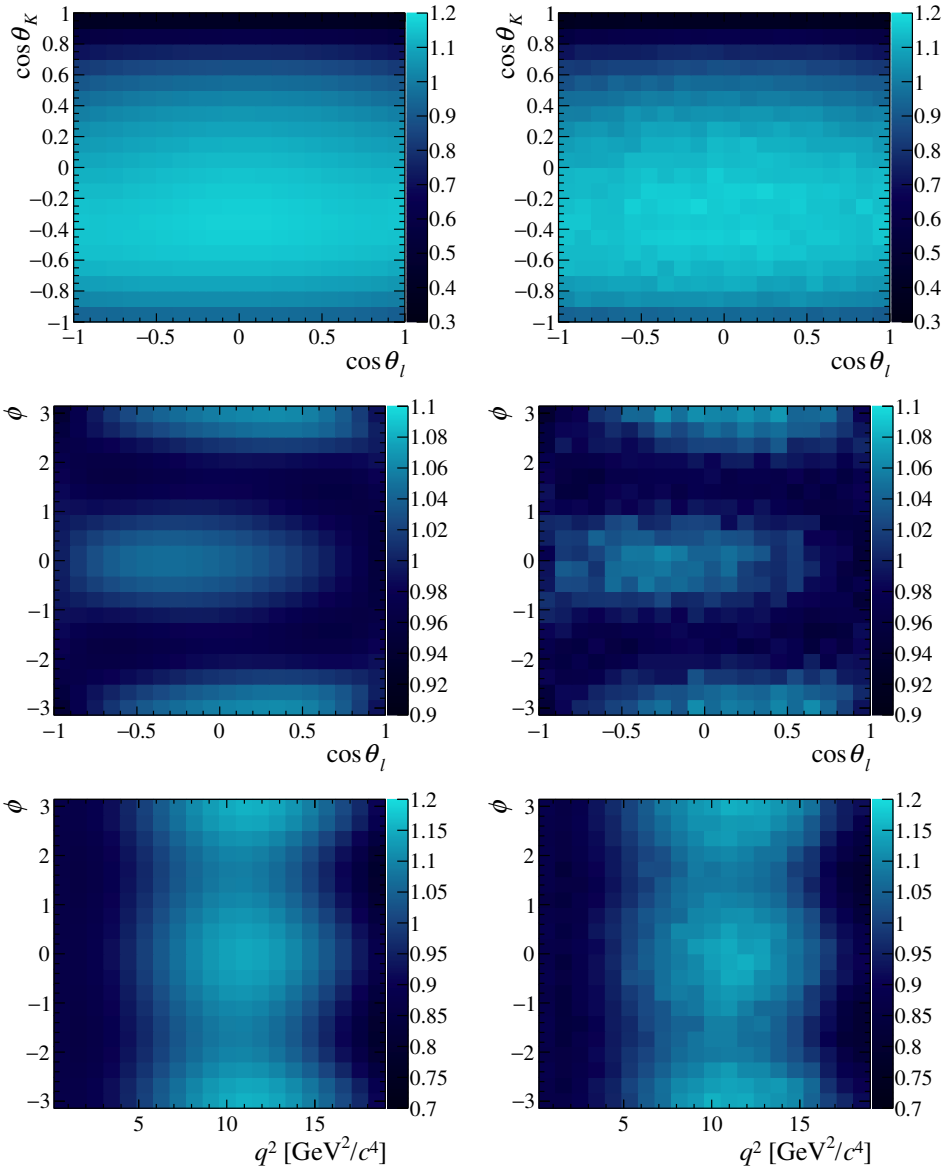


Figure 8.3: Continued from the previous page.

9. Angular fit model

The angular observables for both the S_i and $P_i^{(\prime)}$ bases are determined in bins of q^2. For each q^2 bin, an unbinned maximum-likelihood fit to the distributions of $m_{K\pi\mu\mu}$ and the three decay angles is used to determine the *CP*-averaged angular observables, and a simultaneous fit of the $m(K^+\pi^-)$ invariant mass distribution is used to constrain the S-wave fraction. This chapter describes the expression for the Probability Density Functions (PDFs) used to construct the likelihood function with which the angular observables are determined.

9.1 Probability density function of the reconstructed B^0 mass and the decay angles

The probability density function of the reconstructed B^0 mass ($m_{K\pi\mu\mu}$) and the three decay angles ($\vec{\Omega} = \{\cos\theta_l, \cos\theta_K, \phi\}$) is described using a signal and a background component that depend on the angular observables and nuisance parameters. The PDF is given by

$$\mathcal{P}_{\text{tot}} = f_{\text{sig}}\mathcal{P}_{\text{sig}}(\vec{\Omega}, m_{K\pi\mu\mu}) + (1 - f_{\text{sig}})\mathcal{P}_{\text{bkg}}(\vec{\Omega}, m_{K\pi\mu\mu}), \tag{9.1}$$

with f_{sig} denoting the signal fraction. The signal and background components are both assumed to factorise in the decay angles $\vec{\Omega}$ and $m_{K\pi\mu\mu}$:

$$\mathcal{P}_{\text{sig}}(\vec{\Omega}, m_{K\pi\mu\mu}) = \mathcal{P}_{\text{sig}}(\vec{\Omega}) \times \mathcal{P}_{\text{sig}}(m_{K\pi\mu\mu}) \tag{9.2}$$

$$\mathcal{P}_{\text{bkg}}(\vec{\Omega}, m_{K\pi\mu\mu}) = \mathcal{P}_{\text{bkg}}(\vec{\Omega}) \times \mathcal{P}_{\text{bkg}}(m_{K\pi\mu\mu}). \tag{9.3}$$

The $K^+\pi^-\mu^+\mu^-$ invariant mass distribution of the signal is modelled using the sum of two Crystal Ball functions, as described in Sec. 6. The parameters describing the signal mass shape are determined from a fit to the $B^0 \to J/\psi\, K^{*0}$ control channel and the q^2 dependence is accounted for using a q^2 dependent scale factor obtained from simulation. The mass distribution of the background is modelled using an exponential function. For the fits of the $B^0 \to K^{*0}\mu^+\mu^-$ signal, only τ_m, the inverse of the exponential decay constant, and f_{sig} are floated. Both parameters f_{sig} and τ_m are allowed to vary independently in each q^2 bin.

The angular description of the signal component of the PDF is given by the differential decay rate presented in Sec. 2.9 (Eq. 2.43 and Eq. 2.45). As the data are binned in q^2, the

angular observables are effectively averaged over the width of the q^2 bins. The angular distribution of the background component is described using Chebyshev polynomials, T_i, of second order and lower[a]. The parameterisation of the background is assumed to factorise in the angles[b] with the PDF given by

$$\mathcal{P}_{\text{bkg}}(\cos\theta_l, \cos\theta_K, \phi) = \left[\sum_{i=0}^{2} c_i T_i(\cos\theta_l)\right] \times \left[\sum_{j=0}^{2} c_j T_j(\cos\theta_K)\right] \times \left[\sum_{k=0}^{2} c_k T_k(\phi)\right]. \quad (9.4)$$

Again, the background parameters are allowed to vary independently between the different q^2 bins.

9.2 S-wave and $m_{K\pi}$ distribution

As is apparent from Eq. 2.45, the S-wave contribution results in all P-wave parameters being scaled by a factor of $(1 - F_{\text{S}})$. The S-wave fraction can be constrained by fitting to the $m_{K\pi}$ distribution, which is peaking for the P-wave contribution, but is relatively flat for the S-wave contribution. The $m_{K\pi}$ distribution and the distributions of $m_{K\pi\mu\mu}$ and the three decay angles are fitted simultaneously, allowing for a determination of F_{S} without limiting the precision of the P-wave parameters.

Following the approach of Ref. [133], the PDF describing the $m_{K\pi}$ distribution and expressions for the different decay amplitudes is obtained. To parameterise the $m_{K\pi}$ dependence of the P-wave, a Breit-Wigner distribution is used:

$$\mathcal{A}_P(m_{K\pi}) = \sqrt{kp} \times B'_{L_B}(k, k_0, d) \left(\frac{k}{m_B}\right)^{L_B} \times B'_{L_{K^{*0}}}(p, p_0, d) \left(\frac{p}{m_{K\pi}}\right)^{L_{K^{*0}}} \times \frac{1}{m^2_{K^{*0}} - m^2_{K\pi} - i m_{K^{*0}} \Gamma(m_{K\pi})}, \quad (9.5)$$

where k (p) denotes the K^{*0} (K^+) momentum in the B^0 (K^{*0}) rest frame and k_0 (p_0) is the corresponding quantity at the resonance peak. The orbital angular momenta $L_{K^{*0}}$ and L_B take values 1 and 0, respectively[c]. The Blatt-Weisskopf functions [134] B'_i are defined

[a] The corresponding systematic uncertainty of this assumption is discussed in Sec. 10.4.

[b] This assumption has been verified by comparing the corresponding non-factorisable model with the factorised one. No significant deviations between the two sets of coefficients were found.

[c] The K^{*0} is in a P-wave state and therefore has an angular momentum of 1. The dimuons originate from a spin-one boson. L_B can therefore take values from 0 to 2, and as the dominating decay is the one with the smallest energy $L_B = 0$, to a good approximation.

as

$$B'_0(p, p_0, d) = 1 \tag{9.6}$$

$$B'_1(p, p_0, d) = \sqrt{\frac{1 + d^2 p_0^2}{1 + d^2 p^2}}, \tag{9.7}$$

and thus $B'_{L_B=0} = 1$ and $B'_{L_{K^{*0}}=1} = \sqrt{(1 + d^2 p_0^2) / (1 + d^2 p^2)}$, where $d = 1.6\,\text{GeV}^{-1}$ [135]. The parameter $\Gamma(m_{K\pi})$ is the mass dependent decay width given by

$$\begin{aligned}\Gamma(m_{K\pi}) &= \Gamma(K^{*0}) \left(\frac{p}{p_0}\right)^{2L_{K^{*0}}+1} \frac{m_{K^{*0}}}{m_{K\pi}} B'^2_{L_{K^{*0}}} \\ &= \Gamma(K^{*0}) \left(\frac{p}{p_0}\right)^{3} \frac{m_{K^{*0}}}{m_{K\pi}} \frac{1 + d^2 p_0^2}{1 + d^2 p^2},\end{aligned} \tag{9.8}$$

where $\Gamma(K^{*0})$ is the decay width of the $K^{*0}(892)$ meson.

For the S-wave component, the LASS parameterisation [136] is used:

$$\begin{aligned}\mathcal{A}_S(m_{K\pi}) = \sqrt{kp} \times B'_{L_B}(k, k_0, d) \left(\frac{k}{m_B}\right)^{L_B} \times B'_{L_{K_0^*}}(p, p_0, d) \left(\frac{p}{m_{K\pi}}\right)^{L_{K_0^*}} \\ \times \left(\frac{1}{\cot\delta_B - i} + e^{2i\delta_B} \frac{1}{\cot\delta_R - i}\right),\end{aligned} \tag{9.9}$$

where $\cot\delta_B = \frac{1}{ap} + \frac{1}{2} rp$ and $\cot\delta_R = (m^2_{K_0^*} - m^2_{K\pi})/(m_{K_0^*}\Gamma_0(m_{K\pi}))$. The parameters a and r correspond to the scattering length and range with values $a = 1.95\,\text{GeV}^{-1}c$ and $r = 1.78\,\text{GeV}^{-1}c$ [137]. The angular momenta for the S-wave are $L_{K_0^*} = 0$ and $L_B = 1$. The mass dependent decay width $\Gamma_0(m_{K\pi})$ therefore becomes

$$\Gamma_0(m_{K\pi}) = \Gamma_0(K_0^*) \left(\frac{q}{q_0}\right) \frac{m_{K_0^*}}{m_{K\pi}}, \tag{9.10}$$

where $\Gamma_0(K_0^*)$ is now the decay width of the $K_0^*(1430)$ meson.

Accounting for the $m_{K\pi}$ dependence integrated over the three decay angles Eq. 2.45 becomes

$$\begin{aligned}\frac{1}{\mathrm{d}(\Gamma + \bar{\Gamma})/\mathrm{d}q^2} \frac{\mathrm{d}(\Gamma + \bar{\Gamma})}{\mathrm{d}m_{K\pi}}\bigg|_{\mathrm{S+P}} = (1 - F_{\mathrm{S}}) \sum_{i=1}^{8} \tfrac{9}{32\pi} \xi_i S_i |\mathcal{A}'_{\mathrm{P}}(m_{K\pi})|^2 \\ + \tfrac{3}{16\pi} \big[F_{\mathrm{S}} \xi_{F_{\mathrm{S}}} |\mathcal{A}'_{\mathrm{S}}(m_{K\pi})|^2 \\ + (S_{\mathrm{S}1}\xi_{\mathrm{S}1} + S_{\mathrm{S}2}\xi_{\mathrm{S}2} + S_{\mathrm{S}3}\xi_{\mathrm{S}3}) \,\mathrm{Re}\,(\mathcal{A}'_{\mathrm{S}}(m_{K\pi}) \mathcal{A}^{*\prime}_{\mathrm{P}}(m_{K\pi})) \\ + (S_{\mathrm{S}4}\xi_{\mathrm{S}4} + S_{\mathrm{S}5}\xi_{\mathrm{S}5}) \,\mathrm{Im}\,(\mathcal{A}'_{\mathrm{S}}(m_{K\pi}) \mathcal{A}^{*\prime}_{\mathrm{P}}(m_{K\pi}))\big],\end{aligned} \tag{9.11}$$

where $\xi_{(\mathrm{S})\mathrm{i}}$ denote the angular integrals $\xi_{(\mathrm{S})\mathrm{i}} = \int \varepsilon(\cos\theta_l, \cos\theta_K, \phi) f_{(\mathrm{S})\mathrm{i}}(\cos\theta_l, \cos\theta_K, \phi) \mathrm{d}\vec{\Omega}$. Here, the acceptance function ε is not a function of q^2, as it is evaluated at the centre of the q^2 bin (see Sec. 9.5 for more details). To account for the correct normalisation of the amplitudes, $\mathcal{A}'_{\mathrm{P}}(m_{K\pi})$ and $\mathcal{A}'_{\mathrm{S}}(m_{K\pi})$ are defined as follows:

$$\mathcal{A}'_{\mathrm{P}}(m_{K\pi}) = \frac{\mathcal{A}_{\mathrm{P}}(m_{K\pi})}{\sqrt{\int_{795.9\,\mathrm{MeV}/c^2}^{995.9\,\mathrm{MeV}/c^2} |\mathcal{A}_{\mathrm{P}}(m_{K\pi})|^2 \mathrm{d}m_{K\pi}}},$$
$$\mathcal{A}'_{\mathrm{S}}(m_{K\pi}) = \frac{\mathcal{A}_{\mathrm{S}}(m_{K\pi})}{\sqrt{\int_{795.9\,\mathrm{MeV}/c^2}^{995.9\,\mathrm{MeV}/c^2} |\mathcal{A}_{\mathrm{S}}(m_{K\pi})|^2 \mathrm{d}m_{K\pi}}}.$$

In the case of a constant acceptance the angular integrals of the interference terms $\xi_{S1\ldots5}$ equal zero and the corresponding terms disappear in Eq. 9.11. For the nominal acceptance functions, the interference terms are of the order of a few percent and are therefore included for completeness.

In summary, the full PDF of the $m_{K\pi}$ distribution is defined as follows:

$$\mathcal{P}_{K\pi} = f_{\mathrm{sig}} \mathcal{P}_{\mathrm{sig}}(m_{K\pi}) + (1 - f_{\mathrm{sig}}) \mathcal{P}_{\mathrm{bkg}}(m_{K\pi}), \tag{9.12}$$

where $\mathcal{P}_{\mathrm{sig}}(m_{K\pi})$ is given by Eq. 9.11 and the PDF of the background distribution $\mathcal{P}_{\mathrm{bkg}}(m_{K\pi})$ is modelled using a first order Chebyshev polynomial[d].

9.3 Logarithmic likelihood function

Having defined the PDFs for the four-dimensional description of $m_{K\pi\mu\mu}$ and the three decay angles given by (9.1), and the $m_{K\pi}$ distribution given by (9.12), the negative logarithmic likelihood function is formulated as follows:

$$\begin{aligned} -\log\mathcal{L} = &- \sum_{\text{events } e} \log \mathcal{P}_{\mathrm{tot}}(\vec{\Omega}_e, m_{K\pi\mu\mu,e} | \vec{\lambda}_{\mathrm{phys}}, \vec{\lambda}_{\mathrm{nuisance}}) \\ &- \sum_{\text{events } e} \log \mathcal{P}_{K\pi}(m_{K\pi,e} | \vec{\lambda}_{\mathrm{phys}}, \vec{\lambda}_{\mathrm{nuisance}}), \end{aligned} \tag{9.13}$$

where $\vec{\lambda}_{\mathrm{phys}}$ are the angular observables, including the P-wave observables S_i ($P_i^{(\prime)}$ for the optimised basis), the S-wave fraction F_{S}, and the S-wave/P-wave interference parameters S_{Si}, and $\vec{\lambda}_{\mathrm{nuisance}}$ are the nuisance parameters. The two log terms in Eq. 9.13 are summed

[d]The corresponding systematic uncertainty of this assumption is discussed in Sec. 10.3.2.

over the same events and therefore can be added. This results in the combined term $\log(\mathcal{P}_{\text{tot}}\mathcal{P}_{K\pi})$. As each of $\mathcal{P}_{\text{tot}}$ and $\mathcal{P}_{K\pi}$ is a sum of a background and a signal component, it follows that cross terms of signal and background contribute to the likelihood function. However, this does not result in problematic behaviour of the likelihood function, as the contributions of these cross terms are small. In addition, the pseudoexperiments presented in Sec. 9.6 exhibit good fit behaviour. Nevertheless, future iterations of the analysis will avoid this potential issue by performing a five-dimensional fit rather than a one- plus four-dimensional fit.

Eq. 9.13 does not give the full expression that is minimised when determining the angular observables, as it does not fully account for the acceptance functions. In addition, the two data sets from Run 1 and 2016 are fitted simultaneously. An extension of the likelihood function accounting for these two facts is described in the next two sections.

9.4 Simultaneous fits

The logarithmic likelihoods for the Run 1 and 2016 data samples are combined in a simultaneous fit according to

$$\begin{aligned} -\log\mathcal{L}_{\text{tot}} = &- \sum_{\text{events } e \text{ Run 1}} \log\mathcal{P}_{\text{tot}}(\vec{\Omega}_e, m_{K\pi\mu\mu,e}|\vec{\lambda}_{\text{phys}}, \vec{\lambda}^{\text{Run 1}}_{\text{nuisance}}) \\ &- \sum_{\text{events } e \text{ Run 1}} \log\mathcal{P}_{K\pi}(m_{K\pi,e}|\vec{\lambda}_{\text{phys}}, \vec{\lambda}^{\text{Run 1}}_{\text{nuisance}}) \\ &- \sum_{\text{events } e \text{ 2016}} \log\mathcal{P}_{\text{tot}}(\vec{\Omega}_e, m_{K\pi\mu\mu,e}|\vec{\lambda}_{\text{phys}}, \vec{\lambda}^{\text{2016}}_{\text{nuisance}}) \\ &- \sum_{\text{events } e \text{ 2016}} \log\mathcal{P}_{K\pi}(m_{K\pi,e}|\vec{\lambda}_{\text{phys}}, \vec{\lambda}^{\text{2016}}_{\text{nuisance}}), \end{aligned} \tag{9.14}$$

where the physics parameters $\vec{\lambda}_{\text{phys}}$, namely the P-wave, S-wave and the interference observables, are shared between data samples. In contrast, the nuisance parameters $\vec{\lambda}_{\text{nuisance}}$ are allowed to vary independently. The rational for using the simultaneous fit approach is two-fold: first, the two data samples can potentially exhibit different background levels. Secondly, there exist two separate acceptance functions due to the slight differences in selection between the two data taking periods (see Chpt. 8). The next section will outline how the acceptance functions are implemented in the likelihood fit.

9.5 Acceptance implementation in the likelihood fit

The acceptance effects described in Chpt. 8 can be included either directly in the signal PDFs or by performing a fit in which the events are weighted by $1/\varepsilon(\vec{\Omega}, q^2)$.

In the first option, the angular signal PDFs for the two data taking periods, given by Eq. 2.45, are multiplied by their respective acceptance functions. The same is done for the $m_{K\pi}$ distributions and therefore the subsequent integration of the angular terms also includes the acceptance functions as can be seen in Eq. 9.11. Multiplying the acceptance functions by the signal PDFs is the approach used for the narrow q^2 bins defined in Sec. 4.1. The acceptance functions are evaluated at the mean of each narrow q^2 bin, as these bins have a maximal width of $2\,\mathrm{GeV}^2/c^4$ and the acceptance functions do not vary significantly across q^2. A systematic uncertainty is assigned to this choice in Sec. 10.10.

In the second option, both the signal and background events are corrected for their acceptance effects explicitly by weighing them by $1/\varepsilon(\vec{\Omega}, q^2)$. This approach is adopted for the wide q^2 bins ($1.1 < q^2 < 6.0\,\mathrm{GeV}^2/c^4$ and $15.0 < q^2 < 19.0\,\mathrm{GeV}^2/c^4$), to account for possible variations of the acceptance with q^2. The signal yield in these bins is sufficiently large to render negligible the effect of fluctuations that could be induced by the weighting procedure. The per-event weight is included in the likelihood as follows:

$$
\begin{aligned}
-\log\mathcal{L}_{\mathrm{tot}} = &- \sum_{\text{events } e \text{ Run 1}} \frac{1}{\varepsilon_{\mathrm{Run\,1}}({q^2}_e, \vec{\Omega}_e)} \times \log\mathcal{P}_{\mathrm{tot}}(\vec{\Omega}_e, m_{K\pi\mu\mu,e}|\vec{\lambda}_{\mathrm{phys}}, \vec{\lambda}^{\mathrm{Run\ 1}}_{\mathrm{nuisance}}) \\
&- \sum_{\text{events } e \text{ Run 1}} \frac{1}{\varepsilon_{\mathrm{Run\,1}}({q^2}_e, \vec{\Omega}_e)} \times \log\mathcal{P}_{K\pi}(m_{K\pi,e}|\vec{\lambda}_{\mathrm{phys}}, \vec{\lambda}^{\mathrm{Run\ 1}}_{\mathrm{nuisance}}) \\
&- \sum_{\text{events } e \text{ 2016}} \frac{1}{\varepsilon_{2016}({q^2}_e, \vec{\Omega}_e)} \times \log\mathcal{P}_{\mathrm{tot}}(\vec{\Omega}_e, m_{K\pi\mu\mu,e}|\vec{\lambda}_{\mathrm{phys}}, \vec{\lambda}^{2016}_{\mathrm{nuisance}}) \\
&- \sum_{\text{events } e \text{ 2016}} \frac{1}{\varepsilon_{2016}({q^2}_e, \vec{\Omega}_e)} \times \log\mathcal{P}_{K\pi}(m_{K\pi,e}|\vec{\lambda}_{\mathrm{phys}}, \vec{\lambda}^{2016}_{\mathrm{nuisance}}). \qquad (9.15)
\end{aligned}
$$

To determine the values of the angular observables, the full negative logarithmic likelihood function is minimised with respect to the physics parameters $\vec{\lambda}_{\mathrm{phys}}$ and the nuisance parameters $\vec{\lambda}_{\mathrm{nuisance}}$. The minimisation is performed using the MINUIT software package [138]. When including the acceptance functions by multiplying the corresponding signal PDFs, the uncertainties of the parameters are determined using the second derivative matrix (HESSE). As this method does not guarantee correct coverage for the weighted fits, in this case, the parameter uncertainties are evaluated by taking advantage of the

bootstrapping technique [139]. Large simulation samples were used to demonstrate that the two different approaches of including the acceptance in the likelihood fit are compatible.

9.6 Fit validation using pseudoexperiments

Pseudoexperiments are performed to ensure that the fit is unbiased and that it determines the uncertainties of the angular observables correctly. Two main scenarios are tested and validated. For the first scenario the central values of the P-wave observables are taken from the SM, while for the second scenario they are taken from the final fit to data.

9.6.1 Pseudoexperiments generated with SM predictions

In the first scenario, 500 pseudoexperiments are generated for each q^2 bin using the SM central values for the P-wave observables, $F_{\rm S}$ =10% and setting the S-wave/P-wave interference parameters to zero. The individual pseudoexperiments consist of two sets of events. The first set of events is generated to represent the Run 1 data sample, while the second set of events is generated to represent the 2016 data sample. The signal yields, the signal fractions and the acceptance function are taken from the previous analysis [2] for the Run 1 set. The events corresponding to the 2016 data sample are also generated with the signal yields and signal fractions from the previous analysis, but the 2016 acceptance function is used instead of the Run 1 acceptance function. For both sets of generated pseudodata, the background components are generated flat in the angles and $m_{K\pi}$. The $m_{K\pi\mu\mu}$ distributions for the signal and background components are generated according to the shapes discussed in Chpt. 6.

The same parameters are varied in the fit to the pseudoexperiments as in the nominal fit to data. These include the P-wave observables S_i ($P_i^{(\prime)}$ for the optimised basis), the S-wave fraction $F_{\rm S}$, and the S-wave/P-wave interference parameters $S_{\rm Si}$. Furthermore, the signal fraction $f_{\rm sig}$, the parameter describing the background mass shape τ_m, and the coefficients of the second order Chebyshev polynomials describing the angular background shape are floated. Finally, the first order Chebyshev polynomial describing the $m_{K\pi}$ background shape is varied. The two sets of events corresponding to the Run 1 or 2016 data samples are fitted simultaneously, as described in Sec. 9.4. A weighted fit is performed for the wide q^2 bins $[1.1, 6.0]\,{\rm GeV}^2/c^4$ and $[15.0, 19.0]\,{\rm GeV}^2/c^4$, whereas the acceptance effect is directly included in the PDF for the narrow q^2 bins (see Sec. 9.5).

The distribution of the pull parameter λ_i, defined as $(\lambda_i^{\rm fit} - \lambda_i^{\rm generated})/\sigma(\lambda_i^{\rm fit})$, is used to validate the fit method. If the pull distributions are compatible with Gaussians centred around zero and have a width of one, the fit is unbiased and it estimates the parameter uncertainties correctly.

$4.0 < q^2 < 6.0$ GeV$^2/c^4$				$4.0 < q^2 < 6.0$ GeV$^2/c^4$			
	sensitivity	pull mean	pull width		sensitivity	pull mean	pull width
F_{L}	0.040 ± 0.001	0.029 ± 0.045	1.012 ± 0.032	F_{L}	0.040 ± 0.001	0.033 ± 0.045	1.012 ± 0.032
S_3	0.050 ± 0.002	-0.040 ± 0.047	1.050 ± 0.033	P_1	0.396 ± 0.013	-0.044 ± 0.045	1.016 ± 0.032
S_4	0.058 ± 0.002	0.009 ± 0.046	1.038 ± 0.033	P_2	0.090 ± 0.003	-0.050 ± 0.045	1.006 ± 0.032
S_5	0.059 ± 0.002	-0.024 ± 0.046	1.039 ± 0.033	P_3	0.182 ± 0.006	-0.002 ± 0.042	0.945 ± 0.030
A_{FB}	0.034 ± 0.001	-0.054 ± 0.046	1.027 ± 0.032	P_4'	0.133 ± 0.004	0.022 ± 0.046	1.027 ± 0.032
S_7	0.056 ± 0.002	-0.007 ± 0.045	1.001 ± 0.032	P_5'	0.141 ± 0.004	-0.021 ± 0.044	0.995 ± 0.031
S_8	0.059 ± 0.002	0.023 ± 0.046	1.018 ± 0.032	P_6'	0.131 ± 0.004	0.004 ± 0.045	1.003 ± 0.032
S_9	0.046 ± 0.001	-0.008 ± 0.044	0.983 ± 0.031	P_8'	0.135 ± 0.004	0.023 ± 0.045	1.010 ± 0.032
F_{S}	0.052 ± 0.002	0.012 ± 0.042	0.942 ± 0.030	F_{S}	0.052 ± 0.002	0.002 ± 0.042	0.948 ± 0.030
S_{S1}	0.098 ± 0.003	0.033 ± 0.047	1.046 ± 0.033	S_{S1}	0.099 ± 0.003	0.053 ± 0.047	1.051 ± 0.033
S_{S2}	0.059 ± 0.002	-0.040 ± 0.047	1.052 ± 0.033	S_{S2}	0.059 ± 0.002	-0.045 ± 0.047	1.046 ± 0.033
S_{S3}	0.055 ± 0.002	0.026 ± 0.046	1.031 ± 0.033	S_{S3}	0.055 ± 0.002	0.030 ± 0.046	1.032 ± 0.033
S_{S4}	0.055 ± 0.002	0.105 ± 0.044	0.994 ± 0.031	S_{S4}	0.055 ± 0.002	0.111 ± 0.044	0.994 ± 0.031
S_{S5}	0.062 ± 0.002	0.119 ± 0.047	1.040 ± 0.033	S_{S5}	0.062 ± 0.002	0.122 ± 0.047	1.047 ± 0.033

Table 9.1: Results from 500 pseudoexperiments corresponding to the combined Run 1 and 2016 data for the $[4.0, 6.0]\,\mathrm{GeV}^2/c^4$ q^2 bin. The means and widths of Gaussian functions fitted to the pull distributions for both the S_i and $P_i^{(\prime)}$ bases are provided. In addition, the widths of the distributions of the fitted parameter values are given in the sensitivity column.

The results of the pseudoexperiments for the $[4.0, 6.0]\,\mathrm{GeV}^2/c^4$ bin for both the S_i and $P_i^{(\prime)}$ bases are given in Tab. 9.1. The complete set of results can be found in Tabs. D.1-D.4 in Appendix D. The fit is shown to be unbiased and it yields correct uncertainty estimates for all P-wave parameters. Some of the S-wave parameters and S-wave/P-wave interference parameters, which are nuisances for this measurement, show slight biases and undercoverage. Most notably, the S-wave fraction F_{S} is undercovered, as the parameter is forced to be in the physical range ($F_{\mathrm{S}} > 0$).

9.6.2 Pseudoexperiments generated with best fit values

In the previous section the pseudoexperiments for the fit validation were generated using the predictions of the SM observables, as well as a flat background model and an S-wave fraction of 10%. This results in good fit behaviour. The validation is repeated using pseudoexperiments generated with the best fit values taken from the nominal fit to data for both the signal and nuisance parameters. This approach leads to several complications that will be discussed in the following subsections.

Events with a negative angular signal PDF

When the angular signal probability is calculated using SM predictions for the angular observables, the resulting probability is, by definition, positive. However, in some q^2 bins the SM values (and hence most of the observable values in NP scenarios) lie close to the edge of the allowed physical space. Evaluating the angular probability using the best fit values results in negative angular signal PDFs for some events (although the total PDF, including background, is always positive). The fraction of events with a negative signal PDF for each q^2 bin is shown in Tab. 9.2. This fraction is determined using pseudo-events generated flat across all angles.

q^2 bin $[\,\mathrm{GeV}^2/c^4]$	f_{neg}
$0.1 < q^2 < 1.0$	0
$1.1 < q^2 < 2.5$	0.051
$2.5 < q^2 < 4.0$	0
$4.0 < q^2 < 6.0$	0
$6.0 < q^2 < 8.0$	0.003
$11.0 < q^2 < 12.5$	0.018
$15.0 < q^2 < 17.0$	0.007
$17.0 < q^2 < 19.0$	0.037
$0.1 < q^2 < 6.0$	0
$15.0 < q^2 < 19.0$	0.011

Table 9.2: Fraction of pseudo-events with a negative signal PDF f_{neg} for each q^2 bin, obtained by studying the behaviour of pseudo-events that are generated flat across the three angles.

The physical region of the angular signal PDF is reduced when evaluating the PDF using the values of the best fit observables, instead of the SM predictions. This is demonstrated in Figs. 9.1 and 9.2. The former shows the positive region when evaluating the angular signal PDF with the best fit values, and the latter when evaluating it with the SM values. In Fig. 9.1, one can clearly see that the F_{L} vs S_{6s} (F_{L} vs A_{FB}) plane has a fit value lying outside the positive region for the $[1.1,2.5]\,\mathrm{GeV}^2/c^4$ bin.

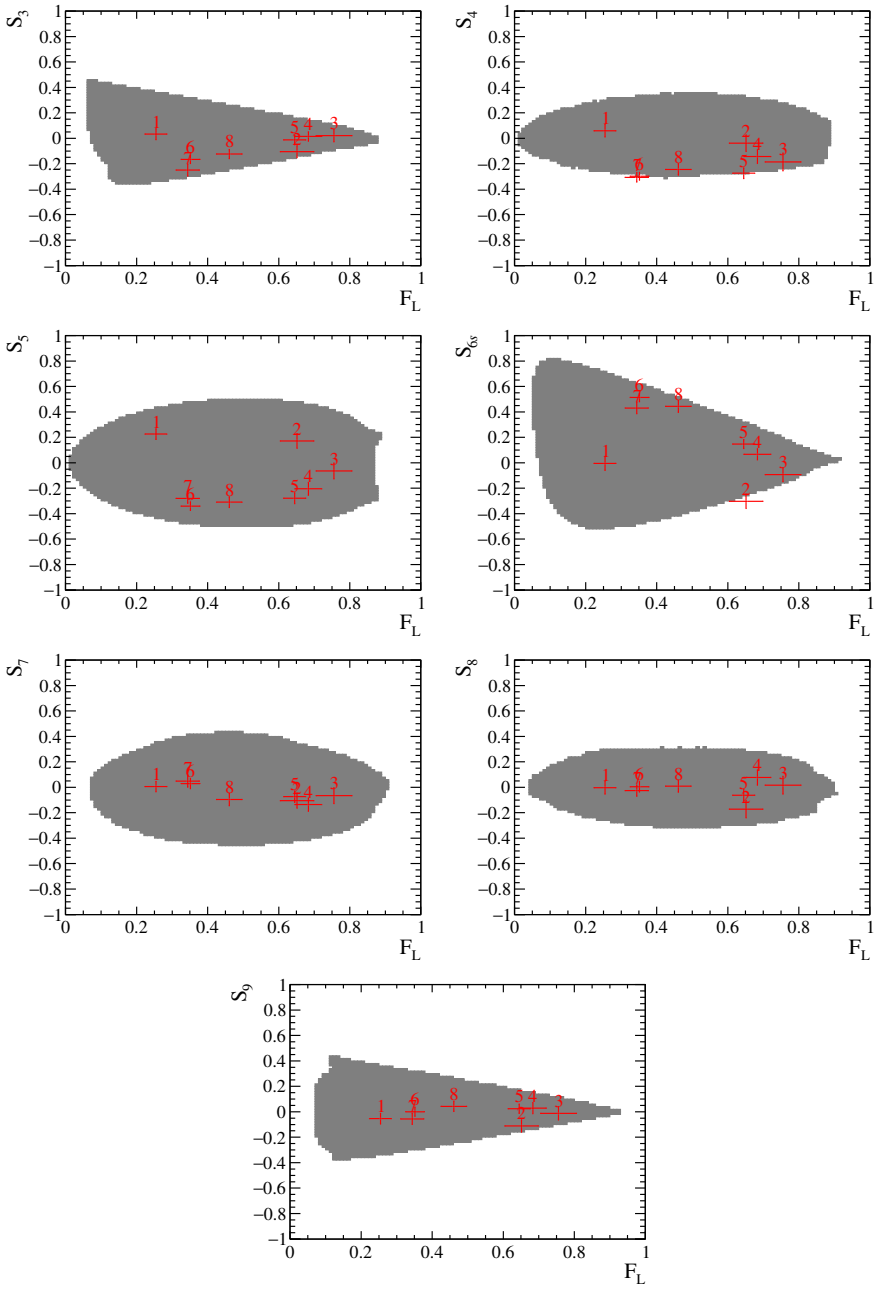


Figure 9.1: Physical region (grey) of the angular signal PDF when evaluated using the best fit values, which are taken from the final fit to data. The physical region is integrated over all q^2 bins. The red points indicate the simultaneous fit results, where each number shows the corresponding q^2 bin. Only narrow bins are shown. Bin numbers are in an ascending order, with the exception of the $11.0 < q^2 < 12.5\,\mathrm{GeV}^2/c^4$ bin, which corresponds to number 8.

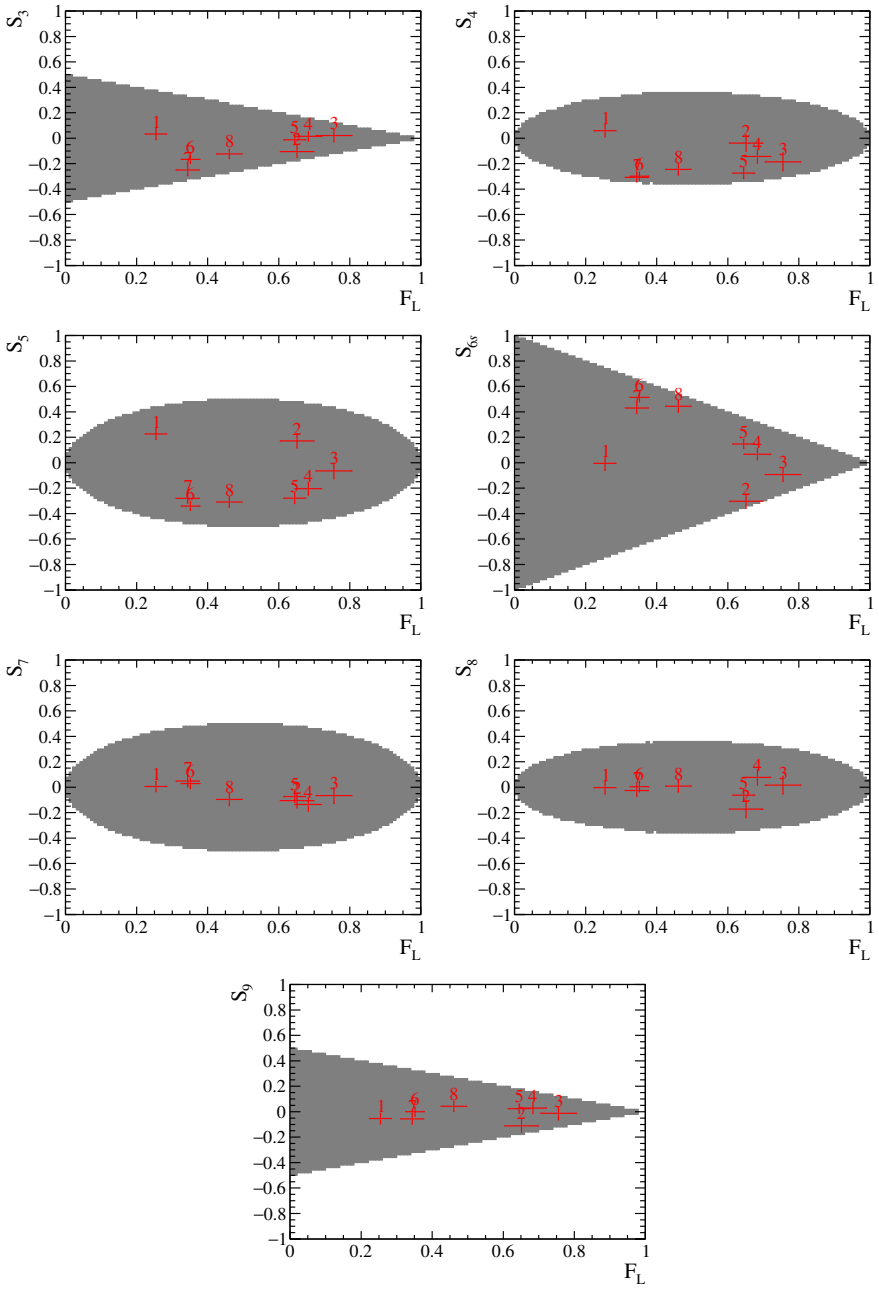


Figure 9.2: Physical region (grey) of the angular signal PDF when evaluated using the SM values. The physical region is integrated over all q^2 bins. The red points indicate the simultaneous fit results, where each number shows the corresponding q^2 bin. Only narrow bins are shown. Bin numbers are in an ascending order, with the exception of the $11.0 < q^2 < 12.5\,\mathrm{GeV}^2/c^4$ bin, which corresponds to number 8.

When evaluating the angular signal probability with the best fit values, some fit results fall into a non-positive region. However, they are inside the positive region when evaluating the angular signal probability using the SM values. In addition, the statistical uncertainties of the angular observables indicate that their central values can easily lie outside the physical region, whilst still being compatible with a true value in the positive region.

Large biases (of order 30% on the pull mean) are seen when generating pseudoexperiments using starting values that result in a nonphysical PDF. Bins further away from the physical region tend to have a worse behaviour, which is not surprising, as it makes little sense to generate a pseudo-experiment using non-physical observables. These pulls are improved by generating pseudo-experiments from the nearest points in the observable space that lie in the physical region. Thus, the pseudoexperiments for those bins in Tab. 9.2 that have negative events are generated using these physical points.

Results of pseudoexperiments generated with best fit values

The results for the $[1.1, 2.5]\,\mathrm{GeV}^2/c^4$ and $[2.5, 4.0]\,\mathrm{GeV}^2/c^4$ q^2 bins are shown in Tab. 9.3. The complete set of results can be found in Tabs. D.5-D.8 in Appendix D. Good fit behaviour is observed in most cases. An exception is the F_L parameter in the bin $[2.5, 4.0]\,\mathrm{GeV}^2/c^4$, which has a significant bias amounting to 16.5% and 20% of the statistical uncertainty for the S_i and $P_i^{(\prime)}$ bases, respectively. In addition, the S_4 and S_5 observables have biases of approximately 15% of the statistical uncertainty in some bins. These remaining biases arise from observable boundaries and in particular from the requirement of the fit that the F_S parameter has to be in the physical range, *i.e.* $F_\mathrm{S} > 0$. This is demonstrated by repeating the experiments and setting the lower bound on F_S to -1, which reduces the bias on F_L in the $[2.5, 4.0]\,\mathrm{GeV}^2/c^4$ bin from $\sim 16\%$ to $\sim -5\%$. The full results are documented in Tabs. D.9-D.12 in Appendix D.

The bias induced by F_S hitting the lower bound of zero can be understood as follows. Generating pseudoexperiments with values of F_S that are close to the boundary will result in a positive bias in F_S and therefore a negative bias in $(1 - F_\mathrm{S})$. As the P-wave observables are scaled by $(1 - F_\mathrm{S})$, the fit tries to compensate for the negative bias in this factor by increasing the values of the P-wave observables. Since all P-wave observables are forced to scale up by the same proportion, those with a larger magnitude experience a larger bias. This explains the particularly large effect for F_L in the $[2.5, 4.0]\,\mathrm{GeV}^2/c^4$ q^2 bin, where the absolute value of F_L is large (0.756 in the case of the measurement presented in this thesis).

$1.1 < q^2 < 2.5$ GeV$^2/c^4$			
	sensitivity	pull mean	pull width
F_{L}	0.052 ± 0.001	0.075 ± 0.022	0.965 ± 0.015
S_3	0.062 ± 0.001	0.003 ± 0.024	1.087 ± 0.017
S_4	0.078 ± 0.001	0.146 ± 0.024	1.065 ± 0.017
S_5	0.067 ± 0.001	-0.094 ± 0.023	1.014 ± 0.016
A_{FB}	0.052 ± 0.001	-0.110 ± 0.024	1.067 ± 0.017
S_7	0.072 ± 0.001	-0.051 ± 0.024	1.059 ± 0.017
S_8	0.082 ± 0.001	-0.014 ± 0.024	1.078 ± 0.017
S_9	0.063 ± 0.001	-0.066 ± 0.025	1.098 ± 0.017
F_{S}	0.055 ± 0.001	0.135 ± 0.018	0.818 ± 0.013
S_{S1}	0.115 ± 0.002	0.123 ± 0.023	1.031 ± 0.016
S_{S2}	0.087 ± 0.001	0.141 ± 0.025	1.121 ± 0.018
S_{S3}	0.073 ± 0.001	-0.082 ± 0.024	1.075 ± 0.017
S_{S4}	0.076 ± 0.001	-0.006 ± 0.024	1.045 ± 0.017
S_{S5}	0.088 ± 0.001	-0.010 ± 0.024	1.059 ± 0.017

$1.1 < q^2 < 2.5$ GeV$^2/c^4$			
	sensitivity	pull mean	pull width
F_{L}	0.053 ± 0.001	0.100 ± 0.023	1.021 ± 0.016
P_1	0.347 ± 0.006	-0.005 ± 0.024	1.053 ± 0.017
P_2	0.107 ± 0.002	-0.113 ± 0.023	1.040 ± 0.017
P_3	0.171 ± 0.003	0.018 ± 0.023	1.002 ± 0.016
P_4'	0.160 ± 0.003	0.114 ± 0.023	1.033 ± 0.016
P_5'	0.138 ± 0.002	-0.050 ± 0.022	0.969 ± 0.015
P_6'	0.145 ± 0.002	-0.012 ± 0.023	1.014 ± 0.016
P_8'	0.170 ± 0.003	-0.011 ± 0.024	1.069 ± 0.017
F_{S}	0.053 ± 0.001	0.230 ± 0.018	0.798 ± 0.013
S_{S1}	0.115 ± 0.002	0.070 ± 0.023	1.025 ± 0.016
S_{S2}	0.085 ± 0.001	0.132 ± 0.025	1.102 ± 0.018
S_{S3}	0.071 ± 0.001	-0.139 ± 0.024	1.044 ± 0.017
S_{S4}	0.075 ± 0.001	0.006 ± 0.023	1.018 ± 0.016
S_{S5}	0.087 ± 0.001	0.020 ± 0.023	1.039 ± 0.017

$2.5 < q^2 < 4.0$ GeV$^2/c^4$			
	sensitivity	pull mean	pull width
F_{L}	0.057 ± 0.001	0.165 ± 0.021	0.923 ± 0.015
S_3	0.069 ± 0.001	0.009 ± 0.025	1.098 ± 0.018
S_4	0.086 ± 0.001	-0.076 ± 0.024	1.042 ± 0.017
S_5	0.082 ± 0.001	-0.087 ± 0.025	1.088 ± 0.017
A_{FB}	0.050 ± 0.001	-0.077 ± 0.024	1.047 ± 0.017
S_7	0.078 ± 0.001	-0.042 ± 0.023	1.030 ± 0.017
S_8	0.086 ± 0.001	-0.006 ± 0.024	1.048 ± 0.017
S_9	0.069 ± 0.001	-0.018 ± 0.024	1.081 ± 0.017
F_{S}	0.047 ± 0.001	0.389 ± 0.014	0.605 ± 0.010
S_{S1}	0.141 ± 0.002	-0.045 ± 0.023	1.030 ± 0.017
S_{S2}	0.097 ± 0.002	-0.011 ± 0.025	1.095 ± 0.018
S_{S3}	0.083 ± 0.001	-0.004 ± 0.024	1.037 ± 0.017
S_{S4}	0.081 ± 0.001	-0.012 ± 0.024	1.051 ± 0.017
S_{S5}	0.094 ± 0.002	-0.028 ± 0.024	1.070 ± 0.017

$2.5 < q^2 < 4.0$ GeV$^2/c^4$			
	sensitivity	pull mean	pull width
F_{L}	0.054 ± 0.001	0.200 ± 0.025	1.078 ± 0.017
P_1	0.637 ± 0.010	-0.009 ± 0.021	0.930 ± 0.015
P_2	0.193 ± 0.003	-0.111 ± 0.022	0.980 ± 0.016
P_3	0.325 ± 0.005	-0.056 ± 0.021	0.928 ± 0.015
P_4'	0.220 ± 0.004	-0.094 ± 0.023	1.009 ± 0.016
P_5'	0.189 ± 0.003	-0.092 ± 0.023	0.988 ± 0.016
P_6'	0.194 ± 0.003	-0.104 ± 0.023	1.009 ± 0.016
P_8'	0.214 ± 0.003	-0.010 ± 0.024	1.035 ± 0.017
F_{S}	0.043 ± 0.001	0.348 ± 0.013	0.550 ± 0.009
S_{S1}	0.142 ± 0.002	-0.010 ± 0.024	1.035 ± 0.017
S_{S2}	0.095 ± 0.002	-0.018 ± 0.025	1.071 ± 0.017
S_{S3}	0.083 ± 0.001	0.002 ± 0.024	1.041 ± 0.017
S_{S4}	0.083 ± 0.001	-0.057 ± 0.024	1.061 ± 0.017
S_{S5}	0.094 ± 0.002	-0.026 ± 0.024	1.061 ± 0.017

Table 9.3: Results from 1000 pseudoexperiments corresponding to the combined Run 1 and 2016 data for the $[1.1, 2.5]\,\mathrm{GeV}^2/c^4$ and $[2.5, 4.0]\,\mathrm{GeV}^2/c^4$ q^2 bins. The means and widths of Gaussian functions fitted to the pull distributions for both the S_i and $P_i^{(\prime)}$ bases are provided. In addition, the widths of the distributions of the fitted parameter values are given in the sensitivity column.

As the remaining biases attributable to F_{S} hitting the physical boundary are understood and relatively small, the lower bound on F_{S} is retained in the nominal fit. All the biases in Tabs. D.5-D.8 are therefore added as systematic uncertainties. In addition, the statistical uncertainties of the nominal fit to data are scaled by the corresponding pull widths in

Tabs. D.5-D.8 to obtain the correct coverage. This coverage correction has a very small effect on the final results, as the pull widths are already very close to one.

9.7 Fit validation on data using $B^0 \to J/\psi K^{*0}$

The fit model and the acceptance description are further validated by analysing the angular distribution of the $B^0 \to J/\psi K^{*0}$ control channel. As described in Sec. 5.4, the $B^0 \to J/\psi K^{*0}$ candidates are separated from the $B^0 \to K^{*0}\mu^+\mu^-$ signal candidates by restricting q^2 to the range $[8.0, 11.0]\,\text{GeV}^2/c^4$. The angular observables are determined via a simultaneous fit to the Run 1 and 2016 data samples. As mentioned in Sec. 6.1, the fit to the control decay also includes a component for the $B_s^0 \to J/\psi K^{*0}$ channel. The angular and mass distributions are assumed to be identical for the $B^0 \to J/\psi K^{*0}$ and the $B_s^0 \to J/\psi K^{*0}$ decays, with the caveat that the mass distribution of the B_s^0 is shifted by the appropriate mass difference. The angular acceptance functions are included directly in the fit by multiplying them by the corresponding signal PDF, as described in Sec. 9.5.

The angular and mass distributions of the $B^0 \to J/\psi K^{*0}$ decay for the Run 1 and 2016 data are given in Fig. 9.3, along with the projections of the simultaneous fit. The sources of the slight inaccuracies of the description of the data in the $m(K^+\pi^-\mu^+\mu^-)$ and $\cos\theta_K$ distributions are understood and can be attributed to four effects. The small bump in the $m(K^+\pi^-\mu^+\mu^-)$ distribution at $5425\,\text{MeV}/c^2$ is due to residual $\Lambda_b^0 \to J/\psi p\pi^-$ background decays, while the overshooting of the data above $5500\,\text{MeV}/c^2$ is a result of the $B^+ \to K^+\mu^+\mu^-$ veto. The slight disagreements between the fit projection and the data in the $\cos\theta_K$ distribution at approximately -0.8 are caused by contributions from exotic $B^0 \to Z^- K^+$ decays [140, 141] (see also Appendix C), while the disagreement close to $+1$ is due to the limited order of the acceptance model. The remaining background of the $\Lambda_b^0 \to J/\psi p\pi^-$ decay is negligible for the $B^0 \to K^{*0}\mu^+\mu^-$ signal and the exotic $B^0 \to Z^- K^+$ decays do not affect the signal decays. However, the effect of the $B^+ \to K^+\mu^+\mu^-$ veto and the limited order of the acceptance model are relevant for the signal decay and are considered as sources of systematic uncertainties (see Sec. 10.6 and Sec. 10.7).

The values of the angular observables of the fits to the $B^0 \to J/\psi K^{*0}$ control mode for the individual Run 1 and 2016 data sets, as well as for their combination are given in Tab. 9.4. The values of the angular observables of the simultaneous fit lie between the values of the individual fits, and their uncertainty also scales approximately by a factor of $1/\sqrt{2}$ as expected. Furthermore, the individual results of the Run 1 and 2016 data

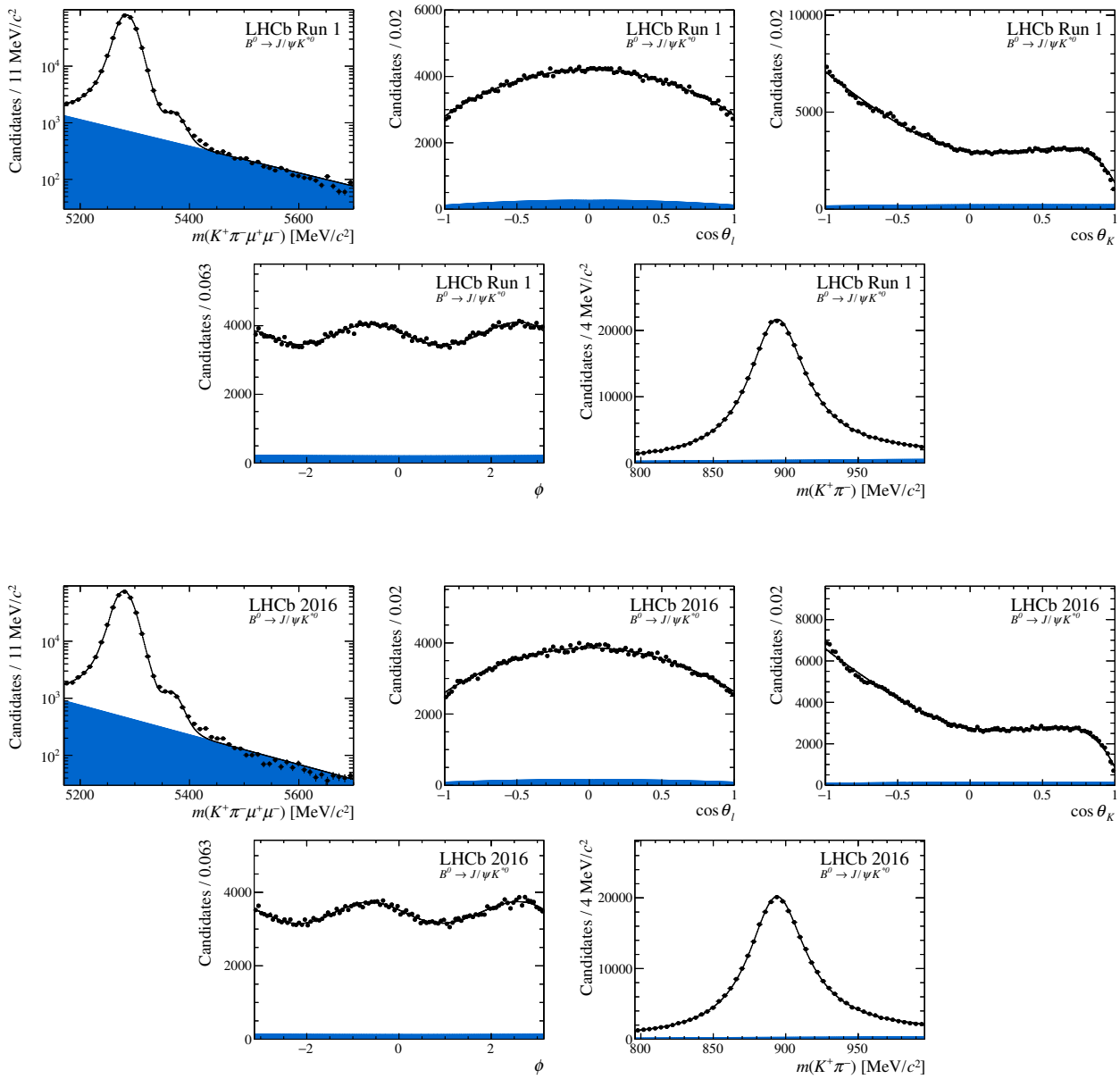


Figure 9.3: Projections of the fitted probability density function on the decay angles, $m(K^+\pi^-)$ and $m(K^+\pi^-\mu^+\mu^-)$ for the decay $B^0 \to J/\psi K^{*0}$. The blue shaded region indicates background. Figure taken from Ref. [1].

sets are in general found to be in good agreement, and the slight tensions that do exist are negligible compared to the expected statistical uncertainties for these parameters in the rare mode. Nevertheless, detailed studies have been performed to understand the differences between the two data sets. These are discussed in Sec. 9.8. The results of the control channel are in good agreement also with the results of previous studies by the

Parameter	Simultaneous fit	Run 1 only	2016 only
F_{L}	0.5609 ± 0.0010	0.5577 ± 0.0014	0.5643 ± 0.0014
S_3	-0.0003 ± 0.0013	0.0001 ± 0.0018	-0.0008 ± 0.0018
S_4	-0.2489 ± 0.0014	-0.2518 ± 0.0020	-0.2459 ± 0.0020
S_5	0.0007 ± 0.0014	-0.0020 ± 0.0019	0.0035 ± 0.0020
A_{FB}	0.0005 ± 0.0009	0.0005 ± 0.0012	0.0005 ± 0.0012
S_7	0.0011 ± 0.0014	0.0005 ± 0.0020	0.0017 ± 0.0020
S_8	-0.0544 ± 0.0014	-0.0517 ± 0.0020	-0.0573 ± 0.0021
S_9	-0.0852 ± 0.0013	-0.0860 ± 0.0018	-0.0844 ± 0.0018
F_{S}	0.0616 ± 0.0015	0.0645 ± 0.0021	0.0586 ± 0.0022
S_{S1}	-0.2282 ± 0.0025	-0.2350 ± 0.0035	-0.2208 ± 0.0036
S_{S2}	0.0221 ± 0.0016	0.0228 ± 0.0022	0.0214 ± 0.0023
S_{S3}	0.0007 ± 0.0015	0.0027 ± 0.0021	-0.0013 ± 0.0021
S_{S4}	0.0000 ± 0.0015	0.0007 ± 0.0021	-0.0007 ± 0.0022
S_{S5}	-0.0671 ± 0.0016	-0.0687 ± 0.0023	-0.0655 ± 0.0024

Table 9.4: Results of the angular fit of the $B^0 \to J/\psi\, K^{*0}$ decay comparing the simultaneous fit with the Run 1 and the 2016 results.

BaBar [142], Belle [143] and LHCb [144] collaborations.

9.8 Validating the Run 1 and 2016 agreement using the $B^0 \to J/\psi\, K^{*0}$ decay

As described in the previous section, there are small differences between the values of the Run 1 and 2016 angular observables as measured in the $B^0 \to J/\psi\, K^{*0}$ channel. Detailed studies on the origin of these differences were performed using a slightly different angular basis, where $F_{\mathrm{L}} \to 1 - \frac{4}{3} S_{1s}$ and $A_{\mathrm{FB}} \to \frac{3}{4} S_{6s}$. Tab. 9.5 gives the results of these fits, which correspond to those given in Tab. 9.4. Considering just the statistical uncertainty, the Run 1 and 2016 angular observables do not agree particularly well for the S_{1s} and S_{S1} observables. However, systematic uncertainties also need to be considered. For example, the systematic uncertainty due to the limited statistics of the simulated samples is of importance. It is obtained by bootstrapping the simulation sample and recalculating the acceptance. A more detailed explanation of the calculation of this systematic is given in Sec. 10.8. Tab. 9.6 is obtained when accounting for this systematic, where the difference

between the variables S_{1s} and S_{S1} is reduced to 2.8 and 2.2 σ respectively.

The source of the remaining discrepancy can be understood by comparing the acceptance corrected *sWeighted* distributions in the angles for the $8.0 < q^2 < 11.0\,\mathrm{GeV}^2/c^4$ bin. These are given in Figure 9.4. While the acceptance corrected distributions agree well for the angles ϕ and $\cos\theta_l$, small differences can be seen at low and high $\cos\theta_K$ values. These differences in the $\cos\theta_K$ distributions result in the discrepancy of the S_{1s} and S_{S1} parameters, as S_{1s} and S_{S1} are proportional to $\cos^2\theta_K$ and $\cos\theta_K$ respectively (Eq. 2.43 and Eq. 2.45). The unphysical turnover at high $\cos\theta_K$ values can be corrected by going to a higher order acceptance, as can be seen in Fig. 9.4(d). A systematic uncertainty is assigned for this in Sec. 10.7.

Further investigation into the $\cos\theta_K$ distributions reveals that there are small differences at small pion momenta between simulation and data, which are explained in detail in Sec. 10.9. Removing events with $p(\pi) < 3000\,\mathrm{MeV}/c$ and $p_{\mathrm{T}}(\pi) < 300\,\mathrm{MeV}/c$ and recalculating the acceptance accordingly, the differences between the angular observables are further reduced, as can be seen in Tab. 9.7. This is the case for the problematic S_{S1} observable in particular.

Furthermore, a systematic uncertainty can be assigned for the discrepancy between the pion momentum spectra in data and simulation, as described in Sec. 10.9. The results of this systematic uncertainty can be seen in Tab. 9.8. As expected, the biggest systematic uncertainty is on the S_{S1} variable, and it fully accounts for the difference between the Run 1 and 2016 results. Even if the individual systematic uncertainties for the Run 1 and 2016 results were fully correlated, the fact that the difference in these systematic uncertainties still covers the absolute difference of the angular observables gives confidence in having understood the source of the difference. In addition, there is a sizeable systematic of the pion momentum discrepancy in data and simulation also on the S_{1s} variable, which reduces the difference between the Run 1 and 2016 results to an acceptable level. The discrepancies between the pion momentum in data and simulation, the higher order acceptance effects and the limited amount of simulated events are all included as systematic uncertainties for the signal mode (see Secs. 10.9, 10.7 and 10.8).

To summarise, the differences between the Run 1 and 2016 results for the $B^0 \to J/\psi\, K^{*0}$ control channel have been understood and reduced to an acceptable level. These differences are very small compared to the statistical precision of the corresponding observables for the signal mode.

Parameter	Run 1 only	2016 only	σ(Run 1/16)
S_{1s}	0.3318 ± 0.0010	0.3268 ± 0.0010	3.5
S_3	0.0001 ± 0.0018	-0.0008 ± 0.0018	0.4
S_4	-0.2518 ± 0.0020	-0.2460 ± 0.0020	2.1
S_5	-0.0020 ± 0.0019	0.0035 ± 0.0020	2.0
S_{6s}	0.0006 ± 0.0016	0.0007 ± 0.0016	0.0
S_7	0.0005 ± 0.0020	0.0017 ± 0.0020	0.4
S_8	-0.0516 ± 0.0020	-0.0573 ± 0.0021	2.0
S_9	-0.0861 ± 0.0018	-0.0844 ± 0.0018	0.7
F_{S}	0.0647 ± 0.0021	0.0584 ± 0.0022	2.1
S_{S1}	-0.2349 ± 0.0035	-0.2209 ± 0.0036	2.8
S_{S2}	0.0228 ± 0.0022	0.0215 ± 0.0023	0.4
S_{S3}	0.0027 ± 0.0021	-0.0013 ± 0.0021	1.3
S_{S4}	0.0007 ± 0.0021	-0.0007 ± 0.0022	0.5
S_{S5}	-0.0687 ± 0.0023	-0.0655 ± 0.0024	1.0

Table 9.5: Results of the angular fit of the $B^0 \to J/\psi K^{*0}$ decay. The third column gives the number of standard deviations between the individual angular observables, using only the statistical uncertainty of the fit.

Parameter	Run 1 only	2016 only	σ(Run 1/16)
S_{1s}	$0.3318 \pm 0.0010 \pm 0.0010$	$0.3268 \pm 0.0010 \pm 0.0004$	2.8
S_3	$0.0001 \pm 0.0018 \pm 0.0015$	$-0.0008 \pm 0.0018 \pm 0.0006$	0.3
S_4	$-0.2518 \pm 0.0020 \pm 0.0016$	$-0.2460 \pm 0.0020 \pm 0.0006$	1.7
S_5	$-0.0020 \pm 0.0019 \pm 0.0018$	$0.0035 \pm 0.0020 \pm 0.0008$	1.6
S_{6s}	$0.0006 \pm 0.0016 \pm 0.0013$	$0.0007 \pm 0.0016 \pm 0.0006$	0.0
S_7	$0.0005 \pm 0.0020 \pm 0.0001$	$0.0017 \pm 0.0020 \pm 0.0001$	0.4
S_8	$-0.0516 \pm 0.0020 \pm 0.0001$	$-0.0573 \pm 0.0021 \pm 0.0001$	2.0
S_9	$-0.0861 \pm 0.0018 \pm 0.0002$	$-0.0844 \pm 0.0018 \pm 0.0001$	0.7
F_{S}	$0.0647 \pm 0.0021 \pm 0.0007$	$0.0584 \pm 0.0022 \pm 0.0003$	2.0
S_{S1}	$-0.2349 \pm 0.0035 \pm 0.0036$	$-0.2209 \pm 0.0036 \pm 0.0015$	2.2
S_{S2}	$0.0228 \pm 0.0022 \pm 0.0019$	$0.0215 \pm 0.0023 \pm 0.0008$	0.3
S_{S3}	$0.0027 \pm 0.0021 \pm 0.0017$	$-0.0013 \pm 0.0021 \pm 0.0007$	1.1
S_{S4}	$0.0007 \pm 0.0021 \pm 0.0002$	$-0.0007 \pm 0.0022 \pm 0.0001$	0.5
S_{S5}	$-0.0687 \pm 0.0023 \pm 0.0002$	$-0.0655 \pm 0.0024 \pm 0.0001$	1.0

Table 9.6: Results of the angular fit of the $B^0 \to J/\psi K^{*0}$ decay. The first uncertainty corresponds to the statistical uncertainty of the fit and the second to the systematic uncertainty due to the limited number of simulated events. The third column gives the number of standard deviations between the individual angular observables accounting for both uncertainties.

Parameter	Run 1 only	2016 only	σ(Run 1/16)
S_{1s}	$0.3327 \pm 0.0011 \pm 0.0010$	$0.3280 \pm 0.0011 \pm 0.0004$	2.4
S_3	$0.0008 \pm 0.0019 \pm 0.0015$	$-0.0007 \pm 0.0019 \pm 0.0006$	0.5
S_4	$-0.2537 \pm 0.0021 \pm 0.0016$	$-0.2468 \pm 0.0021 \pm 0.0006$	2.0
S_5	$-0.0040 \pm 0.0021 \pm 0.0018$	$0.0030 \pm 0.0021 \pm 0.0008$	2.0
S_{6s}	$0.0011 \pm 0.0017 \pm 0.0013$	$0.0009 \pm 0.0017 \pm 0.0006$	0.0
S_7	$0.0014 \pm 0.0021 \pm 0.0001$	$0.0020 \pm 0.0022 \pm 0.0001$	0.2
S_8	$-0.0522 \pm 0.0022 \pm 0.0001$	$-0.0572 \pm 0.0022 \pm 0.0001$	1.6
S_9	$-0.0861 \pm 0.0019 \pm 0.0002$	$-0.0848 \pm 0.0019 \pm 0.0001$	0.5
F_{S}	$0.0664 \pm 0.0022 \pm 0.0007$	$0.0604 \pm 0.0022 \pm 0.0003$	1.9
S_{S1}	$-0.2336 \pm 0.0039 \pm 0.0036$	$-0.2299 \pm 0.0039 \pm 0.0015$	0.5
S_{S2}	$0.0226 \pm 0.0023 \pm 0.0019$	$0.0218 \pm 0.0024 \pm 0.0008$	0.2
S_{S3}	$0.0016 \pm 0.0022 \pm 0.0017$	$-0.0020 \pm 0.0022 \pm 0.0007$	1.0
S_{S4}	$0.0014 \pm 0.0022 \pm 0.0002$	$0.0002 \pm 0.0023 \pm 0.0001$	0.4
S_{S5}	$-0.0688 \pm 0.0024 \pm 0.0002$	$-0.0654 \pm 0.0025 \pm 0.0001$	1.0

Table 9.7: Results of the angular fit of the $B^0 \to J/\psi K^{*0}$ decay, removing events with $p(\pi) < 3000\,\mathrm{MeV}/c$ and $p_{\mathrm{T}}(\pi) < 300\,\mathrm{MeV}/c$ in data and simulation. The first uncertainty corresponds to the statistical uncertainty of the fit and the second to the systematic uncertainty due to the limited number of simulated events. The third column gives the number of standard deviations between the individual angular observables accounting for both uncertainties.

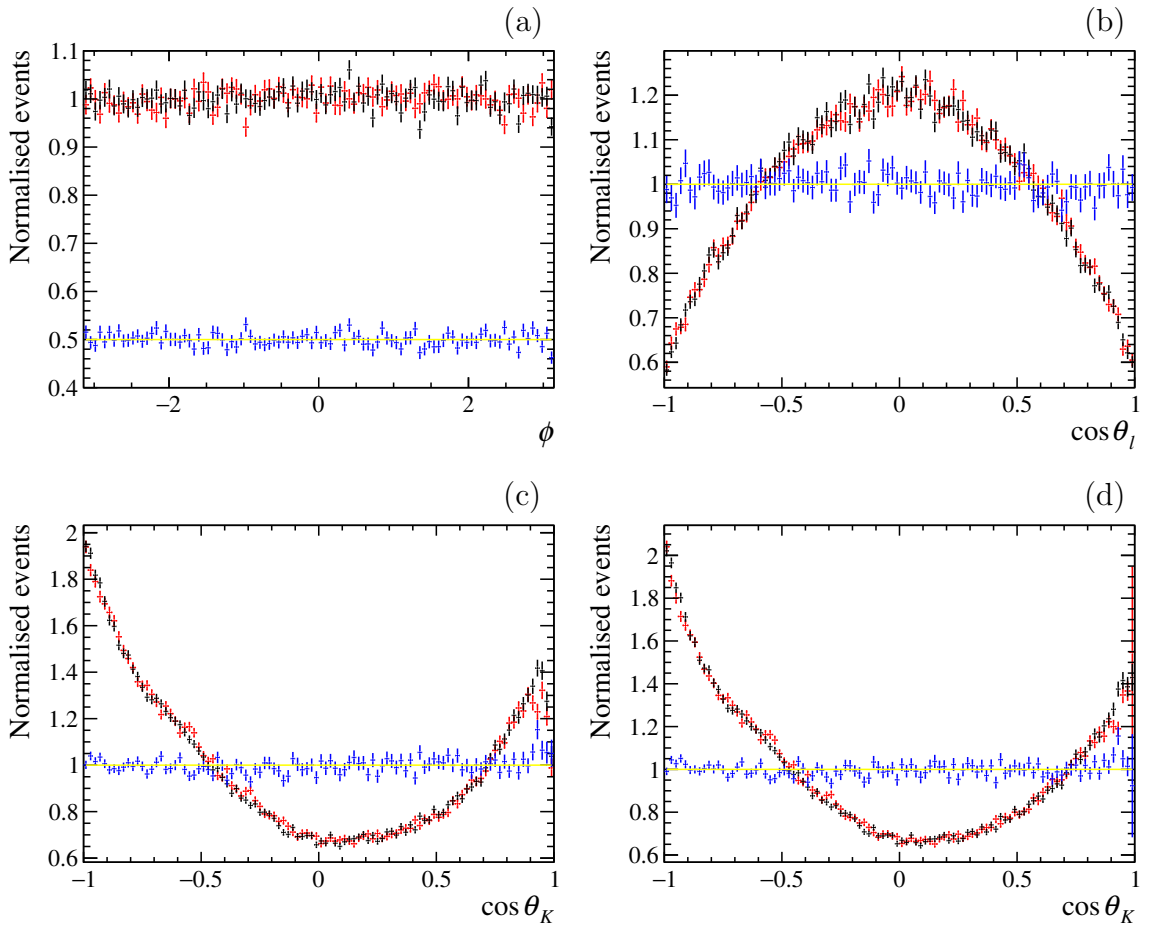


Figure 9.4: Acceptance corrected *sWeighted* $B^0 \to J/\psi K^{*0}$ distributions in the three angles for Run 1 and 2016 in red and black respectively. The ratios of the two distributions for each angle are shown in blue (for the variable ϕ the ratio is shown offset by a half for clarity). Small differences can be seen for low and high $\cos\theta_K$ values in (a)-(c). The unphysical turnover at high $\cos\theta_K$ can be corrected for by using a higher order acceptance function as seen in (d). A systematic is assigned for this in Sec. 10.7.

Parameter	Run 1 only	2016 only	abs. diff.
S_{1s}	$0.3318 \pm 0.0010 \pm 0.0010 \pm 0.0020$	$0.3268 \pm 0.0010 \pm 0.0004 \pm 0.0046$	0.0050
S_3	$0.0001 \pm 0.0018 \pm 0.0015 \pm 0.0002$	$-0.0008 \pm 0.0018 \pm 0.0006 \pm 0.0001$	0.0017
S_4	$-0.2518 \pm 0.0020 \pm 0.0016 \pm 0.0002$	$-0.2460 \pm 0.0020 \pm 0.0006 \pm 0.0010$	0.0058
S_5	$-0.0020 \pm 0.0019 \pm 0.0018 \pm 0.0001$	$0.0035 \pm 0.0020 \pm 0.0008 \pm 0.0009$	0.0055
S_{6s}	$0.0006 \pm 0.0016 \pm 0.0013 \pm 0.0001$	$0.0007 \pm 0.0016 \pm 0.0006 \pm 0.0002$	0.0001
S_7	$0.0005 \pm 0.0020 \pm 0.0001 \pm 0.0000$	$0.0017 \pm 0.0020 \pm 0.0001 \pm 0.0000$	0.0012
S_8	$-0.0516 \pm 0.0020 \pm 0.0001 \pm 0.0001$	$-0.0573 \pm 0.0021 \pm 0.0001 \pm 0.0002$	0.0057
S_9	$-0.0861 \pm 0.0018 \pm 0.0002 \pm 0.0003$	$-0.0844 \pm 0.0018 \pm 0.0001 \pm 0.0009$	0.0017
F_{S}	$0.0647 \pm 0.0021 \pm 0.0007 \pm 0.0001$	$0.0584 \pm 0.0022 \pm 0.0003 \pm 0.0007$	0.0063
S_{S1}	$-0.2349 \pm 0.0035 \pm 0.0036 \pm 0.0249$	$-0.2209 \pm 0.0036 \pm 0.0015 \pm 0.0415$	0.0140
S_{S2}	$0.0228 \pm 0.0022 \pm 0.0019 \pm 0.0012$	$0.0215 \pm 0.0023 \pm 0.0008 \pm 0.0001$	0.0013
S_{S3}	$0.0027 \pm 0.0021 \pm 0.0017 \pm 0.0025$	$-0.0013 \pm 0.0021 \pm 0.0007 \pm 0.0037$	0.0006
S_{S4}	$0.0007 \pm 0.0021 \pm 0.0002 \pm 0.0001$	$-0.0007 \pm 0.0022 \pm 0.0001 \pm 0.0002$	0.0015
S_{S5}	$-0.0687 \pm 0.0023 \pm 0.0002 \pm 0.0003$	$-0.0655 \pm 0.0024 \pm 0.0001 \pm 0.0006$	0.0032

Table 9.8: Results of the angular fit of the $B^0 \to J/\psi K^{*0}$ decay. The first uncertainty corresponds to the statistical uncertainty of the fit, the second to the systematic uncertainty due to the limited number of simulated events and the third to the difference in the pion momentum spectra in simulation and data. The third column gives the absolute difference between the individual angular observables for Run 1 and 2016.

10. Systematic uncertainties

The evaluated systematic effects for this analysis are associated either with the acceptance correction or with the assumptions of the fit model. The procedure for determining the systematic uncertainties uses pseudoexperiments. With the exception of the fit bias, large simulation samples are generated with systematically varied parameters (*e.g.* acceptance or background parameters) and fit back using both the nominal and the systematically varied models. The differences between the angular observables from the varied case and the nominal case are used to calculate the resulting systematic uncertainty. Systematic uncertainties are calculated with 500 pseudoexperiments per q^2 bin, using 200 000 events per experiment[a]. For each individual experiment, the differences between the angular observables in the varied case and the nominal case are computed, and the distributions of differences from all the experiments are then fitted with a Gaussian distribution for each observable. For the systematic uncertainty that evaluates the effect of the limited size of the simulated samples, the width of the corresponding Gaussian is quoted as the systematic on the observable. For the rest of the systematic uncertainties, the mean of the corresponding Gaussian is quoted as the systematic on the observable.

The methods of evaluating each systematic considered in this analysis are given in Secs. 10.1–10.10. Due to the large number of systematic uncertainties, q^2 bins and variables, the complete results are given in Appendix E. A summary of the different sizes of the systematic uncertainties are given in Tab. 10.1. No systematic uncertainty is assigned for the background model of the $K^+\pi^-\mu^+\mu^-$ invariant mass distribution as the effect of using alternative functions instead of the nominal exponential function is negligible.

[a]Large simulation samples are used to avoid any statistical effects that are already taken into account by the statistical uncertainty of the fit.

Source	$F_{\rm L}$	$A_{\rm FB}$, S_3–S_9	P_1–P_8'
Fit Bias	< 0.02	< 0.02	< 0.04
$m(K^+\pi^-\mu^+\mu^-)$ model	< 0.01	< 0.01	< 0.02
$m(K^+\pi^-)$ model	< 0.01	< 0.01	< 0.02
Background model	< 0.01	< 0.01	< 0.03
Peaking backgrounds	< 0.02	< 0.02	< 0.03
$B^+ \to K^+\mu^+\mu^-$ veto	< 0.01	< 0.01	< 0.01
Acceptance stat. uncertainty	< 0.01	< 0.01	< 0.01
Acceptance polynomial order	< 0.01	< 0.01	< 0.02
Data-simulation differences	< 0.01	< 0.01	< 0.01
Acceptance variation with q^2	< 0.03	< 0.03	< 0.09

Table 10.1: Summary of the highest values of the different sources of systematic uncertainties on the angular observables.

10.1 Fit bias

As some of the angular observables of the nominal fit to data are close to physical boundaries and there is a requirement on F_S to be physical, small fit biases exist (see Sec. 9.6.2.) These constitute one of the larger systematic uncertainties but are still small compared to the statistical uncertainty of the nominal fit to data. The majority of observables have a bias that is less than 10% of their statistical uncertainty, with the largest being 17%.

10.2 Signal mass modelling

The signal mass peak is modelled using the sum of two Crystal Ball functions with common mean and tail parameters, but different widths. The nominal signal mass shape parameters are determined from the $B^0 \to J/\psi\, K^{*0}$ control decay and fixed in the nominal fit of the signal decay. The systematic effect of this choice of signal mass model is determined by using an alternative model consisting of a double Gaussian. A fit to the $B^0 \to J/\psi\, K^{*0}$ events determines the parameters of this alternative model. Large simulation samples are then generated using the alternative model and fitted twice, once using the double Gaussian and once using the nominal Crystal Ball parameterisation. The differences in

the values of the angular observables are then used as systematic uncertainties. They are negligible compared to the statistical uncertainties of the nominal fit to data.

10.3 Systematic uncertainties associated with the modelling of the $m_{K\pi}$ distribution

In the nominal fit the $m_{K\pi}$ distribution is used to constrain the S-wave fraction, as described in Sec. 9.2. The modelling of the $m_{K\pi}$ distribution gives rise to three different sources of systematic uncertainties: the parameterisation of the S-wave component, the parameterisation of the background and the effect of a non-flat $m_{K\pi}$ efficiency. These are discussed in turn in the following subsections.

10.3.1 ISOBAR vs LASS for S-wave parameterisation

In the nominal fit, the S-wave contribution of the $m_{K\pi}$ distribution is modelled using the LASS shape. The systematic uncertainty associated with this model is in turn evaluated by using the ISOBAR model. The ISOBAR model is given by the sum of two amplitudes modelling the f_{800} and the $K_0^*(1430)$ resonances:

$$\mathcal{A}_{\text{ISOBAR}}(m_{K\pi}) = |r_{f_{800}}|e^{i\arg\delta_{f_{800}}}\mathcal{A}_{f_{800}}(m_{K\pi}) + (1-|r_{f_{800}}|)\mathcal{A}_{K_0^*(1430)}(m_{K\pi}),$$

where $\mathcal{A}_{f_{800}}(m_{K\pi})$ and $\mathcal{A}_{K_0^{*0}(1430)}(m_{K\pi})$ are modelled as Breit-Wigner amplitudes as defined in Eq. 9.5. The masses and widths of the resonances are taken from Ref. [145] and are set to $m(f_{800}) = 682\,\text{MeV}/c^2$, $\Gamma(f_{800}) = 547\,\text{MeV}/c^2$, $m(K_0^*(1430)) = 1.425\,\text{GeV}/c^2$ and $\Gamma(K_0^*(1430)) = 0.270\,\text{GeV}/c^2$, while a fit to the $m_{K\pi\mu\mu}$ and $m_{K\pi}$ distributions of the $B^0 \to J/\psi\, K^{*0}$ control channel is used to determine $|r_{800}|$ and δ_{800}. Large simulation samples are generated using the ISOBAR model and fit once with the ISOBAR and once with the LASS model. Gaussian fits to the distributions of differences between the angular observables are then used to determine the systematic uncertainties. These uncertainties are very small compared to the statistical uncertainties of the nominal fit to data.

10.3.2 Shape of the $m_{K\pi}$ background distribution

As outlined in Sec. 9.2, the $m_{K\pi}$ background is modelled using a first-order Chebyshev polynomial. The systematic uncertainty due to this assumption is evaluated with pseudoexperiments generated using a fourth order Chebyshev polynomial, where the

corresponding coefficients for each q^2 bin are taken from a fit to the upper mass sideband ($m_{K\pi\mu\mu} > 5450\,\mathrm{MeV}/c^2$). The simulated samples are then fit twice, once with the fourth-order Chebyshev polynomial model, and once with the nominal first-order Chebyshev polynomial model. The observed differences between the values of the angular observables of the two fits are then used to assign a systematic uncertainty. The systematic uncertainties are very small compared to the statistical uncertainties of the nominal fit to data.

10.3.3 Flat efficiency of the $m_{K\pi}$ distribution

In the nominal fit the efficiency over the $m_{K\pi}$ range, $[795.9, 995.9]\,\mathrm{MeV}/c^2$, is assumed to be flat. The systematic uncertainty of this assumption is determined using large simulation samples, which include a $m_{K\pi}$ dependent efficiency. The simulated events are generated using an efficiency function that is linearly rising or falling with a variation of $\pm 5\%$ at the borders of the $m_{K\pi}$ mass range. This efficiency variation is applied in addition to the nominal four-dimensional efficiency functions described in Chpt. 8. The systematic uncertainties are quantified by determining the values of the angular observables with the nominal fit and taking the difference between them and the generated values. The resulting systematic uncertainties are very small compared to the statistical uncertainties of the nominal fit to data.

10.4 Angular background modelling

Chebyshev polynomials of second order and lower are used to describe the background shape of the decay angles in the nominal fit. The systematic effect of this choice of angular background model is estimated by fitting the high mass sideband ($m_{K\pi\mu\mu} \in [5355, 5700]\,\mathrm{MeV}/c^2$) with Chebyshev polynomials of fourth order and lower. Due to the limited number of background events, the BDT requirement is removed when determining Chebyshev coefficients for this systematic uncertainty.

The systematic effect of only fitting the background with polynomials of order two and lower is determined using large simulation samples that are generated with the fourth order angular background model. The pseudoexperiments are then fitted twice, once with the fourth order and once with the second order angular background model. The differences in the values of the angular observables are then used as systematic uncertainties. These uncertainties are small compared to the statistical uncertainties of the nominal fit to data.

10.5 Peaking backgrounds

As described in Sec. 5.2.1, the peaking background levels that remain after the full selection are small enough so that they can be safely neglected in the nominal fit. The largest residual backgrounds are from $\overline{B}^0 \to \overline{K}^{*0}\mu^+\mu^-$ and $B_s^0 \to \phi(1020)(\to K^+K^-)\mu^+\mu^-$ decays, with contributions of $(0.65 \pm 0.02)\%$ and $(0.21 \pm 0.03)\%$ of the signal yield respectively (see Tab. 5.3 for a full summary). Peaking background contributions are introduced to pseudoexperiments according to their expected fraction to quantify the effect of neglecting them in the nominal fit. While the residual background yields are determined from simulation, the background distributions in $m_{K\pi\mu\mu}$ and the angles are taken from data events that are selected so that the peaking background candidates are remaining.

The systematic uncertainty of neglecting the peaking backgrounds is determined using 500 pseudoexperiments of 200 000 events each generated with the nominal model of the fit. For each pseudoexperiment additional events are added to simulate the peaking backgrounds. These additional events are then fitted together with the nominal events. The differences of the values between the resulting observables and the values of the observables used to generate the pseudoexperiments give an estimate of the uncertainties. The peaking background systematic uncertainty is among the three biggest systematic effects, however it is still much smaller than the statistical uncertainty of the nominal fit to data.

10.6 $B^+ \to K^+\mu^+\mu^-$ veto

Fig. 10.1 depicts an example of the background fit to $\cos\theta_K$ for Run 1 and 2016. It can be observed that for high $\cos\theta_K$ values the number of data points fall sharply. Rather than being a physical effect this is an artificial one that is created by applying the $B^+ \to K^+\mu^+\mu^-$ veto. This does not have an effect on the signal, as the veto is only applied for $m_{K\pi\mu\mu} > 5380\,\text{MeV}/c^2$. However, the effect of the veto on the background artificially warps the $\cos\theta_K$ distribution and therefore alters the background coefficients, which can feed into the determination of the angular observables in the signal region.

In order to assign a systematic uncertainty for the effect of the $B^+ \to K^+\mu^+\mu^-$ veto, it is necessary to obtain a parameterisation of the veto in terms of the parameters of the angular fit. Using phase-space simulation, the $B^+ \to K^+\mu^+\mu^-$ veto that is nominally described by $m_{K\pi\mu\mu} > 5380\,\text{MeV}/c^2$ and $5220 < m_{K\mu\mu} < 5340\,\text{MeV}/c^2$ can be expressed

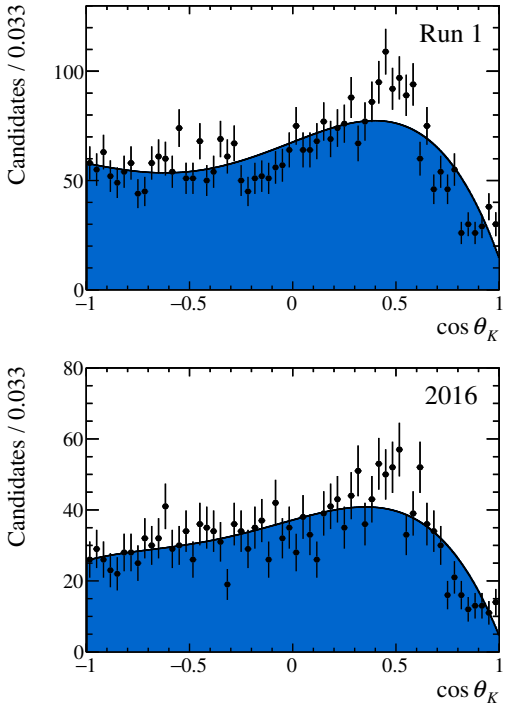


Figure 10.1: An example of the background fit for Run 1 and 2016. The warping at high $\cos\theta_K$ values is caused by the $B^+ \to K^+\mu^+\mu^-$ veto.

in terms of a requirement on $\cos\theta_K$ and $m_{K\pi\mu\mu}$ for each q^2 bin. Having established the parameterisation of the veto in terms of the fit parameters, it is possible to quantify the effect on the angular observables using pseudoexperiments.

The pseudoexperiments are generated using the nuisance parameters of the simultaneous fit and the SM values for the angular observables. They are then fit once directly and once after the requirement has been imposed. The difference of the resulting angular observables gives a quantitative estimate of the effect of not accounting for the veto. The effect is negligible for all the angular observables apart from $F_{\rm L}$, where the systematic is of the same order as the peaking background systematic. However, the $B^+ \to K^+\mu^+\mu^-$ veto systematic on $F_{\rm L}$ is still small compared to the statistical uncertainty of the nominal fit to data.

10.7 Higher order acceptance description

A choice is made regarding the maximum order of Legendre polynomials used to model the four-dimensional acceptance. Higher orders are generally able to describe the acceptance better, however they lead to higher computational requirements and can result in the appearance of oscillations at the borders of the distributions (Runge phenomenon [132]). Hence, it is desirable to choose the lowest order of polynomials that describe the acceptance sufficiently well, and then use a higher order parameterisation to determine a systematic uncertainty associated with that choice.

The nominal acceptance functions use Legendre polynomials of fifth and lower orders for q^2, fourth and lower orders for $\cos\theta_l$, fifth and lower orders for $\cos\theta_K$ and sixth and lower orders for the angle ϕ. As mentioned in Sec. 8.3, small deviations between the acceptance simulation and the acceptance functions are observed for low q^2. In addition, a higher order in the polynomials describing the $\cos\theta_K$ acceptance was needed to correct for the unphysical turnover seen in Fig. 9.4. The systematic uncertainty associated with these and any further imperfections that could arise due to correlations are estimated by increasing the order of the Legendre polynomials by three for the three angles and q^2. The one-dimensional projections of the higher order acceptance functions on q^2 and on the three decay angles are given in Fig. 10.2. The results of the $B^0 \to J/\psi\, K^{*0}$ control channel obtained with the nominal and the higher order acceptances are shown in Tab. 10.2, where the Run 1 and 2016 data have been fitted separately. The deviation seen between the nominal and the higher order acceptance is small compared to the statistical uncertainty of the fit to the signal decay, giving confidence in the choice of the order of the Legendre polynomials.

To quantify the systematic uncertainties corresponding to the signal decay, large simulation samples are generated using the higher order acceptance and fit back with both the nominal and the higher order acceptance model. The differences in the values of the angular observables are then used as systematic uncertainties. They are small compared to the statistical uncertainties of the nominal fit to data.

10.8 Statistical uncertainty of the acceptance

The coefficients of the acceptance functions corresponding to the Run 1 and 2016 data sets are determined using 1.406 M and 7.657 M simulated $B^0 \to K^{*0}\mu^+\mu^-$ events, respectively.

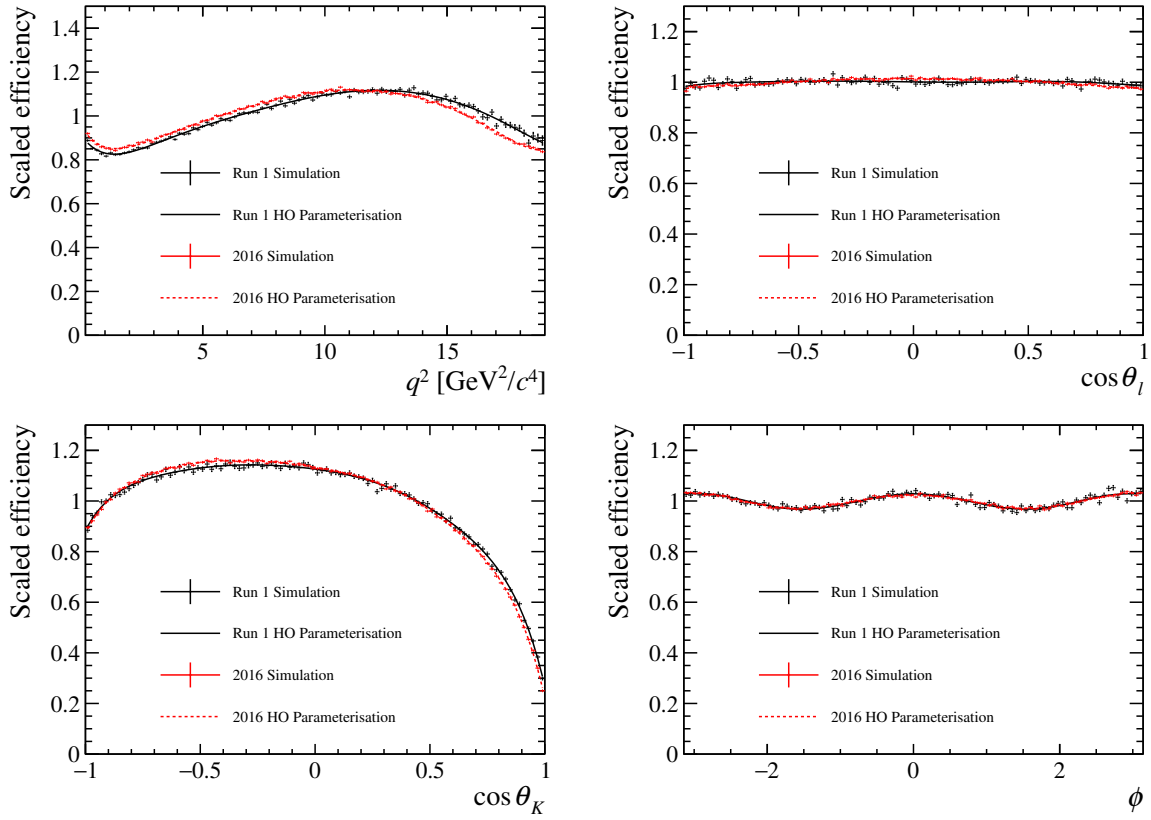


Figure 10.2: Distributions of the Run 1 and 2016 acceptance simulations in q^2, $\cos\theta_l$, $\cos\theta_K$, and ϕ. Corresponding one-dimensional projections of the higher order acceptance functions on q^2, $\cos\theta_l$, $\cos\theta_K$, and ϕ are also shown.

The effect of the limited size of the simulated samples is determined by varying the acceptance functions using the bootstrapping technique [139]. Samples of simulated $B^0 \to K^{*0}\mu^+\mu^-$ events are constructed by randomly picking events from the existing sample until the size of the original sample is reached. The samples are then used to calculate the coefficients of the varied acceptances.

For every varied acceptance 200 000 pseudoevents are generated and fit, once with the varied and once with the nominal acceptance model. The distribution of the differences between the values of the angular observables of the varied and the nominal acceptance model for 500 pseudoexperiments are shown for the first q^2 bin in Fig. 10.3. Gaussian functions are used to fit these distributions, and the corresponding widths are used as systematic uncertainties. These are negligible compared to the statistical uncertainties of the nominal fit to data.

Par.	Run 1 ho	2016 ho	Par.	Run 1 nom	2016 nom
S_{1s}	0.332 ± 0.001	0.327 ± 0.001	S_{1s}	0.331 ± 0.001	0.326 ± 0.001
S_3	0.000 ± 0.002	-0.001 ± 0.002	S_3	0.000 ± 0.002	-0.001 ± 0.002
S_4	-0.252 ± 0.002	-0.246 ± 0.002	S_4	-0.250 ± 0.002	-0.245 ± 0.002
S_5	-0.002 ± 0.002	0.004 ± 0.002	S_5	-0.005 ± 0.002	0.002 ± 0.002
S_{6s}	0.001 ± 0.002	0.001 ± 0.002	S_{6s}	0.003 ± 0.002	0.001 ± 0.002
S_7	0.001 ± 0.002	0.002 ± 0.002	S_7	0.002 ± 0.002	0.002 ± 0.002
S_8	-0.052 ± 0.002	-0.057 ± 0.002	S_8	-0.048 ± 0.002	-0.057 ± 0.002
S_9	-0.086 ± 0.002	-0.084 ± 0.002	S_9	-0.084 ± 0.002	-0.084 ± 0.002
F_{S}	0.065 ± 0.002	0.058 ± 0.002	F_{S}	0.061 ± 0.002	0.057 ± 0.002
S_{S1}	-0.235 ± 0.004	-0.221 ± 0.004	S_{S1}	-0.233 ± 0.004	-0.226 ± 0.004
S_{S2}	0.023 ± 0.002	0.022 ± 0.002	S_{S2}	0.022 ± 0.002	0.021 ± 0.002
S_{S3}	0.003 ± 0.002	-0.001 ± 0.002	S_{S3}	0.002 ± 0.002	-0.001 ± 0.002
S_{S4}	0.001 ± 0.002	-0.001 ± 0.002	S_{S4}	0.001 ± 0.002	-0.001 ± 0.002
S_{S5}	-0.069 ± 0.002	-0.066 ± 0.002	S_{S5}	-0.069 ± 0.002	-0.065 ± 0.002

Table 10.2: Results from the angular fit of the control decay $B^0 \to J/\psi K^{*0}$ using the higher order (ho) acceptance description (left) detailed in Sec. 10.7 and the nominal (nom) acceptance correction (right).

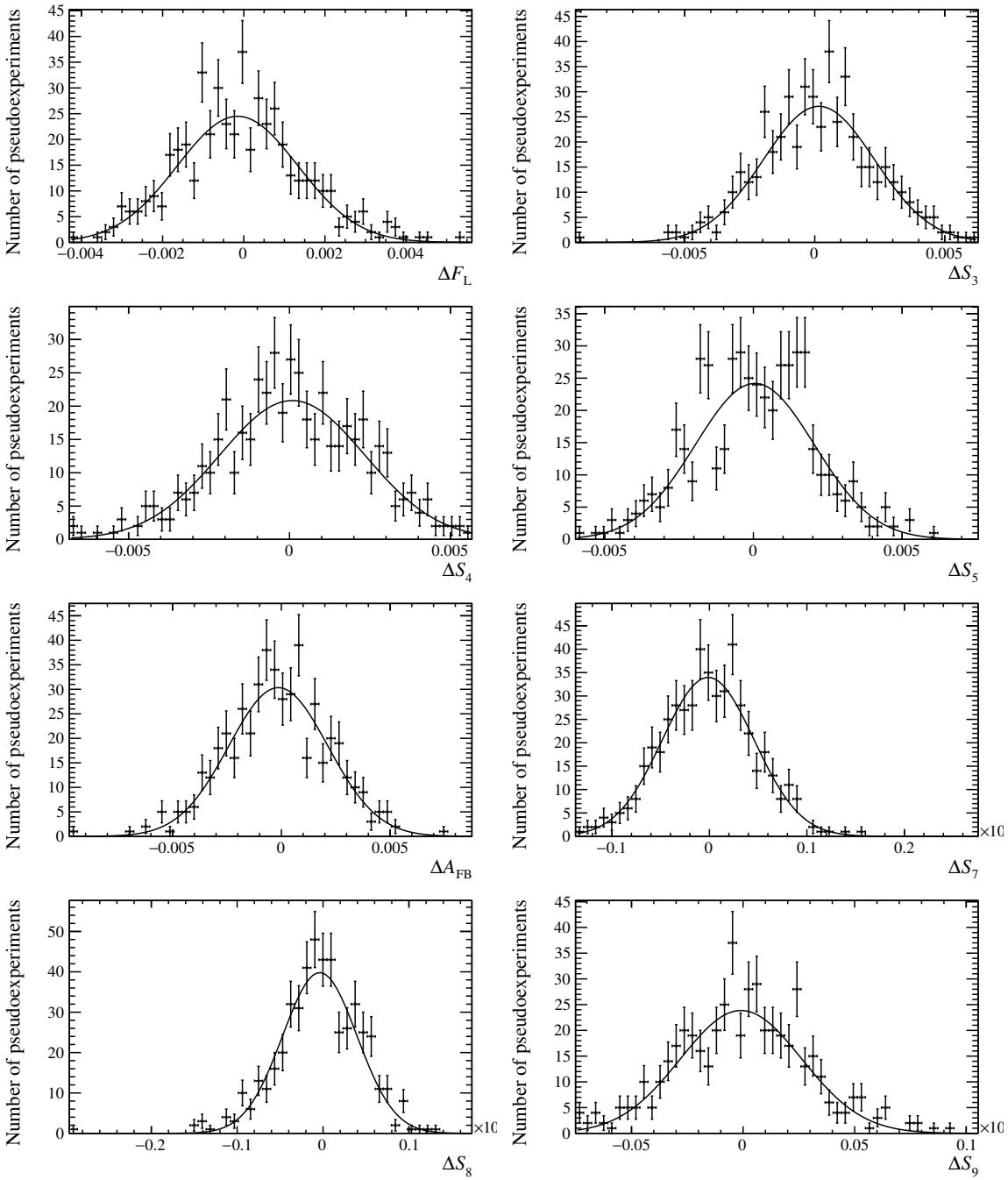


Figure 10.3: Distributions of deviations of observables from pseudoexperiments generated with varied acceptances for the first q^2 bin in the range $0.1 < q^2 < 0.98\,\mathrm{GeV}^2/c^4$.

10.9 Agreement between data and simulation

The description of the acceptance effects rely heavily on the accurate simulation of the $B^0 \to K^{*0}\mu^+\mu^-$ signal decay. Chpt. 7 outlines the two procedures that are used to correct for the unsatisfactory simulation of the PID variables, the number of tracks in the event (`nTracks`), the vertex fit quality of the signal candidate ($\chi^2_{\rm Vtx}$), and the B^0 candidate's transverse momentum $p_{\rm T}(B^0)$. Remaining differences between simulation and data, such as those in the (transverse) momenta of the kaon and pion and the L0 trigger efficiencies, are not corrected explicitly. The following subsections will outline the different systematic uncertainties associated with these choices.

10.9.1 PID systematic

In order to assess the effect of any remaining differences between simulation and data after the PID resampling has been performed, additional weights are calculated using *sWeighted* $B^0 \to J/\psi\, K^{*0}$ data and the resampled simulation. These weights are then applied to the simulation, effectively removing any remaining small discrepancies. The weighted simulation samples are used to calculate a new acceptance, and 500 pseudoexperiments containing 200 000 events each are generated to assess the effect of this reweighting. The PID systematic assigned due to the reweighting is negligible compared to the statistical uncertainty of the nominal fit to data.

10.9.2 Effects of reweighting $\chi^2_{\rm Vtx}$, $p_{\rm T}(B^0)$ and `nTracks`

The effect of reweighting the $\chi^2_{\rm Vtx}$, $p_{\rm T}(B^0)$ and `nTracks` distributions in simulation, as outlined in Sec. 7.2, is evaluated by redetermining the acceptance functions without the reweighting. Three new acceptance functions are calculated, the first only with the $\chi^2_{\rm Vtx}$ and $p_{\rm T}(B^0)$ weights applied, the second only with the $\chi^2_{\rm Vtx}$ and `nTracks` weights applied and the third only with the $p_{\rm T}(B^0)$ and `nTracks` weights applied. For each of the varied acceptance functions 500 pseudoexperiments with 200 000 events per experiment are generated to evaluate the effect on the angular observables. The systematic uncertainties are negligible compared to the statistical uncertainty of the nominal fit to data.

10.9.3 Kaon and pion momenta

Fig. 10.4 shows the (transverse) momentum distributions for the kaon and pion for $B^0 \to J/\psi K^{*0}$ events recorded in Run 1 and 2016, as well as for simulated events. The data distributions are *sWeighted* in order to extract the signal candidates. While the *sWeighted* data contains both a P-wave and an S-wave contribution, the nominal simulation only contains a P-wave component. To account also for the S-wave contribution, weights that are calculated using input from a previous Belle analysis [140] are applied to the simulated events. As a result, a greatly reduced systematic associated with the hadron momentum reweighting is seen compared to the same systematic in the previous analysis [2]. In the analysis presented in Ref. [2] no such S-wave component was introduced into the simulation. The reduction is approximately ten-fold and therefore the systematic uncertainty becomes negligible.

The systematic uncertainties are estimated using the following approach. First, correction factors are determined from two-dimensional distributions of the K^+ and π^- in data and simulation. These depend on the particles' momenta and transverse momenta and are shown in Fig. 10.5 for both Run 1 and 2016. The systematic uncertainties are then evaluated using large simulation samples, where the acceptance is redetermined using the correction factors. Both the systematic uncertainties associated with the pion momenta and those associated with the kaon momenta are small compared to the statistical uncertainty of the nominal fit to data.

10.9.4 Trigger systematic

Sec. 3.8.1 outlined the different L0 trigger lines consisting of the `L0Muon`, `L0DiMuon`, `L0Electron`, `L0Photon` and `L0Hadron` lines. The decisions in the former two lines are based on the muons' p_{T}, while the latter three lines record events that have a large E_{T}. The thresholds at which the trigger lines accept events depend on the data taking conditions. While these were very stable during Run 1, they varied largely during the 2016 data taking period and the corresponding simulation does not replicate these changes very well. Therefore a systematic is assigned for the discrepancy between data and simulation.

To evaluate an appropriate systematic the $B^0 \to J/\psi K^{*0}$ control channel, as well as the TIS, TOS and TISTOS trigger categories defined in Sec. 3.8.1, are used. Taking advantage of the different categories, the trigger efficiency can be obtained by computing

$$\varepsilon_{trigger} = \frac{N(\text{TISTOS})}{N(\text{TIS})}, \tag{10.1}$$

where N(TISTOS) equals the number of TISTOS events in a sample and N(TIS) is the number of TIS events in the same sample. This calculation is accurate when the events in the sample are triggered by TIS trigger lines that are independent of TOS trigger lines. The combined efficiency for the `L0Muon` and `L0DiMuon` trigger lines for the $B^0 \to J/\psi(\to \mu^+\mu^-)K^{*0}$ decay can be obtained by counting the corresponding TIS events that were triggered by the `L0Electron`, `L0Photon` and `L0Hadron` trigger lines, *i.e.*

$$\varepsilon_{\text{L0}} = \frac{N((\texttt{L0Muon}_{\text{TOS}}||\texttt{L0DiMuon}_{\text{TOS}})\&(\texttt{L0Electron}_{\text{TIS}}||\texttt{L0Photon}_{\text{TIS}}||\texttt{L0Hadron}_{\text{TIS}}))}{N(\texttt{L0Electron}_{\text{TIS}}||\texttt{L0Photon}_{\text{TIS}}||\texttt{L0Hadron}_{\text{TIS}})}. \tag{10.2}$$

The efficiency in bins of maximum muon p_{T} for both data and simulation of the $B^0 \to J/\psi K^{*0}$ decay is illustrated in Fig. 10.6(a), where the discrepancies between the two efficiencies can clearly be seen. Fig. 10.6(b) shows the efficiency when aligning the thresholds of simulation and data[b]. Even though the agreement is much better, this option is not used, as it results in a 5% reduction of signal candidates. Instead, a systematic is assigned by reweighting the acceptance simulation by the ratio of the number of data and simulation events given in Fig. 10.6(a). A new acceptance is calculated with the reweighted simulation and used to generate 500 pseudoexperiments of 200 000 events each. As usual, the pseudoexperiments are fit twice, once with the nominal model and once with the varied acceptance model. The differences in the angular observables of the two fits give a quantitative estimate of the systematic uncertainties. These are negligible compared to the statistical uncertainty of the nominal fit to data. Similarly, the effect of the differences between the thresholds in data and simulation for the HLT trigger lines are negligible.

[b]The simulation thresholds are always higher or equal than those in data. The alignment in question is therefore obtained by increasing the thresholds of the data.

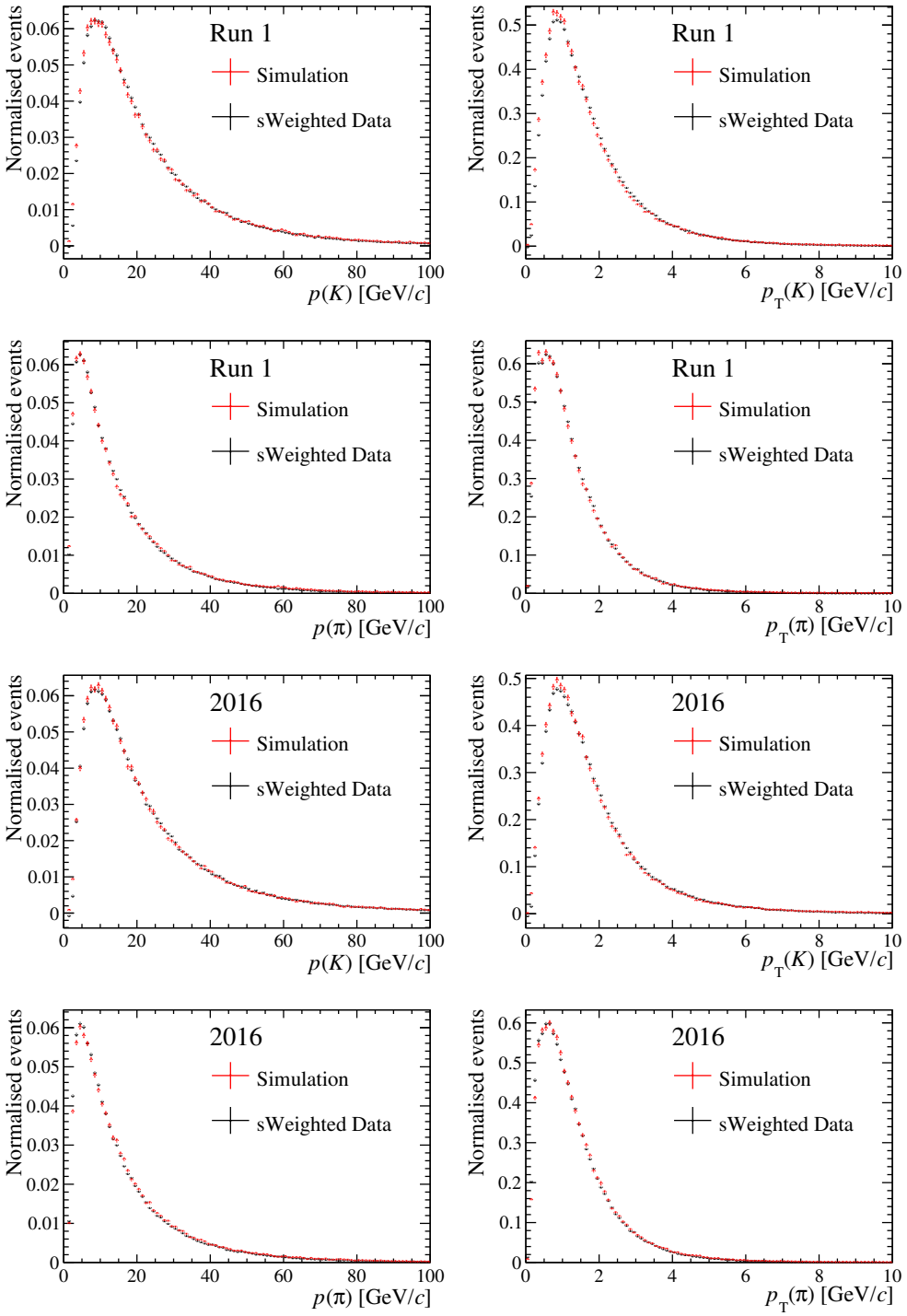


Figure 10.4: Distributions of p and p_{T} for K^+ and π^- for *sWeighted* $B^0 \to J/\psi K^{*0}$ candidates from data and simulation.

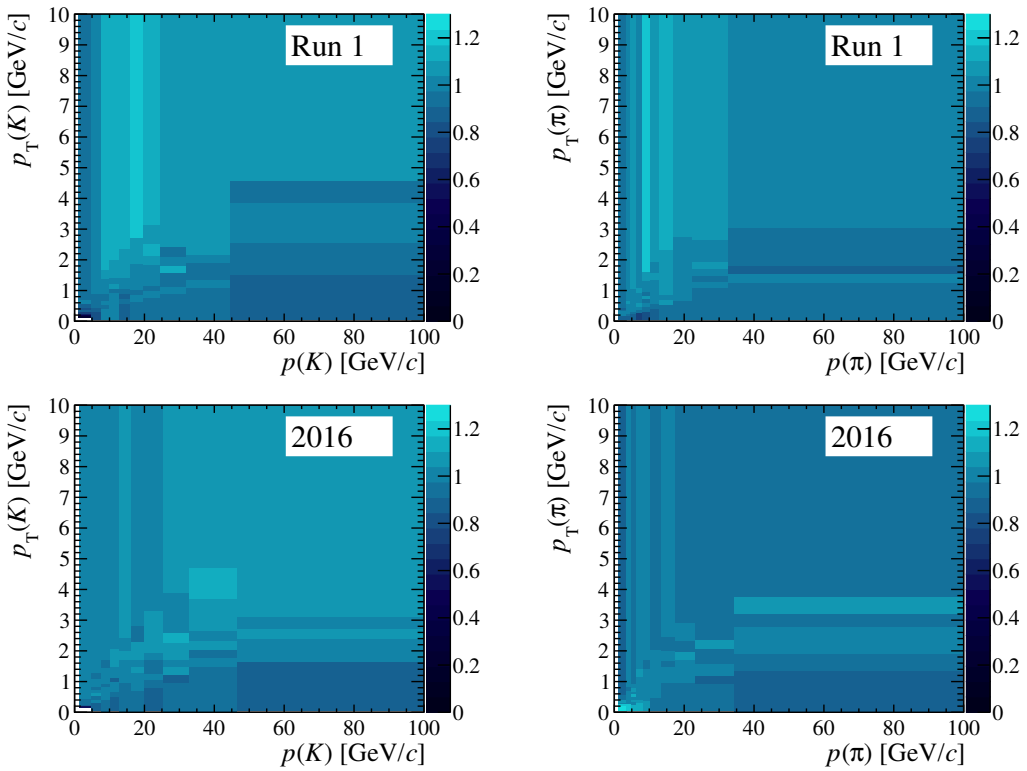


Figure 10.5: Correction factor for simulated events depending on p and p_T for K^+ and π^-.

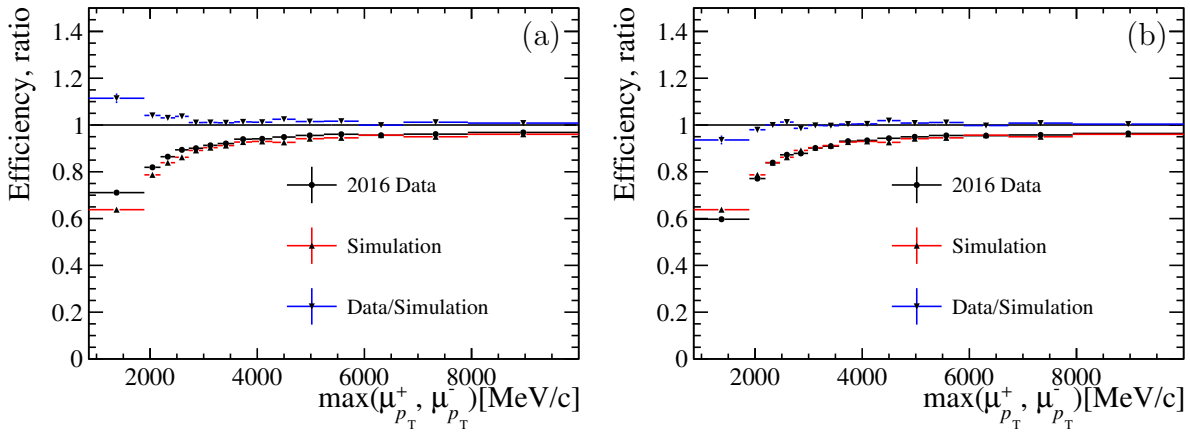


Figure 10.6: Combined efficiency of the `L0Muon` and `L0DiMuon` trigger lines vs maximum muon p_T, obtained using the $B^0 \to J/\psi K^{*0}$ decay candidates of the 2016 data set and simulation. The results when not aligning the trigger thresholds in simulation and data are shown in (a), while in (b) the thresholds are aligned.

10.10 Fixing of q^2 for four-dimensional acceptance

For the narrow q^2 bins the acceptance is included explicitly in the PDF of the fit, which in itself does not depend on q^2. The four-dimensional acceptance functions are therefore evaluated at the centre of the q^2 bin in which the fit is performed. The systematic bias of this choice is determined using two sets of large simulation samples that are generated with the acceptance evaluated either halfway between the bin centre and the upper edge, or halfway between the bin centre and the lower edge. The pseudoexperiments in both sets are fitted with the nominal and the varied model, and the deviations of the angular observables are evaluated in each case. The largest deviation is then taken as the systematic uncertainty. As can be seen in Tab. 10.1, this systematic uncertainty constitutes one of the larger biases. However, it is still small compared to the statistical uncertainty of the fit.

11. Results

The angular observables are determined in bins of q^2 using the maximum likelihood fit described in Chpt. 9. The parameters that are varied in the fit are the signal fraction f_{sig}, the parameter describing the background mass shape τ_m, the coefficients of the second order Chebyshev polynomials describing the angular background shape, the coefficient of the first order Chebyshev polynomial describing the $m_{K\pi}$ background shape and the P-wave observables F_{L}, A_{FB}, $S_{3,4,5,7,8,9}$ (for the case of the $P_i^{(\prime)}$ basis F_{L}, $P_{1,2,3}$, $P'_{4,5,6,8}$) and the S-wave parameters F_{S}, $S_{\text{S1,S2,S3,S4,S5}}$. The Run 1 and 2016 data samples are fit simultaneously, as described in Sec. 9.4, and four-dimensional acceptance functions are included in order to correct for distortions by the detector, reconstruction and selection (see Sec. 8). The P-wave and the S-wave parameters are shared amongst the two data samples, while all other parameters (f_{sig}, τ_m and the background parameters) are fit separately. A weighted fit approach is performed for the wide q^2 bins $[1.1, 6.0]\,\text{GeV}^2/c^4$ and $[15.0, 19.0]\,\text{GeV}^2/c^4$, while the acceptance is included in the PDF for the narrow bins (see Sec. 9.5).

Projections of the fitted probability density function on the decay angles, $m(K^+\pi^-)$ and $m(K^+\pi^-\mu^+\mu^-)$ for the two q^2 bins $[4.0, 6.0]\,\text{GeV}^2/c^4$ and $[1.1, 6.0]\,\text{GeV}^2/c^4$ are given in Figs 11.1 and 11.2. The rest of the fit projections can be found in Appendix F. The results of the observables for the S_i and $P_i^{(\prime)}$ bases are given in Tabs. 11.1 and 11.2, where the first uncertainties are statistical and the second systematic. The statistical uncertainties are determined using Hesse and coverage corrected according to Tabs. D.5-D.8, as explained in Sec. 9.6.2. The second uncertainties are the quadratic sums of the different systematic uncertainties outlined in Chpt. 10. The linear correlations are given in Appendix G. The results for the observables from the simultaneous fits are shown together with their respective SM predictions in Figs 11.3 and 11.4. The SM predictions for the S_i observables are based on the prescription of Ref. [146], which combines light-cone sum rule calculations [77], valid in the low-q^2 region, with lattice determinations at high q^2 [147, 148]. For the $P_i^{(\prime)}$ observables, predictions from Ref. [78] are shown using form factors from Ref. [73]. These predictions are restricted to the region $q^2 < 8.0\,\text{GeV}^2/c^4$. The results of the angular observables from the simultaneous fit are also compared to the results of the previous analysis [2] and the individual fit to the 2016 data. These results can be seen in Figs. 11.5 and 11.6.

A few observations can be made. First, considering the observables individually,

the results are largely in agreement with the SM predictions. Secondly, the results of the wide q^2 bins and the corresponding narrow bins are compatible. Thirdly, all the individual results from Run 1 and the 2016 data are in excellent agreement. Fourthly, the central values of A_{FB} and S_5 (P_5') of the simultaneous fit lie closer to the SM predictions than the corresponding values of the Run-1-only fit. Considering also the change in the uncertainties, the local discrepancy in the P_5' observable in the $4.0 < q^2 < 6.0\,\mathrm{GeV}^2/c^4$ and $6.0 < q^2 < 8.0\,\mathrm{GeV}^2/c^4$ bins is slightly reduced from the 2.8 and $3.0\,\sigma$ observed in Ref. [2] to 2.5 and $2.9\,\sigma$. The value of F_{L} in the $2.5 < q^2 < 4.0\,\mathrm{GeV}^2/c^4$ bin, which was very close to the physical boundary of the PDF in the Run 1-only analysis, is now well within the physical boundaries.

The values of the angular observables are also studied for the individual data sets corresponding to the two polarities of the magnet. The results of these, together with the simultaneous fit results are given in Figs. 11.7 and 11.8. Again, the agreement between the two data sets is very good.

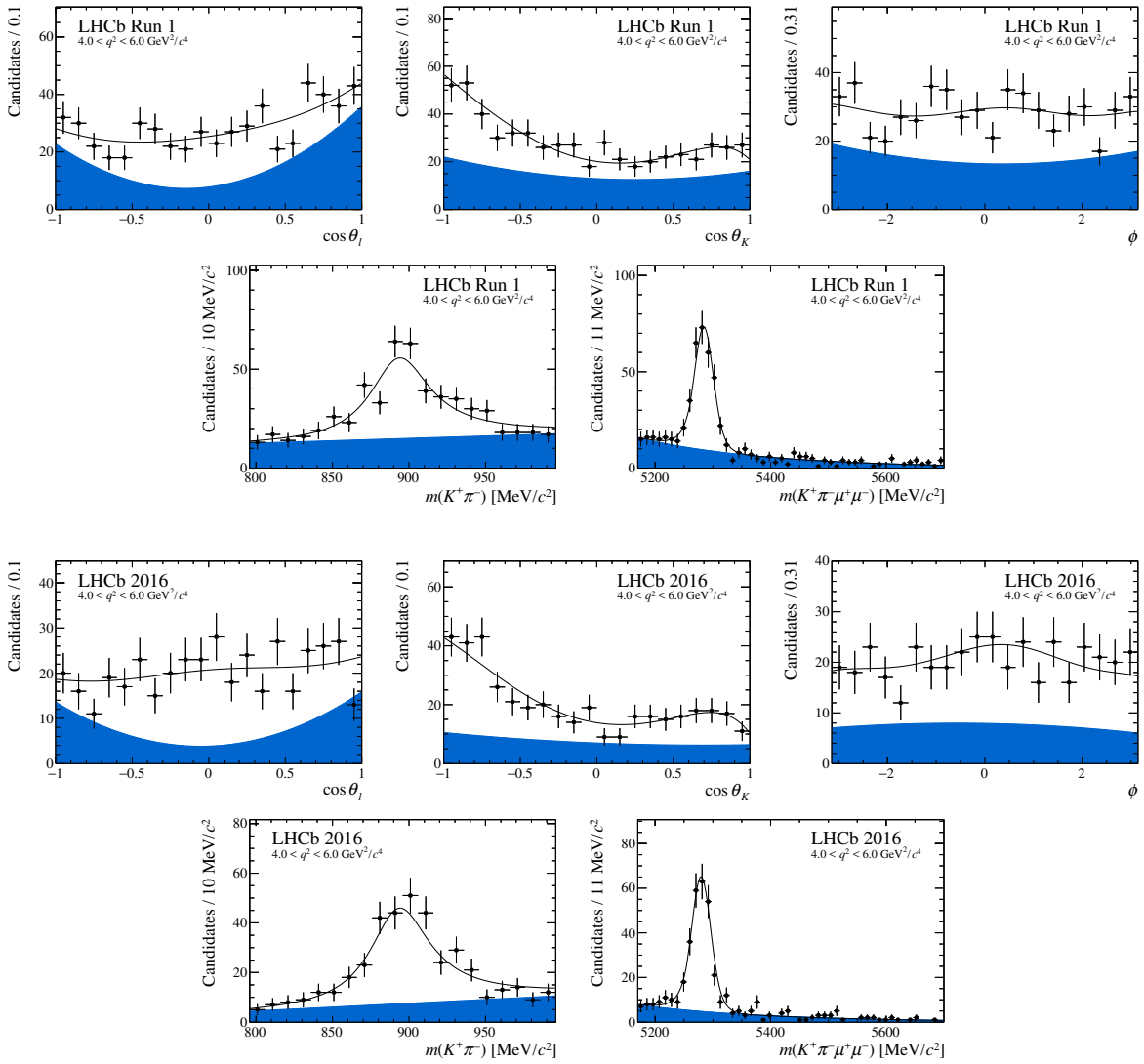


Figure 11.1: Projections of the fitted probability density function on the decay angles, $m(K^+\pi^-)$ and $m(K^+\pi^-\mu^+\mu^-)$ for the bin $4.0 < q^2 < 6.0\,\mathrm{GeV}^2/c^4$. The blue shaded region indicates background. Figure taken from Ref. [1].

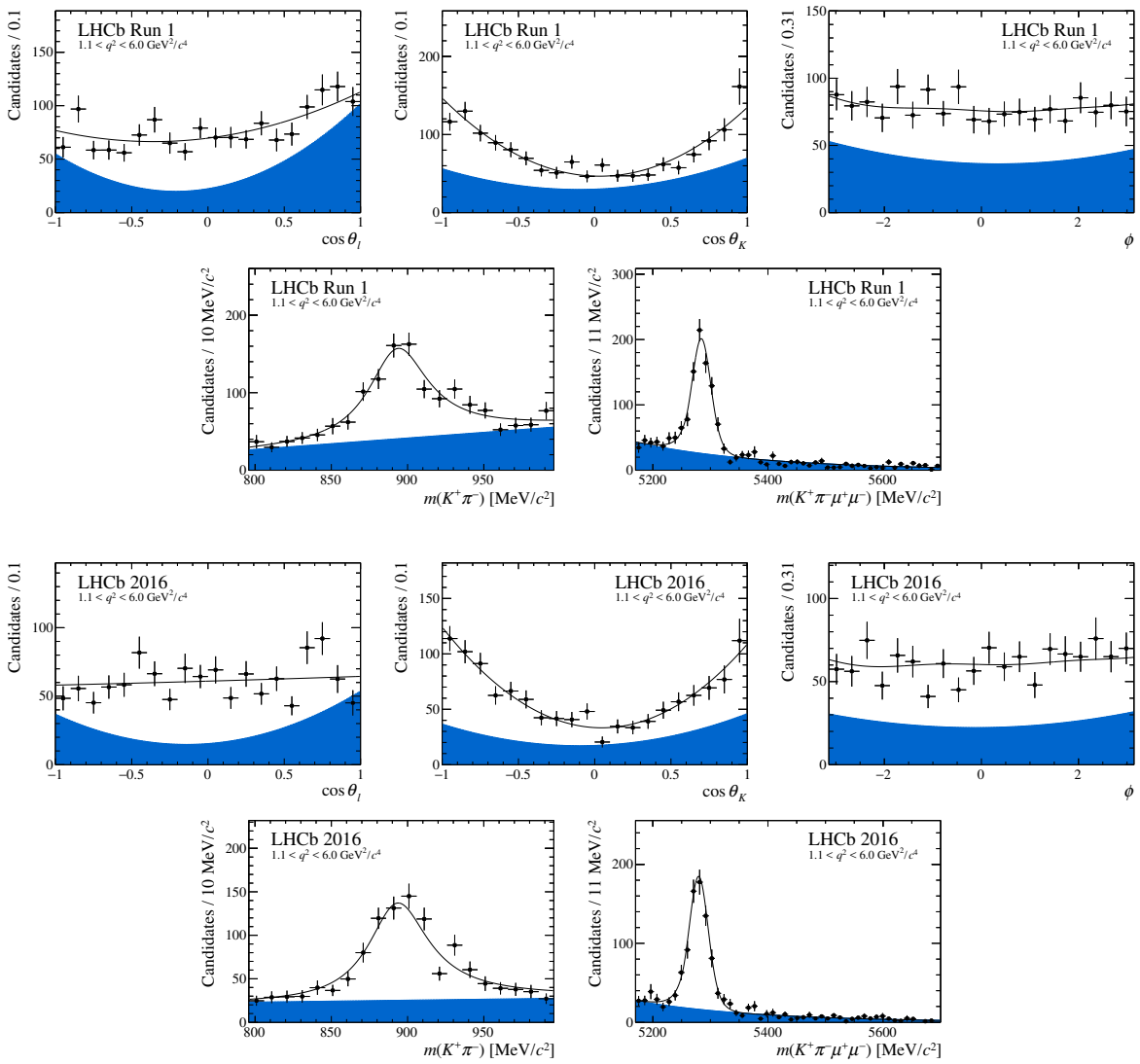


Figure 11.2: Projections of the fitted probability density function on the decay angles, $m(K^+\pi^-)$ and $m(K^+\pi^-\mu^+\mu^-)$ for the bin $1.1 < q^2 < 6.0\,\mathrm{GeV}^2/c^4$. The blue shaded region indicates background. Figure taken from Ref. [1].

$0.10 < q^2 < 0.98\,\mathrm{GeV}^2/c^4$	
F_L	$0.255 \pm 0.032 \pm 0.007$
S_3	$0.034 \pm 0.044 \pm 0.003$
S_4	$0.059 \pm 0.050 \pm 0.004$
S_5	$0.227 \pm 0.041 \pm 0.008$
A_FB	$-0.004 \pm 0.040 \pm 0.004$
S_7	$0.006 \pm 0.042 \pm 0.002$
S_8	$-0.003 \pm 0.051 \pm 0.001$
S_9	$-0.055 \pm 0.041 \pm 0.002$

$1.1 < q^2 < 2.5\,\mathrm{GeV}^2/c^4$	
F_L	$0.655 \pm 0.046 \pm 0.017$
S_3	$-0.107 \pm 0.052 \pm 0.003$
S_4	$-0.038 \pm 0.070 \pm 0.011$
S_5	$0.174 \pm 0.060 \pm 0.007$
A_FB	$-0.229 \pm 0.046 \pm 0.009$
S_7	$-0.107 \pm 0.063 \pm 0.004$
S_8	$-0.174 \pm 0.075 \pm 0.002$
S_9	$-0.112 \pm 0.054 \pm 0.005$

$2.5 < q^2 < 4.0\,\mathrm{GeV}^2/c^4$	
F_L	$0.756 \pm 0.047 \pm 0.023$
S_3	$0.020 \pm 0.053 \pm 0.002$
S_4	$-0.187 \pm 0.074 \pm 0.008$
S_5	$-0.064 \pm 0.068 \pm 0.010$
A_FB	$-0.070 \pm 0.043 \pm 0.006$
S_7	$-0.066 \pm 0.065 \pm 0.004$
S_8	$0.016 \pm 0.074 \pm 0.002$
S_9	$-0.012 \pm 0.055 \pm 0.003$

$4.0 < q^2 < 6.0\,\mathrm{GeV}^2/c^4$	
F_L	$0.684 \pm 0.035 \pm 0.015$
S_3	$0.014 \pm 0.038 \pm 0.003$
S_4	$-0.145 \pm 0.057 \pm 0.004$
S_5	$-0.204 \pm 0.051 \pm 0.013$
A_FB	$0.050 \pm 0.033 \pm 0.002$
S_7	$-0.136 \pm 0.053 \pm 0.002$
S_8	$0.077 \pm 0.062 \pm 0.001$
S_9	$0.029 \pm 0.045 \pm 0.002$

$6.0 < q^2 < 8.0\,\mathrm{GeV}^2/c^4$	
F_L	$0.645 \pm 0.030 \pm 0.011$
S_3	$-0.013 \pm 0.038 \pm 0.004$
S_4	$-0.275 \pm 0.045 \pm 0.006$
S_5	$-0.279 \pm 0.043 \pm 0.013$
A_FB	$0.110 \pm 0.027 \pm 0.005$
S_7	$-0.074 \pm 0.046 \pm 0.003$
S_8	$-0.062 \pm 0.047 \pm 0.001$
S_9	$0.024 \pm 0.035 \pm 0.002$

$11.0 < q^2 < 12.5\,\mathrm{GeV}^2/c^4$	
F_L	$0.461 \pm 0.031 \pm 0.010$
S_3	$-0.124 \pm 0.037 \pm 0.003$
S_4	$-0.245 \pm 0.047 \pm 0.007$
S_5	$-0.310 \pm 0.043 \pm 0.011$
A_FB	$0.333 \pm 0.030 \pm 0.008$
S_7	$-0.096 \pm 0.050 \pm 0.003$
S_8	$0.009 \pm 0.049 \pm 0.001$
S_9	$0.042 \pm 0.040 \pm 0.003$

$15.0 < q^2 < 17.0\,\mathrm{GeV}^2/c^4$	
F_L	$0.352 \pm 0.026 \pm 0.009$
S_3	$-0.166 \pm 0.034 \pm 0.007$
S_4	$-0.299 \pm 0.033 \pm 0.008$
S_5	$-0.341 \pm 0.034 \pm 0.009$
A_FB	$0.385 \pm 0.024 \pm 0.007$
S_7	$0.029 \pm 0.039 \pm 0.001$
S_8	$0.003 \pm 0.042 \pm 0.002$
S_9	$0.000 \pm 0.037 \pm 0.002$

$17.0 < q^2 < 19.0\,\mathrm{GeV}^2/c^4$	
F_L	$0.344 \pm 0.032 \pm 0.025$
S_3	$-0.250 \pm 0.050 \pm 0.025$
S_4	$-0.307 \pm 0.041 \pm 0.008$
S_5	$-0.280 \pm 0.040 \pm 0.014$
A_FB	$0.323 \pm 0.032 \pm 0.019$
S_7	$0.049 \pm 0.049 \pm 0.007$
S_8	$-0.026 \pm 0.046 \pm 0.002$
S_9	$-0.056 \pm 0.045 \pm 0.002$

$1.1 < q^2 < 6.0\,\mathrm{GeV}^2/c^4$	
F_L	$0.700 \pm 0.025 \pm 0.013$
S_3	$-0.012 \pm 0.025 \pm 0.003$
S_4	$-0.136 \pm 0.039 \pm 0.003$
S_5	$-0.052 \pm 0.034 \pm 0.007$
A_FB	$-0.073 \pm 0.021 \pm 0.002$
S_7	$-0.090 \pm 0.034 \pm 0.002$
S_8	$-0.009 \pm 0.037 \pm 0.002$
S_9	$-0.025 \pm 0.026 \pm 0.002$

$15.0 < q^2 < 19.0\,\mathrm{GeV}^2/c^4$	
F_L	$0.345 \pm 0.020 \pm 0.007$
S_3	$-0.189 \pm 0.030 \pm 0.009$
S_4	$-0.303 \pm 0.024 \pm 0.008$
S_5	$-0.317 \pm 0.024 \pm 0.011$
A_FB	$0.353 \pm 0.020 \pm 0.010$
S_7	$0.035 \pm 0.030 \pm 0.003$
S_8	$0.005 \pm 0.031 \pm 0.001$
S_9	$-0.031 \pm 0.029 \pm 0.001$

Table 11.1: Results for the *CP*-averaged observables F_L, A_FB and S_3–S_9. The first uncertainties are statistical and the second systematic.

$0.10 < q^2 < 0.98\,\mathrm{GeV}^2/c^4$		$1.1 < q^2 < 2.5\,\mathrm{GeV}^2/c^4$		$2.5 < q^2 < 4.0\,\mathrm{GeV}^2/c^4$	
P_1	$0.090 \pm 0.119 \pm 0.009$	P_1	$-0.617 \pm 0.296 \pm 0.023$	P_1	$0.168 \pm 0.371 \pm 0.043$
P_2	$-0.003 \pm 0.038 \pm 0.003$	P_2	$-0.443 \pm 0.100 \pm 0.027$	P_2	$-0.191 \pm 0.116 \pm 0.043$
P_3	$0.073 \pm 0.057 \pm 0.003$	P_3	$0.324 \pm 0.147 \pm 0.014$	P_3	$0.049 \pm 0.195 \pm 0.014$
P_4'	$0.135 \pm 0.118 \pm 0.010$	P_4'	$-0.080 \pm 0.142 \pm 0.019$	P_4'	$-0.435 \pm 0.169 \pm 0.035$
P_5'	$0.521 \pm 0.095 \pm 0.024$	P_5'	$0.365 \pm 0.122 \pm 0.013$	P_5'	$-0.150 \pm 0.144 \pm 0.032$
P_6'	$0.015 \pm 0.094 \pm 0.007$	P_6'	$-0.226 \pm 0.128 \pm 0.005$	P_6'	$-0.155 \pm 0.148 \pm 0.024$
P_8'	$-0.007 \pm 0.122 \pm 0.002$	P_8'	$-0.366 \pm 0.158 \pm 0.005$	P_8'	$0.037 \pm 0.169 \pm 0.007$

$4.0 < q^2 < 6.0\,\mathrm{GeV}^2/c^4$		$6.0 < q^2 < 8.0\,\mathrm{GeV}^2/c^4$		$11.0 < q^2 < 12.5\,\mathrm{GeV}^2/c^4$	
P_1	$0.088 \pm 0.235 \pm 0.029$	P_1	$-0.071 \pm 0.211 \pm 0.020$	P_1	$-0.460 \pm 0.132 \pm 0.015$
P_2	$0.105 \pm 0.068 \pm 0.009$	P_2	$0.207 \pm 0.048 \pm 0.013$	P_2	$0.411 \pm 0.033 \pm 0.008$
P_3	$-0.090 \pm 0.139 \pm 0.006$	P_3	$-0.068 \pm 0.104 \pm 0.007$	P_3	$-0.078 \pm 0.077 \pm 0.007$
P_4'	$-0.312 \pm 0.115 \pm 0.013$	P_4'	$-0.574 \pm 0.091 \pm 0.018$	P_4'	$-0.491 \pm 0.095 \pm 0.013$
P_5'	$-0.439 \pm 0.111 \pm 0.036$	P_5'	$-0.583 \pm 0.090 \pm 0.030$	P_5'	$-0.622 \pm 0.088 \pm 0.017$
P_6'	$-0.293 \pm 0.117 \pm 0.004$	P_6'	$-0.155 \pm 0.098 \pm 0.009$	P_6'	$-0.193 \pm 0.100 \pm 0.003$
P_8'	$0.166 \pm 0.127 \pm 0.004$	P_8'	$-0.129 \pm 0.098 \pm 0.005$	P_8'	$0.018 \pm 0.099 \pm 0.009$

$15.0 < q^2 < 17.0\,\mathrm{GeV}^2/c^4$		$17.0 < q^2 < 19.0\,\mathrm{GeV}^2/c^4$		$1.1 < q^2 < 6.0\,\mathrm{GeV}^2/c^4$	
P_1	$-0.511 \pm 0.096 \pm 0.020$	P_1	$-0.763 \pm 0.152 \pm 0.094$	P_1	$-0.079 \pm 0.159 \pm 0.021$
P_2	$0.396 \pm 0.022 \pm 0.004$	P_2	$0.328 \pm 0.032 \pm 0.017$	P_2	$-0.162 \pm 0.050 \pm 0.012$
P_3	$-0.000 \pm 0.056 \pm 0.003$	P_3	$0.085 \pm 0.068 \pm 0.004$	P_3	$0.085 \pm 0.090 \pm 0.005$
P_4'	$-0.626 \pm 0.069 \pm 0.018$	P_4'	$-0.647 \pm 0.086 \pm 0.057$	P_4'	$-0.298 \pm 0.087 \pm 0.016$
P_5'	$-0.714 \pm 0.074 \pm 0.021$	P_5'	$-0.590 \pm 0.084 \pm 0.059$	P_5'	$-0.114 \pm 0.068 \pm 0.026$
P_6'	$0.061 \pm 0.085 \pm 0.003$	P_6'	$0.103 \pm 0.105 \pm 0.016$	P_6'	$-0.197 \pm 0.075 \pm 0.009$
P_8'	$0.007 \pm 0.086 \pm 0.002$	P_8'	$-0.055 \pm 0.099 \pm 0.006$	P_8'	$-0.020 \pm 0.089 \pm 0.009$

$15.0 < q^2 < 19.0\,\mathrm{GeV}^2/c^4$	
P_1	$-0.577 \pm 0.090 \pm 0.031$
P_2	$0.359 \pm 0.018 \pm 0.009$
P_3	$0.048 \pm 0.045 \pm 0.002$
P_4'	$-0.638 \pm 0.055 \pm 0.020$
P_5'	$-0.667 \pm 0.053 \pm 0.029$
P_6'	$0.073 \pm 0.067 \pm 0.006$
P_8'	$0.011 \pm 0.069 \pm 0.003$

Table 11.2: Results for the optimised observables $P_i^{(\prime)}$. The first uncertainties are statistical and the second systematic.

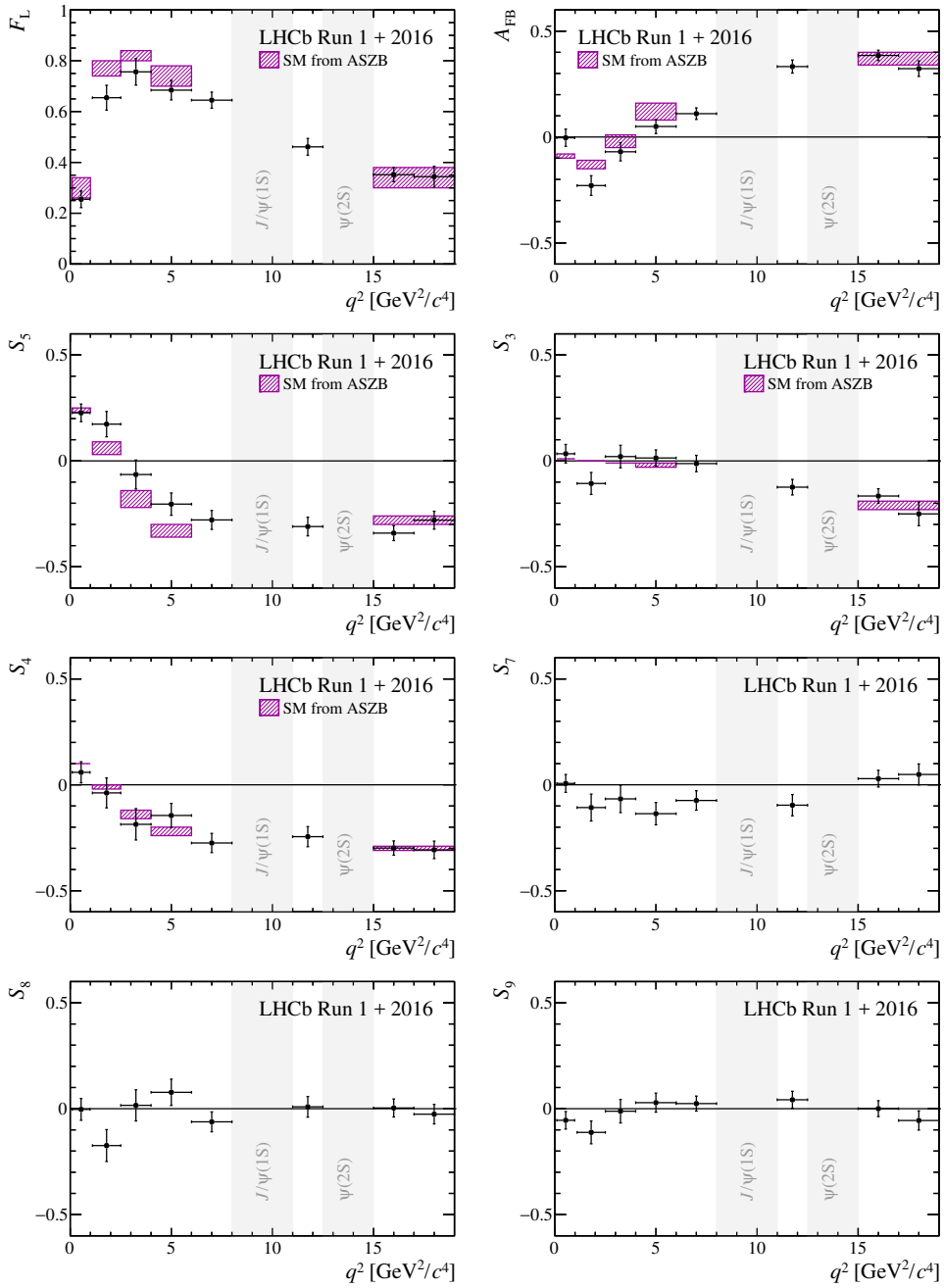


Figure 11.3: Results of the fits for the *CP*-averaged angular observables. The data are compared to SM predictions based on the prescription of Refs. [77, 146]. Figure taken from Ref. [1].

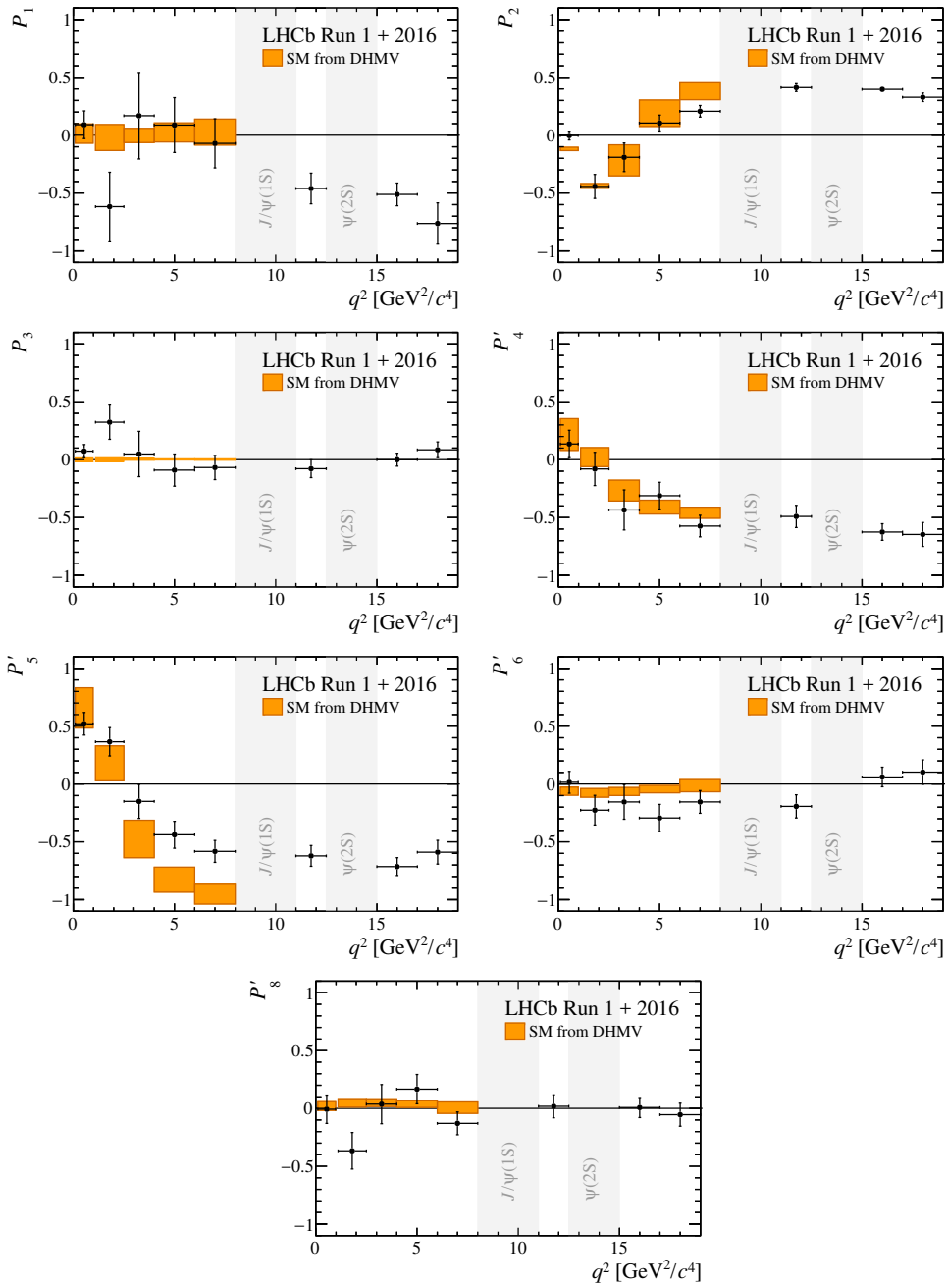


Figure 11.4: Results of the fits for the optimised angular observables in bins of dimuon invariant mass squared, q^2. The data are compared to SM predictions based on Refs. [73, 78]. Figure taken from Ref. [1].

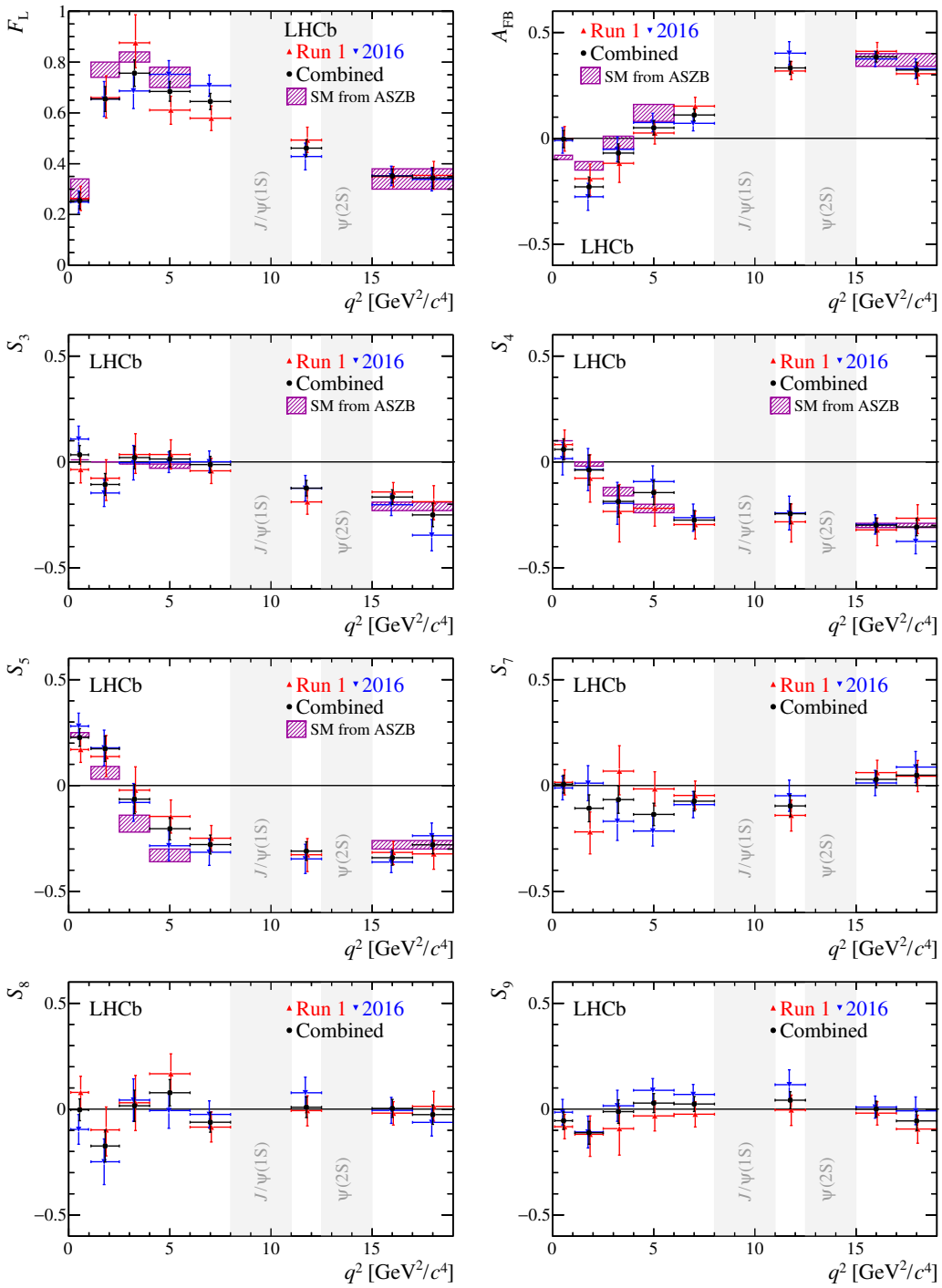


Figure 11.5: Results for the *CP*-averaged angular observables $F_{\rm L}$, $A_{\rm FB}$ and S_3–S_9 in bins of q^2 compared to the Run 1 results from the previous analysis [2], as well as the individual fit results for the 2016 data. The data are compared to SM predictions based on the prescription of Refs. [77, 146]. These figures are for illustrative purposes only, as the results shown for the 2016 data are not coverage- and bias-corrected, and the error bars do not include systematic uncertainties. Figure taken from Ref. [1].

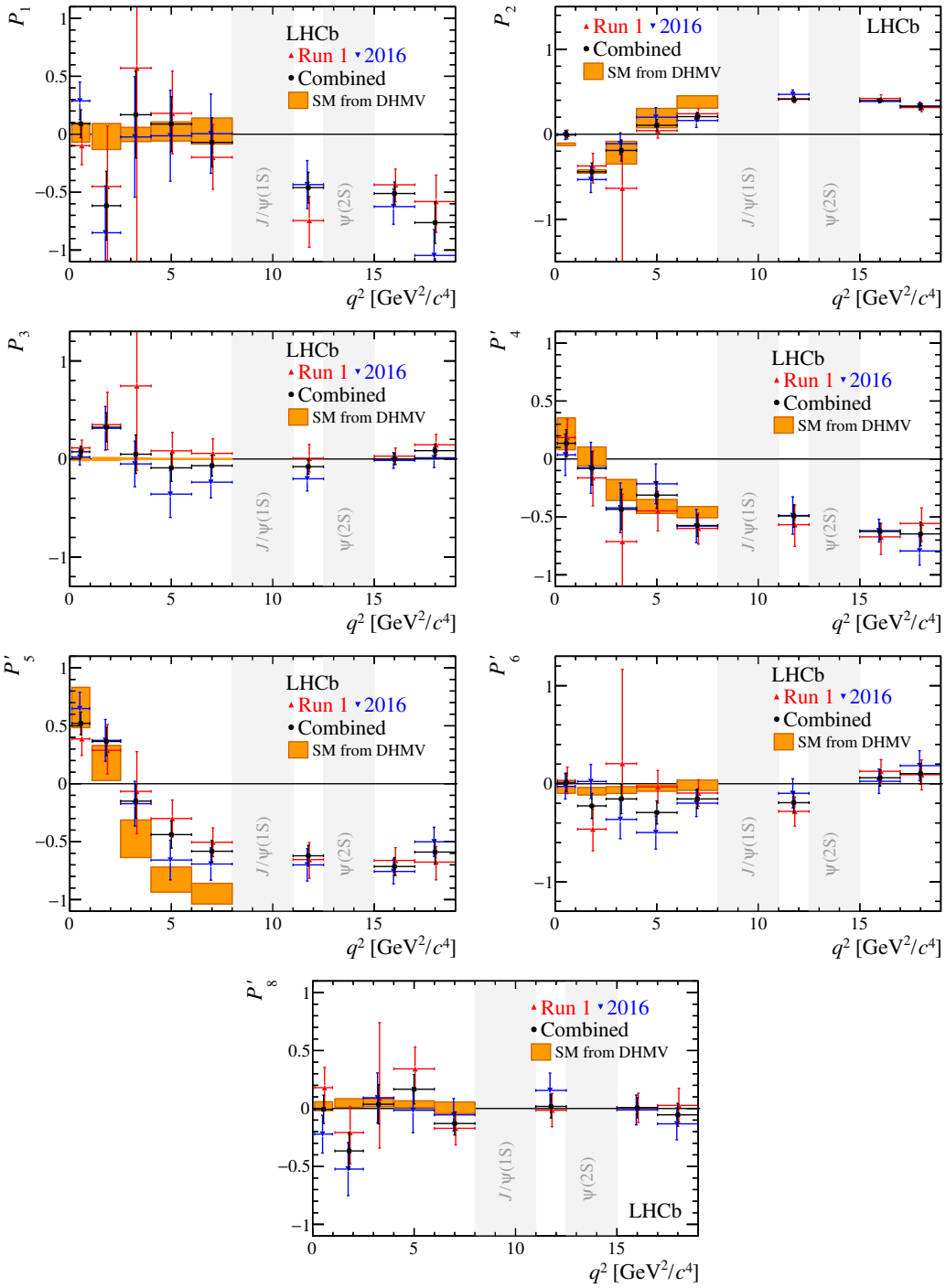


Figure 11.6: Results for the optimised angular observables P_1–P_3 and P'_4–P'_8 in bins of q^2 compared to the Run 1 results from the previous analysis [2], as well as the individual fit results for the 2016 data. The data are compared to SM predictions based on Refs. [73, 78]. These figures are for illustrative purposes only, as the results shown for the 2016 data are not coverage- and bias-corrected, and the error bars do not include systematic uncertainties. Figure taken from Ref. [1].

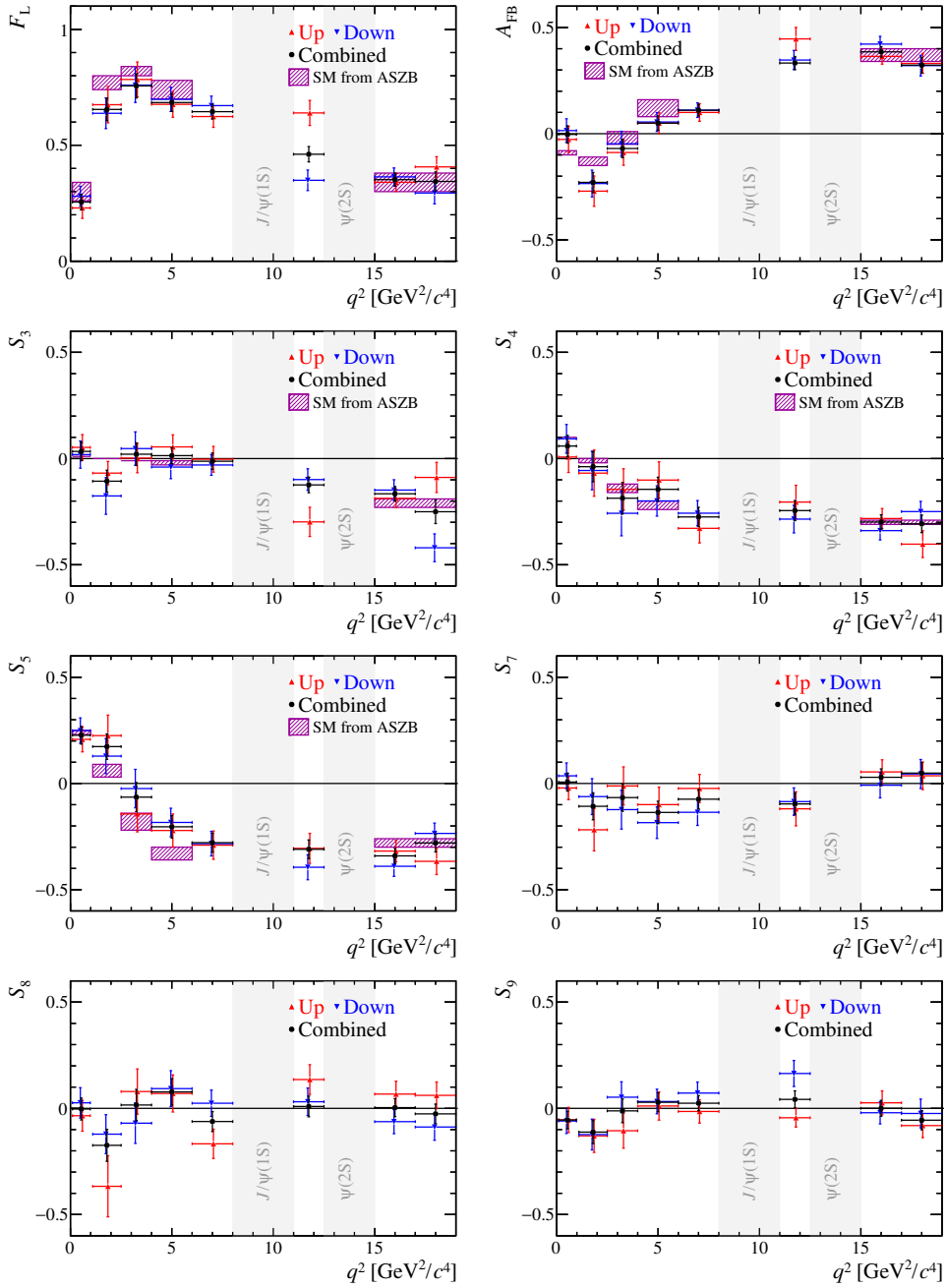


Figure 11.7: Results for the *CP*-averaged angular observables $F_{\rm L}$, $A_{\rm FB}$ and S_3–S_9 in bins of q^2 compared to the results of the fits to the individual data sets corresponding to the two polarities of the magnet (Up and Down). The data are compared to SM predictions based on the prescription of Refs. [77, 146]. These figures are for illustrative purposes only, as the results shown for the separate polarity data sets are not coverage- and bias-corrected, and the error bars do not include systematic uncertainties.

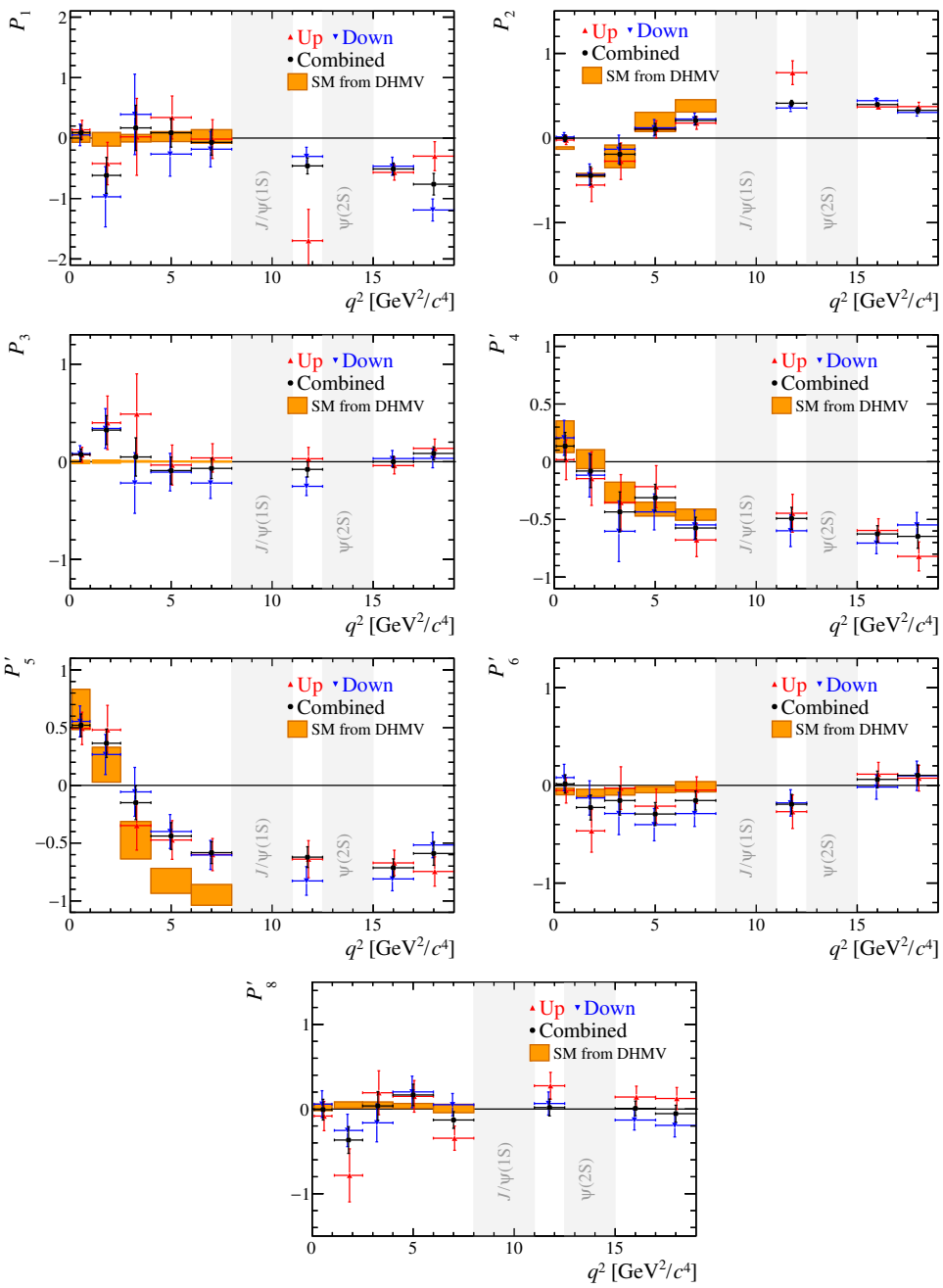


Figure 11.8: Results for the optimised angular observables P_1–P_3 and P'_4–P'_8 in bins of q^2 compared to the results of the fits to the individual data sets corresponding to the two polarities of the magnet (Up and Down). The data are compared to SM predictions based on Refs. [73, 78]. These figures are for illustrative purposes only, as the results shown for the separate polarity data sets are not coverage- and bias-corrected, and the error bars do not include systematic uncertainties.

12. Interpretation of results

In Chpt. 11 the measurements of the individual angular observables were compared to their theoretical predictions. However, this is insufficient to understand the compatibility with the SM, as the individual observables are correlated. A fit to the results of the complete set of observables is therefore performed using the FLAVIO software package [149] and varying the Wilson coefficients $\mathcal{R}e(C_9)$ and $\mathcal{R}e(C_{10})$. Throughout this chapter the default FLAVIO SM nuisance parameters, including form-factor parameters and subleading corrections are used. The latter account for long-distance QCD interference effects with the charmonium decay modes [77, 146].

As a first step, likelihood scans of $\Delta\mathcal{R}e(C_9)$, the shift of $\mathcal{R}e(C_9)$ from its SM value, are obtained using the results of the *CP*-averaged angular observables for Run 1 only, 2016 only and the combined data set. The q^2 bins included in the scans are the narrow q^2 bins in the ranges $0.10 < q^2 < 0.98\,\text{GeV}^2/c^4$ and $1.1 < q^2 < 8.0\,\text{GeV}^2/c^4$, and the wide q^2 bin $15.0 < q^2 < 19.0\,\text{GeV}^2/c^4$. The likelihood profiles are shown in Fig. 12.1 and the minima for Run 1, 2016 and the combined data set are found to be at $\Delta\mathcal{R}e(C_9) = -1.04^{+0.28}_{-0.24}$, $\Delta\mathcal{R}e(C_9) = -0.89^{+0.28}_{-0.24}$ and $\Delta\mathcal{R}e(C_9) = -0.99^{+0.25}_{-0.22}$ respectively[a]. The discrepancies with respect to the SM are found to be $3.0\,\sigma$, $2.7\,\sigma$ and $3.3\,\sigma$ for Run 1, 2016 and the combined data set respectively. Note that the results for the 2016 data set have been obtained with values of the *CP*-averaged angular observables that are not coverage- and bias-corrected and that do not include systematic uncertainties[b]. Furthermore, the observed tensions will depend on the Wilson coefficients varied, how the SM nuisance parameters are treated and which q^2 bins are included in the fit. In particular the $6.0 < q^2 < 8.0\,\text{GeV}^2/c^4$ bin should be treated with caution due to its proximity to the charmonium resonances. Repeating the fits without this bin results in tensions with the SM at the level of $2.5\,\sigma$, $2.1\,\sigma$ and $2.7\,\sigma$ using the results of the Run 1, 2016 and combined data sets respectively.

A further study of the *CP*-averaged angular observables can be performed by varying both $\mathcal{R}e(C_9)$ and $\mathcal{R}e(C_{10})$. Again, the narrow q^2 bins in the ranges $0.10 < q^2 < 0.98\,\text{GeV}^2/c^4$ and $1.1 < q^2 < 8.0\,\text{GeV}^2/c^4$ and the wide q^2 bin

[a] The naive scaling of the uncertainties by the factor $1/\sqrt{2}$ for the combined data set does not occur as the theory uncertainties start to dominate in the fit.

[b] The individual results of the fits to the 2016 data set were not coverage- and bias-corrected, as this would have required the Feldman-Cousins method. This would have resulted in very high computational requirements. The systematic uncertainties were also not included due to high computational requirements.

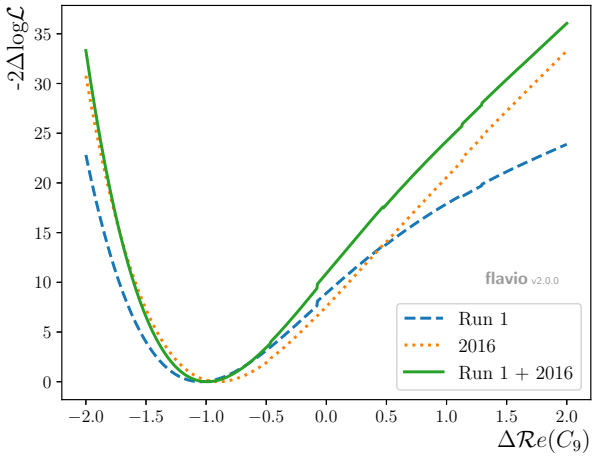


Figure 12.1: Likelihood scan of $\Delta\mathcal{R}e(C_9)$ using the results of the *CP*-averaged angular observables for Run 1 only (blue dashed), 2016 only (orange dotted) and the combined data set (solid green). The result for the 2016 data set is shown for illustrative purposes only, as the *CP*-averaged angular observables are not coverage- and bias-corrected, and do not include systematic uncertainties.

$15.0 < q^2 < 19.0\,\mathrm{GeV}^2/c^4$ are included in the fit. The contour plots obtained by fitting to the results of the observables of the different data sets are shown in Fig. 12.2. As already observed in Figs. 11.5, 11.6 and 12.1, the compatibility between the Run 1 and 2016 data sets is extremely good. Furthermore, due to varying two Wilson coefficients, the tensions with the SM decrease to $2.6\,\sigma$, $2.5\,\sigma$ and $3.0\,\sigma$ for Run 1, 2016 and the combined data set respectively.

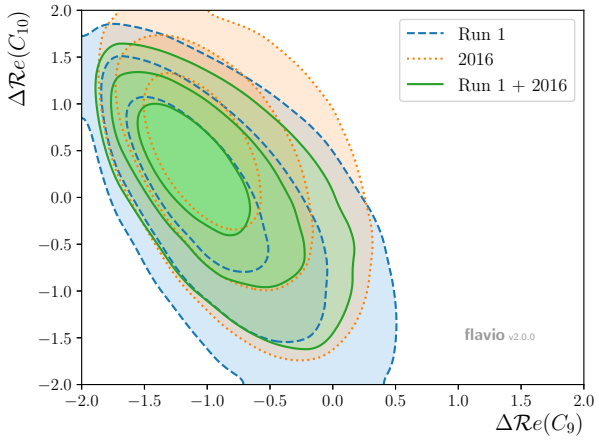


Figure 12.2: Fit to $\Delta\mathcal{R}e(C_9)$ and $\Delta\mathcal{R}e(C_{10})$, the shift in the values of $\mathcal{R}e(C_9)$ and $\mathcal{R}e(C_{10})$ from their SM values, using the results of the *CP*-averaged angular observables for Run 1, 2016 and the combined data set. The SM point lies at the origin. The lines show the $1, 2$ and $3\,\sigma$ contours of the fit to all angular observables. The contour plot obtained by fitting to the *CP*-averaged angular observables of the 2016 data set is shown for illustrative purposes only, as the *CP*-averaged angular observables are not coverage- and bias-corrected, and do not include systematic uncertainties.

It is also of interest to investigate the compatibility of the eight angular observables within the different data sets. This can be illustrated with contour plots in the 2D $\mathcal{R}e(C_9)/\mathcal{R}e(C_{10})$ plane for each of the *CP*-averaged observables separately, as shown in Fig. 12.3. While the agreement between the different angular observables is good for all three data sets, the coherence between the observables in the 2016 plot is the most striking. This gives insight into why the results of the FLAVIO fits to the values of the angular observables of the 2016 data set give very similar results to the corresponding fits of the Run 1 data set. Naively, one might have expected the discrepancy with the SM to be smaller for the 2016 data set due to the better agreement between the SM predictions and the measurements of the A_{FB} and P_5' observables, as shown in Figs. 11.5 and 11.6. However, due to the consistent picture across the angular observables, the tension remains. Finally, this also improves the coherence of the simultaneous fit results to the Run 1 and 2016 data sets. This is confirmed by comparing the measurements of the F_{L}, A_{FB} and S_5 observables with the $\Delta\mathcal{R}e(C_9) = -1$ NP physics scenario, as shown in Fig. 12.4. An impressive agreement is seen between the NP scenario and the measurements of the angular observables obtained by the simultaneous fit. Adding the 2016 data set to the analysis does therefore not only result in a mild increase in the tension with the SM in the scenarios investigated, but also leads to a much more coherent picture in the context of NP models.

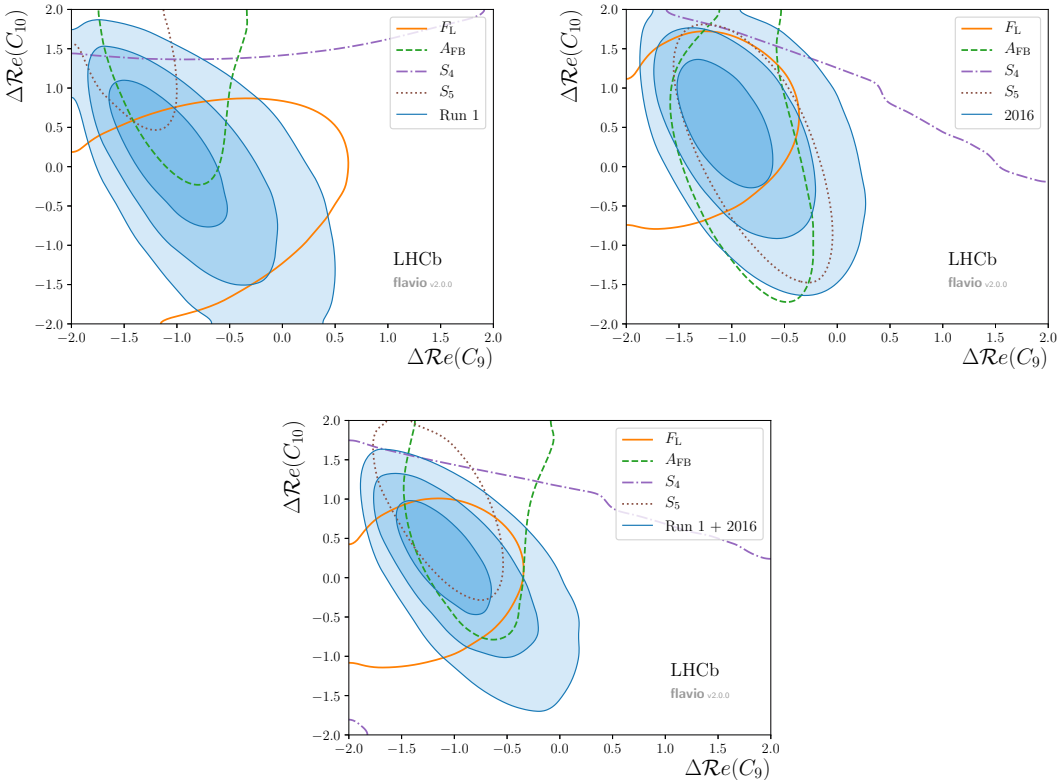


Figure 12.3: Fits to $\Delta\mathcal{R}e(C_9)$ and $\Delta\mathcal{R}e(C_{10})$, the shift in the values of $\mathcal{R}e(C_9)$ and $\mathcal{R}e(C_{10})$ from their SM values, using the results of the *CP*-averaged angular observables for Run 1, 2016 and the combined data set. The SM point lies at the origin. The blue lines show the $1, 2$ and $3\,\sigma$ contours of the fit to all angular observables. The other coloured lines show the 1σ contours of the fits to the individual angular observables. The angular observables that are not shown have 1σ contours which extend beyond the range of the plots. The area below the S_4 line is the one that is favoured. The contour plot obtained by fitting to the *CP*-averaged angular observables of the 2016 data set is shown for illustrative purposes only, as the *CP*-averaged angular observables are not coverage- and bias-corrected, and do not include systematic uncertainties. Figure taken from Ref. [1].

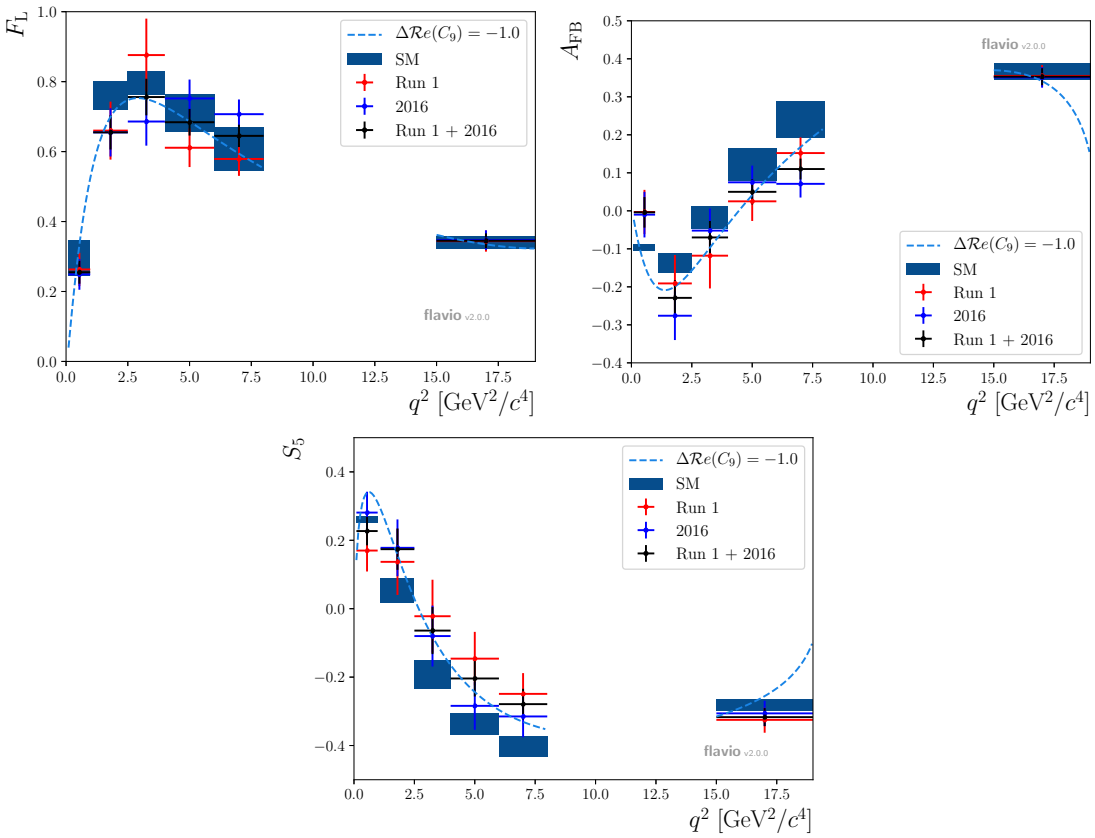


Figure 12.4: Observable measurements of F_L, A_{FB} and S_5 compared with their SM predictions and with predictions that shift the effective coupling $\mathcal{R}e(C_9)$ by -1.0. All predictions are obtained using the FLAVIO software package [149].

13. Conclusion and outlook

This thesis presents an angular analysis of the $B^0 \to K^{*0}\mu^+\mu^-$ decay using data collected with the LHCb detector during 2011, 2012 and 2016. The resulting angular observables are the most precise to date, reducing the uncertainty of the previously measured observables by approximately 30%. The local discrepancy with SM predictions in the P_5' variable persists, and fits to the complete set of observables using the FLAVIO software package even indicate a slight increase in the overall tension. The precise level of the discrepancy depends on the choice of theory nuisance parameters and the corresponding theoretical uncertainties. In particular, the uncertainties related to the charmonium resonance contributions are still the subject of intense discussions. Despite this ongoing debate, two observations can be made. First, the contour plots of the different angular observables in the 2D $\mathcal{R}e(C_9)/\mathcal{R}e(C_{10})$ plane agree extremely well. Secondly, the coherence between the predictions of a $\Delta\mathcal{R}e(C_9) = -1$ NP physics scenario and the measurements of the individual observables is clearly improved compared to the previous LHCb measurements. Experimentally, the large number of signal events allows for several cross-checks on subsets of the data. Excellent agreement is observed between the individual 2011/2012 and 2016 results, as well as between the two data sets corresponding to the polarities of the LHCb magnet.

Looking into the future, several analyses are under way, which will further investigate the $B^0 \to K^{*0}\mu^+\mu^-$ decay. Simply adding the 2017 and 2018 data sets will result in an additional 3.8 fb^{-1} of pp collision data at a centre-of-mass energy of 13 TeV. This will further reduce the statistical uncertainty on the angular observables by approximately 30%. Furthermore, new analysis techniques can be employed to take into account some of the theory uncertainties by directly including the charmonium resonance decays in the angular fit. This has already been done in the the case of the $B^+ \to K^+\mu^+\mu^-$ decay in Ref. [150], and a similar approach can be used in the case of the $B^0 \to K^{*0}\mu^+\mu^-$ decay.

In the broader context of $b \to s\ell^+\ell^-$ decays, updates to the measurements of the lepton flavour universality ratios of the R_K and R_{K^*} observables are highly anticipated. The last updates to these ratios have included approximately a half and a quarter of the recorded LHCb events for the R_K and R_{K^*} measurements respectively. As both of the measurements are statistically dominated, future analysis with the full Run 1 and Run 2 data sets will be of significant interest.

In addition, the Belle II detector begun taking data in 2019, which will provide

unprecedented opportunities to perform and double check the $b \to s\ell^+\ell^-$ measurements of the LHCb detector and also to give access to new channels, such as those including τ leptons in their final states. The next years will therefore be decisive in solving the mysteries surrounding $b \to s\ell^+\ell^-$ decays and will hopefully shed light on whether NP has been observed in the $B^0 \to K^{*0}\mu^+\mu^-$ decay.

Bibliography

[1] LHCb collaboration, R. Aaij *et al.*, *Measurement of CP-averaged observables in the $B^0 \to K^{*0}\mu^+\mu^-$ decay*, arXiv:2003.04831, to appear in Phys. Rev. Lett.

[2] LHCb collaboration, R. Aaij *et al.*, *Angular analysis of the $B^0 \to K^{*0}\mu^+\mu^-$ decay using $3\,fb^{-1}$ of integrated luminosity*, JHEP **02** (2016) 104, arXiv:1512.04442.

[3] D. Hanneke, S. Fogwell, and G. Gabrielse, *New measurement of the electron magnetic moment and the fine structure constant*, Phys. Rev. Lett. **100** (2008) .

[4] T. Aoyama, T. Kinoshita, and M. Nio, *Theory of the anomalous magnetic moment of the electron*, Atoms **7** (2019), no. 1 28.

[5] M. Schumann, *Dark Matter 2014*, EPJ Web Conf. **96** (2015) 01027, arXiv:1501.01200.

[6] Planck collaboration, P. A. R. Ade *et al.*, *Planck 2013 results. XVI. Cosmological parameters*, Astron. Astrophys. **571** (2014) A16, arXiv:1303.5076.

[7] J. M. Cline, *Baryogenesis*, in *Les Houches Summer School - Session 86: Particle Physics and Cosmology: The Fabric of Spacetime*, 9, 2006. arXiv:hep-ph/0609145.

[8] P. Huet and E. Sather, *Electroweak baryogenesis and standard model CP violation*, Phys. Rev. D **51** (1995) 379, arXiv:hep-ph/9404302.

[9] ATLAS collaboration, G. Aad *et al.*, *Observation of a new particle in the search for the Standard Model Higgs boson with the ATLAS detector at the LHC*, Phys. Lett. B **716** (2012) 1, arXiv:1207.7214.

[10] CMS collaboration, S. Chatrchyan *et al.*, *Observation of a New Boson at a Mass of 125 GeV with the CMS Experiment at the LHC*, Phys. Lett. B **716** (2012) 30, arXiv:1207.7235.

[11] R. D. Stutzke *et al.*, *Search for the decay ${K_S}^0 \to \mu^+\mu^-$*, Phys. Rev. **177** (1969) 2009.

[12] S. L. Glashow, J. Iliopoulos, and L. Maiani, *Weak interactions with lepton-hadron symmetry*, Phys. Rev. D **2** (1970) 1285.

[13] J. J. Aubert *et al.*, *Experimental observation of a heavy particle J*, Phys. Rev. Lett. **33** (1974) 1404.

[14] J.-E. Augustin *et al.*, *Discovery of a narrow resonance in e^+e^- annihilation*, Phys. Rev. Lett. **33** (1974) 1406.

[15] CMS collaboration, A. M. Sirunyan *et al.*, *Measurement of angular parameters from the decay $B^0 \to K^{*0}\mu^+\mu^-$ in proton-proton collisions at $\sqrt{s} = 8$ TeV*, Phys. Lett. **B781** (2018) 517, arXiv:1710.02846.

[16] ATLAS collaboration, M. Aaboud *et al.*, *Angular analysis of $B^0_d \to K^*\mu^+\mu^-$ decays in pp collisions at $\sqrt{s} = 8$ TeV with the ATLAS detector*, JHEP **10** (2018) 047, arXiv:1805.04000.

[17] Belle collaboration, S. Wehle *et al.*, *Lepton-flavor-dependent angular analysis of $B \to K^*\ell^+\ell^-$*, Phys. Rev. Lett. **118** (2017) 111801, arXiv:1612.05014.

[18] BaBar collaboration, B. Aubert *et al.*, *Measurements of branching fractions, rate asymmetries, and angular distributions in the rare decays $B \to K\ell^+\ell^-$ and $B \to K^*\ell^+\ell^-$*, Phys. Rev. **D73** (2006) 092001, arXiv:hep-ex/0604007.

[19] CDF collaboration, T. Aaltonen *et al.*, *Measurements of the angular distributions in the decays $B \to K^{(*)}\mu^+\mu^-$ at CDF*, Phys. Rev. Lett. **108** (2012) 081807, arXiv:1108.0695.

[20] LHCb collaboration, R. Aaij *et al.*, *Angular moments of the decay $\Lambda^0_b \to \Lambda\mu^+\mu^-$ at low hadronic recoil*, JHEP **09** (2018) 146, arXiv:1808.00264.

[21] LHCb collaboration, R. Aaij *et al.*, *Angular analysis and differential branching fraction of the decay $B^0_s \to \phi\mu^+\mu^-$*, JHEP **09** (2015) 179, arXiv:1506.08777.

[22] LHCb collaboration, R. Aaij *et al.*, *Measurements of the S-wave fraction in $B^0 \to K^+\pi^-\mu^+\mu^-$ decays and the $B^0 \to K^*(892)^0\mu^+\mu^-$ differential branching fraction*, JHEP **11** (2016) 047, Erratum ibid. **04** (2017) 142, arXiv:1606.04731.

[23] LHCb collaboration, R. Aaij *et al.*, *Differential branching fraction and angular analysis of $\Lambda^0_b \to \Lambda\mu^+\mu^-$ decays*, JHEP **06** (2015) 115, Erratum ibid. **09** (2018) 145, arXiv:1503.07138.

[24] LHCb collaboration, R. Aaij *et al.*, *Differential branching fractions and isospin asymmetries of $B \to K^{(*)}\mu^+\mu^-$ decays*, JHEP **06** (2014) 133, arXiv:1403.8044.

[25] LHCb collaboration, R. Aaij *et al.*, *Test of lepton universality using $\Lambda_b^0 \to pK^-\ell^+\ell^-$ decays*, JHEP **05** (2020) 040, arXiv:1912.08139.

[26] LHCb collaboration, R. Aaij *et al.*, *Search for lepton-universality violation in $B^+ \to K^+\ell^+\ell^-$ decays*, Phys. Rev. Lett. **122** (2019) 191801, arXiv:1903.09252.

[27] Belle collaboration, A. Abdesselam *et al.*, *Test of lepton flavor universality in $B \to K\ell^+\ell^-$ decays*, arXiv:1908.01848.

[28] BaBar collaboration, J. P. Lees *et al.*, *Measurement of branching fractions and rate asymmetries in the rare decays $B \to K^{(*)}\ell^+\ell^-$*, Phys. Rev. **D86** (2012) 032012, arXiv:1204.3933.

[29] LHCb collaboration, R. Aaij *et al.*, *Test of lepton universality with $B^0 \to K^{*0}\ell^+\ell^-$ decays*, JHEP **08** (2017) 055, arXiv:1705.05802.

[30] Belle collaboration, A. Abdesselam *et al.*, *Test of lepton flavor universality in $B \to K^*\ell^+\ell^-$ decays at Belle*, arXiv:1904.02440.

[31] M. Algueró *et al.*, *Emerging patterns of new physics with and without Lepton flavour universal contributions*, Eur. Phys. J. **C79** (2019), no. 8 714, arXiv:1903.09578.

[32] J. Aebischer *et al.*, *B-decay discrepancies after Moriond 2019*, arXiv:1903.10434.

[33] A. Arbey *et al.*, *Update on the $b \to s$ anomalies*, Phys. Rev. **D100** (2019), no. 1 015045, arXiv:1904.08399.

[34] M. Ciuchini *et al.*, *New physics in $b \to s\ell^+\ell^-$ confronts new data on lepton universality*, Eur. Phys. J. **C79** (2019), no. 8 719, arXiv:1903.09632.

[35] K. Kowalska, D. Kumar, and E. M. Sessolo, *Implications for new physics in $b \to s\mu\mu$ transitions after recent measurements by Belle and LHCb*, Eur. Phys. J. **C79** (2019), no. 10 840, arXiv:1903.10932.

[36] W. Altmannshofer, S. Gori, M. Pospelov, and I. Yavin, *Quark flavor transitions in $L_\mu - L_\tau$ models*, Phys. Rev. **D89** (2014) 095033, arXiv:1403.1269.

[37] A. Celis, J. Fuentes-Martín, M. Jung, and H. Serôdio, *Family nonuniversal Z' models with protected flavor-changing interactions*, Phys. Rev. **D92** (2015) 015007, arXiv:1505.03079.

[38] A. Falkowski, M. Nardecchia, and R. Ziegler, *Lepton flavor non-universality in B-meson decays from a $U(2)$ flavor model*, JHEP **11** (2015) 173, arXiv:1509.01249.

[39] G. Hiller and M. Schmaltz, *R_K and future $b \to s\ell\ell$ physics beyond the standard model opportunities*, Phys. Rev. **D90** (2014) 054014, arXiv:1408.1627.

[40] B. Gripaios, M. Nardecchia, and S. A. Renner, *Composite leptoquarks and anomalies in B-meson decays*, JHEP **05** (2015) 006, arXiv:1412.1791.

[41] I. de Medeiros Varzielas and G. Hiller, *Clues for flavor from rare lepton and quark decays*, JHEP **06** (2015) 072, arXiv:1503.01084.

[42] R. Barbieri, C. W. Murphy, and F. Senia, *B-decay anomalies in a composite leptoquark model*, Eur. Phys. J. **C77** (2017) 8, arXiv:1611.04930.

[43] G. Hiller, D. Loose, and I. Nišandžić, *Flavorful leptoquarks at hadron colliders*, Phys. Rev. **D97** (2018), no. 7 075004, arXiv:1801.09399.

[44] A. Crivellin, D. Müller, and T. Ota, *Simultaneous explanation of $R(D^{(*)})$ and $b \to s\mu^+\mu^-$: the last scalar leptoquarks standing*, JHEP **09** (2017) 040, arXiv:1703.09226.

[45] F. Sala and D. M. Straub, *A new light particle in B decays?*, Phys. Lett. **B774** (2017) 205209.

[46] P. Ko, Y. Omura, Y. Shigekami, and C. Yu, *LHCb anomaly and B physics in flavored $Z^{'}$ models with flavored Higgs doublets*, Phys. Rev. **D95** (2017) 115040.

[47] M. D. Schwartz, *Quantum Field Theory and the Standard Model*, Cambridge University Press, 2014.

[48] M. Thomson, *Modern particle physics*, Cambridge University Press, New York, 2013.

[49] M. E. Peskin and D. V. Schroeder, *An Introduction to quantum field theory*, Addison-Wesley, Reading, USA, 1995.

[50] Particle Data Group, C. Patrignani *et al.*, *Review of particle physics*, Chin. Phys. **C40** (2016) 100001.

[51] T. Humair, *Testing lepton universality in penguin decays of beauty mesons using the LHCb detector*, CERN-THESIS-2019-044.

[52] S. L. Glashow, *Partial Symmetries of Weak Interactions*, Nucl. Phys. **22** (1961) 579.

[53] S. Weinberg, *A Model of Leptons*, Phys. Rev. Lett. **19** (1967) 1264.

[54] A. Salam and J. C. Ward, *Electromagnetic and weak interactions*, Phys. Lett. **13** (1964) 168.

[55] P. W. Higgs, *Broken Symmetries and the Masses of Gauge Bosons*, Phys. Rev. Lett. **13** (1964) 508.

[56] F. Englert and R. Brout, *Broken Symmetry and the Mass of Gauge Vector Mesons*, Phys. Rev. Lett. **13** (1964) 321.

[57] N. Cabibbo, *Unitary symmetry and leptonic decays*, Phys. Rev. Lett. **10** (1963) 531.

[58] M. Kobayashi and T. Maskawa, *CP-Violation in the Renormalizable Theory of Weak Interaction*, Progress of Theoretical Physics **49** (1973) 652, arXiv:https://academic.oup.com/ptp/article-pdf/49/2/652/5257692/49-2-652.pdf.

[59] L.-L. Chau and W.-Y. Keung, *Comments on the parametrization of the kobayashi-maskawa matrix*, Phys. Rev. Lett. **53** (1984) 1802.

[60] L. Wolfenstein, *Parametrization of the kobayashi-maskawa matrix*, Phys. Rev. Lett. **51** (1983) 1945.

[61] H. Georgi, *Effective field theory*, Ann. Rev. Nucl. Part. Sci. **43** (1993) 209.

[62] T. Blake, T. Gershon, and G. Hiller, *Rare b hadron decays at the LHC*, Ann. Rev. Nucl. Part. Sci. **65** (2015) 113, arXiv:1501.03309.

[63] LHCb collaboration, R. Aaij *et al.*, *Measurement of CP asymmetries in the decays* $B^0 \to K^{*0}\mu^+\mu^-$ *and* $B^+ \to K^+\mu^+\mu^-$, JHEP **09** (2014) 177, arXiv:1408.0978.

[64] W. Altmannshofer *et al.*, *Symmetries and Asymmetries of* $B^0 \to K^{*0}\mu^+\mu^-$ *Decays in the Standard Model and Beyond*, JHEP **01** (2009) 019, arXiv:0811.1214.

[65] C. Bobeth, G. Hiller, and G. Piranishvili, *CP Asymmetries in bar $B \to \bar{K}^*(\to \bar{K}\pi)\bar{\ell}\ell$ and Untagged $\bar{B}_s$, $B_s \to \phi(\to K^+K^-)\bar{\ell}\ell$ Decays at NLO*, JHEP **07** (2008) 106, arXiv:0805.2525.

[66] LHCb collaboration, R. Aaij *et al.*, *Measurement of form-factor-independent observables in the decay $B^0 \to K^{*0}\mu^+\mu^-$*, Phys. Rev. Lett. **111** (2013) 191801, arXiv:1308.1707.

[67] LHCb collaboration, R. Aaij *et al.*, *Differential branching fraction and angular analysis of the decay $B^0 \to K^{*0}\mu^+\mu^-$*, JHEP **08** (2013) 131, arXiv:1304.6325.

[68] S. Descotes-Genon, J. Matias, M. Ramon, and J. Virto, *Implications from clean observables for the binned analysis of $B \to K^*\mu^+\mu^-$ at large recoil*, JHEP **01** (2013) 048, arXiv:1207.2753.

[69] G. Buchalla, *Heavy quark theory*, in *Heavy flavor physics: Theory and experimental results in heavy quark physics and CP violation. Proceedings, 55th Scottish Universities Summer School in Physics, SUSSP 2001, St. Andrews, UK, August 7-23, 2001*, pp. 57–104, 2002. arXiv:hep-ph/0202092.

[70] M. Beylich, G. Buchalla, and T. Feldmann, *Theory of $B \to K^{(*)}\ell^+\ell^-$ decays at high q^2: OPE and quark-hadron duality*, Eur. Phys. J. C **71** (2011) 1635, arXiv:1101.5118.

[71] S. Jäger and J. Martin Camalich, *Reassessing the discovery potential of the $B \to K^*\ell^+\ell^-$ decays in the large-recoil region: SM challenges and BSM opportunities*, Phys. Rev. **D93** (2016) 014028, arXiv:1412.3183.

[72] M. Della Morte, J. Heitger, H. Simma, and R. Sommer, *Non-perturbative Heavy Quark Effective Theory: An application to semi-leptonic B-decays*, Nucl. Part. Phys. Proc. **261-262** (2015) 368, arXiv:1501.03328.

[73] A. Khodjamirian, T. Mannel, A. A. Pivovarov, and Y.-M. Wang, *Charm-loop effect in $B \to K^{(*)}\ell^+\ell^-$ and $B \to K^*\gamma$*, JHEP **09** (2010) 089, arXiv:1006.4945.

[74] J. Lyon and R. Zwicky, *Resonances gone topsy turvy - the charm of QCD or new physics in $b \to s\ell^+\ell^-$?*, arXiv:1406.0566.

[75] M. Ciuchini *et al.*, *$B \to K^*\ell^+\ell^-$ decays at large recoil in the Standard Model: a theoretical reappraisal*, JHEP **06** (2016) 116, arXiv:1512.07157.

[76] C. Bobeth, M. Chrzaszcz, D. van Dyk, and J. Virto, *Long-distance effects in $B \to K^* \ell\ell$ from analyticity*, Eur. Phys. J. **C78** (2018), no. 6 451, arXiv:1707.07305.

[77] A. Bharucha, D. M. Straub, and R. Zwicky, *$B \to V \ell^+ \ell^-$ in the Standard Model from light-cone sum rules*, JHEP **08** (2016) 098, arXiv:1503.05534.

[78] S. Descotes-Genon, L. Hofer, J. Matias, and J. Virto, *On the impact of power corrections in the prediction of $B \to K^* \mu^+ \mu^-$ observables*, JHEP **12** (2014) 125, arXiv:1407.8526.

[79] LHCb collaboration, R. Aaij *et al.*, *Measurement of the $B^\pm$ production cross-section in pp collisions at $\sqrt{s}$ =7 and 13 TeV* , JHEP **12** (2017) 026, arXiv:1710.04921.

[80] M. Bordone, G. Isidori, and A. Pattori, *On the Standard Model predictions for R_K and R_{K^*}*, Eur. Phys. J. **C76** (2016) 440, arXiv:1605.07633.

[81] ATLAS collaboration, G. Aad *et al.*, *Search for the lepton flavor violating decay $Z \to e\mu$ in pp collisions at $\sqrt{s}$ TeV with the ATLAS detector*, Phys. Rev. D **90** (2014), no. 7 072010, arXiv:1408.5774.

[82] CMS collaboration, V. Khachatryan *et al.*, *Search for Lepton-Flavour-Violating Decays of the Higgs Boson*, Phys. Lett. B **749** (2015) 337, arXiv:1502.07400.

[83] MEG collaboration, A. M. Baldini *et al.*, *Search for the lepton flavour violating decay $\mu^+ \to e^+ \gamma$ with the full dataset of the MEG experiment*, Eur. Phys. J. C **76** (2016), no. 8 434, arXiv:1605.05081.

[84] LHCb collaboration, R. Aaij *et al.*, *Search for the lepton-flavour violating decay $D^0 \to e^\pm \mu^\mp$*, Phys. Lett. **B754** (2016) 167, arXiv:1512.00322.

[85] LHCb collaboration, R. Aaij *et al.*, *Search for the lepton-flavour violating decays $B^0_{(s)} \to e^\pm \mu^\mp$*, JHEP **03** (2018) 078, arXiv:1710.04111.

[86] LHCb collaboration, R. Aaij *et al.*, *Search for the lepton flavour violating decay $\tau^- \to \mu^- \mu^+ \mu^-$*, JHEP **02** (2015) 121, arXiv:1409.8548.

[87] LHCb collaboration, R. Aaij *et al.*, *Observation of B^0_s–$\overline{B}^0_s$ mixing and measurement of mixing frequencies using semileptonic B decays*, Eur. Phys. J. **C73** (2013) 2655, arXiv:1308.1302.

[88] LHCb collaboration, R. Aaij *et al.*, *Measurement of the B^0–$\overline{B}^0$ oscillation frequency Δm_d with the decays $B^0 \to D^- \pi^+$ and $B^0 \to J/\psi\, K^{*0}$*, Phys. Lett. **B719** (2013) 318, arXiv:1210.6750.

[89] LHCb collaboration, R. Aaij *et al.*, *Measurement of the B_s^0–$\overline{B}_s^0$ oscillation frequency Δm_s in $B_s^0 \to D_s^-(3)\pi$ decays*, Phys. Lett. **B709** (2012) 177, arXiv:1112.4311.

[90] CMS collaboration, A. M. Sirunyan *et al.*, *Search for leptoquarks coupled to third-generation quarks in proton-proton collisions at $\sqrt{s} = 13$ TeV*, Phys. Rev. Lett. **121** (2018), no. 24 241802, arXiv:1809.05558.

[91] ATLAS collaboration, M. Aaboud *et al.*, *Searches for third-generation scalar leptoquarks in $\sqrt{s} = 13$ TeV pp collisions with the ATLAS detector*, JHEP **06** (2019) 144, arXiv:1902.08103.

[92] Belle collaboration, A. Abdesselam *et al.*, *Measurement of $\mathcal{R}(D)$ and $\mathcal{R}(D^*)$ with a semileptonic tagging method*, arXiv:1904.08794.

[93] Belle collaboration, Y. Sato *et al.*, *Measurement of the branching ratio of $\bar{B}^0 \to D^{*+}\tau^-\bar{\nu}_\tau$ relative to $\bar{B}^0 \to D^{*+}\ell^-\bar{\nu}_\ell$ decays with a semileptonic tagging method*, Phys. Rev. D **94** (2016), no. 7 072007, arXiv:1607.07923.

[94] Belle collaboration, M. Huschle *et al.*, *Measurement of the branching ratio of $\bar{B} \to D^{(*)}\tau^-\bar{\nu}_\tau$ relative to $\bar{B} \to D^{(*)}\ell^-\bar{\nu}_\ell$ decays with hadronic tagging at Belle*, Phys. Rev. D **92** (2015), no. 7 072014, arXiv:1507.03233.

[95] Belle collaboration, S. Hirose *et al.*, *Measurement of the τ lepton polarization and $R(D^*)$ in the decay $\bar{B} \to D^*\tau^-\bar{\nu}_\tau$*, Phys. Rev. Lett. **118** (2017), no. 21 211801, arXiv:1612.00529.

[96] LHCb collaboration, R. Aaij *et al.*, *Measurement of the ratio of the $\mathcal{B}(B^0 \to D^{*-}\tau^+\nu_\tau)$ and $\mathcal{B}(B^0 \to D^{*-}\mu^+\nu_\mu)$ branching fractions using three-prong τ-lepton decays*, Phys. Rev. Lett. **120** (2018) 171802, arXiv:1708.08856.

[97] LHCb collaboration, R. Aaij *et al.*, *Measurement of the ratio of branching fractions $\mathcal{B}(\overline{B}^0 \to D^{*+}\tau^-\overline{\nu}_\tau)/\mathcal{B}(\overline{B}^0 \to D^{*+}\mu^-\overline{\nu}_\mu)$*, Phys. Rev. Lett. **115** (2015) 111803, Publisher's Note ibid. **115** (2015) 159901, arXiv:1506.08614.

[98] BaBar collaboration, J. P. Lees *et al.*, *Measurement of an Excess of $\bar{B} \to D^{(*)}\tau^-\bar{\nu}_\tau$ Decays and Implications for Charged Higgs Bosons*, Phys. Rev. D **88** (2013), no. 7 072012, arXiv:1303.0571.

[99] BaBar collaboration, J. P. Lees *et al.*, *Evidence for an excess of $\bar{B} \to D^{(*)}\tau^-\bar{\nu}_\tau$ decays*, Phys. Rev. Lett. **109** (2012) 101802, arXiv:1205.5442.

[100] O. S. Brning *et al.*, *LHC Design Report*, CERN Yellow Reports: Monographs, CERN, Geneva, 2004.

[101] CMS collaboration, S. Chatrchyan *et al.*, *The CMS Experiment at the CERN LHC*, JINST **3** (2008) S08004.

[102] ATLAS collaboration, G. Aad *et al.*, *The ATLAS Experiment at the CERN Large Hadron Collider*, JINST **3** (2008) S08003.

[103] ALICE collaboration, K. Aamodt *et al.*, *The ALICE experiment at the CERN LHC*, JINST **3** (2008) S08002.

[104] LHCb collaboration, A. A. Alves Jr. *et al.*, *The LHCb detector at the LHC*, JINST **3** (2008) S08005.

[105] LHCb collaboration, R. Aaij *et al.*, *Measurement of $\sigma(pp \to b\bar{b}X$ at $\sqrt{s} = 7\,TeV$ in the forward region*, Phys. Lett. **B694** (2010) 209, arXiv:1009.2731.

[106] LHCb collaboration, R. Aaij *et al.*, *Measurement of the b-quark production cross-section in 7 and 13 TeV pp collisions*, Phys. Rev. Lett. **118** (2017) 052002, arXiv:1612.05140, [Erratum: Phys. Rev. Lett.119,no.16,169901(2017)].

[107] LHCb collaboration, C. Elsässer, *$\bar{b}b$ production angle plots*, .

[108] LHCb collaboration, R. Aaij *et al.*, *LHCb Detector Performance*, Int. J. Mod. Phys. **A30** (2015), no. 07 1530022, arXiv:1412.6352.

[109] LHCb collaboration, R. Aaij *et al.*, *Performance of the LHCb Vertex Locator*, JINST **9** (2014) P09007, arXiv:1405.7808.

[110] LHCb collaboration, *LHCb reoptimized detector design and performance: Technical Design Report*, CERN-LHCC-2003-030. LHCb-TDR-009.

[111] R. E. Kalman, *A New Approach to Linear Filtering and Prediction Problems*, Transactions of the ASME Journal of Basic Engineering (1960), no. 82 (Series D) 35.

[112] R. Fruhwirth, *Application of Kalman filtering to track and vertex fitting*, Nucl. Instrum. Meth. **A262** (1987) 444.

[113] M. Needham, *Identification of Ghost Tracks using a Likelihood Method*, Tech. Rep. LHCb-2008-026. CERN-LHCb-2008-026. LPHE-2008-004, CERN, Geneva, May, 2008. `https://cds.cern.ch/record/1107564`.

[114] A. Perieanu, *Identification of Ghost Tracks using Neural Networks*, Tech. Rep. LHCb-2007-158. CERN-LHCb-2007-158, CERN, Geneva, Jan, 2008. `https://cds.cern.ch/record/1079949`.

[115] M. Needham, *Performance of the LHCb Track Reconstruction Software*, Tech. Rep. LHCb-2007-144. CERN-LHCb-2007-144, CERN, Geneva, Jan, 2008. `https://cds.cern.ch/record/1080556`.

[116] LHCb collaboration, *LHCb RICH: Technical Design Report*, CERN-LHCC-2000-037. LHCb-TDR-003.

[117] LHCb collaboration, B. Quintana, *Particle identification of neutral particles at LHCb*, PoS **LHCP2018** (2018) 046.

[118] A. Kashchuk *et al.*, *Asymmetric and double-cathode-pad wire chambers for the LHCb muon system*, Nucl. Instrum. Meth. **A555** (2005) 48.

[119] T. Head, *The LHCb trigger system*, JINST **9** (2014) C09015.

[120] T. Sjöstrand, S. Mrenna, and P. Skands, *PYTHIA 6.4 physics and manual*, JHEP **05** (2006) 026, `arXiv:hep-ph/0603175`.

[121] T. Sjöstrand, S. Mrenna, and P. Skands, *A brief introduction to PYTHIA 8.1*, Comput. Phys. Commun. **178** (2008) 852, `arXiv:0710.3820`.

[122] I. Belyaev *et al.*, *Handling of the generation of primary events in Gauss, the LHCb simulation framework*, J. Phys. Conf. Ser. **331** (2011) 032047.

[123] D. J. Lange, *The EvtGen particle decay simulation package*, Nucl. Instrum. Meth. **A462** (2001) 152.

[124] P. Golonka and Z. Was, *PHOTOS Monte Carlo: A precision tool for QED corrections in Z and W decays*, Eur. Phys. J. **C45** (2006) 97, arXiv:hep-ph/0506026.

[125] Geant4 collaboration, J. Allison *et al.*, *Geant4 developments and applications*, IEEE Trans. Nucl. Sci. **53** (2006) 270.

[126] L. Breiman, J. H. Friedman, R. A. Olshen, and C. J. Stone, *Classification and regression trees*, Wadsworth international group, Belmont, California, USA, 1984.

[127] M. Pivk and F. R. Le Diberder, *sPlot: A statistical tool to unfold data distributions*, Nucl. Instrum. Meth. **A555** (2005) 356, arXiv:physics/0402083.

[128] R. E. Schapire and Y. Freund, *A decision-theoretic generalization of on-line learning and an application to boosting*, J. Comput. Syst. Sci. **55** (1997) 119.

[129] A. Hoecker *et al.*, *TMVA - Toolkit for Multivariate Data Analysis*, ArXiv Physics e-prints (2007) arXiv:physics/0703039.

[130] A. Blum, A. Kalai, and J. Langford, *Beating the Hold-Out: Bounds for K-fold and Progressive Cross-Validation*, in *Proceedings of the Twelfth Annual Conference on Computational Learning Theory, COLT 1999, Santa Cruz, CA, USA, July 7-9, 1999*, pp. 203–208, 1999. doi: 10.1145/307400.307439.

[131] A. Poluektov, *Kernel density estimation of a multidimensional efficiency profile*, JINST **10** (2015), no. 02 P02011, arXiv:1411.5528.

[132] C. Runge, *Über empirische Funktionen und die Interpolation zwischen äquidistanten Ordinaten*, Zeitschrift für Mathematik und Physik **46** (1901) 224.

[133] D. Becirevic and A. Tayduganov, *Impact of $B \to K_0^* \ell^+ \ell^-$ on the New Physics search in $B \to K^* \ell^+ \ell^-$ decay*, Nucl. Phys. **B868** (2013) 368, arXiv:1207.4004.

[134] J. M. Blatt and V. F. Weisskopf, *Theoretical Nuclear Physics*, Springer-Verlag, 1952.

[135] Belle collaboration, K. Chilikin *et al.*, *Experimental constraints on the spin and parity of the $Z(4430)^+$*, Phys. Rev. D **88** (2013), no. 7 074026, arXiv:1306.4894.

[136] D. Aston *et al.*, *A Study of $K^-\pi^+$ scattering in the reaction $K^-\pi^+ \to K^-\pi^+ n$ at 11 GeV/c*, Nucl. Phys. **B296** (1988) 493.

[137] Bill Dunwoodie, *Fits to $K\pi$ $I = 1/2$ S-wave Amplitude and Phase Data*, `http://www.slac.stanford.edu/~wmd/kpi_swave/kpi_swave_fit.note`, 2013. Using 34 pts result, Accessed: 2019-04-09.

[138] F. a. James, *MINUIT: Function Minimization and Error Analysis Reference Manual*, 1998. CERN Program Library Long Writeups, `https://cds.cern.ch/record/2296388`.

[139] B. Efron, *Bootstrap methods: Another look at the jackknife*, The Annals of Statistics **7** (1979), no. 1 1.

[140] Belle collaboration, K. Chilikin *et al.*, *Observation of a new charged charmoniumlike state in $\bar{B}^0 \to J/\psi K^- \pi^+$ decays*, Phys. Rev. D **90** (2014), no. 11 112009, `arXiv:1408.6457`.

[141] LHCb collaboration, R. Aaij *et al.*, *Observation of the resonant character of the $Z(4430)^-$ state*, Phys. Rev. Lett. **112** (2014) 222002, `arXiv:1404.1903`.

[142] BaBar collaboration, B. Aubert *et al.*, *Measurement of decay amplitudes of $B \to J/\psi K^*, \psi(2S)K^*$, and $\chi_{c1}K^*$ with an angular analysis*, Phys. Rev. **D76** (2007) 031102, `arXiv:0704.0522`.

[143] Belle collaboration, R. Itoh *et al.*, *Studies of CP violation in $B \to J/\psi K^*$ decays*, Phys. Rev. Lett. **95** (2005) 091601, `arXiv:hep-ex/0504030`.

[144] LHCb collaboration, R. Aaij *et al.*, *Measurement of the polarization amplitudes in $B^0 \to J/\psi K^*(892)^0$ decays*, Phys. Rev. **D88** (2013) 052002, `arXiv:1307.2782`.

[145] Particle Data Group, J. Beringer *et al.*, *Review of particle physics*, Phys. Rev. **D86** (2012) 010001, and 2013 partial update for the 2014 edition.

[146] W. Altmannshofer and D. M. Straub, *New physics in $b \to s$ transitions after LHC run 1*, Eur. Phys. J. **C75** (2015), no. 8 382, `arXiv:1411.3161`.

[147] R. R. Horgan, Z. Liu, S. Meinel, and M. Wingate, *Lattice QCD calculation of form factors describing the rare decays $B \to K^* \ell^+ \ell^-$ and $B_s \to \phi \ell^+ \ell^-$*, Phys. Rev. **D89** (2014) 094501, `arXiv:1310.3722`.

[148] R. R. Horgan, Z. Liu, S. Meinel, and M. Wingate, *Rare B decays using lattice QCD form factors*, PoS LATTICE2014 (2015) 372, `arXiv:1501.00367`.

[149] D. M. Straub, *flavio: A python package for flavour and precision phenomenology in the Standard Model and beyond*, arXiv:1810.08132.

[150] LHCb collaboration, R. Aaij *et al.*, *Measurement of the phase difference between short- and long-distance amplitudes in the $B^+ \to K^+\mu^+\mu^-$ decay*, Eur. Phys. J. **C77** (2017) 161, arXiv:1612.06764.

Part III

Appendices

Appendix A

Mass fits

The fits to the $K^+\pi^-\mu^+\mu^-$ invariant mass distribution of $B^0 \to K^{*0}\mu^+\mu^-$ candidates, which have not been shown in Sec. 6.2 are presented below in Fig. A.1 and Fig. A.2.

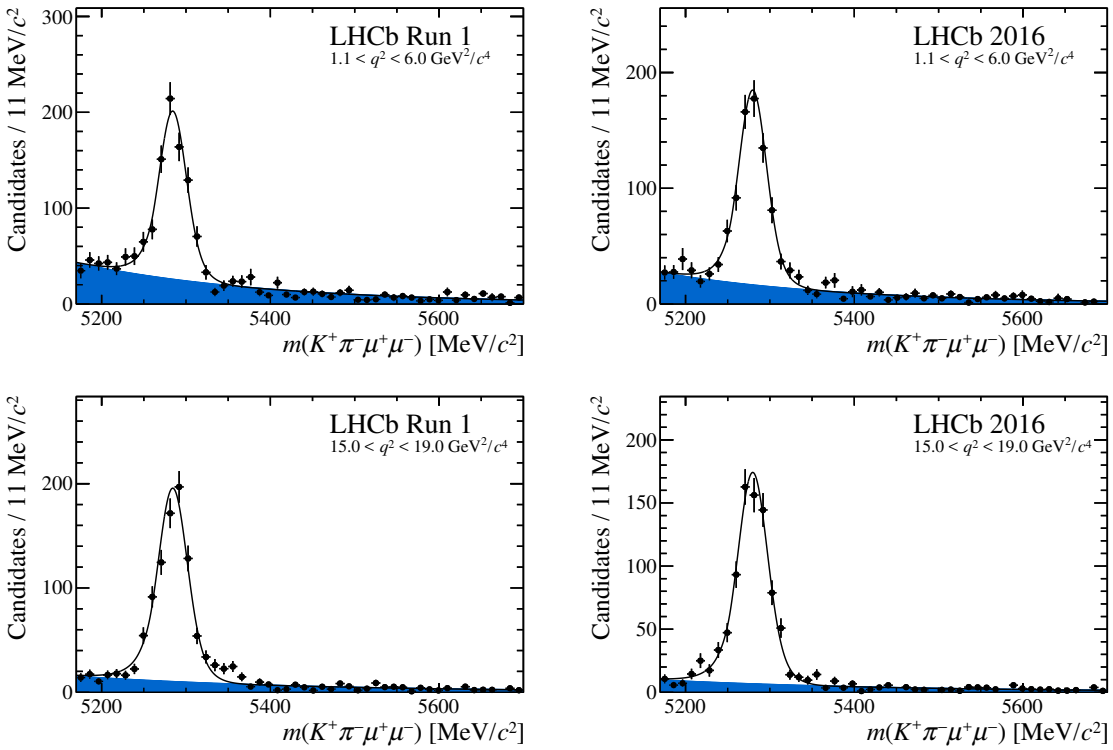


Figure A.1: The $K^+\pi^-\mu^+\mu^-$ invariant mass distribution of $B^0 \to K^{*0}\mu^+\mu^-$ candidates in the wide q^2 bins for Run 1 and 2016. Figure taken from Ref. [1].

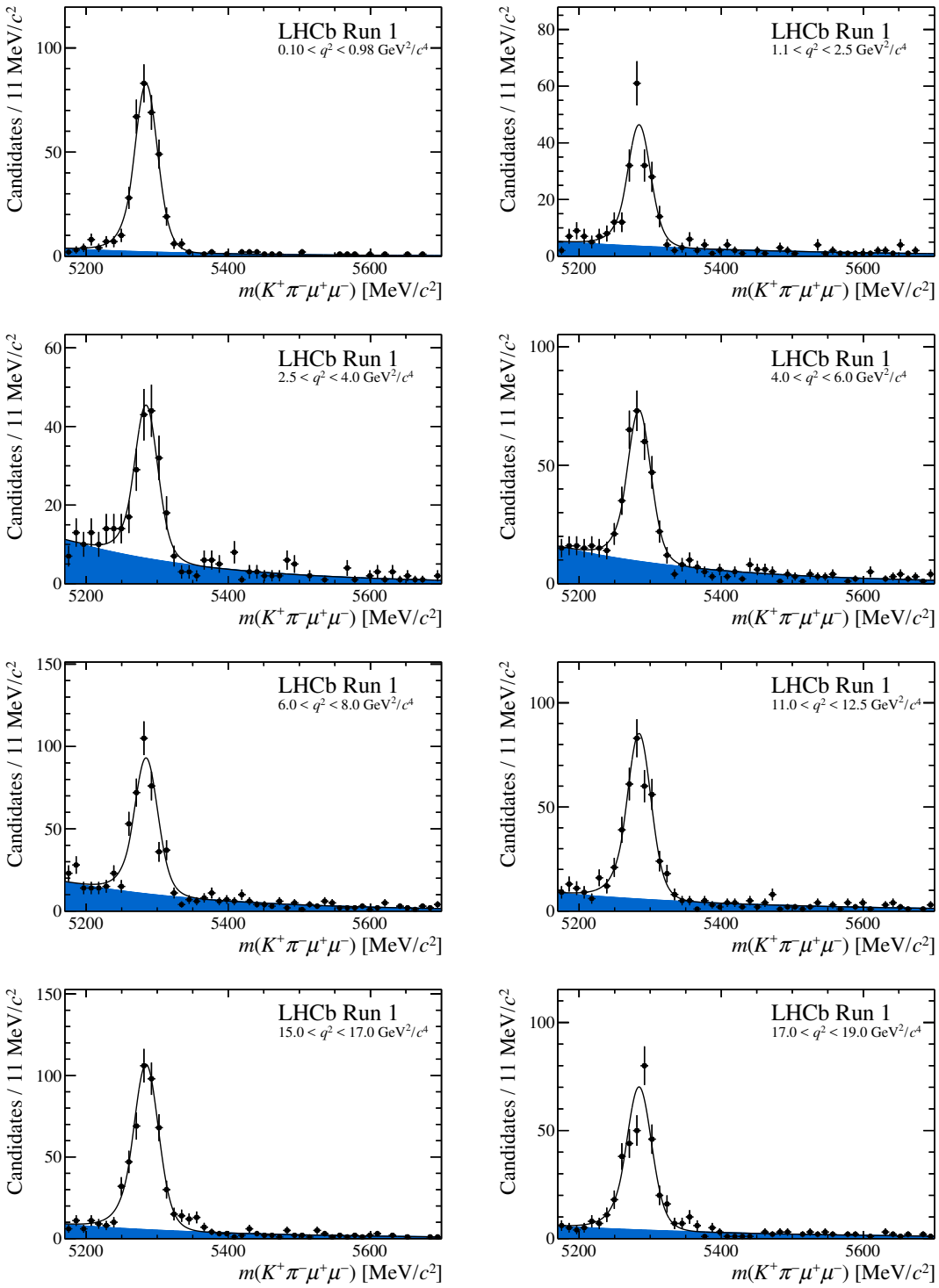


Figure A.2: The $K^+\pi^-\mu^+\mu^-$ invariant mass distribution of $B^0 \to K^{*0}\mu^+\mu^-$ candidates in the narrow q^2 bins for Run 1. Figure taken from Ref. [1].

Appendix B

Acceptance projections

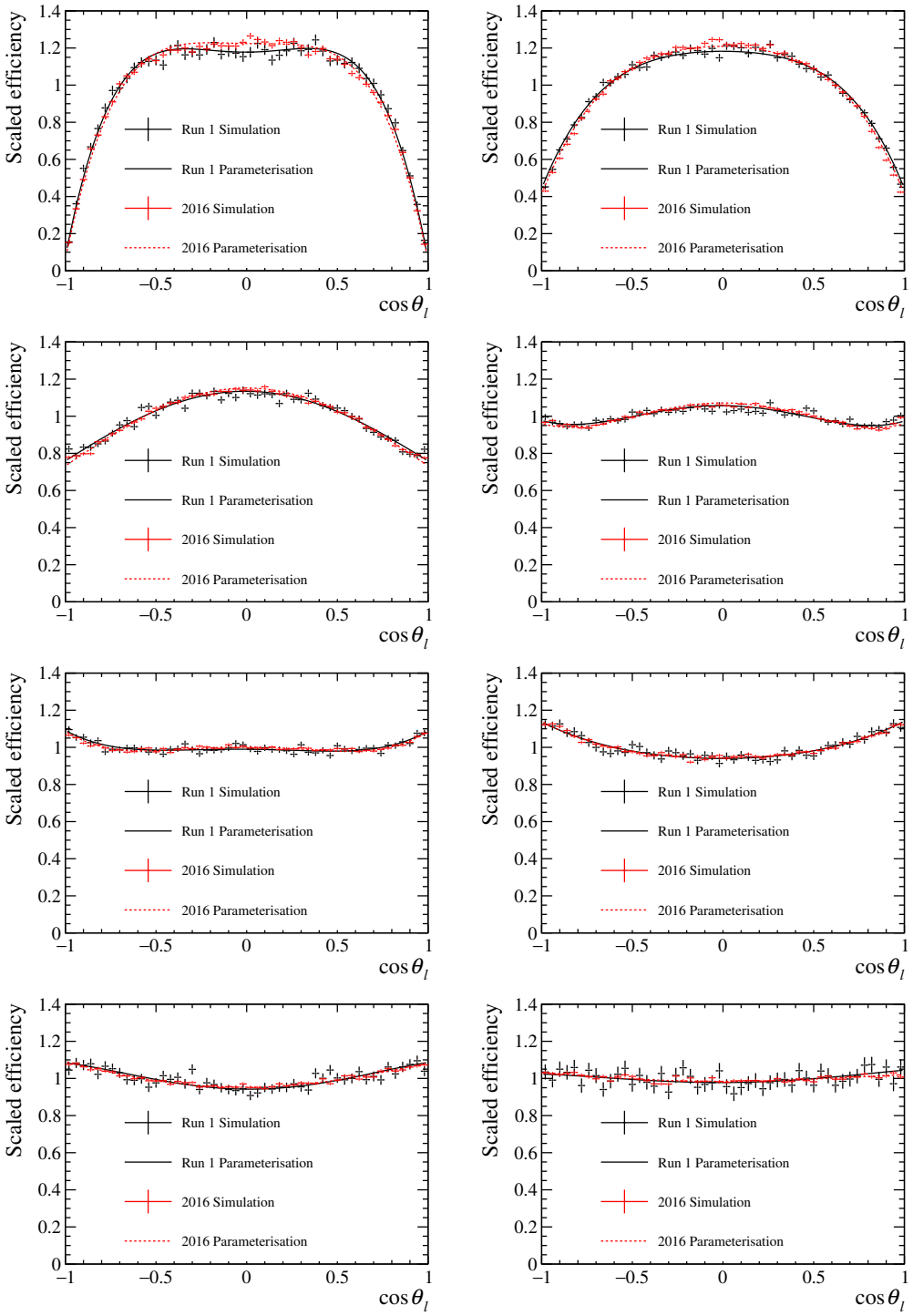


Figure B.1: One-dimensional projections of the four-dimensional acceptance parametrisation on $\cos\theta_l$ for Run 1 and 2016, given in bins of q^2. The order of the plots is the same as in Tab. 4.1 and only the projections for the narrow q^2 bins are shown.

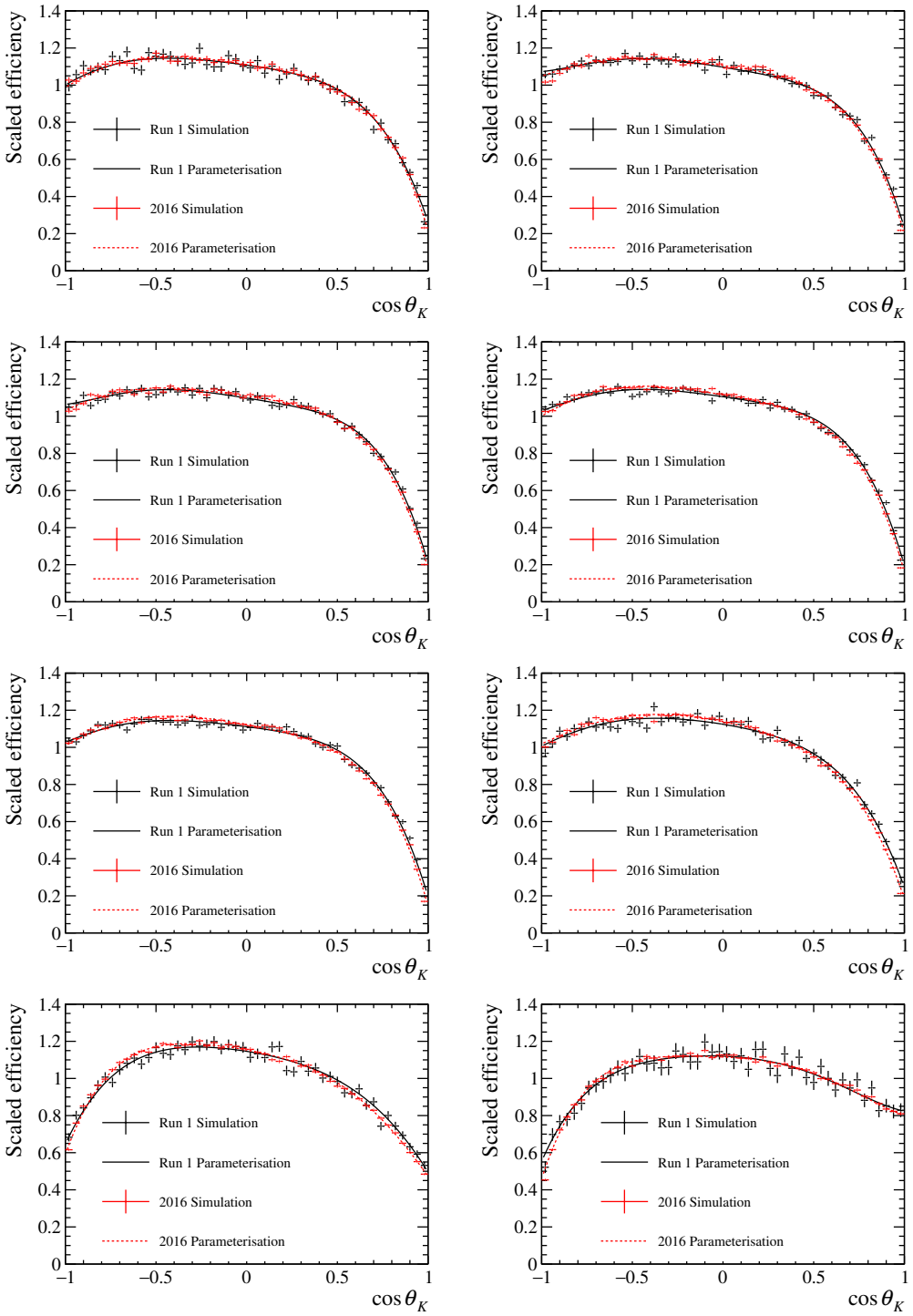


Figure B.2: One-dimensional projections of the four-dimensional acceptance parametrisation on $\cos\theta_K$ for Run 1 and 2016, given in bins of q^2. The order of the plots is the same as in Tab. 4.1 and only the projections for the narrow q^2 bins are shown.

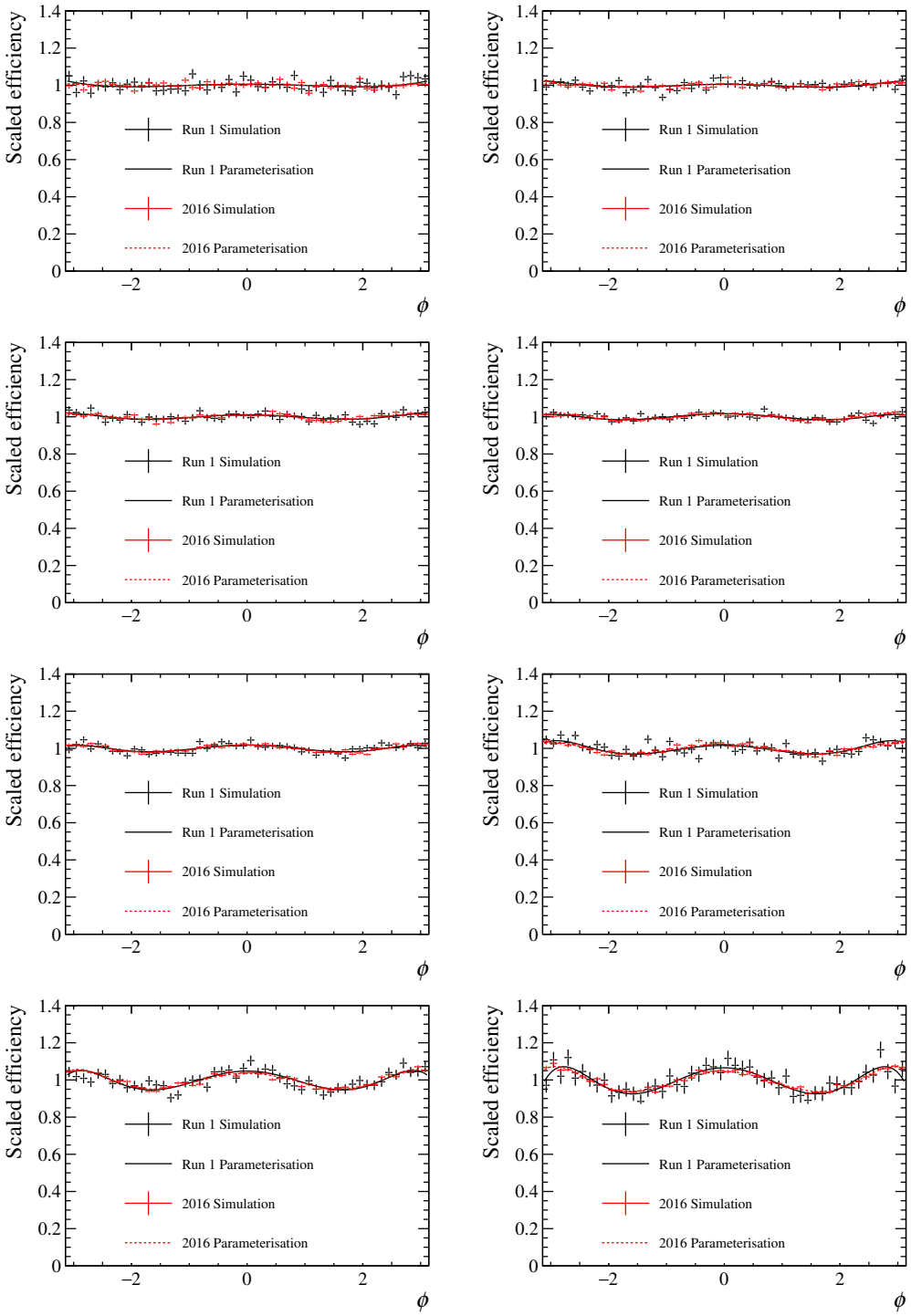


Figure B.3: One-dimensional projections of the four-dimensional acceptance parametrisation on $\cos\theta_K$ for Run 1 and 2016, given in bins of q^2. The order of the plots is the same as in Tab. 4.1 and only the projections for the narrow q^2 bins are shown.

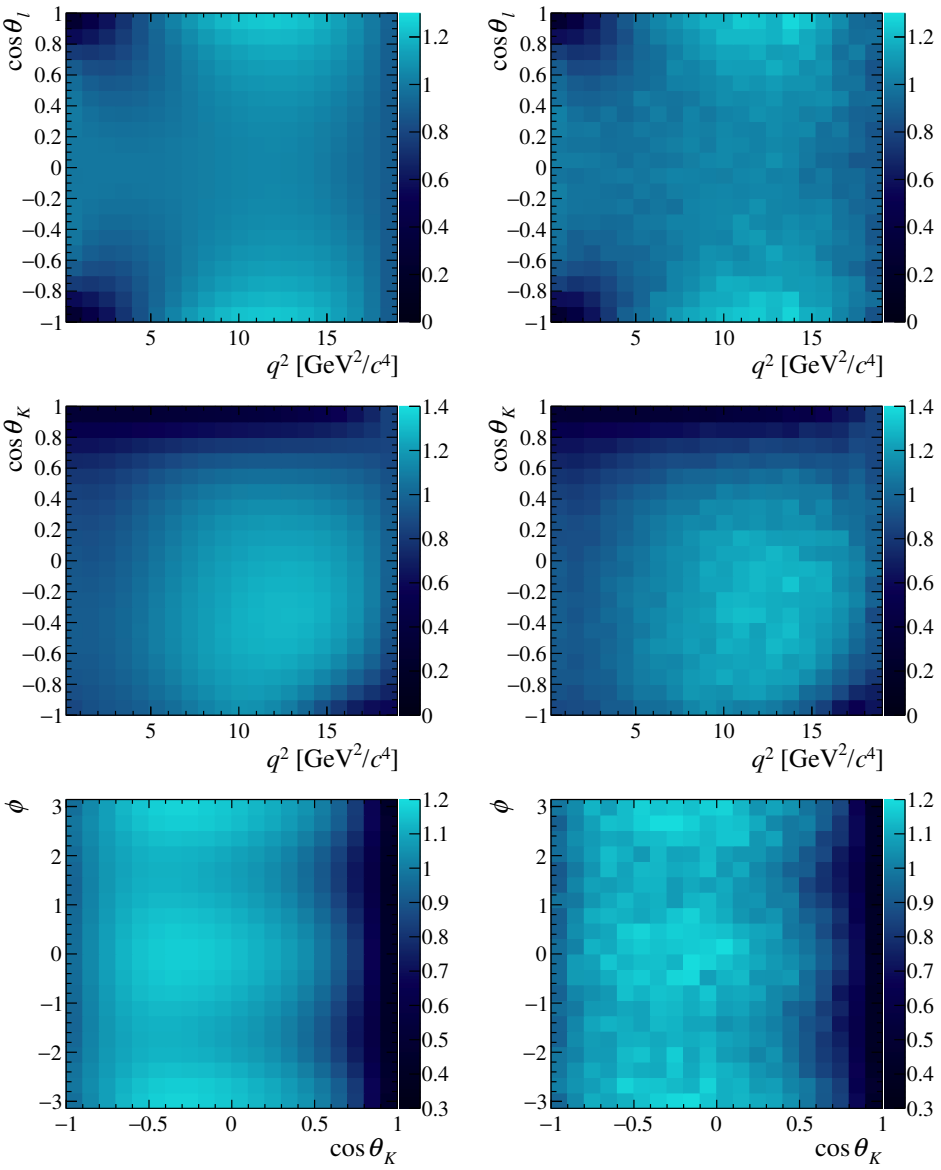


Figure B.4: Two-dimensional projections of the four-dimensional acceptance parameterisation on q^2, $\cos\theta_l$, $\cos\theta_K$, and ϕ for Run 1 (to the left) and comparison with the corresponding acceptance projection determined from the simulation histograms (to the right).

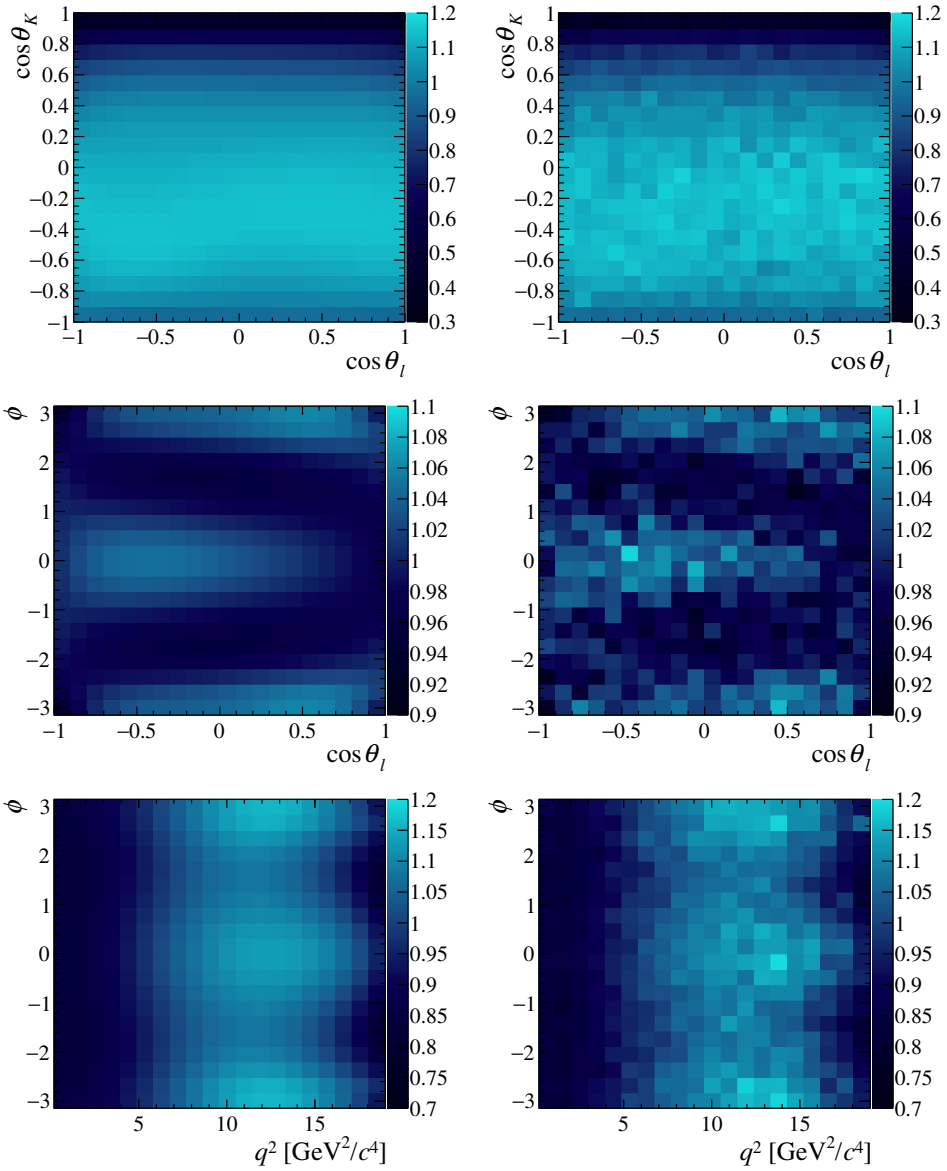


Figure B.4: Continued from the previous page.

Appendix C

Exotic charmonium states in $B^0 \to J/\psi\, K^+\pi^-$

The Belle experiment sees evidence for two exotic charmonium states, $Z_c^+(4200)$ and $Z_c^+(4430)$, decaying to $J/\psi\,\pi^+$ in an amplitude analysis of $B^0 \to J/\psi\, K^+\pi^-$ decays [140]. The two states have a favoured J^P of 1^+. The $Z_c^+(4430)$ is consistent with LHCb's amplitude analysis of the $B^0 \to \psi(2S)K^+\pi^-$ decay [141].

To study the possible impact of these Z_c^+ states in the $795 < m(K^+\pi^-) < 995\,\mathrm{MeV}/c^2$ mass window used in the analysis, toy experiments were generated using a matrix element squared,

$$|\mathcal{M}|^2 = \sum_{\lambda_\psi=-1,0,1} \left| \sum_k A_{k,\lambda_\psi} R(m_{K^+\pi^-}|m_k,\Gamma_k) d^{J_k}_{\lambda_\psi,0}(\theta_K) + \right. \tag{C.1}$$

$$\left. \sum_{\lambda_\psi^Z=-1,0,1} d^1_{\lambda_\psi^z,\lambda_\psi}(\theta_{K,Z}) A_{Z,\lambda_\psi^Z} R(m_{\psi\pi^-}|m_Z,\Gamma_Z) d^{J_Z}_{0,\lambda_\psi^z}(\theta_Z) \right|. \tag{C.2}$$

Here, the $d^J_{m',m}$ are Wigner d-functions and the functions R are relativistic Breit-Wigner functions describing the line shapes of the different states. The amplitudes A_{k,λ_ψ} and A_{Z,λ_ψ^Z} were taken from Belle's result. By parity conservation

$$A_{Z,-1} = A_{Z,+1} \tag{C.3}$$

for a $J^P = 1^+$ state.

The P-wave observables are not significantly affected by the presence of the Z_c^+, but a sizeable difference is seen in the S-wave fraction, F_S. Interestingly in toys included the Z_c^+ states, a difference is seen between the value of F_S estimated by the angular fit/moments and the $m(K^+\pi^-)$ mass fit (see Table C.1). This difference is consistent with what is seen in data. The $\cos\theta_K$ and $m(K^+\pi^-)$ distribution of toys with and without the Z are included in Fig. C.1. Small differences are seen in the $795 < m(K^+\pi^-) < 995\,\mathrm{MeV}/c^2$ mass window.

model	angular	$m(K^+\pi^-)$
$J \leq 4 + Z(4200) + Z(4430)$	0.067 ± 0.002	0.050 ± 0.002
$J \leq 4$	0.057 ± 0.002	0.053 ± 0.002
$K^*(892) + K_0(800) + K_0(1430)$	0.052 ± 0.002	0.047 ± 0.02

Table C.1: Result of fitting either the angular or $m(K^+\pi^-)$ distribution of toy experiments for the S-wave fraction, $F_{\rm S}$, in three configurations: one in which only the $K^*(892)$, $K_0(800)$ and $K_0(1430)$ were included in the toy; one in which K^* states up-to $J = 4$ were included; and finally one in which the Z_c^+ states were added.

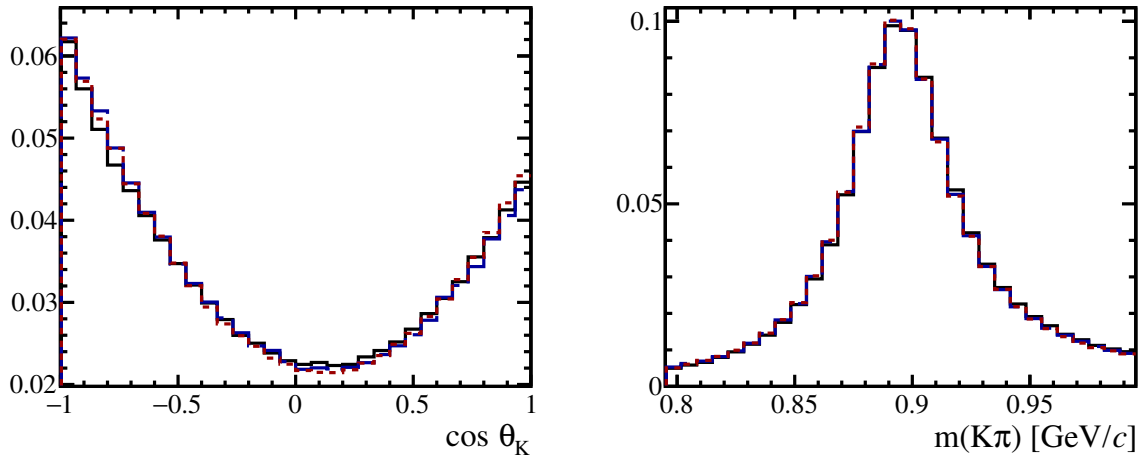


Figure C.1: The $\cos\theta_K$ and $m(K^+\pi^-)$ distributions of toy experiments produced with: only the $K^*(892)$, $K_0(800)$ and $K_0(1430)$ (red short-dashed); all K^* states up to $J = 4$ (blue long-dashed); and adding the two Z_c^+ states observed by Belle (black solid-line). In each case only events in the $795 < m(K^+\pi^-) < 995\,\text{MeV}/c^2$ mass window are shown.

Appendix D

Fit validation using pseudoexperiments

$0.1 < q^2 < 0.98\ \mathrm{GeV}^2/c^4$

	sensitivity	pull mean	pull width
F_L	0.031 ± 0.001	-0.069 ± 0.043	0.973 ± 0.031
S_3	0.045 ± 0.001	0.031 ± 0.044	0.993 ± 0.031
S_4	0.053 ± 0.002	0.045 ± 0.047	1.055 ± 0.033
S_5	0.046 ± 0.001	-0.116 ± 0.047	1.053 ± 0.033
A_FB	0.041 ± 0.001	-0.093 ± 0.043	0.972 ± 0.031
S_7	0.044 ± 0.001	-0.013 ± 0.045	1.002 ± 0.032
S_8	0.048 ± 0.002	0.030 ± 0.042	0.939 ± 0.030
S_9	0.046 ± 0.001	-0.025 ± 0.045	1.009 ± 0.032
F_S	0.038 ± 0.001	-0.010 ± 0.042	0.944 ± 0.030
S_S1	0.064 ± 0.002	-0.096 ± 0.046	1.028 ± 0.033
S_S2	0.063 ± 0.002	0.021 ± 0.046	1.021 ± 0.032
S_S3	0.051 ± 0.002	0.006 ± 0.044	0.995 ± 0.031
S_S4	0.051 ± 0.002	-0.013 ± 0.045	1.006 ± 0.032
S_S5	0.061 ± 0.002	0.085 ± 0.043	0.958 ± 0.030

$1.1 < q^2 < 2.5\ \mathrm{GeV}^2/c^4$

	sensitivity	pull mean	pull width
F_L	0.056 ± 0.002	0.055 ± 0.045	1.013 ± 0.032
S_3	0.056 ± 0.002	-0.035 ± 0.044	0.979 ± 0.031
S_4	0.081 ± 0.003	-0.034 ± 0.048	1.068 ± 0.034
S_5	0.074 ± 0.002	-0.005 ± 0.048	1.062 ± 0.034
A_FB	0.051 ± 0.002	-0.097 ± 0.047	1.059 ± 0.034
S_7	0.065 ± 0.002	0.024 ± 0.043	0.952 ± 0.030
S_8	0.077 ± 0.002	0.037 ± 0.046	1.018 ± 0.032
S_9	0.061 ± 0.002	-0.001 ± 0.047	1.057 ± 0.033
F_S	0.058 ± 0.002	0.078 ± 0.040	0.891 ± 0.028
S_S1	0.114 ± 0.004	0.032 ± 0.046	1.031 ± 0.033
S_S2	0.080 ± 0.003	-0.013 ± 0.047	1.050 ± 0.033
S_S3	0.069 ± 0.002	-0.011 ± 0.046	1.038 ± 0.033
S_S4	0.068 ± 0.002	0.035 ± 0.045	1.006 ± 0.032
S_S5	0.089 ± 0.003	-0.017 ± 0.052	1.157 ± 0.037

$2.5 < q^2 < 4.0\ \mathrm{GeV}^2/c^4$

	sensitivity	pull mean	pull width
F_L	0.061 ± 0.002	0.041 ± 0.046	1.036 ± 0.033
S_3	0.067 ± 0.002	0.012 ± 0.049	1.085 ± 0.034
S_4	0.086 ± 0.003	0.059 ± 0.047	1.055 ± 0.033
S_5	0.075 ± 0.002	0.063 ± 0.045	1.003 ± 0.032
A_FB	0.050 ± 0.002	0.013 ± 0.048	1.069 ± 0.034
S_7	0.078 ± 0.002	0.055 ± 0.047	1.040 ± 0.033
S_8	0.083 ± 0.003	-0.054 ± 0.046	1.019 ± 0.032
S_9	0.065 ± 0.002	-0.106 ± 0.046	1.032 ± 0.033
F_S	0.067 ± 0.002	0.054 ± 0.042	0.929 ± 0.029
S_S1	0.122 ± 0.004	0.015 ± 0.044	0.976 ± 0.031
S_S2	0.089 ± 0.003	-0.086 ± 0.050	1.109 ± 0.035
S_S3	0.071 ± 0.002	0.044 ± 0.045	1.003 ± 0.032
S_S4	0.078 ± 0.002	0.100 ± 0.048	1.079 ± 0.034
S_S5	0.085 ± 0.003	0.053 ± 0.048	1.062 ± 0.034

$4.0 < q^2 < 6.0\ \mathrm{GeV}^2/c^4$

	sensitivity	pull mean	pull width
F_L	0.040 ± 0.001	0.029 ± 0.045	1.012 ± 0.032
S_3	0.050 ± 0.002	-0.040 ± 0.047	1.050 ± 0.033
S_4	0.058 ± 0.002	0.009 ± 0.046	1.038 ± 0.033
S_5	0.059 ± 0.002	-0.024 ± 0.046	1.039 ± 0.033
A_FB	0.034 ± 0.001	-0.054 ± 0.046	1.027 ± 0.032
S_7	0.056 ± 0.002	-0.007 ± 0.045	1.001 ± 0.032
S_8	0.059 ± 0.002	0.023 ± 0.046	1.018 ± 0.032
S_9	0.046 ± 0.001	-0.008 ± 0.044	0.983 ± 0.031
F_S	0.052 ± 0.002	0.012 ± 0.042	0.942 ± 0.030
S_S1	0.098 ± 0.003	0.033 ± 0.047	1.046 ± 0.033
S_S2	0.059 ± 0.002	-0.040 ± 0.047	1.052 ± 0.033
S_S3	0.055 ± 0.002	0.026 ± 0.046	1.031 ± 0.033
S_S4	0.055 ± 0.002	0.105 ± 0.044	0.994 ± 0.031
S_S5	0.062 ± 0.002	0.119 ± 0.047	1.040 ± 0.033

$6.0 < q^2 < 8.0\ \mathrm{GeV}^2/c^4$

	sensitivity	pull mean	pull width
F_L	0.032 ± 0.001	-0.050 ± 0.042	0.947 ± 0.030
S_3	0.043 ± 0.001	-0.028 ± 0.044	0.992 ± 0.031
S_4	0.048 ± 0.002	-0.010 ± 0.046	1.018 ± 0.032
S_5	0.051 ± 0.002	-0.076 ± 0.045	0.998 ± 0.032
A_FB	0.031 ± 0.001	0.059 ± 0.046	1.036 ± 0.033
S_7	0.051 ± 0.002	-0.044 ± 0.045	1.013 ± 0.032
S_8	0.050 ± 0.002	-0.089 ± 0.044	0.991 ± 0.031
S_9	0.044 ± 0.001	-0.065 ± 0.045	1.010 ± 0.032
F_S	0.047 ± 0.001	0.002 ± 0.042	0.929 ± 0.029
S_S1	0.079 ± 0.002	0.054 ± 0.042	0.950 ± 0.030
S_S2	0.049 ± 0.002	-0.063 ± 0.044	0.985 ± 0.031
S_S3	0.051 ± 0.002	0.012 ± 0.046	1.038 ± 0.033
S_S4	0.054 ± 0.002	-0.113 ± 0.047	1.055 ± 0.033
S_S5	0.056 ± 0.002	-0.029 ± 0.047	1.047 ± 0.033

Table D.1: Results from 500 pseudoexperiments corresponding to the combined Run 1 and 2016 data for the q^2 bins $[0.1, 0.98]\,\mathrm{GeV}^2/c^4$, $[1.1, 2.5]\,\mathrm{GeV}^2/c^4$, $[2.5, 4.0]\,\mathrm{GeV}^2/c^4$, $[4.0, 6.0]\,\mathrm{GeV}^2/c^4$ and $[6.0, 8.0]\,\mathrm{GeV}^2/c^4$. The means and widths of Gaussian functions fitted to the pull distributions for the S_i basis are provided. In addition, the widths of the distributions of the fitted parameter values are given in the sensitivity column.

$15.0 < q^2 < 17.0$ GeV$^2/c^4$

	sensitivity	pull mean	pull width
F_{L}	0.031 ± 0.001	-0.011 ± 0.046	1.035 ± 0.033
S_3	0.040 ± 0.001	-0.114 ± 0.045	1.015 ± 0.032
S_4	0.038 ± 0.001	0.083 ± 0.045	1.013 ± 0.032
S_5	0.042 ± 0.001	0.007 ± 0.048	1.066 ± 0.034
A_{FB}	0.030 ± 0.001	0.062 ± 0.047	1.053 ± 0.033
S_7	0.045 ± 0.001	0.065 ± 0.047	1.043 ± 0.033
S_8	0.042 ± 0.001	-0.000 ± 0.045	0.999 ± 0.032
S_9	0.038 ± 0.001	0.012 ± 0.045	1.002 ± 0.032
F_{S}	0.042 ± 0.001	0.059 ± 0.046	1.029 ± 0.033
S_{S1}	0.060 ± 0.002	0.012 ± 0.044	0.987 ± 0.031
S_{S2}	0.042 ± 0.001	-0.022 ± 0.046	1.027 ± 0.032
S_{S3}	0.042 ± 0.001	-0.030 ± 0.045	1.008 ± 0.032
S_{S4}	0.050 ± 0.002	-0.006 ± 0.045	1.012 ± 0.032
S_{S5}	0.052 ± 0.002	-0.023 ± 0.048	1.077 ± 0.034

$17.0 < q^2 < 19.0$ GeV$^2/c^4$

	sensitivity	pull mean	pull width
F_{L}	0.035 ± 0.001	0.074 ± 0.044	0.979 ± 0.031
S_3	0.050 ± 0.002	-0.054 ± 0.045	0.991 ± 0.031
S_4	0.051 ± 0.002	0.163 ± 0.048	1.066 ± 0.034
S_5	0.049 ± 0.002	0.013 ± 0.047	1.048 ± 0.033
A_{FB}	0.036 ± 0.001	-0.041 ± 0.045	0.992 ± 0.032
S_7	0.058 ± 0.002	-0.097 ± 0.048	1.076 ± 0.034
S_8	0.056 ± 0.002	0.007 ± 0.046	1.029 ± 0.033
S_9	0.050 ± 0.002	-0.021 ± 0.046	1.021 ± 0.032
F_{S}	0.046 ± 0.001	0.007 ± 0.039	0.875 ± 0.028
S_{S1}	0.077 ± 0.002	-0.010 ± 0.046	1.031 ± 0.033
S_{S2}	0.059 ± 0.002	-0.009 ± 0.049	1.088 ± 0.035
S_{S3}	0.055 ± 0.002	-0.006 ± 0.050	1.107 ± 0.035
S_{S4}	0.066 ± 0.002	0.021 ± 0.047	1.053 ± 0.033
S_{S5}	0.068 ± 0.002	0.012 ± 0.047	1.039 ± 0.033

$11.0 < q^2 < 12.5$ GeV$^2/c^4$

	sensitivity	pull mean	pull width
F_{L}	0.035 ± 0.001	-0.015 ± 0.045	1.011 ± 0.032
S_3	0.046 ± 0.001	-0.032 ± 0.045	1.006 ± 0.032
S_4	0.048 ± 0.002	0.095 ± 0.048	1.064 ± 0.034
S_5	0.049 ± 0.002	0.066 ± 0.045	0.995 ± 0.032
A_{FB}	0.035 ± 0.001	0.073 ± 0.047	1.055 ± 0.033
S_7	0.051 ± 0.002	0.080 ± 0.044	0.987 ± 0.031
S_8	0.052 ± 0.002	0.038 ± 0.048	1.061 ± 0.034
S_9	0.047 ± 0.002	0.022 ± 0.047	1.038 ± 0.033
F_{S}	0.046 ± 0.001	0.067 ± 0.041	0.922 ± 0.029
S_{S1}	0.081 ± 0.003	-0.010 ± 0.047	1.047 ± 0.033
S_{S2}	0.056 ± 0.002	-0.111 ± 0.051	1.125 ± 0.036
S_{S3}	0.054 ± 0.002	0.015 ± 0.047	1.050 ± 0.033
S_{S4}	0.057 ± 0.002	0.002 ± 0.045	0.998 ± 0.032
S_{S5}	0.060 ± 0.002	0.027 ± 0.049	1.085 ± 0.034

$1.1 < q^2 < 6.0$ GeV$^2/c^4$

	sensitivity	pull mean	pull width
F_{L}	0.0305 ± 0.0010	0.040 ± 0.046	1.023 ± 0.032
S_3	0.0336 ± 0.0011	-0.060 ± 0.045	1.015 ± 0.032
S_4	0.0423 ± 0.0013	0.018 ± 0.046	1.024 ± 0.032
S_5	0.0403 ± 0.0013	-0.033 ± 0.046	1.020 ± 0.032
A_{FB}	0.0256 ± 0.0008	0.007 ± 0.046	1.030 ± 0.033
S_7	0.0373 ± 0.0012	-0.025 ± 0.042	0.945 ± 0.030
S_8	0.0431 ± 0.0014	-0.016 ± 0.045	1.014 ± 0.032
S_9	0.0334 ± 0.0011	-0.002 ± 0.045	1.014 ± 0.032
F_{S}	0.0375 ± 0.0012	0.028 ± 0.045	0.999 ± 0.032
S_{S1}	0.0679 ± 0.0021	0.027 ± 0.045	0.999 ± 0.032
S_{S2}	0.0434 ± 0.0014	0.036 ± 0.047	1.044 ± 0.033
S_{S3}	0.0395 ± 0.0012	-0.009 ± 0.046	1.023 ± 0.032
S_{S4}	0.0382 ± 0.0012	0.001 ± 0.044	0.994 ± 0.031
S_{S5}	0.0449 ± 0.0014	-0.108 ± 0.047	1.052 ± 0.033

$15.0 < q^2 < 19.0$ GeV$^2/c^4$

	sensitivity	pull mean	pull width
F_{L}	0.0228 ± 0.0007	-0.023 ± 0.043	0.970 ± 0.031
S_3	0.0307 ± 0.0010	0.049 ± 0.043	0.972 ± 0.031
S_4	0.0296 ± 0.0009	0.070 ± 0.045	0.999 ± 0.032
S_5	0.0310 ± 0.0010	0.010 ± 0.047	1.045 ± 0.033
A_{FB}	0.0215 ± 0.0007	-0.059 ± 0.042	0.944 ± 0.030
S_7	0.0367 ± 0.0012	-0.018 ± 0.047	1.059 ± 0.033
S_8	0.0348 ± 0.0011	0.047 ± 0.045	1.010 ± 0.032
S_9	0.0317 ± 0.0010	-0.019 ± 0.045	1.013 ± 0.032
F_{S}	0.0301 ± 0.0010	-0.000 ± 0.046	1.026 ± 0.032
S_{S1}	0.0509 ± 0.0016	-0.005 ± 0.046	1.031 ± 0.033
S_{S2}	0.0349 ± 0.0011	-0.003 ± 0.045	1.017 ± 0.032
S_{S3}	0.0329 ± 0.0010	-0.038 ± 0.044	0.985 ± 0.031
S_{S4}	0.0367 ± 0.0012	0.094 ± 0.041	0.910 ± 0.029
S_{S5}	0.0387 ± 0.0012	-0.031 ± 0.043	0.958 ± 0.030

Table D.2: Results from 500 pseudoexperiments corresponding to the combined Run 1 and 2016 data for the q^2 bins $[11.0, 12.5]\,\mathrm{GeV}^2/c^4$, $[15.0, 17.0]\,\mathrm{GeV}^2/c^4$, $[17.0, 19.0]\,\mathrm{GeV}^2/c^4$, $[1.1, 6.0]\,\mathrm{GeV}^2/c^4$ and $[15.0, 19.0]\,\mathrm{GeV}^2/c^4$. The means and widths of Gaussian functions fitted to the pull distributions for the S_i basis are provided. In addition, the widths of the distributions of the fitted parameter values are given in the sensitivity column.

$0.1 < q^2 < 0.98\ \mathrm{GeV}^2/c^4$

	sensitivity	pull mean	pull width
F_L	0.032 ± 0.001	-0.076 ± 0.044	0.993 ± 0.031
P_1	0.118 ± 0.004	0.026 ± 0.045	0.997 ± 0.032
P_2	0.035 ± 0.001	-0.076 ± 0.043	0.964 ± 0.030
P_3	0.059 ± 0.002	0.015 ± 0.045	1.005 ± 0.032
P_4'	0.130 ± 0.004	0.032 ± 0.048	1.075 ± 0.034
P_5'	0.111 ± 0.004	-0.148 ± 0.046	1.022 ± 0.032
P_6'	0.106 ± 0.003	-0.029 ± 0.046	1.019 ± 0.032
P_8'	0.115 ± 0.004	0.029 ± 0.042	0.935 ± 0.030
F_S	0.037 ± 0.001	0.004 ± 0.040	0.897 ± 0.028
S_S1	0.065 ± 0.002	-0.080 ± 0.047	1.041 ± 0.033
S_S2	0.062 ± 0.002	0.010 ± 0.045	1.017 ± 0.032
S_S3	0.051 ± 0.002	0.002 ± 0.044	0.995 ± 0.031
S_S4	0.051 ± 0.002	-0.013 ± 0.045	1.000 ± 0.032
S_S5	0.061 ± 0.002	0.109 ± 0.043	0.957 ± 0.030

$1.1 < q^2 < 2.5\ \mathrm{GeV}^2/c^4$

	sensitivity	pull mean	pull width
F_L	0.054 ± 0.002	0.040 ± 0.045	0.998 ± 0.032
P_1	0.405 ± 0.013	-0.034 ± 0.043	0.955 ± 0.030
P_2	0.143 ± 0.005	-0.003 ± 0.044	0.977 ± 0.031
P_3	0.212 ± 0.007	0.020 ± 0.044	0.976 ± 0.031
P_4'	0.179 ± 0.006	-0.025 ± 0.047	1.051 ± 0.033
P_5'	0.166 ± 0.005	-0.007 ± 0.047	1.061 ± 0.034
P_6'	0.145 ± 0.005	0.037 ± 0.043	0.955 ± 0.030
P_8'	0.171 ± 0.005	0.037 ± 0.045	1.008 ± 0.032
F_S	0.058 ± 0.002	0.070 ± 0.039	0.869 ± 0.027
S_S1	0.114 ± 0.004	0.023 ± 0.046	1.031 ± 0.033
S_S2	0.079 ± 0.003	-0.025 ± 0.047	1.040 ± 0.033
S_S3	0.069 ± 0.002	-0.002 ± 0.046	1.038 ± 0.033
S_S4	0.068 ± 0.002	0.035 ± 0.046	1.018 ± 0.032
S_S5	0.091 ± 0.003	-0.022 ± 0.053	1.175 ± 0.037

$2.5 < q^2 < 4.0\ \mathrm{GeV}^2/c^4$

	sensitivity	pull mean	pull width
F_L	0.060 ± 0.002	0.083 ± 0.054	1.200 ± 0.038
P_1	0.863 ± 0.027	0.007 ± 0.043	0.954 ± 0.030
P_2	0.319 ± 0.010	0.087 ± 0.043	0.972 ± 0.031
P_3	0.474 ± 0.015	0.089 ± 0.040	0.905 ± 0.029
P_4'	0.242 ± 0.008	0.031 ± 0.045	1.014 ± 0.032
P_5'	0.224 ± 0.007	0.045 ± 0.043	0.966 ± 0.031
P_6'	0.205 ± 0.006	0.074 ± 0.044	0.994 ± 0.031
P_8'	0.225 ± 0.007	-0.042 ± 0.044	0.990 ± 0.031
F_S	0.067 ± 0.002	0.050 ± 0.042	0.936 ± 0.030
S_S1	0.122 ± 0.004	0.018 ± 0.044	0.974 ± 0.031
S_S2	0.086 ± 0.003	-0.081 ± 0.048	1.077 ± 0.034
S_S3	0.071 ± 0.002	0.044 ± 0.044	0.994 ± 0.031
S_S4	0.078 ± 0.002	0.077 ± 0.049	1.091 ± 0.034
S_S5	0.085 ± 0.003	0.061 ± 0.047	1.055 ± 0.033

$4.0 < q^2 < 6.0\ \mathrm{GeV}^2/c^4$

	sensitivity	pull mean	pull width
F_L	0.040 ± 0.001	0.033 ± 0.045	1.012 ± 0.032
P_1	0.396 ± 0.013	-0.044 ± 0.045	1.016 ± 0.032
P_2	0.090 ± 0.003	-0.050 ± 0.045	1.006 ± 0.032
P_3	0.182 ± 0.006	-0.002 ± 0.042	0.945 ± 0.030
P_4'	0.133 ± 0.004	0.022 ± 0.046	1.027 ± 0.032
P_5'	0.141 ± 0.004	-0.021 ± 0.044	0.995 ± 0.031
P_6'	0.131 ± 0.004	0.004 ± 0.045	1.003 ± 0.032
P_8'	0.135 ± 0.004	0.023 ± 0.045	1.010 ± 0.032
F_S	0.052 ± 0.002	0.002 ± 0.042	0.948 ± 0.030
S_S1	0.099 ± 0.003	0.053 ± 0.047	1.051 ± 0.033
S_S2	0.059 ± 0.002	-0.045 ± 0.047	1.046 ± 0.033
S_S3	0.055 ± 0.002	0.030 ± 0.046	1.032 ± 0.033
S_S4	0.055 ± 0.002	0.111 ± 0.044	0.994 ± 0.031
S_S5	0.062 ± 0.002	0.122 ± 0.047	1.047 ± 0.033

$6.0 < q^2 < 8.0\ \mathrm{GeV}^2/c^4$

	sensitivity	pull mean	pull width
F_L	0.032 ± 0.001	-0.046 ± 0.042	0.942 ± 0.030
P_1	0.243 ± 0.008	-0.020 ± 0.044	0.990 ± 0.031
P_2	0.059 ± 0.002	0.020 ± 0.046	1.021 ± 0.032
P_3	0.124 ± 0.004	0.070 ± 0.044	0.994 ± 0.031
P_4'	0.100 ± 0.003	-0.010 ± 0.045	1.012 ± 0.032
P_5'	0.109 ± 0.003	-0.067 ± 0.045	0.999 ± 0.032
P_6'	0.108 ± 0.003	-0.046 ± 0.046	1.017 ± 0.032
P_8'	0.104 ± 0.003	-0.102 ± 0.044	0.979 ± 0.031
F_S	0.047 ± 0.001	0.001 ± 0.042	0.932 ± 0.029
S_S1	0.079 ± 0.002	0.050 ± 0.043	0.952 ± 0.030
S_S2	0.050 ± 0.002	-0.063 ± 0.045	0.997 ± 0.032
S_S3	0.052 ± 0.002	0.015 ± 0.047	1.052 ± 0.033
S_S4	0.054 ± 0.002	-0.113 ± 0.047	1.048 ± 0.033
S_S5	0.056 ± 0.002	-0.030 ± 0.047	1.043 ± 0.033

Table D.3: Results from 500 pseudoexperiments corresponding to the combined Run 1 and 2016 data for the q^2 bins $[0.1, 0.98]\,\mathrm{GeV}^2/c^4$, $[1.1, 2.5]\,\mathrm{GeV}^2/c^4$, $[2.5, 4.0]\,\mathrm{GeV}^2/c^4$, $[4.0, 6.0]\,\mathrm{GeV}^2/c^4$ and $[6.0, 8.0]\,\mathrm{GeV}^2/c^4$. The means and widths of Gaussian functions fitted to the pull distributions for the $P_i^{(\prime)}$ basis are provided. In addition, the widths of the distributions of the fitted parameter values are given in the sensitivity column.

$15.0 < q^2 < 17.0$ GeV$^2/c^4$

	sensitivity	pull mean	pull width
F_{L}	0.031 ± 0.001	-0.013 ± 0.046	1.035 ± 0.033
P_1	0.120 ± 0.004	-0.116 ± 0.045	1.007 ± 0.032
P_2	0.026 ± 0.001	0.107 ± 0.048	1.068 ± 0.034
P_3	0.059 ± 0.002	-0.010 ± 0.045	1.002 ± 0.032
P_4'	0.082 ± 0.003	0.091 ± 0.045	1.004 ± 0.032
P_5'	0.090 ± 0.003	0.027 ± 0.048	1.073 ± 0.034
P_6'	0.095 ± 0.003	0.058 ± 0.046	1.039 ± 0.033
P_8'	0.089 ± 0.003	-0.005 ± 0.045	0.998 ± 0.032
F_{S}	0.042 ± 0.001	0.066 ± 0.046	1.022 ± 0.032
S_{S1}	0.061 ± 0.002	0.010 ± 0.044	0.989 ± 0.031
S_{S2}	0.042 ± 0.001	-0.022 ± 0.046	1.023 ± 0.032
S_{S3}	0.042 ± 0.001	-0.039 ± 0.045	1.009 ± 0.032
S_{S4}	0.050 ± 0.002	-0.003 ± 0.045	1.011 ± 0.032
S_{S5}	0.052 ± 0.002	-0.017 ± 0.048	1.077 ± 0.034

$17.0 < q^2 < 19.0$ GeV$^2/c^4$

	sensitivity	pull mean	pull width
F_{L}	0.035 ± 0.001	0.072 ± 0.044	0.981 ± 0.031
P_1	0.152 ± 0.005	-0.081 ± 0.045	1.002 ± 0.032
P_2	0.035 ± 0.001	0.023 ± 0.046	1.035 ± 0.033
P_3	0.076 ± 0.002	0.025 ± 0.046	1.021 ± 0.032
P_4'	0.112 ± 0.004	0.157 ± 0.047	1.053 ± 0.033
P_5'	0.105 ± 0.003	0.025 ± 0.046	1.035 ± 0.033
P_6'	0.124 ± 0.004	-0.102 ± 0.048	1.074 ± 0.034
P_8'	0.118 ± 0.004	0.000 ± 0.046	1.022 ± 0.032
F_{S}	0.046 ± 0.001	0.008 ± 0.039	0.863 ± 0.027
S_{S1}	0.077 ± 0.002	-0.018 ± 0.046	1.031 ± 0.033
S_{S2}	0.058 ± 0.002	-0.004 ± 0.048	1.083 ± 0.034
S_{S3}	0.054 ± 0.002	-0.006 ± 0.049	1.099 ± 0.035
S_{S4}	0.067 ± 0.002	0.018 ± 0.047	1.058 ± 0.033
S_{S5}	0.068 ± 0.002	0.019 ± 0.046	1.040 ± 0.033

$11.0 < q^2 < 12.5$ GeV$^2/c^4$

	sensitivity	pull mean	pull width
F_{L}	0.035 ± 0.001	-0.013 ± 0.045	1.012 ± 0.032
P_1	0.161 ± 0.005	-0.026 ± 0.045	1.014 ± 0.032
P_2	0.037 ± 0.001	0.094 ± 0.048	1.082 ± 0.034
P_3	0.082 ± 0.003	-0.019 ± 0.046	1.038 ± 0.033
P_4'	0.097 ± 0.003	0.084 ± 0.047	1.055 ± 0.033
P_5'	0.100 ± 0.003	0.085 ± 0.044	0.985 ± 0.031
P_6'	0.103 ± 0.003	0.075 ± 0.044	0.983 ± 0.031
P_8'	0.106 ± 0.003	0.035 ± 0.048	1.063 ± 0.034
F_{S}	0.046 ± 0.001	0.061 ± 0.041	0.917 ± 0.029
S_{S1}	0.080 ± 0.003	-0.006 ± 0.047	1.043 ± 0.033
S_{S2}	0.057 ± 0.002	-0.107 ± 0.050	1.124 ± 0.036
S_{S3}	0.054 ± 0.002	0.012 ± 0.047	1.052 ± 0.033
S_{S4}	0.057 ± 0.002	0.012 ± 0.045	1.009 ± 0.032
S_{S5}	0.060 ± 0.002	0.032 ± 0.048	1.078 ± 0.034

$1.1 < q^2 < 6.0$ GeV$^2/c^4$

	sensitivity	pull mean	pull width
F_{L}	0.0301 ± 0.0010	0.031 ± 0.045	1.007 ± 0.032
P_1	0.2610 ± 0.0083	0.043 ± 0.044	0.991 ± 0.031
P_2	0.0676 ± 0.0021	0.062 ± 0.046	1.030 ± 0.033
P_3	0.1259 ± 0.0040	-0.069 ± 0.044	0.977 ± 0.031
P_4'	0.1033 ± 0.0033	0.011 ± 0.049	1.090 ± 0.035
P_5'	0.0909 ± 0.0029	-0.007 ± 0.044	0.989 ± 0.031
P_6'	0.0927 ± 0.0029	0.027 ± 0.046	1.018 ± 0.032
P_8'	0.0953 ± 0.0030	0.036 ± 0.044	0.984 ± 0.031
F_{S}	0.0384 ± 0.0012	0.055 ± 0.047	1.047 ± 0.033
S_{S1}	0.0675 ± 0.0021	-0.065 ± 0.045	1.005 ± 0.032
S_{S2}	0.0419 ± 0.0013	0.015 ± 0.044	0.987 ± 0.031
S_{S3}	0.0350 ± 0.0011	-0.074 ± 0.041	0.906 ± 0.029
S_{S4}	0.0387 ± 0.0012	-0.059 ± 0.044	0.992 ± 0.031
S_{S5}	0.0428 ± 0.0014	-0.078 ± 0.045	0.999 ± 0.032

$15.0 < q^2 < 19.0$ GeV$^2/c^4$

	sensitivity	pull mean	pull width
F_{L}	0.0239 ± 0.0008	-0.000 ± 0.046	1.022 ± 0.032
P_1	0.0941 ± 0.0030	-0.002 ± 0.044	0.989 ± 0.031
P_2	0.0212 ± 0.0007	0.006 ± 0.045	1.010 ± 0.032
P_3	0.0497 ± 0.0016	0.006 ± 0.047	1.048 ± 0.033
P_4'	0.0671 ± 0.0021	0.021 ± 0.047	1.051 ± 0.033
P_5'	0.0664 ± 0.0021	0.019 ± 0.046	1.038 ± 0.033
P_6'	0.0700 ± 0.0022	-0.011 ± 0.043	0.964 ± 0.030
P_8'	0.0744 ± 0.0024	-0.018 ± 0.046	1.026 ± 0.032
F_{S}	0.0299 ± 0.0009	-0.020 ± 0.046	1.028 ± 0.033
S_{S1}	0.0492 ± 0.0016	-0.081 ± 0.044	0.991 ± 0.031
S_{S2}	0.0322 ± 0.0010	-0.037 ± 0.042	0.939 ± 0.030
S_{S3}	0.0317 ± 0.0010	-0.021 ± 0.042	0.941 ± 0.030
S_{S4}	0.0391 ± 0.0012	-0.007 ± 0.043	0.969 ± 0.031
S_{S5}	0.0420 ± 0.0013	0.010 ± 0.047	1.043 ± 0.033

Table D.4: Results from 500 pseudoexperiments corresponding to the combined Run 1 and 2016 data for the q^2 bins $[11.0, 12.5]\,\mathrm{GeV}^2/c^4$, $[15.0, 17.0]\,\mathrm{GeV}^2/c^4$, $[17.0, 19.0]\,\mathrm{GeV}^2/c^4$, $[1.1, 6.0]\,\mathrm{GeV}^2/c^4$ and $[15.0, 19.0]\,\mathrm{GeV}^2/c^4$. The means and widths of Gaussian functions fitted to the pull distributions for the $P_i^{(\prime)}$ basis are provided. In addition, the widths of the distributions of the fitted parameter values are given in the sensitivity column.

$0.1 < q^2 < 0.98\ \mathrm{GeV}^2/c^4$

	sensitivity	pull mean	pull width
F_L	0.031 ± 0.001	-0.042 ± 0.023	1.033 ± 0.016
S_3	0.043 ± 0.001	-0.007 ± 0.023	1.007 ± 0.016
S_4	0.049 ± 0.001	-0.035 ± 0.023	1.000 ± 0.016
S_5	0.042 ± 0.001	0.038 ± 0.022	0.985 ± 0.016
A_FB	0.040 ± 0.001	0.010 ± 0.022	0.986 ± 0.016
S_7	0.042 ± 0.001	-0.021 ± 0.023	1.037 ± 0.017
S_8	0.049 ± 0.001	0.004 ± 0.023	1.001 ± 0.016
S_9	0.042 ± 0.001	-0.039 ± 0.022	0.995 ± 0.016
F_S	0.026 ± 0.000	0.208 ± 0.014	0.637 ± 0.010
S_S1	0.068 ± 0.001	0.016 ± 0.024	1.050 ± 0.017
S_S2	0.065 ± 0.001	0.016 ± 0.023	1.012 ± 0.016
S_S3	0.054 ± 0.001	-0.009 ± 0.023	1.019 ± 0.016
S_S4	0.053 ± 0.001	0.053 ± 0.023	1.038 ± 0.017
S_S5	0.063 ± 0.001	-0.020 ± 0.022	0.980 ± 0.016

$1.1 < q^2 < 2.5\ \mathrm{GeV}^2/c^4$

	sensitivity	pull mean	pull width
F_L	0.052 ± 0.001	0.075 ± 0.022	0.965 ± 0.015
S_3	0.062 ± 0.001	0.003 ± 0.024	1.087 ± 0.017
S_4	0.078 ± 0.001	0.146 ± 0.024	1.065 ± 0.017
S_5	0.067 ± 0.001	-0.094 ± 0.023	1.014 ± 0.016
A_FB	0.052 ± 0.001	-0.110 ± 0.024	1.067 ± 0.017
S_7	0.072 ± 0.001	-0.051 ± 0.024	1.059 ± 0.017
S_8	0.082 ± 0.001	-0.014 ± 0.024	1.078 ± 0.017
S_9	0.063 ± 0.001	-0.066 ± 0.025	1.098 ± 0.017
F_S	0.055 ± 0.001	0.135 ± 0.018	0.818 ± 0.013
S_S1	0.115 ± 0.002	0.123 ± 0.023	1.031 ± 0.016
S_S2	0.087 ± 0.001	0.141 ± 0.025	1.121 ± 0.018
S_S3	0.073 ± 0.001	-0.082 ± 0.024	1.075 ± 0.017
S_S4	0.076 ± 0.001	-0.006 ± 0.024	1.045 ± 0.017
S_S5	0.088 ± 0.001	-0.010 ± 0.024	1.059 ± 0.017

$2.5 < q^2 < 4.0\ \mathrm{GeV}^2/c^4$

	sensitivity	pull mean	pull width
F_L	0.057 ± 0.001	0.165 ± 0.021	0.923 ± 0.015
S_3	0.069 ± 0.001	0.009 ± 0.025	1.098 ± 0.018
S_4	0.086 ± 0.001	-0.076 ± 0.024	1.042 ± 0.017
S_5	0.082 ± 0.001	-0.087 ± 0.025	1.088 ± 0.017
A_FB	0.050 ± 0.001	-0.077 ± 0.024	1.047 ± 0.017
S_7	0.078 ± 0.001	-0.042 ± 0.023	1.030 ± 0.017
S_8	0.086 ± 0.001	-0.006 ± 0.024	1.048 ± 0.017
S_9	0.069 ± 0.001	-0.018 ± 0.024	1.081 ± 0.017
F_S	0.047 ± 0.001	0.389 ± 0.014	0.605 ± 0.010
S_S1	0.141 ± 0.002	-0.045 ± 0.023	1.030 ± 0.017
S_S2	0.097 ± 0.002	-0.011 ± 0.025	1.095 ± 0.018
S_S3	0.083 ± 0.001	-0.004 ± 0.024	1.037 ± 0.017
S_S4	0.081 ± 0.001	-0.012 ± 0.024	1.051 ± 0.017
S_S5	0.094 ± 0.002	-0.028 ± 0.024	1.070 ± 0.017

$4.0 < q^2 < 6.0\ \mathrm{GeV}^2/c^4$

	sensitivity	pull mean	pull width
F_L	0.041 ± 0.001	0.103 ± 0.021	0.936 ± 0.015
S_3	0.050 ± 0.001	0.024 ± 0.022	1.003 ± 0.016
S_4	0.063 ± 0.001	-0.020 ± 0.023	1.047 ± 0.017
S_5	0.058 ± 0.001	-0.134 ± 0.022	1.002 ± 0.016
A_FB	0.036 ± 0.001	0.001 ± 0.023	1.006 ± 0.016
S_7	0.058 ± 0.001	0.006 ± 0.022	0.991 ± 0.016
S_8	0.063 ± 0.001	-0.000 ± 0.023	1.031 ± 0.016
S_9	0.051 ± 0.001	-0.044 ± 0.023	1.029 ± 0.016
F_S	0.036 ± 0.001	0.430 ± 0.013	0.588 ± 0.009
S_S1	0.111 ± 0.002	0.080 ± 0.023	1.034 ± 0.016
S_S2	0.069 ± 0.001	-0.018 ± 0.023	1.018 ± 0.016
S_S3	0.064 ± 0.001	-0.102 ± 0.023	1.014 ± 0.016
S_S4	0.063 ± 0.001	0.092 ± 0.023	1.019 ± 0.016
S_S5	0.069 ± 0.001	-0.014 ± 0.023	1.025 ± 0.016

$6.0 < q^2 < 8.0\ \mathrm{GeV}^2/c^4$

	sensitivity	pull mean	pull width
F_L	0.034 ± 0.001	0.067 ± 0.022	0.963 ± 0.015
S_3	0.044 ± 0.001	0.056 ± 0.023	1.016 ± 0.016
S_4	0.053 ± 0.001	-0.062 ± 0.024	1.053 ± 0.017
S_5	0.050 ± 0.001	-0.082 ± 0.022	1.004 ± 0.016
A_FB	0.031 ± 0.000	-0.002 ± 0.023	1.012 ± 0.016
S_7	0.052 ± 0.001	-0.052 ± 0.023	1.026 ± 0.016
S_8	0.052 ± 0.001	-0.002 ± 0.023	1.012 ± 0.016
S_9	0.042 ± 0.001	0.027 ± 0.022	0.965 ± 0.015
F_S	0.031 ± 0.000	0.392 ± 0.013	0.592 ± 0.009
S_S1	0.094 ± 0.001	-0.013 ± 0.023	1.015 ± 0.016
S_S2	0.057 ± 0.001	0.048 ± 0.022	0.997 ± 0.016
S_S3	0.055 ± 0.001	-0.027 ± 0.022	0.994 ± 0.016
S_S4	0.055 ± 0.001	0.008 ± 0.023	1.014 ± 0.016
S_S5	0.059 ± 0.001	-0.013 ± 0.023	1.012 ± 0.016

Table D.5: Results from 1000 pseudoexperiments generated using the best fit parameters for the q^2 bins $[0.1, 0.98]\,\mathrm{GeV}^2/c^4$, $[1.1, 2.5]\,\mathrm{GeV}^2/c^4$, $[2.5, 4.0]\,\mathrm{GeV}^2/c^4$, $[4.0, 6.0]\,\mathrm{GeV}^2/c^4$ and $[6.0, 8.0]\,\mathrm{GeV}^2/c^4$. The means and widths of Gaussian functions fitted to the pull distributions for the S_i basis are provided. In addition, the widths of the distributions of the fitted parameter values are given in the sensitivity column.

$15.0 < q^2 < 17.0$ GeV$^2/c^4$

	sensitivity	pull mean	pull width
F_{L}	0.030 ± 0.000	0.014 ± 0.022	0.980 ± 0.016
S_3	0.039 ± 0.001	-0.115 ± 0.024	1.054 ± 0.017
S_4	0.038 ± 0.001	-0.147 ± 0.024	1.071 ± 0.017
S_5	0.036 ± 0.001	-0.151 ± 0.023	1.019 ± 0.016
A_{FB}	0.027 ± 0.000	0.024 ± 0.021	0.933 ± 0.015
S_7	0.042 ± 0.001	0.014 ± 0.022	0.997 ± 0.016
S_8	0.044 ± 0.001	0.031 ± 0.024	1.053 ± 0.017
S_9	0.038 ± 0.001	0.006 ± 0.023	1.034 ± 0.016
F_{S}	0.030 ± 0.000	0.164 ± 0.017	0.744 ± 0.012
S_{S1}	0.068 ± 0.001	0.021 ± 0.024	1.044 ± 0.017
S_{S2}	0.047 ± 0.001	0.029 ± 0.024	1.068 ± 0.017
S_{S3}	0.047 ± 0.001	0.001 ± 0.025	1.095 ± 0.017
S_{S4}	0.052 ± 0.001	-0.018 ± 0.023	1.008 ± 0.016
S_{S5}	0.055 ± 0.001	0.006 ± 0.023	1.041 ± 0.017

$17.0 < q^2 < 19.0$ GeV$^2/c^4$

	sensitivity	pull mean	pull width
F_{L}	0.039 ± 0.001	-0.026 ± 0.023	1.000 ± 0.016
S_3	0.054 ± 0.001	0.033 ± 0.023	1.041 ± 0.017
S_4	0.054 ± 0.001	-0.025 ± 0.024	1.079 ± 0.017
S_5	0.050 ± 0.001	-0.151 ± 0.024	1.045 ± 0.017
A_{FB}	0.039 ± 0.001	-0.035 ± 0.022	0.955 ± 0.015
S_7	0.057 ± 0.001	0.010 ± 0.023	1.021 ± 0.016
S_8	0.059 ± 0.001	0.018 ± 0.023	1.033 ± 0.016
S_9	0.054 ± 0.001	0.028 ± 0.024	1.048 ± 0.017
F_{S}	0.048 ± 0.001	0.127 ± 0.019	0.863 ± 0.014
S_{S1}	0.084 ± 0.001	0.001 ± 0.023	1.031 ± 0.016
S_{S2}	0.065 ± 0.001	0.103 ± 0.024	1.074 ± 0.017
S_{S3}	0.059 ± 0.001	-0.050 ± 0.024	1.049 ± 0.017
S_{S4}	0.069 ± 0.001	-0.058 ± 0.023	1.033 ± 0.016
S_{S5}	0.073 ± 0.001	0.033 ± 0.023	1.032 ± 0.016

$11.0 < q^2 < 12.5$ GeV$^2/c^4$

	sensitivity	pull mean	pull width
F_{L}	0.036 ± 0.001	-0.063 ± 0.022	0.974 ± 0.015
S_3	0.050 ± 0.001	-0.030 ± 0.023	1.026 ± 0.016
S_4	0.050 ± 0.001	-0.114 ± 0.023	1.038 ± 0.016
S_5	0.047 ± 0.001	-0.173 ± 0.022	0.994 ± 0.016
A_{FB}	0.036 ± 0.001	0.090 ± 0.021	0.946 ± 0.015
S_7	0.054 ± 0.001	-0.058 ± 0.023	1.032 ± 0.016
S_8	0.054 ± 0.001	0.018 ± 0.023	1.026 ± 0.016
S_9	0.050 ± 0.001	0.040 ± 0.023	1.018 ± 0.016
F_{S}	0.033 ± 0.001	0.457 ± 0.014	0.631 ± 0.010
S_{S1}	0.088 ± 0.001	0.035 ± 0.024	1.051 ± 0.017
S_{S2}	0.061 ± 0.001	0.032 ± 0.023	1.014 ± 0.016
S_{S3}	0.058 ± 0.001	-0.104 ± 0.022	0.999 ± 0.016
S_{S4}	0.066 ± 0.001	-0.066 ± 0.023	1.025 ± 0.016
S_{S5}	0.069 ± 0.001	0.011 ± 0.023	1.022 ± 0.016

$1.1 < q^2 < 6.0$ GeV$^2/c^4$

	sensitivity	pull mean	pull width
F_{L}	0.027 ± 0.001	0.163 ± 0.046	0.999 ± 0.032
S_3	0.030 ± 0.001	0.097 ± 0.045	0.988 ± 0.032
S_4	0.039 ± 0.001	-0.053 ± 0.044	0.965 ± 0.031
S_5	0.037 ± 0.001	-0.103 ± 0.046	1.005 ± 0.032
A_{FB}	0.023 ± 0.001	-0.057 ± 0.044	0.966 ± 0.031
S_7	0.036 ± 0.001	0.080 ± 0.043	0.951 ± 0.031
S_8	0.038 ± 0.001	-0.032 ± 0.043	0.942 ± 0.030
S_9	0.029 ± 0.001	0.003 ± 0.043	0.945 ± 0.031
F_{S}	0.025 ± 0.001	0.542 ± 0.060	1.312 ± 0.042
S_{S1}	0.069 ± 0.002	0.101 ± 0.046	1.008 ± 0.033
S_{S2}	0.042 ± 0.001	0.097 ± 0.045	0.986 ± 0.032
S_{S3}	0.036 ± 0.001	-0.162 ± 0.042	0.929 ± 0.030
S_{S4}	0.037 ± 0.001	0.084 ± 0.043	0.945 ± 0.030
S_{S5}	0.046 ± 0.001	0.011 ± 0.048	1.056 ± 0.034

$15.0 < q^2 < 19.0$ GeV$^2/c^4$

	sensitivity	pull mean	pull width
F_{L}	0.021 ± 0.001	-0.093 ± 0.044	0.985 ± 0.031
S_3	0.029 ± 0.001	-0.050 ± 0.045	1.012 ± 0.032
S_4	0.027 ± 0.001	-0.023 ± 0.042	0.931 ± 0.029
S_5	0.026 ± 0.001	-0.068 ± 0.042	0.938 ± 0.030
A_{FB}	0.021 ± 0.001	-0.006 ± 0.044	0.984 ± 0.031
S_7	0.031 ± 0.001	-0.004 ± 0.043	0.968 ± 0.031
S_8	0.032 ± 0.001	-0.022 ± 0.044	0.984 ± 0.031
S_9	0.029 ± 0.001	-0.002 ± 0.045	1.004 ± 0.032
F_{S}	0.025 ± 0.001	-0.244 ± 0.074	1.657 ± 0.052
S_{S1}	0.047 ± 0.001	0.022 ± 0.043	0.967 ± 0.031
S_{S2}	0.036 ± 0.001	0.050 ± 0.045	1.013 ± 0.032
S_{S3}	0.032 ± 0.001	-0.072 ± 0.043	0.971 ± 0.031
S_{S4}	0.040 ± 0.001	-0.034 ± 0.045	1.002 ± 0.032
S_{S5}	0.041 ± 0.001	0.023 ± 0.044	0.990 ± 0.031

Table D.6: Results from 1000 pseudoexperiments generated using the best fit parameters for the q^2 bins $[11.0, 12.5]\,\mathrm{GeV}^2/c^4$, $[15.0, 17.0]\,\mathrm{GeV}^2/c^4$, $[17.0, 19.0]\,\mathrm{GeV}^2/c^4$, $[1.1, 6.0]\,\mathrm{GeV}^2/c^4$ and $[15.0, 19.0]\,\mathrm{GeV}^2/c^4$. The means and widths of Gaussian functions fitted to the pull distributions for the S_i basis are provided. In addition, the widths of the distributions of the fitted parameter values are given in the sensitivity column.

$0.1 < q^2 < 0.98\ \text{GeV}^2/c^4$

	sensitivity	pull mean	pull width
F_L	0.031 ± 0.000	-0.040 ± 0.023	1.024 ± 0.016
P_1	0.116 ± 0.002	0.042 ± 0.023	1.020 ± 0.016
P_2	0.037 ± 0.001	-0.015 ± 0.023	1.026 ± 0.016
P_3	0.058 ± 0.001	0.041 ± 0.023	1.018 ± 0.016
P_4'	0.116 ± 0.002	0.039 ± 0.023	1.030 ± 0.016
P_5'	0.098 ± 0.002	0.103 ± 0.022	0.990 ± 0.016
P_6'	0.096 ± 0.002	-0.042 ± 0.023	1.008 ± 0.016
P_8'	0.117 ± 0.002	-0.015 ± 0.023	1.037 ± 0.016
F_S	0.027 ± 0.000	0.228 ± 0.014	0.643 ± 0.010
S_S1	0.067 ± 0.001	-0.027 ± 0.023	1.040 ± 0.017
S_S2	0.066 ± 0.001	0.005 ± 0.023	1.026 ± 0.016
S_S3	0.054 ± 0.001	-0.030 ± 0.023	1.020 ± 0.016
S_S4	0.052 ± 0.001	0.035 ± 0.023	1.010 ± 0.016
S_S5	0.066 ± 0.001	-0.021 ± 0.023	1.023 ± 0.016

$1.1 < q^2 < 2.5\ \text{GeV}^2/c^4$

	sensitivity	pull mean	pull width
F_L	0.053 ± 0.001	0.100 ± 0.023	1.021 ± 0.016
P_1	0.347 ± 0.006	-0.005 ± 0.024	1.053 ± 0.017
P_2	0.107 ± 0.002	-0.113 ± 0.023	1.040 ± 0.017
P_3	0.171 ± 0.003	0.018 ± 0.023	1.002 ± 0.016
P_4'	0.160 ± 0.003	0.114 ± 0.023	1.033 ± 0.016
P_5'	0.138 ± 0.002	-0.050 ± 0.022	0.969 ± 0.015
P_6'	0.145 ± 0.002	-0.012 ± 0.023	1.014 ± 0.016
P_8'	0.170 ± 0.003	-0.011 ± 0.024	1.069 ± 0.017
F_S	0.053 ± 0.001	0.230 ± 0.018	0.798 ± 0.013
S_S1	0.115 ± 0.002	0.070 ± 0.023	1.025 ± 0.016
S_S2	0.085 ± 0.001	0.132 ± 0.025	1.102 ± 0.018
S_S3	0.071 ± 0.001	-0.139 ± 0.024	1.044 ± 0.017
S_S4	0.075 ± 0.001	0.006 ± 0.023	1.018 ± 0.016
S_S5	0.087 ± 0.001	0.020 ± 0.023	1.039 ± 0.017

$2.5 < q^2 < 4.0\ \text{GeV}^2/c^4$

	sensitivity	pull mean	pull width
F_L	0.054 ± 0.001	0.200 ± 0.025	1.078 ± 0.017
P_1	0.637 ± 0.010	-0.009 ± 0.021	0.930 ± 0.015
P_2	0.193 ± 0.003	-0.111 ± 0.022	0.980 ± 0.016
P_3	0.325 ± 0.005	-0.056 ± 0.021	0.928 ± 0.015
P_4'	0.220 ± 0.004	-0.094 ± 0.023	1.009 ± 0.016
P_5'	0.189 ± 0.003	-0.092 ± 0.023	0.988 ± 0.016
P_6'	0.194 ± 0.003	-0.104 ± 0.023	1.009 ± 0.016
P_8'	0.214 ± 0.003	-0.010 ± 0.024	1.035 ± 0.017
F_S	0.043 ± 0.001	0.348 ± 0.013	0.550 ± 0.009
S_S1	0.142 ± 0.002	-0.010 ± 0.024	1.035 ± 0.017
S_S2	0.095 ± 0.002	-0.018 ± 0.025	1.071 ± 0.017
S_S3	0.083 ± 0.001	0.002 ± 0.024	1.041 ± 0.017
S_S4	0.083 ± 0.001	-0.057 ± 0.024	1.061 ± 0.017
S_S5	0.094 ± 0.002	-0.026 ± 0.024	1.061 ± 0.017

$4.0 < q^2 < 6.0\ \text{GeV}^2/c^4$

	sensitivity	pull mean	pull width
F_L	0.042 ± 0.001	0.090 ± 0.021	0.958 ± 0.015
P_1	0.333 ± 0.005	0.027 ± 0.022	0.978 ± 0.015
P_2	0.081 ± 0.001	-0.015 ± 0.022	0.978 ± 0.015
P_3	0.169 ± 0.003	0.030 ± 0.022	1.000 ± 0.016
P_4'	0.133 ± 0.002	-0.028 ± 0.022	0.987 ± 0.016
P_5'	0.131 ± 0.002	-0.164 ± 0.022	1.000 ± 0.016
P_6'	0.131 ± 0.002	0.004 ± 0.023	1.016 ± 0.016
P_8'	0.131 ± 0.002	0.006 ± 0.022	0.971 ± 0.015
F_S	0.038 ± 0.001	0.444 ± 0.014	0.604 ± 0.010
S_S1	0.109 ± 0.002	0.055 ± 0.023	1.017 ± 0.016
S_S2	0.069 ± 0.001	0.026 ± 0.023	1.018 ± 0.016
S_S3	0.065 ± 0.001	-0.050 ± 0.023	1.031 ± 0.016
S_S4	0.062 ± 0.001	0.035 ± 0.022	1.002 ± 0.016
S_S5	0.071 ± 0.001	-0.023 ± 0.023	1.035 ± 0.016

$6.0 < q^2 < 8.0\ \text{GeV}^2/c^4$

	sensitivity	pull mean	pull width
F_L	0.035 ± 0.001	0.115 ± 0.022	0.976 ± 0.015
P_1	0.252 ± 0.004	0.004 ± 0.022	0.995 ± 0.016
P_2	0.059 ± 0.001	0.053 ± 0.022	0.980 ± 0.016
P_3	0.130 ± 0.002	-0.047 ± 0.023	1.013 ± 0.016
P_4'	0.107 ± 0.002	-0.144 ± 0.023	1.009 ± 0.016
P_5'	0.107 ± 0.002	-0.135 ± 0.022	0.992 ± 0.016
P_6'	0.113 ± 0.002	-0.077 ± 0.023	1.046 ± 0.017
P_8'	0.110 ± 0.002	-0.039 ± 0.023	1.013 ± 0.016
F_S	0.033 ± 0.001	0.327 ± 0.014	0.619 ± 0.010
S_S1	0.093 ± 0.001	0.016 ± 0.022	1.001 ± 0.016
S_S2	0.060 ± 0.001	0.034 ± 0.024	1.060 ± 0.017
S_S3	0.055 ± 0.001	-0.021 ± 0.023	1.009 ± 0.016
S_S4	0.057 ± 0.001	-0.025 ± 0.023	1.020 ± 0.016
S_S5	0.059 ± 0.001	0.027 ± 0.022	0.993 ± 0.016

Table D.7: Results from 1000 pseudoexperiments generated using the best fit parameters for the q^2 bins $[0.1, 0.98]\,\text{GeV}^2/c^4$, $[1.1, 2.5]\,\text{GeV}^2/c^4$, $[2.5, 4.0]\,\text{GeV}^2/c^4$, $[4.0, 6.0]\,\text{GeV}^2/c^4$ and $[6.0, 8.0]\,\text{GeV}^2/c^4$. The means and widths of Gaussian functions fitted to the pull distributions for the $P_i^{(\prime)}$ basis are provided. In addition, the widths of the distributions of the fitted parameter values are given in the sensitivity column.

$15.0 < q^2 < 17.0$ GeV$^2/c^4$

	sensitivity	pull mean	pull width
F_{L}	0.029 ± 0.000	-0.065 ± 0.023	1.004 ± 0.016
P_1	0.114 ± 0.002	-0.109 ± 0.023	1.012 ± 0.016
P_2	0.025 ± 0.000	0.115 ± 0.022	0.989 ± 0.016
P_3	0.057 ± 0.001	-0.021 ± 0.022	0.998 ± 0.016
P_4'	0.082 ± 0.001	-0.149 ± 0.024	1.064 ± 0.017
P_5'	0.080 ± 0.001	-0.171 ± 0.023	1.036 ± 0.016
P_6'	0.091 ± 0.001	0.012 ± 0.023	1.021 ± 0.016
P_8'	0.091 ± 0.001	0.014 ± 0.023	1.026 ± 0.016
F_{S}	0.028 ± 0.000	0.229 ± 0.015	0.676 ± 0.011
S_{S1}	0.068 ± 0.001	-0.058 ± 0.024	1.052 ± 0.017
S_{S2}	0.047 ± 0.001	0.007 ± 0.024	1.058 ± 0.017
S_{S3}	0.044 ± 0.001	-0.015 ± 0.023	1.022 ± 0.016
S_{S4}	0.053 ± 0.001	0.005 ± 0.023	1.006 ± 0.016
S_{S5}	0.053 ± 0.001	0.012 ± 0.023	1.003 ± 0.016

$17.0 < q^2 < 19.0$ GeV$^2/c^4$

	sensitivity	pull mean	pull width
F_{L}	0.039 ± 0.001	0.010 ± 0.023	1.039 ± 0.017
P_1	0.162 ± 0.003	-0.071 ± 0.024	1.049 ± 0.017
P_2	0.038 ± 0.001	0.030 ± 0.023	1.017 ± 0.016
P_3	0.080 ± 0.001	-0.040 ± 0.023	1.036 ± 0.017
P_4'	0.114 ± 0.002	-0.086 ± 0.024	1.071 ± 0.017
P_5'	0.106 ± 0.002	-0.110 ± 0.023	1.037 ± 0.017
P_6'	0.123 ± 0.002	-0.051 ± 0.023	1.035 ± 0.016
P_8'	0.127 ± 0.002	-0.042 ± 0.024	1.053 ± 0.017
F_{S}	0.045 ± 0.001	0.118 ± 0.018	0.821 ± 0.013
S_{S1}	0.082 ± 0.001	-0.008 ± 0.023	1.019 ± 0.016
S_{S2}	0.061 ± 0.001	-0.000 ± 0.023	1.039 ± 0.017
S_{S3}	0.058 ± 0.001	-0.045 ± 0.024	1.059 ± 0.017
S_{S4}	0.071 ± 0.001	-0.025 ± 0.024	1.054 ± 0.017
S_{S5}	0.072 ± 0.001	0.009 ± 0.023	1.021 ± 0.016

$11.0 < q^2 < 12.5$ GeV$^2/c^4$

	sensitivity	pull mean	pull width
F_{L}	0.036 ± 0.001	0.026 ± 0.023	1.019 ± 0.016
P_1	0.179 ± 0.003	-0.062 ± 0.024	1.053 ± 0.017
P_2	0.039 ± 0.001	0.137 ± 0.023	1.005 ± 0.016
P_3	0.089 ± 0.001	-0.063 ± 0.023	1.038 ± 0.017
P_4'	0.100 ± 0.002	-0.086 ± 0.024	1.047 ± 0.017
P_5'	0.099 ± 0.002	-0.073 ± 0.023	1.027 ± 0.016
P_6'	0.108 ± 0.002	-0.014 ± 0.023	1.026 ± 0.016
P_8'	0.109 ± 0.002	0.076 ± 0.023	1.037 ± 0.017
F_{S}	0.039 ± 0.001	0.208 ± 0.017	0.767 ± 0.012
S_{S1}	0.088 ± 0.001	0.016 ± 0.023	1.023 ± 0.016
S_{S2}	0.058 ± 0.001	-0.051 ± 0.024	1.048 ± 0.017
S_{S3}	0.056 ± 0.001	-0.023 ± 0.023	1.026 ± 0.016
S_{S4}	0.062 ± 0.001	-0.056 ± 0.023	1.026 ± 0.016
S_{S5}	0.064 ± 0.001	0.027 ± 0.024	1.047 ± 0.017

$1.1 < q^2 < 6.0$ GeV$^2/c^4$

	sensitivity	pull mean	pull width
F_{L}	0.027 ± 0.001	0.077 ± 0.046	0.977 ± 0.032
P_1	0.192 ± 0.006	0.030 ± 0.042	0.906 ± 0.030
P_2	0.054 ± 0.002	-0.139 ± 0.046	0.985 ± 0.032
P_3	0.098 ± 0.003	0.025 ± 0.043	0.929 ± 0.031
P_4'	0.090 ± 0.003	-0.018 ± 0.047	1.018 ± 0.034
P_5'	0.074 ± 0.002	-0.127 ± 0.043	0.923 ± 0.030
P_6'	0.082 ± 0.003	-0.038 ± 0.046	0.997 ± 0.033
P_8'	0.090 ± 0.003	-0.033 ± 0.047	1.009 ± 0.033
F_{S}	0.024 ± 0.001	0.518 ± 0.031	0.674 ± 0.022
S_{S1}	0.069 ± 0.002	0.113 ± 0.047	1.006 ± 0.033
S_{S2}	0.041 ± 0.001	-0.118 ± 0.045	0.960 ± 0.032
S_{S3}	0.038 ± 0.001	-0.085 ± 0.046	0.976 ± 0.032
S_{S4}	0.038 ± 0.001	0.091 ± 0.046	0.987 ± 0.033
S_{S5}	0.044 ± 0.001	0.073 ± 0.047	1.003 ± 0.033

$15.0 < q^2 < 19.0$ GeV$^2/c^4$

	sensitivity	pull mean	pull width
F_{L}	0.020 ± 0.001	-0.037 ± 0.043	0.939 ± 0.030
P_1	0.084 ± 0.003	-0.061 ± 0.044	0.960 ± 0.031
P_2	0.019 ± 0.001	0.035 ± 0.045	0.976 ± 0.031
P_3	0.045 ± 0.001	0.006 ± 0.047	1.027 ± 0.033
P_4'	0.060 ± 0.002	-0.102 ± 0.046	1.002 ± 0.032
P_5'	0.057 ± 0.002	-0.206 ± 0.046	1.001 ± 0.032
P_6'	0.066 ± 0.002	0.032 ± 0.045	0.987 ± 0.032
P_8'	0.068 ± 0.002	0.007 ± 0.046	1.003 ± 0.032
F_{S}	0.021 ± 0.001	-0.101 ± 0.065	1.418 ± 0.046
S_{S1}	0.049 ± 0.002	0.022 ± 0.046	1.008 ± 0.033
S_{S2}	0.035 ± 0.001	0.010 ± 0.046	1.011 ± 0.033
S_{S3}	0.031 ± 0.001	-0.025 ± 0.043	0.947 ± 0.031
S_{S4}	0.040 ± 0.001	0.055 ± 0.046	1.006 ± 0.032
S_{S5}	0.042 ± 0.001	-0.069 ± 0.046	1.017 ± 0.033

Table D.8: Results from 1000 pseudoexperiments generated using the best fit parameters for the q^2 bins $[11.0, 12.5]\,\mathrm{GeV}^2/c^4$, $[15.0, 17.0]\,\mathrm{GeV}^2/c^4$, $[17.0, 19.0]\,\mathrm{GeV}^2/c^4$, $[1.1, 6.0]\,\mathrm{GeV}^2/c^4$ and $[15.0, 19.0]\,\mathrm{GeV}^2/c^4$. The means and widths of Gaussian functions fitted to the pull distributions for the $P_i^{(\prime)}$ basis are provided. In addition, the widths of the distributions of the fitted parameter values are given in the sensitivity column.

$0.1 < q^2 < 0.98\ \mathrm{GeV}^2/c^4$

	sensitivity	pull mean	pull width
F_L	0.031 ± 0.001	-0.000 ± 0.032	1.020 ± 0.023
S_3	0.042 ± 0.001	0.038 ± 0.032	1.002 ± 0.023
S_4	0.047 ± 0.001	0.030 ± 0.031	0.977 ± 0.022
S_5	0.041 ± 0.001	0.016 ± 0.031	0.979 ± 0.022
A_FB	0.040 ± 0.001	0.017 ± 0.032	0.997 ± 0.022
S_7	0.042 ± 0.001	0.012 ± 0.033	1.047 ± 0.024
S_8	0.049 ± 0.001	0.020 ± 0.032	1.008 ± 0.023
S_9	0.044 ± 0.001	0.006 ± 0.033	1.045 ± 0.023
F_S	0.039 ± 0.001	0.005 ± 0.030	0.938 ± 0.021
S_S1	0.065 ± 0.002	0.018 ± 0.032	1.007 ± 0.023
S_S2	0.067 ± 0.002	0.043 ± 0.033	1.046 ± 0.024
S_S3	0.052 ± 0.001	0.001 ± 0.032	0.994 ± 0.022
S_S4	0.050 ± 0.001	-0.014 ± 0.031	0.974 ± 0.022
S_S5	0.063 ± 0.001	-0.027 ± 0.031	0.972 ± 0.022

$1.1 < q^2 < 2.5\ \mathrm{GeV}^2/c^4$

	sensitivity	pull mean	pull width
F_L	0.050 ± 0.001	0.022 ± 0.029	0.924 ± 0.021
S_3	0.062 ± 0.001	0.035 ± 0.035	1.097 ± 0.025
S_4	0.078 ± 0.002	0.113 ± 0.034	1.075 ± 0.024
S_5	0.070 ± 0.002	-0.052 ± 0.034	1.061 ± 0.024
A_FB	0.052 ± 0.001	0.002 ± 0.034	1.064 ± 0.024
S_7	0.071 ± 0.002	0.006 ± 0.033	1.045 ± 0.023
S_8	0.083 ± 0.002	0.016 ± 0.035	1.109 ± 0.025
S_9	0.059 ± 0.001	-0.025 ± 0.033	1.052 ± 0.024
F_S	0.063 ± 0.001	0.018 ± 0.028	0.897 ± 0.020
S_S1	0.114 ± 0.003	0.035 ± 0.032	1.023 ± 0.023
S_S2	0.086 ± 0.002	0.067 ± 0.035	1.116 ± 0.025
S_S3	0.072 ± 0.002	-0.011 ± 0.034	1.073 ± 0.024
S_S4	0.076 ± 0.002	0.037 ± 0.033	1.039 ± 0.023
S_S5	0.090 ± 0.002	0.046 ± 0.034	1.065 ± 0.024

$2.5 < q^2 < 4.0\ \mathrm{GeV}^2/c^4$

	sensitivity	pull mean	pull width
F_L	0.059 ± 0.001	-0.056 ± 0.031	0.972 ± 0.022
S_3	0.064 ± 0.001	0.048 ± 0.034	1.059 ± 0.024
S_4	0.085 ± 0.002	-0.072 ± 0.034	1.049 ± 0.024
S_5	0.076 ± 0.002	-0.028 ± 0.033	1.044 ± 0.024
A_FB	0.049 ± 0.001	0.008 ± 0.033	1.041 ± 0.024
S_7	0.079 ± 0.002	0.023 ± 0.034	1.069 ± 0.024
S_8	0.083 ± 0.002	0.021 ± 0.033	1.027 ± 0.023
S_9	0.065 ± 0.002	-0.027 ± 0.034	1.078 ± 0.024
F_S	0.082 ± 0.002	-0.021 ± 0.031	0.961 ± 0.022
S_S1	0.144 ± 0.003	0.001 ± 0.034	1.050 ± 0.024
S_S2	0.097 ± 0.002	-0.077 ± 0.035	1.080 ± 0.024
S_S3	0.081 ± 0.002	-0.071 ± 0.033	1.033 ± 0.023
S_S4	0.082 ± 0.002	-0.051 ± 0.035	1.081 ± 0.024
S_S5	0.097 ± 0.002	-0.021 ± 0.035	1.094 ± 0.025

$4.0 < q^2 < 6.0\ \mathrm{GeV}^2/c^4$

	sensitivity	pull mean	pull width
F_L	0.040 ± 0.001	0.007 ± 0.030	0.938 ± 0.021
S_3	0.050 ± 0.001	0.047 ± 0.033	1.036 ± 0.023
S_4	0.062 ± 0.001	0.039 ± 0.033	1.044 ± 0.023
S_5	0.058 ± 0.001	-0.137 ± 0.032	0.998 ± 0.022
A_FB	0.038 ± 0.001	0.030 ± 0.033	1.056 ± 0.024
S_7	0.060 ± 0.001	0.072 ± 0.033	1.051 ± 0.024
S_8	0.063 ± 0.001	-0.031 ± 0.033	1.038 ± 0.023
S_9	0.051 ± 0.001	-0.012 ± 0.033	1.052 ± 0.024
F_S	0.060 ± 0.001	0.125 ± 0.030	0.943 ± 0.021
S_S1	0.110 ± 0.003	0.109 ± 0.033	1.032 ± 0.023
S_S2	0.068 ± 0.002	0.010 ± 0.032	1.013 ± 0.023
S_S3	0.064 ± 0.001	-0.077 ± 0.033	1.030 ± 0.023
S_S4	0.062 ± 0.001	0.067 ± 0.032	1.010 ± 0.023
S_S5	0.071 ± 0.002	-0.039 ± 0.033	1.047 ± 0.023

Table D.9: Results from 500 pseudoexperiments generated using the best fit parameters, with the bound on F_S set to -1, for the q^2 bins $[0.1, 0.98]\,\mathrm{GeV}^2/c^4$, $[1.1, 2.5]\,\mathrm{GeV}^2/c^4$, $[2.5, 4.0]\,\mathrm{GeV}^2/c^4$ and $[4.0, 6.0]\,\mathrm{GeV}^2/c^4$. The means and widths of Gaussian functions fitted to the pull distributions for the S_i basis are provided. In addition, the widths of the distributions of the fitted parameter values are given in the sensitivity column.

$6.0 < q^2 < 8.0$ GeV$^2/c^4$

	sensitivity	pull mean	pull width
F_{L}	0.034 ± 0.001	0.067 ± 0.022	0.963 ± 0.015
S_3	0.044 ± 0.001	0.056 ± 0.023	1.016 ± 0.016
S_4	0.053 ± 0.001	-0.062 ± 0.024	1.053 ± 0.017
S_5	0.050 ± 0.001	-0.082 ± 0.022	1.004 ± 0.016
A_{FB}	0.031 ± 0.000	-0.002 ± 0.023	1.012 ± 0.016
S_7	0.052 ± 0.001	-0.052 ± 0.023	1.026 ± 0.016
S_8	0.052 ± 0.001	-0.002 ± 0.023	1.012 ± 0.016
S_9	0.042 ± 0.001	0.027 ± 0.022	0.965 ± 0.015
F_{S}	0.031 ± 0.000	0.392 ± 0.013	0.592 ± 0.009
S_{S1}	0.094 ± 0.001	-0.013 ± 0.023	1.015 ± 0.016
S_{S2}	0.057 ± 0.001	0.048 ± 0.022	0.997 ± 0.016
S_{S3}	0.055 ± 0.001	-0.027 ± 0.022	0.994 ± 0.016
S_{S4}	0.055 ± 0.001	0.008 ± 0.023	1.014 ± 0.016
S_{S5}	0.059 ± 0.001	-0.013 ± 0.023	1.012 ± 0.016

$15.0 < q^2 < 17.0$ GeV$^2/c^4$

	sensitivity	pull mean	pull width
F_{L}	0.030 ± 0.000	0.014 ± 0.022	0.980 ± 0.016
S_3	0.039 ± 0.001	-0.115 ± 0.024	1.054 ± 0.017
S_4	0.038 ± 0.001	-0.147 ± 0.024	1.071 ± 0.017
S_5	0.036 ± 0.001	-0.151 ± 0.023	1.019 ± 0.016
A_{FB}	0.027 ± 0.000	0.024 ± 0.021	0.933 ± 0.015
S_7	0.042 ± 0.001	0.014 ± 0.022	0.997 ± 0.016
S_8	0.044 ± 0.001	0.031 ± 0.024	1.053 ± 0.017
S_9	0.038 ± 0.001	0.006 ± 0.023	1.034 ± 0.016
F_{S}	0.030 ± 0.000	0.164 ± 0.017	0.744 ± 0.012
S_{S1}	0.068 ± 0.001	0.021 ± 0.024	1.044 ± 0.017
S_{S2}	0.047 ± 0.001	0.029 ± 0.024	1.068 ± 0.017
S_{S3}	0.047 ± 0.001	0.001 ± 0.025	1.095 ± 0.017
S_{S4}	0.052 ± 0.001	-0.018 ± 0.023	1.008 ± 0.016
S_{S5}	0.055 ± 0.001	0.006 ± 0.023	1.041 ± 0.017

$17.0 < q^2 < 19.0$ GeV$^2/c^4$

	sensitivity	pull mean	pull width
F_{L}	0.039 ± 0.001	-0.026 ± 0.023	1.000 ± 0.016
S_3	0.054 ± 0.001	0.033 ± 0.023	1.041 ± 0.017
S_4	0.054 ± 0.001	-0.025 ± 0.024	1.079 ± 0.017
S_5	0.050 ± 0.001	-0.151 ± 0.024	1.045 ± 0.017
A_{FB}	0.039 ± 0.001	-0.035 ± 0.022	0.955 ± 0.015
S_7	0.057 ± 0.001	0.010 ± 0.023	1.021 ± 0.016
S_8	0.059 ± 0.001	0.018 ± 0.023	1.033 ± 0.016
S_9	0.054 ± 0.001	0.028 ± 0.024	1.048 ± 0.017
F_{S}	0.048 ± 0.001	0.127 ± 0.019	0.863 ± 0.014
S_{S1}	0.084 ± 0.001	0.001 ± 0.023	1.031 ± 0.016
S_{S2}	0.065 ± 0.001	0.103 ± 0.024	1.074 ± 0.017
S_{S3}	0.059 ± 0.001	-0.050 ± 0.024	1.049 ± 0.017
S_{S4}	0.069 ± 0.001	-0.058 ± 0.023	1.033 ± 0.016
S_{S5}	0.073 ± 0.001	0.033 ± 0.023	1.032 ± 0.016

$11.0 < q^2 < 12.5$ GeV$^2/c^4$

	sensitivity	pull mean	pull width
F_{L}	0.036 ± 0.001	-0.063 ± 0.022	0.974 ± 0.015
S_3	0.050 ± 0.001	-0.030 ± 0.023	1.026 ± 0.016
S_4	0.050 ± 0.001	-0.114 ± 0.023	1.038 ± 0.016
S_5	0.047 ± 0.001	-0.173 ± 0.022	0.994 ± 0.016
A_{FB}	0.036 ± 0.001	0.090 ± 0.021	0.946 ± 0.015
S_7	0.054 ± 0.001	-0.058 ± 0.023	1.032 ± 0.016
S_8	0.054 ± 0.001	0.018 ± 0.023	1.026 ± 0.016
S_9	0.050 ± 0.001	0.040 ± 0.023	1.018 ± 0.016
F_{S}	0.033 ± 0.001	0.457 ± 0.014	0.631 ± 0.010
S_{S1}	0.088 ± 0.001	0.035 ± 0.024	1.051 ± 0.017
S_{S2}	0.061 ± 0.001	0.032 ± 0.023	1.014 ± 0.016
S_{S3}	0.058 ± 0.001	-0.104 ± 0.022	0.999 ± 0.016
S_{S4}	0.066 ± 0.001	-0.066 ± 0.023	1.025 ± 0.016
S_{S5}	0.069 ± 0.001	0.011 ± 0.023	1.022 ± 0.016

Table D.10: Results from 500 pseudoexperiments generated using the best fit parameters, with the lower bound on F_{S} set to -1, for the q^2 bins $[6.0, 8.0]\,\mathrm{GeV}^2/c^4$, $[11.0, 12.5]\,\mathrm{GeV}^2/c^4$, $[15.0, 17.0]\,\mathrm{GeV}^2/c^4$ and $[17.0, 19.0]\,\mathrm{GeV}^2/c^4$. The means and widths of Gaussian functions fitted to the pull distributions for the S_i basis are provided. In addition, the widths of the distributions of the fitted parameter values are given in the sensitivity column.

$0.1 < q^2 < 0.98\ \mathrm{GeV}^2/c^4$

	sensitivity	pull mean	pull width
F_L	0.031 ± 0.001	-0.067 ± 0.032	1.014 ± 0.023
P_1	0.109 ± 0.002	0.023 ± 0.031	0.974 ± 0.022
P_2	0.037 ± 0.001	-0.067 ± 0.033	1.033 ± 0.023
P_3	0.058 ± 0.001	0.032 ± 0.033	1.031 ± 0.023
P_4'	0.116 ± 0.003	0.003 ± 0.033	1.037 ± 0.023
P_5'	0.095 ± 0.002	0.003 ± 0.031	0.971 ± 0.022
P_6'	0.089 ± 0.002	0.004 ± 0.031	0.961 ± 0.022
P_8'	0.113 ± 0.003	0.010 ± 0.032	1.012 ± 0.023
F_S	0.037 ± 0.001	-0.016 ± 0.029	0.900 ± 0.020
S_S1	0.066 ± 0.002	-0.029 ± 0.033	1.024 ± 0.023
S_S2	0.064 ± 0.001	-0.008 ± 0.032	0.996 ± 0.022
S_S3	0.056 ± 0.001	0.000 ± 0.034	1.070 ± 0.024
S_S4	0.052 ± 0.001	-0.007 ± 0.032	1.017 ± 0.023
S_S5	0.063 ± 0.001	0.018 ± 0.031	0.976 ± 0.022

$1.1 < q^2 < 2.5\ \mathrm{GeV}^2/c^4$

	sensitivity	pull mean	pull width
F_L	0.053 ± 0.001	0.069 ± 0.033	1.022 ± 0.023
P_1	0.378 ± 0.009	-0.121 ± 0.034	1.058 ± 0.024
P_2	0.125 ± 0.003	0.022 ± 0.034	1.069 ± 0.024
P_3	0.207 ± 0.005	0.025 ± 0.033	1.020 ± 0.023
P_4'	0.167 ± 0.004	0.020 ± 0.033	1.039 ± 0.024
P_5'	0.138 ± 0.003	-0.040 ± 0.030	0.941 ± 0.021
P_6'	0.149 ± 0.003	0.054 ± 0.032	1.003 ± 0.023
P_8'	0.170 ± 0.004	-0.003 ± 0.033	1.038 ± 0.023
F_S	0.070 ± 0.002	0.088 ± 0.032	1.001 ± 0.023
S_S1	0.116 ± 0.003	-0.001 ± 0.033	1.030 ± 0.023
S_S2	0.086 ± 0.002	0.029 ± 0.036	1.120 ± 0.025
S_S3	0.071 ± 0.002	0.015 ± 0.034	1.066 ± 0.024
S_S4	0.076 ± 0.002	0.035 ± 0.034	1.046 ± 0.024
S_S5	0.082 ± 0.002	0.034 ± 0.032	1.003 ± 0.023

$2.5 < q^2 < 4.0\ \mathrm{GeV}^2/c^4$

	sensitivity	pull mean	pull width
F_L	0.053 ± 0.001	-0.014 ± 0.030	0.935 ± 0.021
P_1	0.587 ± 0.013	-0.093 ± 0.032	0.993 ± 0.023
P_2	0.148 ± 0.003	-0.029 ± 0.032	0.977 ± 0.022
P_3	0.295 ± 0.007	-0.060 ± 0.031	0.959 ± 0.022
P_4'	0.210 ± 0.005	0.013 ± 0.033	1.034 ± 0.024
P_5'	0.178 ± 0.004	-0.066 ± 0.032	1.001 ± 0.023
P_6'	0.178 ± 0.004	-0.038 ± 0.032	1.004 ± 0.023
P_8'	0.197 ± 0.005	-0.020 ± 0.032	1.002 ± 0.023
F_S	0.082 ± 0.002	-0.046 ± 0.031	0.944 ± 0.022
S_S1	0.138 ± 0.003	-0.008 ± 0.033	1.019 ± 0.023
S_S2	0.097 ± 0.002	0.023 ± 0.036	1.099 ± 0.025
S_S3	0.085 ± 0.002	-0.085 ± 0.035	1.082 ± 0.025
S_S4	0.083 ± 0.002	-0.007 ± 0.035	1.069 ± 0.024
S_S5	0.089 ± 0.002	-0.076 ± 0.032	1.000 ± 0.023

$4.0 < q^2 < 6.0\ \mathrm{GeV}^2/c^4$

	sensitivity	pull mean	pull width
F_L	0.041 ± 0.001	0.023 ± 0.030	0.944 ± 0.021
P_1	0.328 ± 0.008	0.010 ± 0.031	0.991 ± 0.022
P_2	0.081 ± 0.002	-0.050 ± 0.032	1.015 ± 0.023
P_3	0.160 ± 0.004	0.070 ± 0.031	0.985 ± 0.022
P_4'	0.134 ± 0.003	-0.034 ± 0.032	1.021 ± 0.023
P_5'	0.130 ± 0.003	-0.136 ± 0.032	1.009 ± 0.023
P_6'	0.124 ± 0.003	0.035 ± 0.031	0.988 ± 0.022
P_8'	0.134 ± 0.003	-0.007 ± 0.032	1.005 ± 0.023
F_S	0.059 ± 0.001	0.138 ± 0.029	0.911 ± 0.020
S_S1	0.107 ± 0.002	0.091 ± 0.032	1.007 ± 0.023
S_S2	0.072 ± 0.002	-0.004 ± 0.034	1.071 ± 0.024
S_S3	0.064 ± 0.001	-0.108 ± 0.033	1.027 ± 0.023
S_S4	0.063 ± 0.001	-0.011 ± 0.033	1.027 ± 0.023
S_S5	0.069 ± 0.002	-0.003 ± 0.032	1.018 ± 0.023

Table D.11: Results from 500 pseudoexperiments generated using the best fit parameters, with the lower bound on F_S set to -1, for the q^2 bins $[0.1, 0.98]\,\mathrm{GeV}^2/c^4$, $[1.1, 2.5]\,\mathrm{GeV}^2/c^4$, $[2.5, 4.0]\,\mathrm{GeV}^2/c^4$ and $[4.0, 6.0]\,\mathrm{GeV}^2/c^4$. The means and widths of Gaussian functions fitted to the pull distributions for the $P_i^{(\prime)}$ basis are provided. In addition, the widths of the distributions of the fitted parameter values are given in the sensitivity column.

$6.0 < q^2 < 8.0$ GeV$^2/c^4$

	sensitivity	pull mean	pull width
F_{L}	0.033 ± 0.001	-0.026 ± 0.030	0.942 ± 0.021
P_1	0.247 ± 0.006	0.008 ± 0.032	1.013 ± 0.023
P_2	0.058 ± 0.001	-0.039 ± 0.031	0.994 ± 0.022
P_3	0.125 ± 0.003	-0.024 ± 0.032	1.020 ± 0.023
P_4'	0.108 ± 0.002	-0.101 ± 0.033	1.046 ± 0.023
P_5'	0.107 ± 0.002	-0.034 ± 0.033	1.045 ± 0.023
P_6'	0.101 ± 0.002	0.009 ± 0.031	0.977 ± 0.022
P_8'	0.109 ± 0.002	-0.033 ± 0.032	1.024 ± 0.023
F_{S}	0.050 ± 0.001	0.061 ± 0.028	0.895 ± 0.020
S_{S1}	0.090 ± 0.002	0.034 ± 0.031	0.972 ± 0.022
S_{S2}	0.058 ± 0.001	0.011 ± 0.033	1.031 ± 0.023
S_{S3}	0.055 ± 0.001	-0.067 ± 0.032	1.016 ± 0.023
S_{S4}	0.056 ± 0.001	-0.030 ± 0.032	1.026 ± 0.023
S_{S5}	0.060 ± 0.001	-0.019 ± 0.032	1.009 ± 0.023

$15.0 < q^2 < 17.0$ GeV$^2/c^4$

	sensitivity	pull mean	pull width
F_{L}	0.028 ± 0.001	0.077 ± 0.032	1.017 ± 0.023
P_1	0.119 ± 0.003	-0.080 ± 0.034	1.073 ± 0.024
P_2	0.026 ± 0.001	0.087 ± 0.033	1.021 ± 0.023
P_3	0.057 ± 0.001	-0.004 ± 0.033	1.024 ± 0.023
P_4'	0.080 ± 0.002	0.015 ± 0.034	1.079 ± 0.024
P_5'	0.081 ± 0.002	-0.019 ± 0.035	1.083 ± 0.024
P_6'	0.087 ± 0.002	-0.025 ± 0.032	0.995 ± 0.022
P_8'	0.091 ± 0.002	-0.021 ± 0.033	1.048 ± 0.024
F_{S}	0.042 ± 0.001	-0.031 ± 0.031	0.975 ± 0.022
S_{S1}	0.067 ± 0.002	-0.013 ± 0.033	1.037 ± 0.023
S_{S2}	0.044 ± 0.001	-0.053 ± 0.032	1.003 ± 0.023
S_{S3}	0.045 ± 0.001	-0.011 ± 0.034	1.060 ± 0.024
S_{S4}	0.055 ± 0.001	-0.040 ± 0.034	1.052 ± 0.024
S_{S5}	0.054 ± 0.001	-0.001 ± 0.033	1.032 ± 0.023

$17.0 < q^2 < 19.0$ GeV$^2/c^4$

	sensitivity	pull mean	pull width
F_{L}	0.038 ± 0.001	-0.046 ± 0.032	1.009 ± 0.023
P_1	0.160 ± 0.004	-0.022 ± 0.034	1.070 ± 0.024
P_2	0.036 ± 0.001	-0.010 ± 0.031	0.987 ± 0.022
P_3	0.074 ± 0.002	-0.045 ± 0.032	0.992 ± 0.022
P_4'	0.119 ± 0.003	-0.125 ± 0.035	1.090 ± 0.025
P_5'	0.105 ± 0.002	-0.082 ± 0.032	1.009 ± 0.023
P_6'	0.118 ± 0.003	-0.009 ± 0.031	0.978 ± 0.022
P_8'	0.121 ± 0.003	-0.043 ± 0.031	0.982 ± 0.022
F_{S}	0.055 ± 0.001	-0.023 ± 0.030	0.953 ± 0.021
S_{S1}	0.086 ± 0.002	0.048 ± 0.034	1.067 ± 0.024
S_{S2}	0.063 ± 0.001	-0.037 ± 0.034	1.058 ± 0.024
S_{S3}	0.060 ± 0.001	-0.015 ± 0.035	1.094 ± 0.025
S_{S4}	0.067 ± 0.002	-0.007 ± 0.031	0.988 ± 0.022
S_{S5}	0.075 ± 0.002	-0.016 ± 0.033	1.043 ± 0.024

$11.0 < q^2 < 12.5$ GeV$^2/c^4$

	sensitivity	pull mean	pull width
F_{L}	0.037 ± 0.001	0.047 ± 0.033	1.034 ± 0.023
P_1	0.171 ± 0.004	0.008 ± 0.031	0.988 ± 0.022
P_2	0.039 ± 0.001	0.082 ± 0.032	0.995 ± 0.022
P_3	0.090 ± 0.002	-0.033 ± 0.033	1.029 ± 0.023
P_4'	0.098 ± 0.002	-0.063 ± 0.032	1.002 ± 0.023
P_5'	0.104 ± 0.002	-0.042 ± 0.032	1.040 ± 0.023
P_6'	0.111 ± 0.003	-0.014 ± 0.033	1.036 ± 0.023
P_8'	0.111 ± 0.003	-0.002 ± 0.033	1.037 ± 0.023
F_{S}	0.051 ± 0.001	0.050 ± 0.030	0.946 ± 0.021
S_{S1}	0.089 ± 0.002	-0.004 ± 0.033	1.021 ± 0.023
S_{S2}	0.057 ± 0.001	-0.047 ± 0.032	1.015 ± 0.023
S_{S3}	0.055 ± 0.001	-0.016 ± 0.031	0.980 ± 0.022
S_{S4}	0.062 ± 0.001	-0.009 ± 0.032	1.006 ± 0.023
S_{S5}	0.065 ± 0.002	0.021 ± 0.034	1.062 ± 0.024

Table D.12: Results from 500 pseudoexperiments generated using the best fit parameters, with the lower bound on F_{S} set to -1, for the q^2 bins $[6.0, 8.0]\,\mathrm{GeV}^2/c^4$, $[11.0, 12.5]\,\mathrm{GeV}^2/c^4$, $[15.0, 17.0]\,\mathrm{GeV}^2/c^4$ and $[17.0, 19.0]\,\mathrm{GeV}^2/c^4$. The means and widths of Gaussian functions fitted to the pull distributions for the $P_i^{(\prime)}$ basis are provided. In addition, the widths of the distributions of the fitted parameter values are given in the sensitivity column.

Appendix E

Systematic uncertainties

Table E.1: Summary of systematic uncertainties for the *CP*-averaged observables S_i in the q^2 bin $0.1 < q^2 < 0.98\,\mathrm{GeV}^2/c^4$.

	$0.1 < q^2 < 0.98\,\mathrm{GeV}^2/c^4$							
σ	F_L	S_3	S_4	S_5	A_FB	S_7	S_8	S_9
$\sigma_\mathrm{stat.}$	0.0320	0.0438	0.0497	0.0408	0.0405	0.0422	0.0514	0.0412
π reweighting	0.0033	0.0001	0.0001	0.0002	0.0005	0.0000	0.0000	0.0000
K reweighting	0.0010	0.0002	0.0000	0.0004	0.0000	0.0000	0.0000	0.0000
$p_\mathrm{T}(B^0)$ reweighting	0.0038	0.0005	0.0001	0.0007	0.0008	0.0000	0.0000	0.0000
$\chi^2_\mathrm{Vtx.}$ reweighting	0.0001	0.0000	0.0001	0.0001	0.0000	0.0000	0.0000	0.0000
N_tracks reweighting	0.0015	0.0007	0.0004	0.0001	0.0001	0.0001	0.0000	0.0000
higher order acc.	0.0015	0.0009	0.0008	0.0044	0.0017	0.0022	0.0001	0.0009
$\epsilon(q^2)$	0.0007	0.0010	0.0016	0.0013	0.0019	0.0001	0.0003	0.0005
peaking bkg.	0.0027	0.0011	0.0023	0.0056	0.0019	0.0005	0.0007	0.0005
angular bkg. model	0.0005	0.0010	0.0005	0.0002	0.0000	0.0003	0.0001	0.0010
sig. mass	0.0001	0.0000	0.0000	0.0001	0.0001	0.0000	0.0000	0.0000
$m_{K\pi}$ isobar	0.0001	0.0000	0.0001	0.0002	0.0001	0.0000	0.0000	0.0000
$m_{K\pi}$ bkg.	0.0003	0.0000	0.0002	0.0005	0.0002	0.0000	0.0000	0.0000
$m_{K\pi}$ eff.	0.0006	0.0003	0.0004	0.0010	0.0004	0.0001	0.0001	0.0000
acc. stat.	0.0015	0.0021	0.0023	0.0020	0.0023	0.0000	0.0000	0.0000
trigger	0.0003	0.0001	0.0000	0.0003	0.0001	0.0000	0.0000	0.0000
$B^+ \to K^+\mu^+\mu^-$ veto	0.0030	0.0000	0.0002	0.0001	0.0002	0.0002	0.0000	0.0000
PID	0.0003	0.0004	0.0001	0.0002	0.0003	0.0000	0.0000	0.0000
fit bias	0.0009	0.0003	0.0017	0.0018	0.0004	0.0009	0.0002	0.0016
$\sigma_\mathrm{syst.}$	0.0072	0.0031	0.0042	0.0078	0.0041	0.0025	0.0008	0.0022

Table E.2: Summary of systematic uncertainties for the *CP*-averaged observables S_i in the q^2 bin $1.1 < q^2 < 2.5\,\mathrm{GeV}^2/c^4$.

	$1.1 < q^2 < 2.5\,\mathrm{GeV}^2/c^4$							
σ	F_L	S_3	S_4	S_5	A_FB	S_7	S_8	S_9
$\sigma_\mathrm{stat.}$	0.0460	0.0517	0.0698	0.0595	0.0457	0.0634	0.0753	0.0537
π reweighting	0.0026	0.0000	0.0001	0.0000	0.0012	0.0001	0.0000	0.0000
K reweighting	0.0020	0.0000	0.0004	0.0002	0.0009	0.0000	0.0000	0.0000
$p_\mathrm{T}(B^0)$ reweighting	0.0024	0.0000	0.0000	0.0003	0.0016	0.0002	0.0000	0.0000
$\chi^2_\mathrm{Vtx.}$ reweighting	0.0003	0.0000	0.0003	0.0004	0.0002	0.0000	0.0000	0.0000
N_tracks reweighting	0.0015	0.0001	0.0002	0.0003	0.0004	0.0001	0.0000	0.0000
higher order acc.	0.0058	0.0014	0.0002	0.0037	0.0019	0.0010	0.0010	0.0005
$\epsilon(q^2)$	0.0088	0.0012	0.0018	0.0017	0.0027	0.0009	0.0004	0.0004
peaking bkg.	0.0074	0.0013	0.0009	0.0027	0.0038	0.0004	0.0008	0.0008
angular bkg. model	0.0031	0.0002	0.0005	0.0006	0.0006	0.0002	0.0002	0.0002
sig. mass	0.0003	0.0000	0.0000	0.0001	0.0001	0.0000	0.0000	0.0000
$m_{K\pi}$ isobar	0.0002	0.0000	0.0000	0.0001	0.0001	0.0000	0.0000	0.0000
$m_{K\pi}$ bkg.	0.0016	0.0000	0.0001	0.0007	0.0007	0.0002	0.0000	0.0000
$m_{K\pi}$ eff.	0.0011	0.0001	0.0003	0.0005	0.0004	0.0001	0.0002	0.0001
acc. stat.	0.0010	0.0008	0.0014	0.0014	0.0007	0.0000	0.0000	0.0000
trigger	0.0004	0.0000	0.0000	0.0001	0.0001	0.0000	0.0000	0.0000
$B^+ \to K^+\mu^+\mu^-$ veto	0.0062	0.0000	0.0001	0.0006	0.0023	0.0004	0.0000	0.0000
PID	0.0006	0.0001	0.0005	0.0001	0.0001	0.0000	0.0000	0.0000
fit bias	0.0062	0.0005	0.0106	0.0043	0.0062	0.0041	0.0011	0.0045
$\sigma_\mathrm{syst.}$	0.0166	0.0025	0.0110	0.0068	0.0087	0.0044	0.0018	0.0046

Table E.3: Summary of systematic uncertainties for the *CP*-averaged observables S_i in the q^2 bin $2.5 < q^2 < 4.0\,\mathrm{GeV}^2/c^4$.

	$2.5 < q^2 < 4.0\,\mathrm{GeV}^2/c^4$							
σ	F_L	S_3	S_4	S_5	A_FB	S_7	S_8	S_9
$\sigma_\mathrm{stat.}$	0.0469	0.0531	0.0735	0.0677	0.0427	0.0645	0.0735	0.0554
π reweighting	0.0018	0.0000	0.0003	0.0004	0.0005	0.0001	0.0000	0.0000
K reweighting	0.0019	0.0001	0.0002	0.0003	0.0006	0.0000	0.0000	0.0000
$p_\mathrm{T}(B^0)$ reweighting	0.0021	0.0001	0.0002	0.0010	0.0008	0.0002	0.0001	0.0000
$\chi^2_\mathrm{Vtx.}$ reweighting	0.0003	0.0000	0.0003	0.0002	0.0001	0.0000	0.0000	0.0000
N_tracks reweighting	0.0012	0.0001	0.0002	0.0002	0.0004	0.0000	0.0000	0.0000
higher order acc.	0.0027	0.0006	0.0004	0.0003	0.0003	0.0015	0.0012	0.0010
$\epsilon(q^2)$	0.0100	0.0006	0.0017	0.0006	0.0026	0.0005	0.0001	0.0001
peaking bkg.	0.0137	0.0014	0.0028	0.0066	0.0022	0.0013	0.0016	0.0006
angular bkg. model	0.0029	0.0003	0.0013	0.0012	0.0011	0.0000	0.0004	0.0026
sig. mass	0.0004	0.0000	0.0001	0.0001	0.0001	0.0000	0.0000	0.0000
$m_{K\pi}$ isobar	0.0002	0.0000	0.0000	0.0001	0.0000	0.0000	0.0000	0.0000
$m_{K\pi}$ bkg.	0.0027	0.0001	0.0006	0.0013	0.0004	0.0003	0.0001	0.0000
$m_{K\pi}$ eff.	0.0010	0.0001	0.0002	0.0005	0.0002	0.0002	0.0003	0.0003
acc. stat.	0.0007	0.0007	0.0010	0.0012	0.0005	0.0000	0.0000	0.0000
trigger	0.0001	0.0000	0.0001	0.0001	0.0000	0.0000	0.0000	0.0000
$B^+ \to K^+\mu^+\mu^-$ veto	0.0076	0.0000	0.0012	0.0001	0.0018	0.0005	0.0002	0.0001
PID	0.0004	0.0002	0.0005	0.0001	0.0000	0.0000	0.0000	0.0000
fit bias	0.0118	0.0011	0.0069	0.0070	0.0042	0.0035	0.0005	0.0011
$\sigma_\mathrm{syst.}$	0.0228	0.0021	0.0080	0.0100	0.0060	0.0041	0.0022	0.0031

Table E.4: Summary of systematic uncertainties for the *CP*-averaged observables S_i in the q^2 bin $4.0 < q^2 < 6.0\,\mathrm{GeV}^2/c^4$.

	$4.0 < q^2 < 6.0\,\mathrm{GeV}^2/c^4$							
σ	F_L	S_3	S_4	S_5	A_FB	S_7	S_8	S_9
$\sigma_\mathrm{stat.}$	0.0355	0.0379	0.0568	0.0511	0.0333	0.0527	0.0622	0.0449
π reweighting	0.0018	0.0001	0.0005	0.0005	0.0003	0.0000	0.0000	0.0000
K reweighting	0.0021	0.0001	0.0000	0.0003	0.0002	0.0000	0.0000	0.0000
$p_\mathrm{T}(B^0)$ reweighting	0.0031	0.0002	0.0002	0.0014	0.0006	0.0001	0.0001	0.0000
$\chi^2_\mathrm{Vtx.}$ reweighting	0.0002	0.0001	0.0001	0.0002	0.0000	0.0000	0.0000	0.0000
N_tracks reweighting	0.0011	0.0002	0.0002	0.0002	0.0001	0.0000	0.0000	0.0000
higher order acc.	0.0013	0.0002	0.0001	0.0002	0.0003	0.0004	0.0002	0.0005
$\epsilon(q^2)$	0.0092	0.0005	0.0008	0.0018	0.0012	0.0008	0.0004	0.0002
peaking bkg.	0.0069	0.0004	0.0034	0.0085	0.0014	0.0011	0.0008	0.0003
angular bkg. model	0.0019	0.0026	0.0009	0.0008	0.0007	0.0002	0.0000	0.0006
sig. mass	0.0003	0.0000	0.0001	0.0002	0.0000	0.0000	0.0000	0.0000
$m_{K\pi}$ isobar	0.0001	0.0000	0.0001	0.0002	0.0000	0.0000	0.0000	0.0000
$m_{K\pi}$ bkg.	0.0017	0.0002	0.0010	0.0024	0.0003	0.0002	0.0001	0.0000
$m_{K\pi}$ eff.	0.0008	0.0002	0.0004	0.0009	0.0002	0.0004	0.0005	0.0003
acc. stat.	0.0006	0.0006	0.0008	0.0009	0.0004	0.0000	0.0000	0.0000
trigger	0.0001	0.0000	0.0000	0.0001	0.0000	0.0000	0.0000	0.0000
$B^+ \to K^+\mu^+\mu^-$ veto	0.0064	0.0001	0.0017	0.0016	0.0003	0.0004	0.0001	0.0000
PID	0.0001	0.0000	0.0003	0.0002	0.0001	0.0000	0.0000	0.0000
fit bias	0.0050	0.0014	0.0012	0.0083	0.0001	0.0000	0.0000	0.0018
$\sigma_\mathrm{syst.}$	0.0150	0.0031	0.0045	0.0125	0.0022	0.0016	0.0011	0.0021

Table E.5: Summary of systematic uncertainties for the *CP*-averaged observables S_i in the q^2 bin $6.0 < q^2 < 8.0\,\mathrm{GeV}^2/c^4$.

	$6.0 < q^2 < 8.0\,\mathrm{GeV}^2/c^4$							
σ	F_L	S_3	S_4	S_5	A_FB	S_7	S_8	S_9
$\sigma_\mathrm{stat.}$	0.0296	0.0384	0.0450	0.0428	0.0267	0.0458	0.0470	0.0354
π reweighting	0.0018	0.0002	0.0004	0.0006	0.0009	0.0000	0.0000	0.0000
K reweighting	0.0023	0.0001	0.0001	0.0000	0.0009	0.0000	0.0000	0.0000
$p_\mathrm{T}(B^0)$ reweighting	0.0043	0.0002	0.0001	0.0012	0.0019	0.0001	0.0001	0.0000
$\chi^2_\mathrm{Vtx.}$ reweighting	0.0002	0.0001	0.0000	0.0003	0.0001	0.0000	0.0000	0.0000
N_tracks reweighting	0.0008	0.0000	0.0003	0.0001	0.0001	0.0000	0.0000	0.0000
higher order acc.	0.0031	0.0010	0.0004	0.0010	0.0016	0.0002	0.0005	0.0012
$\epsilon(q^2)$	0.0045	0.0008	0.0009	0.0023	0.0017	0.0007	0.0001	0.0003
peaking bkg.	0.0039	0.0009	0.0040	0.0107	0.0037	0.0001	0.0011	0.0000
angular bkg. model	0.0008	0.0031	0.0003	0.0008	0.0012	0.0001	0.0000	0.0003
sig. mass	0.0001	0.0001	0.0001	0.0002	0.0001	0.0000	0.0000	0.0000
$m_{K\pi}$ isobar	0.0001	0.0000	0.0001	0.0002	0.0001	0.0000	0.0000	0.0000
$m_{K\pi}$ bkg.	0.0009	0.0003	0.0012	0.0030	0.0009	0.0002	0.0001	0.0000
$m_{K\pi}$ eff.	0.0003	0.0002	0.0005	0.0011	0.0004	0.0001	0.0004	0.0002
acc. stat.	0.0007	0.0007	0.0007	0.0007	0.0005	0.0000	0.0000	0.0000
trigger	0.0003	0.0000	0.0000	0.0000	0.0001	0.0000	0.0000	0.0000
$B^+ \to K^+\mu^+\mu^-$ veto	0.0069	0.0002	0.0020	0.0027	0.0018	0.0006	0.0000	0.0001
PID	0.0004	0.0002	0.0001	0.0003	0.0001	0.0000	0.0000	0.0000
fit bias	0.0024	0.0024	0.0031	0.0046	0.0002	0.0026	0.0000	0.0013
$\sigma_\mathrm{syst.}$	0.0113	0.0044	0.0058	0.0128	0.0055	0.0028	0.0013	0.0018

Table E.6: Summary of systematic uncertainties for the *CP*-averaged observables S_i in the q^2 bin $11.0 < q^2 < 12.5\,\mathrm{GeV}^2/c^4$.

	$11.0 < q^2 < 12.5\,\mathrm{GeV}^2/c^4$							
σ	F_L	S_3	S_4	S_5	A_FB	S_7	S_8	S_9
$\sigma_\mathrm{stat.}$	0.0315	0.0366	0.0469	0.0426	0.0297	0.0502	0.0487	0.0400
π reweighting	0.0020	0.0002	0.0003	0.0005	0.0013	0.0000	0.0000	0.0000
K reweighting	0.0016	0.0000	0.0001	0.0003	0.0009	0.0000	0.0000	0.0000
$p_\mathrm{T}(B^0)$ reweighting	0.0058	0.0000	0.0005	0.0001	0.0035	0.0000	0.0000	0.0000
$\chi^2_\mathrm{Vtx.}$ reweighting	0.0006	0.0001	0.0000	0.0001	0.0004	0.0000	0.0000	0.0000
N_tracks reweighting	0.0005	0.0006	0.0001	0.0001	0.0003	0.0000	0.0000	0.0000
higher order acc.	0.0027	0.0003	0.0002	0.0012	0.0017	0.0010	0.0011	0.0005
$\epsilon(q^2)$	0.0013	0.0017	0.0007	0.0004	0.0007	0.0002	0.0003	0.0000
peaking bkg.	0.0012	0.0002	0.0033	0.0065	0.0042	0.0003	0.0002	0.0000
angular bkg. model	0.0032	0.0017	0.0016	0.0008	0.0008	0.0002	0.0001	0.0025
sig. mass	0.0001	0.0001	0.0001	0.0002	0.0002	0.0000	0.0000	0.0000
$m_{K\pi}$ isobar	0.0001	0.0001	0.0002	0.0003	0.0002	0.0000	0.0000	0.0000
$m_{K\pi}$ bkg.	0.0004	0.0005	0.0009	0.0020	0.0012	0.0000	0.0000	0.0000
$m_{K\pi}$ eff.	0.0003	0.0005	0.0008	0.0011	0.0007	0.0003	0.0001	0.0002
acc. stat.	0.0008	0.0008	0.0006	0.0008	0.0006	0.0000	0.0000	0.0000
trigger	0.0003	0.0000	0.0000	0.0000	0.0002	0.0000	0.0000	0.0000
$B^+ \to K^+\mu^+\mu^-$ veto	0.0055	0.0004	0.0015	0.0015	0.0033	0.0005	0.0000	0.0000
PID	0.0005	0.0003	0.0003	0.0001	0.0003	0.0000	0.0000	0.0000
fit bias	0.0030	0.0015	0.0053	0.0086	0.0042	0.0031	0.0009	0.0023
$\sigma_\mathrm{syst.}$	0.0101	0.0032	0.0069	0.0113	0.0082	0.0034	0.0015	0.0034

Table E.7: Summary of systematic uncertainties for the *CP*-averaged observables S_i in the q^2 bin $15.0 < q^2 < 17.0\,\mathrm{GeV}^2/c^4$.

	$15.0 < q^2 < 17.0\,\mathrm{GeV}^2/c^4$							
σ	F_L	S_3	S_4	S_5	A_FB	S_7	S_8	S_9
$\sigma_\mathrm{stat.}$	0.0261	0.0335	0.0328	0.0340	0.0237	0.0394	0.0424	0.0374
π reweighting	0.0014	0.0004	0.0001	0.0000	0.0008	0.0000	0.0000	0.0000
K reweighting	0.0001	0.0001	0.0003	0.0001	0.0000	0.0000	0.0000	0.0000
$p_\mathrm{T}(B^0)$ reweighting	0.0056	0.0006	0.0001	0.0005	0.0032	0.0000	0.0000	0.0000
$\chi^2_\mathrm{Vtx.}$ reweighting	0.0011	0.0000	0.0001	0.0001	0.0007	0.0000	0.0000	0.0000
N_tracks reweighting	0.0010	0.0005	0.0000	0.0001	0.0006	0.0000	0.0000	0.0000
higher order acc.	0.0018	0.0011	0.0001	0.0008	0.0010	0.0000	0.0008	0.0016
$\epsilon(q^2)$	0.0035	0.0033	0.0030	0.0018	0.0021	0.0002	0.0004	0.0001
peaking bkg.	0.0017	0.0021	0.0032	0.0049	0.0039	0.0003	0.0004	0.0003
angular bkg. model	0.0041	0.0029	0.0035	0.0028	0.0015	0.0004	0.0001	0.0009
sig. mass	0.0001	0.0002	0.0000	0.0001	0.0002	0.0000	0.0000	0.0000
$m_{K\pi}$ isobar	0.0003	0.0006	0.0005	0.0008	0.0007	0.0000	0.0000	0.0000
$m_{K\pi}$ bkg.	0.0004	0.0008	0.0007	0.0011	0.0009	0.0000	0.0000	0.0000
$m_{K\pi}$ eff.	0.0003	0.0008	0.0006	0.0008	0.0006	0.0002	0.0000	0.0001
acc. stat.	0.0014	0.0014	0.0010	0.0012	0.0010	0.0000	0.0000	0.0000
trigger	0.0002	0.0000	0.0000	0.0000	0.0001	0.0000	0.0000	0.0000
$B^+ \to K^+\mu^+\mu^-$ veto	0.0036	0.0003	0.0012	0.0016	0.0023	0.0004	0.0000	0.0000
PID	0.0001	0.0004	0.0001	0.0001	0.0001	0.0000	0.0000	0.0000
fit bias	0.0002	0.0043	0.0050	0.0055	0.0015	0.0007	0.0013	0.0002
$\sigma_\mathrm{syst.}$	0.0093	0.0070	0.0077	0.0085	0.0067	0.0010	0.0016	0.0018

Table E.8: Summary of systematic uncertainties for the *CP*-averaged observables S_i in the q^2 bin $17.0 < q^2 < 19.0\,\mathrm{GeV}^2/c^4$.

	$17.0 < q^2 < 19.0\,\mathrm{GeV}^2/c^4$							
σ	F_L	S_3	S_4	S_5	A_FB	S_7	S_8	S_9
$\sigma_\mathrm{stat.}$	0.0323	0.0496	0.0406	0.0397	0.0315	0.0491	0.0460	0.0451
π reweighting	0.0008	0.0003	0.0001	0.0001	0.0003	0.0000	0.0000	0.0000
K reweighting	0.0002	0.0000	0.0001	0.0003	0.0001	0.0000	0.0000	0.0000
$p_\mathrm{T}(B^0)$ reweighting	0.0041	0.0018	0.0014	0.0003	0.0020	0.0000	0.0000	0.0000
$\chi^2_\mathrm{Vtx.}$ reweighting	0.0014	0.0005	0.0003	0.0003	0.0007	0.0000	0.0000	0.0000
N_tracks reweighting	0.0006	0.0002	0.0006	0.0000	0.0005	0.0000	0.0000	0.0000
higher order acc.	0.0074	0.0010	0.0005	0.0016	0.0048	0.0067	0.0009	0.0011
$\epsilon(q^2)$	0.0232	0.0238	0.0058	0.0103	0.0173	0.0006	0.0007	0.0006
peaking bkg.	0.0016	0.0036	0.0031	0.0034	0.0032	0.0002	0.0006	0.0006
angular bkg. model	0.0013	0.0055	0.0012	0.0009	0.0001	0.0000	0.0001	0.0014
sig. mass	0.0001	0.0003	0.0001	0.0001	0.0002	0.0000	0.0000	0.0000
$m_{K\pi}$ isobar	0.0010	0.0031	0.0021	0.0023	0.0022	0.0000	0.0000	0.0000
$m_{K\pi}$ bkg.	0.0004	0.0014	0.0010	0.0010	0.0010	0.0000	0.0000	0.0000
$m_{K\pi}$ eff.	0.0001	0.0001	0.0001	0.0000	0.0001	0.0000	0.0002	0.0001
acc. stat.	0.0020	0.0023	0.0015	0.0021	0.0017	0.0000	0.0000	0.0000
trigger	0.0001	0.0000	0.0000	0.0000	0.0001	0.0000	0.0000	0.0000
$B^+ \to K^+\mu^+\mu^-$ veto	0.0017	0.0003	0.0016	0.0009	0.0015	0.0014	0.0001	0.0001
PID	0.0001	0.0006	0.0001	0.0000	0.0000	0.0000	0.0000	0.0000
fit bias	0.0014	0.0010	0.0012	0.0081	0.0004	0.0009	0.0010	0.0010
$\sigma_\mathrm{syst.}$	0.0250	0.0252	0.0077	0.0141	0.0187	0.0070	0.0017	0.0022

Table E.9: Summary of systematic uncertainties for the *CP*-averaged observables S_i in the q^2 bin $1.1 < q^2 < 6.0\,\mathrm{GeV}^2/c^4$.

	$1.1 < q^2 < 6.0\,\mathrm{GeV}^2/c^4$							
σ	F_L	S_3	S_4	S_5	A_FB	S_7	S_8	S_9
$\sigma_\mathrm{stat.}$	0.0254	0.0251	0.0390	0.0341	0.0213	0.0340	0.0374	0.0259
π reweighting	0.0030	0.0001	0.0002	0.0004	0.0005	0.0001	0.0000	0.0000
K reweighting	0.0017	0.0000	0.0002	0.0003	0.0002	0.0000	0.0000	0.0000
$p_\mathrm{T}(B^0)$ reweighting	0.0043	0.0001	0.0001	0.0010	0.0008	0.0002	0.0001	0.0000
$\chi^2_\mathrm{Vtx.}$ reweighting	0.0005	0.0001	0.0003	0.0001	0.0001	0.0000	0.0000	0.0000
N_tracks reweighting	0.0017	0.0000	0.0004	0.0002	0.0003	0.0000	0.0000	0.0000
higher order acc.	0.0010	0.0001	0.0001	0.0002	0.0002	0.0009	0.0007	0.0004
$\epsilon(q^2)$	0.0000	0.0000	0.0000	0.0000	0.0000	0.0000	0.0000	0.0000
peaking bkg.	0.0074	0.0014	0.0022	0.0044	0.0007	0.0011	0.0007	0.0002
angular bkg. model	0.0007	0.0014	0.0005	0.0004	0.0002	0.0001	0.0001	0.0005
sig. mass	0.0004	0.0000	0.0001	0.0001	0.0000	0.0000	0.0000	0.0000
$m_{K\pi}$ isobar	0.0001	0.0000	0.0000	0.0001	0.0000	0.0000	0.0000	0.0000
$m_{K\pi}$ bkg.	0.0018	0.0001	0.0006	0.0011	0.0002	0.0003	0.0001	0.0000
$m_{K\pi}$ eff.	0.0009	0.0004	0.0002	0.0007	0.0004	0.0008	0.0008	0.0001
acc. stat.	0.0007	0.0006	0.0009	0.0011	0.0004	0.0001	0.0001	0.0001
trigger	0.0000	0.0000	0.0001	0.0001	0.0000	0.0000	0.0000	0.0000
$B^+ \to K^+\mu^+\mu^-$ veto	0.0075	0.0000	0.0011	0.0003	0.0012	0.0003	0.0001	0.0000
PID	0.0006	0.0001	0.0007	0.0003	0.0000	0.0000	0.0000	0.0000
fit bias	0.0038	0.0019	0.0005	0.0045	0.0006	0.0011	0.0009	0.0020
$\sigma_\mathrm{syst.}$	0.0129	0.0028	0.0029	0.0066	0.0019	0.0020	0.0015	0.0021

Table E.10: Summary of systematic uncertainties for the *CP*-averaged observables S_i in the q^2 bin $15.0 < q^2 < 19.0\,\mathrm{GeV}^2/c^4$.

	$15.0 < q^2 < 19.0\,\mathrm{GeV}^2/c^4$							
σ	F_L	S_3	S_4	S_5	A_FB	S_7	S_8	S_9
$\sigma_\mathrm{stat.}$	0.0202	0.0299	0.0239	0.0244	0.0202	0.0305	0.0313	0.0289
π reweighting	0.0011	0.0004	0.0001	0.0001	0.0005	0.0000	0.0000	0.0000
K reweighting	0.0000	0.0000	0.0001	0.0001	0.0000	0.0000	0.0000	0.0000
$p_\mathrm{T}(B^0)$ reweighting	0.0052	0.0012	0.0006	0.0002	0.0027	0.0000	0.0000	0.0000
$\chi^2_\mathrm{Vtx.}$ reweighting	0.0013	0.0002	0.0002	0.0002	0.0008	0.0000	0.0000	0.0000
N_tracks reweighting	0.0007	0.0003	0.0003	0.0001	0.0005	0.0000	0.0000	0.0000
higher order acc.	0.0005	0.0008	0.0001	0.0001	0.0004	0.0022	0.0001	0.0002
$\epsilon(q^2)$	0.0000	0.0000	0.0000	0.0000	0.0000	0.0000	0.0000	0.0000
peaking bkg.	0.0034	0.0065	0.0065	0.0094	0.0085	0.0003	0.0006	0.0002
angular bkg. model	0.0016	0.0044	0.0020	0.0016	0.0002	0.0002	0.0000	0.0002
sig. mass	0.0001	0.0003	0.0001	0.0002	0.0003	0.0000	0.0000	0.0000
$m_{K\pi}$ isobar	0.0004	0.0011	0.0009	0.0013	0.0011	0.0000	0.0000	0.0000
$m_{K\pi}$ bkg.	0.0004	0.0013	0.0012	0.0016	0.0014	0.0000	0.0000	0.0000
$m_{K\pi}$ eff.	0.0014	0.0037	0.0029	0.0050	0.0045	0.0007	0.0007	0.0001
acc. stat.	0.0013	0.0015	0.0010	0.0013	0.0010	0.0001	0.0001	0.0001
trigger	0.0002	0.0000	0.0000	0.0000	0.0001	0.0000	0.0000	0.0000
$B^+ \to K^+\mu^+\mu^-$ veto	0.0023	0.0002	0.0013	0.0007	0.0019	0.0009	0.0000	0.0001
PID	0.0000	0.0005	0.0002	0.0000	0.0001	0.0000	0.0000	0.0000
fit bias	0.0006	0.0014	0.0020	0.0025	0.0001	0.0015	0.0010	0.0010
$\sigma_\mathrm{syst.}$	0.0074	0.0092	0.0080	0.0114	0.0104	0.0029	0.0014	0.0011

Table E.11: Summary of systematic uncertainties for the *CP*-averaged observables $P_i^{(\prime)}$ in the q^2 bins $0.1 < q^2 < 0.98\,\mathrm{GeV}^2/c^4$.

	$0.1 < q^2 < 0.98\,\mathrm{GeV}^2/c^4$							
σ	F_L	P_1	P_2	P_3	P_4'	P_5'	P_6'	P_8'
$\sigma_\mathrm{stat.}$	0.0318	0.1191	0.0377	0.0566	0.1179	0.0946	0.0941	0.1222
π reweighting	0.0033	0.0003	0.0001	0.0000	0.0007	0.0023	0.0002	0.0000
K reweighting	0.0010	0.0004	0.0001	0.0000	0.0003	0.0002	0.0000	0.0000
$p_\mathrm{T}(B^0)$ reweighting	0.0037	0.0013	0.0003	0.0000	0.0010	0.0048	0.0004	0.0000
$\chi^2_\mathrm{Vtx.}$ reweighting	0.0001	0.0000	0.0000	0.0000	0.0003	0.0002	0.0000	0.0000
N_tracks reweighting	0.0015	0.0019	0.0002	0.0000	0.0005	0.0010	0.0001	0.0000
higher order acc.	0.0015	0.0024	0.0014	0.0012	0.0015	0.0093	0.0053	0.0001
$\epsilon(q^2)$	0.0010	0.0015	0.0003	0.0005	0.0014	0.0003	0.0006	0.0007
peaking bkg.	0.0026	0.0029	0.0013	0.0007	0.0066	0.0165	0.0014	0.0015
angular bkg. model	0.0005	0.0027	0.0000	0.0013	0.0013	0.0010	0.0006	0.0002
sig. mass	0.0001	0.0006	0.0002	0.0001	0.0006	0.0001	0.0001	0.0001
$m_{K\pi}$ isobar	0.0001	0.0000	0.0001	0.0000	0.0002	0.0007	0.0001	0.0000
$m_{K\pi}$ bkg.	0.0001	0.0002	0.0000	0.0003	0.0009	0.0010	0.0000	0.0010
$m_{K\pi}$ eff.	0.0006	0.0006	0.0003	0.0000	0.0014	0.0028	0.0004	0.0001
acc. stat.	0.0015	0.0056	0.0020	0.0000	0.0052	0.0044	0.0001	0.0001
trigger	0.0003	0.0002	0.0001	0.0000	0.0001	0.0004	0.0000	0.0000
$B^+ \to K^+\mu^+\mu^-$ veto	0.0030	0.0000	0.0001	0.0000	0.0017	0.0030	0.0001	0.0001
PID	0.0003	0.0009	0.0002	0.0000	0.0000	0.0007	0.0001	0.0000
fit bias	0.0009	0.0052	0.0005	0.0025	0.0044	0.0117	0.0036	0.0010
$\sigma_\mathrm{syst.}$	0.0071	0.0094	0.0029	0.0032	0.0102	0.0238	0.0067	0.0022

Table E.12: Summary of systematic uncertainties for the *CP*-averaged observables $P_i^{(\prime)}$ in the q^2 bins $1.1 < q^2 < 2.5\,\mathrm{GeV}^2/c^4$.

	$1.1 < q^2 < 2.5\,\mathrm{GeV}^2/c^4$							
σ	F_L	P_1	P_2	P_3	P_4'	P_5'	P_6'	P_8'
$\sigma_\mathrm{stat.}$	0.0479	0.2960	0.0999	0.1473	0.1424	0.1218	0.1280	0.1578
π reweighting	0.0026	0.0002	0.0008	0.0000	0.0000	0.0007	0.0001	0.0000
K reweighting	0.0020	0.0001	0.0008	0.0000	0.0008	0.0008	0.0001	0.0000
$p_\mathrm{T}(B^0)$ reweighting	0.0024	0.0001	0.0004	0.0000	0.0002	0.0001	0.0002	0.0000
$\chi^2_\mathrm{Vtx.}$ reweighting	0.0003	0.0000	0.0001	0.0000	0.0007	0.0009	0.0000	0.0000
N_tracks reweighting	0.0015	0.0009	0.0011	0.0000	0.0006	0.0004	0.0002	0.0000
higher order acc.	0.0059	0.0096	0.0035	0.0019	0.0001	0.0095	0.0017	0.0022
$\epsilon(q^2)$	0.0005	0.0013	0.0006	0.0007	0.0025	0.0006	0.0010	0.0009
peaking bkg.	0.0076	0.0094	0.0165	0.0023	0.0025	0.0076	0.0016	0.0015
angular bkg. model	0.0031	0.0012	0.0051	0.0007	0.0009	0.0007	0.0003	0.0003
sig. mass	0.0003	0.0004	0.0001	0.0002	0.0003	0.0001	0.0002	0.0003
$m_{K\pi}$ isobar	0.0002	0.0000	0.0004	0.0000	0.0000	0.0002	0.0001	0.0000
$m_{K\pi}$ bkg.	0.0001	0.0021	0.0002	0.0006	0.0003	0.0003	0.0003	0.0007
$m_{K\pi}$ eff.	0.0011	0.0006	0.0018	0.0002	0.0005	0.0012	0.0003	0.0002
acc. stat.	0.0009	0.0054	0.0010	0.0001	0.0030	0.0031	0.0001	0.0001
trigger	0.0004	0.0001	0.0003	0.0000	0.0001	0.0002	0.0001	0.0000
$B^+ \to K^+\mu^+\mu^-$ veto	0.0063	0.0002	0.0028	0.0001	0.0001	0.0001	0.0004	0.0000
PID	0.0006	0.0006	0.0004	0.0000	0.0011	0.0000	0.0001	0.0000
fit bias	0.0065	0.0182	0.0205	0.0133	0.0185	0.0019	0.0037	0.0036
$\sigma_\mathrm{syst.}$	0.0144	0.0235	0.0273	0.0137	0.0192	0.0129	0.0046	0.0047

Table E.13: Summary of systematic uncertainties for the *CP*-averaged observables $P_i^{(\prime)}$ in the q^2 bins $2.5 < q^2 < 4.0\,\mathrm{GeV}^2/c^4$.

	$2.5 < q^2 < 4.0\,\mathrm{GeV}^2/c^4$							
σ	F_L	P_1	P_2	P_3	P_4'	P_5'	P_6'	P_8'
$\sigma_\mathrm{stat.}$	0.0541	0.3711	0.1159	0.1952	0.1694	0.1436	0.1477	0.1690
π reweighting	0.0018	0.0001	0.0005	0.0000	0.0002	0.0002	0.0001	0.0000
K reweighting	0.0019	0.0005	0.0005	0.0000	0.0013	0.0004	0.0002	0.0000
$p_\mathrm{T}(B^0)$ reweighting	0.0021	0.0011	0.0000	0.0001	0.0006	0.0011	0.0001	0.0000
$\chi^2_\mathrm{Vtx.}$ reweighting	0.0003	0.0005	0.0001	0.0000	0.0005	0.0007	0.0000	0.0000
N_tracks reweighting	0.0012	0.0007	0.0003	0.0000	0.0000	0.0014	0.0002	0.0001
higher order acc.	0.0028	0.0053	0.0025	0.0046	0.0023	0.0027	0.0041	0.0028
$\epsilon(q^2)$	0.0003	0.0042	0.0010	0.0027	0.0002	0.0016	0.0011	0.0034
peaking bkg.	0.0136	0.0107	0.0212	0.0029	0.0119	0.0237	0.0053	0.0048
angular bkg. model	0.0030	0.0031	0.0000	0.0129	0.0017	0.0009	0.0004	0.0006
sig. mass	0.0001	0.0010	0.0001	0.0013	0.0000	0.0003	0.0001	0.0008
$m_{K\pi}$ isobar	0.0002	0.0001	0.0003	0.0000	0.0002	0.0003	0.0001	0.0000
$m_{K\pi}$ bkg.	0.0002	0.0011	0.0001	0.0004	0.0001	0.0008	0.0001	0.0002
$m_{K\pi}$ eff.	0.0010	0.0016	0.0018	0.0013	0.0009	0.0019	0.0003	0.0007
acc. stat.	0.0007	0.0066	0.0013	0.0001	0.0028	0.0031	0.0001	0.0001
trigger	0.0001	0.0003	0.0001	0.0000	0.0001	0.0003	0.0000	0.0000
$B^+ \to K^+\mu^+\mu^-$ veto	0.0077	0.0011	0.0033	0.0006	0.0005	0.0044	0.0024	0.0002
PID	0.0004	0.0015	0.0005	0.0000	0.0011	0.0006	0.0001	0.0000
fit bias	0.0107	0.0399	0.0366	0.0015	0.0327	0.0204	0.0227	0.0015
$\sigma_\mathrm{syst.}$	0.0198	0.0426	0.0425	0.0145	0.0351	0.0321	0.0238	0.0068

Table E.14: Summary of systematic uncertainties for the *CP*-averaged observables $P_i^{(\prime)}$ in the q^2 bins $4.0 < q^2 < 6.0\,\mathrm{GeV}^2/c^4$.

	$4.0 < q^2 < 6.0\,\mathrm{GeV}^2/c^4$							
σ	F_L	P_1	P_2	P_3	P_4'	P_5'	P_6'	P_8'
$\sigma_\mathrm{stat.}$	0.0362	0.2351	0.0678	0.1386	0.1151	0.1107	0.1173	0.1267
π reweighting	0.0018	0.0007	0.0004	0.0000	0.0001	0.0004	0.0000	0.0000
K reweighting	0.0021	0.0001	0.0009	0.0000	0.0011	0.0012	0.0001	0.0000
$p_\mathrm{T}(B^0)$ reweighting	0.0031	0.0019	0.0007	0.0001	0.0013	0.0003	0.0000	0.0001
$\chi^2_\mathrm{Vtx.}$ reweighting	0.0002	0.0012	0.0001	0.0000	0.0001	0.0003	0.0000	0.0000
N_tracks reweighting	0.0011	0.0010	0.0011	0.0000	0.0000	0.0014	0.0001	0.0001
higher order acc.	0.0013	0.0016	0.0017	0.0019	0.0009	0.0007	0.0009	0.0003
$\epsilon(q^2)$	0.0006	0.0010	0.0002	0.0012	0.0010	0.0016	0.0005	0.0002
peaking bkg.	0.0070	0.0009	0.0079	0.0012	0.0111	0.0249	0.0030	0.0025
angular bkg. model	0.0019	0.0202	0.0005	0.0024	0.0010	0.0000	0.0002	0.0000
sig. mass	0.0002	0.0003	0.0004	0.0007	0.0004	0.0001	0.0008	0.0011
$m_{K\pi}$ isobar	0.0001	0.0001	0.0001	0.0000	0.0002	0.0005	0.0000	0.0000
$m_{K\pi}$ bkg.	0.0003	0.0031	0.0000	0.0011	0.0003	0.0005	0.0011	0.0002
$m_{K\pi}$ eff.	0.0008	0.0006	0.0010	0.0012	0.0012	0.0027	0.0008	0.0012
acc. stat.	0.0006	0.0045	0.0011	0.0001	0.0018	0.0021	0.0001	0.0001
trigger	0.0001	0.0003	0.0000	0.0000	0.0001	0.0001	0.0000	0.0000
$B^+ \to K^+\mu^+\mu^-$ veto	0.0065	0.0006	0.0038	0.0001	0.0005	0.0021	0.0004	0.0001
PID	0.0001	0.0002	0.0001	0.0000	0.0006	0.0006	0.0000	0.0000
fit bias	0.0045	0.0192	0.0019	0.0045	0.0050	0.0253	0.0015	0.0021
$\sigma_\mathrm{syst.}$	0.0117	0.0286	0.0094	0.0059	0.0126	0.0358	0.0039	0.0036

Table E.15: Summary of systematic uncertainties for the *CP*-averaged observables $P_i^{(\prime)}$ in the q^2 bins $6.0 < q^2 < 8.0\,\mathrm{GeV}^2/c^4$.

	$6.0 < q^2 < 8.0\,\mathrm{GeV}^2/c^4$							
σ	F_L	P_1	P_2	P_3	P_4'	P_5'	P_6'	P_8'
$\sigma_\mathrm{stat.}$	0.0300	0.2111	0.0484	0.1042	0.0912	0.0897	0.0977	0.0983
π reweighting	0.0018	0.0007	0.0004	0.0000	0.0003	0.0002	0.0000	0.0000
K reweighting	0.0023	0.0002	0.0008	0.0000	0.0004	0.0011	0.0001	0.0000
$p_\mathrm{T}(B^0)$ reweighting	0.0043	0.0021	0.0011	0.0001	0.0015	0.0001	0.0000	0.0001
$\chi^2_\mathrm{Vtx.}$ reweighting	0.0002	0.0009	0.0001	0.0000	0.0000	0.0004	0.0000	0.0000
N_tracks reweighting	0.0008	0.0001	0.0006	0.0000	0.0005	0.0007	0.0001	0.0000
higher order acc.	0.0031	0.0049	0.0003	0.0034	0.0001	0.0037	0.0005	0.0010
$\epsilon(q^2)$	0.0002	0.0025	0.0009	0.0007	0.0005	0.0002	0.0007	0.0018
peaking bkg.	0.0040	0.0044	0.0106	0.0001	0.0092	0.0244	0.0003	0.0023
angular bkg. model	0.0008	0.0173	0.0030	0.0008	0.0008	0.0021	0.0001	0.0001
sig. mass	0.0001	0.0006	0.0001	0.0009	0.0004	0.0001	0.0008	0.0009
$m_{K\pi}$ isobar	0.0001	0.0001	0.0002	0.0000	0.0002	0.0005	0.0000	0.0000
$m_{K\pi}$ bkg.	0.0006	0.0029	0.0007	0.0007	0.0004	0.0006	0.0006	0.0004
$m_{K\pi}$ eff.	0.0003	0.0008	0.0011	0.0005	0.0011	0.0024	0.0003	0.0007
acc. stat.	0.0007	0.0041	0.0006	0.0000	0.0013	0.0015	0.0001	0.0000
trigger	0.0003	0.0002	0.0001	0.0000	0.0002	0.0001	0.0000	0.0000
$B^+ \to K^+\mu^+\mu^-$ veto	0.0070	0.0004	0.0041	0.0001	0.0021	0.0020	0.0009	0.0000
PID	0.0004	0.0014	0.0002	0.0000	0.0003	0.0004	0.0000	0.0000
fit bias	0.0040	0.0055	0.0047	0.0053	0.0156	0.0168	0.0085	0.0040
$\sigma_\mathrm{syst.}$	0.0110	0.0203	0.0129	0.0065	0.0184	0.0302	0.0087	0.0053

Table E.16: Summary of systematic uncertainties for the *CP*-averaged observables $P_i^{(\prime)}$ in the q^2 bins $11.0 < q^2 < 12.5\,\mathrm{GeV}^2/c^4$.

	$11.0 < q^2 < 12.5\,\mathrm{GeV}^2/c^4$							
σ	F_L	P_1	P_2	P_3	P_4'	P_5'	P_6'	P_8'
$\sigma_\mathrm{stat.}$	0.0315	0.1315	0.0326	0.0767	0.0949	0.0881	0.1000	0.0988
π reweighting	0.0020	0.0001	0.0001	0.0000	0.0009	0.0015	0.0000	0.0000
K reweighting	0.0016	0.0005	0.0002	0.0000	0.0004	0.0002	0.0000	0.0000
$p_\mathrm{T}(B^0)$ reweighting	0.0058	0.0020	0.0007	0.0000	0.0000	0.0013	0.0000	0.0000
$\chi^2_\mathrm{Vtx.}$ reweighting	0.0006	0.0002	0.0000	0.0000	0.0002	0.0000	0.0000	0.0000
N_tracks reweighting	0.0005	0.0023	0.0000	0.0000	0.0004	0.0001	0.0000	0.0000
higher order acc.	0.0027	0.0002	0.0002	0.0008	0.0008	0.0018	0.0019	0.0023
$\epsilon(q^2)$	0.0002	0.0007	0.0002	0.0005	0.0009	0.0006	0.0014	0.0007
peaking bkg.	0.0012	0.0009	0.0038	0.0001	0.0071	0.0136	0.0006	0.0004
angular bkg. model	0.0032	0.0047	0.0034	0.0043	0.0039	0.0027	0.0004	0.0002
sig. mass	0.0002	0.0024	0.0000	0.0002	0.0008	0.0015	0.0003	0.0010
$m_{K\pi}$ isobar	0.0001	0.0003	0.0002	0.0000	0.0003	0.0007	0.0000	0.0000
$m_{K\pi}$ bkg.	0.0004	0.0024	0.0002	0.0001	0.0005	0.0007	0.0009	0.0013
$m_{K\pi}$ eff.	0.0003	0.0017	0.0006	0.0002	0.0018	0.0023	0.0004	0.0002
acc. stat.	0.0008	0.0027	0.0002	0.0000	0.0013	0.0016	0.0000	0.0000
trigger	0.0003	0.0001	0.0000	0.0000	0.0000	0.0000	0.0000	0.0000
$B^+ \to K^+\mu^+\mu^-$ veto	0.0055	0.0006	0.0007	0.0000	0.0040	0.0046	0.0010	0.0000
PID	0.0005	0.0013	0.0001	0.0000	0.0004	0.0001	0.0000	0.0000
fit bias	0.0004	0.0129	0.0056	0.0054	0.0084	0.0081	0.0014	0.0087
$\sigma_\mathrm{syst.}$	0.0096	0.0149	0.0077	0.0070	0.0127	0.0173	0.0032	0.0092

Table E.17: Summary of systematic uncertainties for the *CP*-averaged observables $P_i^{(\prime)}$ in the q^2 bins $15.0 < q^2 < 17.0\,\mathrm{GeV}^2/c^4$.

	$15.0 < q^2 < 17.0\,\mathrm{GeV}^2/c^4$							
σ	F_L	P_1	P_2	P_3	P_4'	P_5'	P_6'	P_8'
$\sigma_\mathrm{stat.}$	0.0263	0.0960	0.0221	0.0556	0.0693	0.0743	0.0846	0.0865
π reweighting	0.0014	0.0003	0.0001	0.0000	0.0008	0.0005	0.0000	0.0000
K reweighting	0.0001	0.0004	0.0001	0.0000	0.0006	0.0003	0.0000	0.0000
$p_\mathrm{T}(B^0)$ reweighting	0.0056	0.0057	0.0006	0.0000	0.0020	0.0017	0.0000	0.0000
$\chi^2_\mathrm{Vtx.}$ reweighting	0.0011	0.0008	0.0000	0.0000	0.0003	0.0008	0.0000	0.0000
N_tracks reweighting	0.0010	0.0022	0.0001	0.0000	0.0004	0.0004	0.0000	0.0000
higher order acc.	0.0018	0.0023	0.0002	0.0024	0.0009	0.0008	0.0001	0.0018
$\epsilon(q^2)$	0.0001	0.0005	0.0003	0.0008	0.0014	0.0010	0.0013	0.0003
peaking bkg.	0.0017	0.0055	0.0029	0.0005	0.0074	0.0111	0.0010	0.0009
angular bkg. model	0.0041	0.0117	0.0012	0.0013	0.0090	0.0079	0.0009	0.0001
sig. mass	0.0002	0.0016	0.0001	0.0012	0.0004	0.0014	0.0011	0.0003
$m_{K\pi}$ isobar	0.0003	0.0016	0.0005	0.0000	0.0012	0.0019	0.0000	0.0000
$m_{K\pi}$ bkg.	0.0002	0.0002	0.0000	0.0002	0.0002	0.0004	0.0002	0.0000
$m_{K\pi}$ eff.	0.0003	0.0022	0.0005	0.0002	0.0016	0.0019	0.0004	0.0001
acc. stat.	0.0014	0.0042	0.0004	0.0000	0.0020	0.0023	0.0000	0.0000
trigger	0.0002	0.0001	0.0000	0.0000	0.0001	0.0001	0.0000	0.0000
$B^+ \to K^+\mu^+\mu^-$ veto	0.0036	0.0015	0.0001	0.0001	0.0039	0.0051	0.0009	0.0000
PID	0.0001	0.0012	0.0000	0.0000	0.0002	0.0002	0.0000	0.0000
fit bias	0.0021	0.0125	0.0027	0.0009	0.0119	0.0138	0.0013	0.0014
$\sigma_\mathrm{syst.}$	0.0089	0.0200	0.0043	0.0033	0.0176	0.0206	0.0027	0.0025

Table E.18: Summary of systematic uncertainties for the *CP*-averaged observables $P_i^{(\prime)}$ in the q^2 bins $17.0 < q^2 < 19.0\,\mathrm{GeV}^2/c^4$.

	$17.0 < q^2 < 19.0\,\mathrm{GeV}^2/c^4$							
σ	F_L	P_1	P_2	P_3	P_4'	P_5'	P_6'	P_8'
$\sigma_\mathrm{stat.}$	0.0333	0.1517	0.0324	0.0678	0.0862	0.0838	0.1046	0.0993
π reweighting	0.0008	0.0002	0.0001	0.0000	0.0002	0.0002	0.0000	0.0000
K reweighting	0.0002	0.0002	0.0001	0.0000	0.0002	0.0007	0.0000	0.0000
$p_\mathrm{T}(B^0)$ reweighting	0.0041	0.0097	0.0002	0.0000	0.0049	0.0023	0.0000	0.0000
$\chi^2_\mathrm{Vtx.}$ reweighting	0.0014	0.0000	0.0000	0.0000	0.0000	0.0001	0.0000	0.0000
N_tracks reweighting	0.0006	0.0010	0.0002	0.0000	0.0016	0.0001	0.0000	0.0000
higher order acc.	0.0074	0.0044	0.0009	0.0016	0.0047	0.0003	0.0143	0.0019
$\epsilon(q^2)$	0.0106	0.0894	0.0170	0.0005	0.0540	0.0567	0.0007	0.0005
peaking bkg.	0.0016	0.0094	0.0024	0.0009	0.0074	0.0078	0.0004	0.0014
angular bkg. model	0.0013	0.0179	0.0008	0.0021	0.0031	0.0024	0.0000	0.0003
sig. mass	0.0001	0.0004	0.0000	0.0000	0.0001	0.0003	0.0005	0.0020
$m_{K\pi}$ isobar	0.0010	0.0084	0.0017	0.0000	0.0050	0.0052	0.0000	0.0000
$m_{K\pi}$ bkg.	0.0001	0.0011	0.0003	0.0005	0.0004	0.0011	0.0005	0.0004
$m_{K\pi}$ eff.	0.0001	0.0002	0.0000	0.0001	0.0003	0.0001	0.0001	0.0003
acc. stat.	0.0019	0.0070	0.0012	0.0000	0.0033	0.0041	0.0000	0.0000
trigger	0.0001	0.0002	0.0000	0.0000	0.0001	0.0001	0.0000	0.0000
$B^+ \to K^+\mu^+\mu^-$ veto	0.0029	0.0028	0.0001	0.0003	0.0052	0.0015	0.0040	0.0003
PID	0.0001	0.0019	0.0001	0.0000	0.0002	0.0001	0.0000	0.0000
fit bias	0.0000	0.0133	0.0013	0.0023	0.0113	0.0132	0.0046	0.0046
$\sigma_\mathrm{syst.}$	0.0143	0.0939	0.0174	0.0038	0.0567	0.0592	0.0156	0.0056

Table E.19: Summary of systematic uncertainties for the *CP*-averaged observables $P_i^{(\prime)}$ in the q^2 bins $1.1 < q^2 < 6.0\,\mathrm{GeV}^2/c^4$.

	$1.1 < q^2 < 6.0\,\mathrm{GeV}^2/c^4$							
σ	F_L	P_1	P_2	P_3	P_4'	P_5'	P_6'	P_8'
$\sigma_\mathrm{stat.}$	0.0253	0.1593	0.0503	0.0901	0.0866	0.0683	0.0754	0.0892
π reweighting	0.0030	0.0004	0.0003	0.0000	0.0004	0.0004	0.0002	0.0000
K reweighting	0.0017	0.0001	0.0002	0.0000	0.0010	0.0001	0.0002	0.0000
$p_\mathrm{T}(B^0)$ reweighting	0.0043	0.0011	0.0001	0.0001	0.0014	0.0004	0.0000	0.0000
$\chi^2_\mathrm{Vtx.}$ reweighting	0.0005	0.0006	0.0001	0.0000	0.0004	0.0004	0.0001	0.0000
N_tracks reweighting	0.0017	0.0000	0.0000	0.0000	0.0006	0.0012	0.0002	0.0001
higher order acc.	0.0010	0.0007	0.0001	0.0016	0.0000	0.0000	0.0020	0.0014
$\epsilon(q^2)$	0.0000	0.0000	0.0000	0.0000	0.0000	0.0000	0.0000	0.0000
peaking bkg.	0.0073	0.0088	0.0048	0.0009	0.0069	0.0125	0.0031	0.0018
angular bkg. model	0.0007	0.0109	0.0008	0.0018	0.0010	0.0006	0.0003	0.0002
sig. mass	0.0002	0.0011	0.0013	0.0009	0.0003	0.0002	0.0008	0.0013
$m_{K\pi}$ isobar	0.0001	0.0000	0.0001	0.0000	0.0001	0.0002	0.0000	0.0000
$m_{K\pi}$ bkg.	0.0112	0.0042	0.0081	0.0005	0.0117	0.0201	0.0046	0.0013
$m_{K\pi}$ eff.	0.0009	0.0035	0.0014	0.0004	0.0009	0.0016	0.0008	0.0016
acc. stat.	0.0007	0.0045	0.0011	0.0003	0.0019	0.0024	0.0002	0.0002
trigger	0.0000	0.0002	0.0000	0.0000	0.0001	0.0002	0.0000	0.0000
$B^+ \to K^+\mu^+\mu^-$ veto	0.0077	0.0008	0.0005	0.0000	0.0004	0.0023	0.0001	0.0000
PID	0.0006	0.0006	0.0004	0.0000	0.0014	0.0008	0.0001	0.0000
fit bias	0.0036	0.0136	0.0062	0.0046	0.0078	0.0087	0.0061	0.0089
$\sigma_\mathrm{syst.}$	0.0170	0.0209	0.0115	0.0054	0.0161	0.0255	0.0086	0.0095

Table E.20: Summary of systematic uncertainties for the *CP*-averaged observables $P_i^{(\prime)}$ in the q^2 bins $15.0 < q^2 < 19.0\,\mathrm{GeV}^2/c^4$.

	$15.0 < q^2 < 19.0\,\mathrm{GeV}^2/c^4$							
σ	F_L	P_1	P_2	P_3	P_4'	P_5'	P_6'	P_8'
$\sigma_\mathrm{stat.}$	0.0200	0.0899	0.0181	0.0454	0.0548	0.0531	0.0667	0.0691
π reweighting	0.0011	0.0002	0.0002	0.0000	0.0004	0.0003	0.0000	0.0000
K reweighting	0.0000	0.0001	0.0000	0.0000	0.0002	0.0002	0.0000	0.0000
$p_\mathrm{T}(B^0)$ reweighting	0.0052	0.0079	0.0005	0.0000	0.0034	0.0018	0.0000	0.0000
$\chi^2_\mathrm{Vtx.}$ reweighting	0.0013	0.0003	0.0000	0.0000	0.0001	0.0002	0.0000	0.0000
N_tracks reweighting	0.0007	0.0016	0.0001	0.0000	0.0009	0.0001	0.0000	0.0000
higher order acc.	0.0005	0.0030	0.0001	0.0003	0.0002	0.0004	0.0046	0.0000
$\epsilon(q^2)$	0.0000	0.0000	0.0000	0.0000	0.0000	0.0000	0.0000	0.0000
peaking bkg.	0.0033	0.0174	0.0066	0.0001	0.0150	0.0210	0.0009	0.0013
angular bkg. model	0.0016	0.0146	0.0008	0.0003	0.0048	0.0041	0.0004	0.0000
sig. mass	0.0014	0.0122	0.0034	0.0002	0.0081	0.0106	0.0014	0.0012
$m_{K\pi}$ isobar	0.0004	0.0031	0.0009	0.0000	0.0021	0.0029	0.0000	0.0000
$m_{K\pi}$ bkg.	0.0005	0.0031	0.0018	0.0001	0.0021	0.0043	0.0008	0.0015
$m_{K\pi}$ eff.	0.0014	0.0109	0.0037	0.0001	0.0067	0.0111	0.0011	0.0017
acc. stat.	0.0013	0.0046	0.0006	0.0001	0.0022	0.0028	0.0003	0.0003
trigger	0.0002	0.0002	0.0000	0.0000	0.0001	0.0001	0.0000	0.0000
$B^+ \to K^+\mu^+\mu^-$ veto	0.0023	0.0012	0.0005	0.0002	0.0036	0.0025	0.0018	0.0001
PID	0.0000	0.0016	0.0000	0.0000	0.0004	0.0000	0.0000	0.0000
fit bias	0.0008	0.0065	0.0010	0.0017	0.0031	0.0103	0.0016	0.0019
$\sigma_\mathrm{syst.}$	0.0075	0.0307	0.0086	0.0018	0.0202	0.0291	0.0057	0.0035

Appendix F

Fit projections of the signal channel

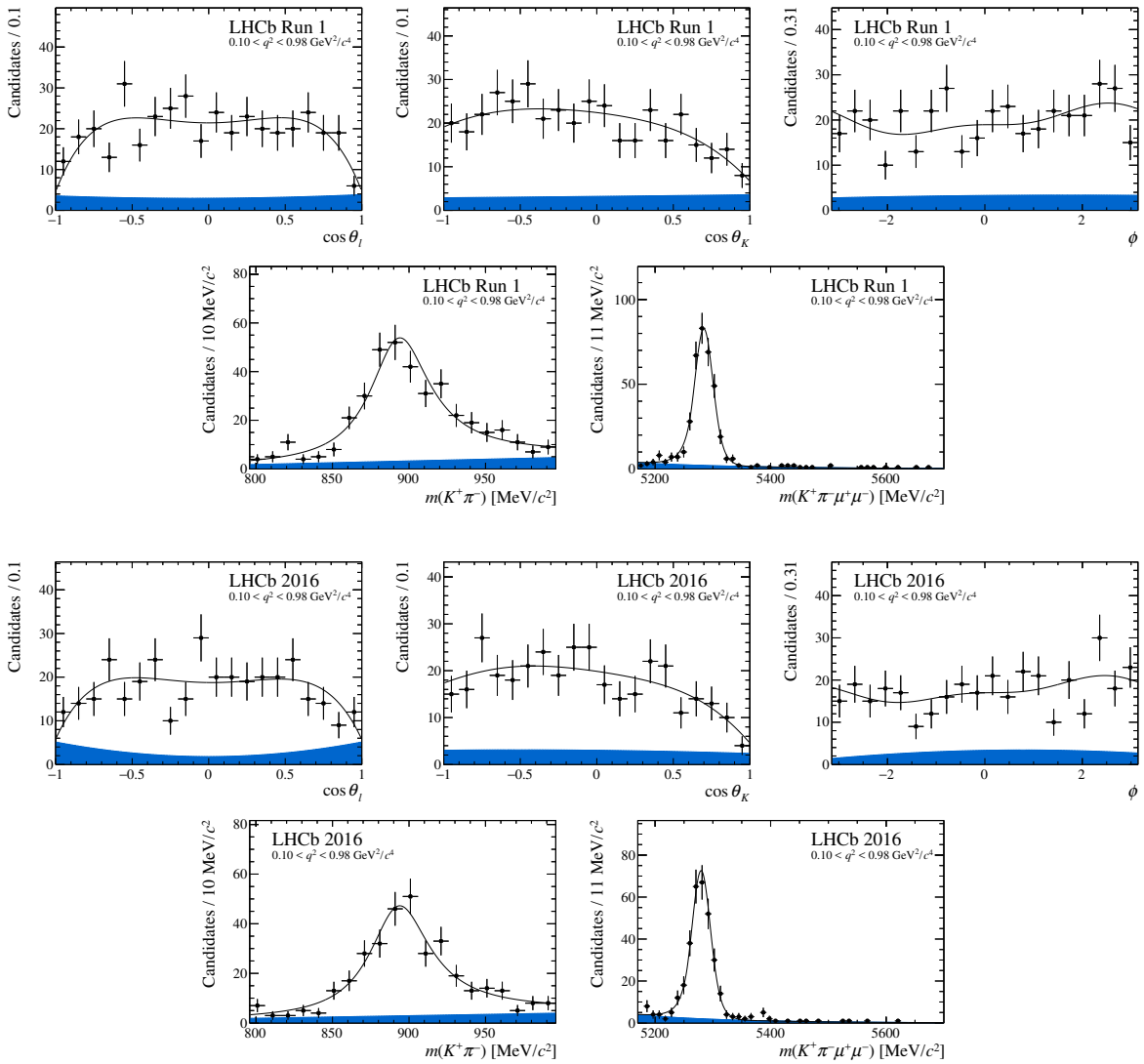


Figure F.1: Projections of the fitted probability density function on the decay angles, $m(K^+\pi^-)$ and $m(K^+\pi^-\mu^+\mu^-)$ for the bin $0.10 < q^2 < 0.98\,\mathrm{GeV}^2/c^4$. The blue shaded region indicates background. Figure taken from Ref. [1].

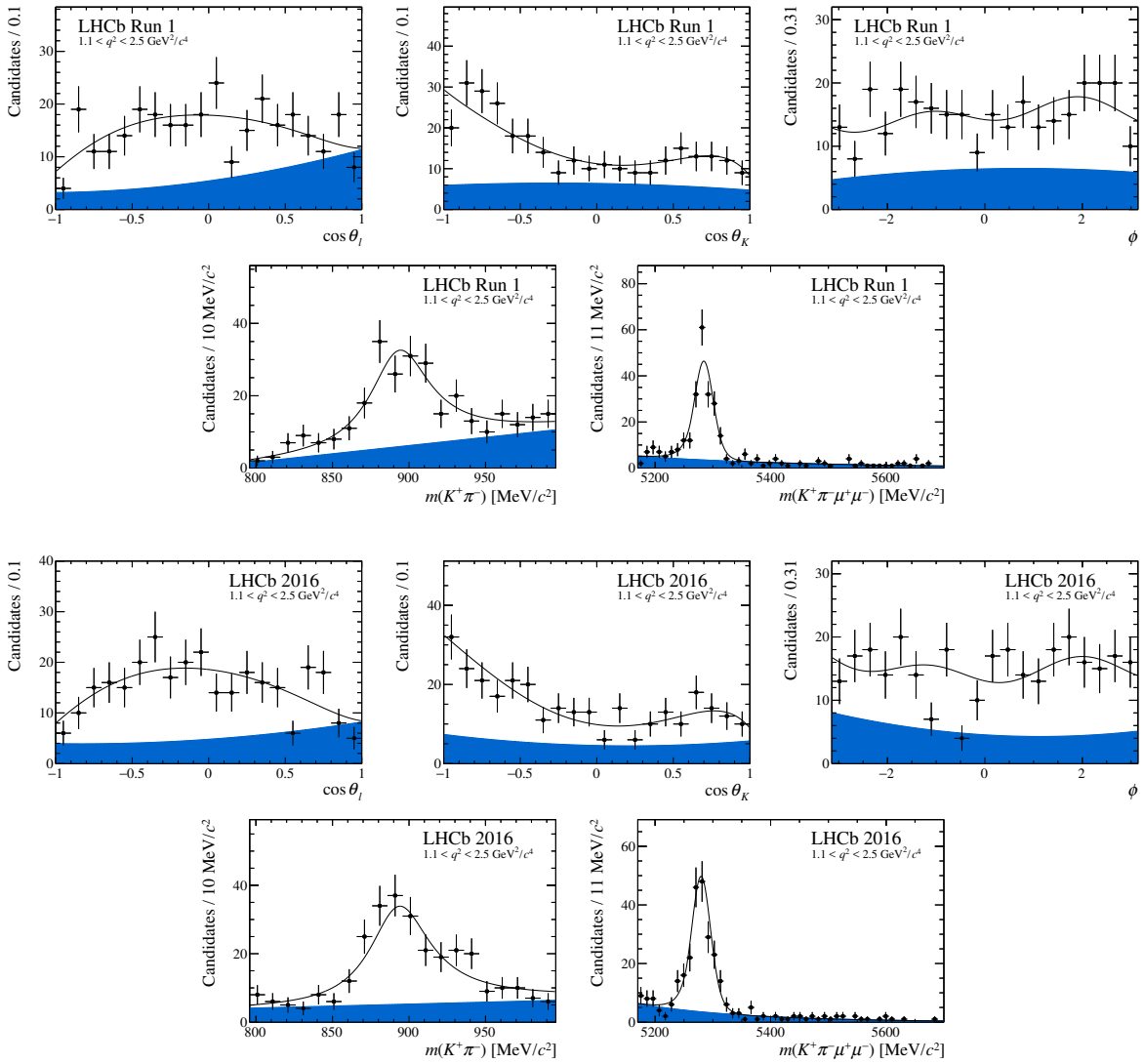


Figure F.2: Projections of the fitted probability density function on the decay angles, $m(K^+\pi^-)$ and $m(K^+\pi^-\mu^+\mu^-)$ for the bin $1.1 < q^2 < 2.5\,\mathrm{GeV}^2/c^4$. The blue shaded region indicates background. Figure taken from Ref. [1].

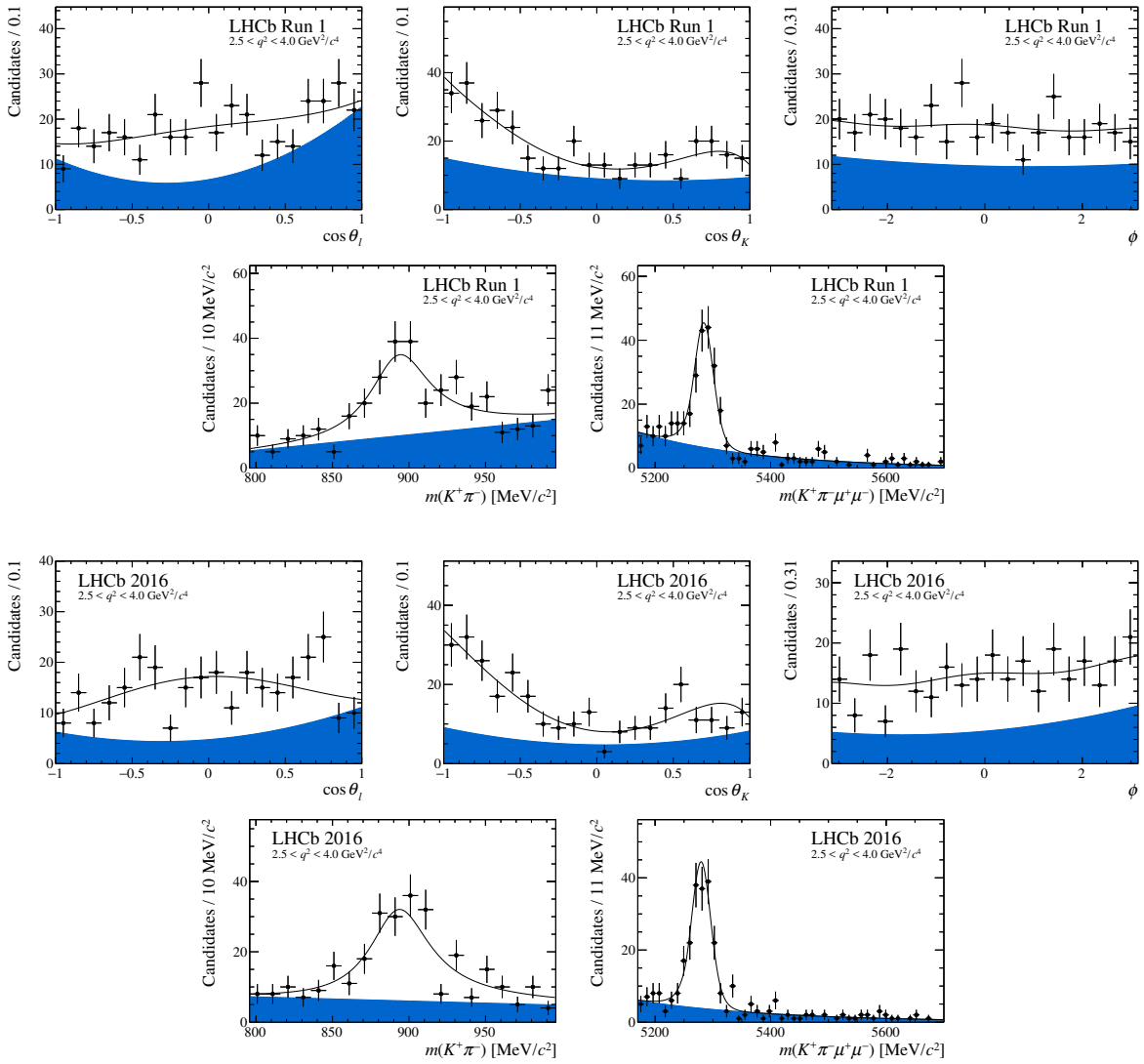


Figure F.3: Projections of the fitted probability density function on the decay angles, $m(K^+\pi^-)$ and $m(K^+\pi^-\mu^+\mu^-)$ for the bin $2.5 < q^2 < 4.0\,\mathrm{GeV}^2/c^4$. The blue shaded region indicates background. Figure taken from Ref. [1].

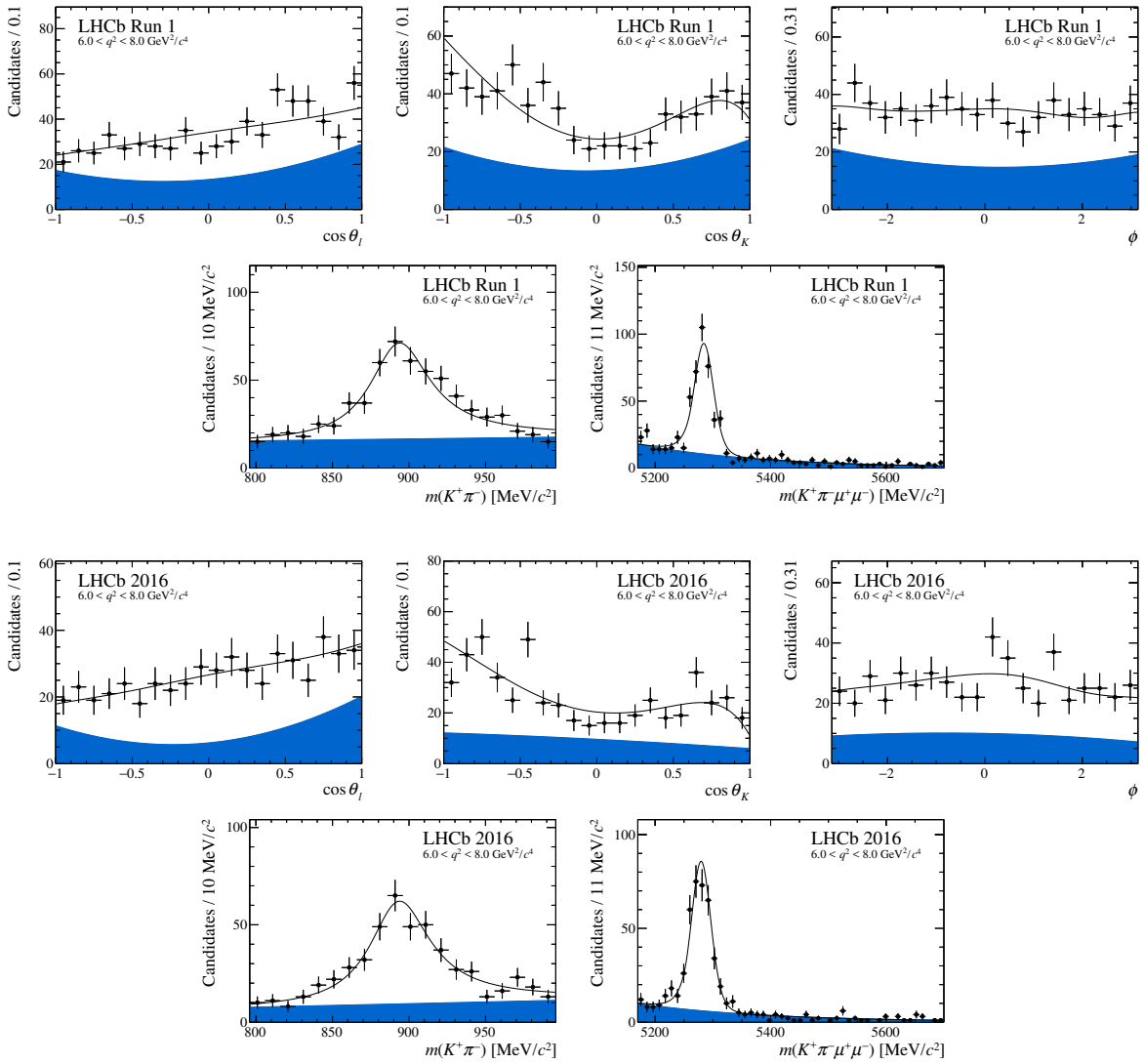


Figure F.4: Projections of the fitted probability density function on the decay angles, $m(K^+\pi^-)$ and $m(K^+\pi^-\mu^+\mu^-)$ for the bin $6.0 < q^2 < 8.0\,\mathrm{GeV}^2/c^4$. The blue shaded region indicates background. Figure taken from Ref. [1].

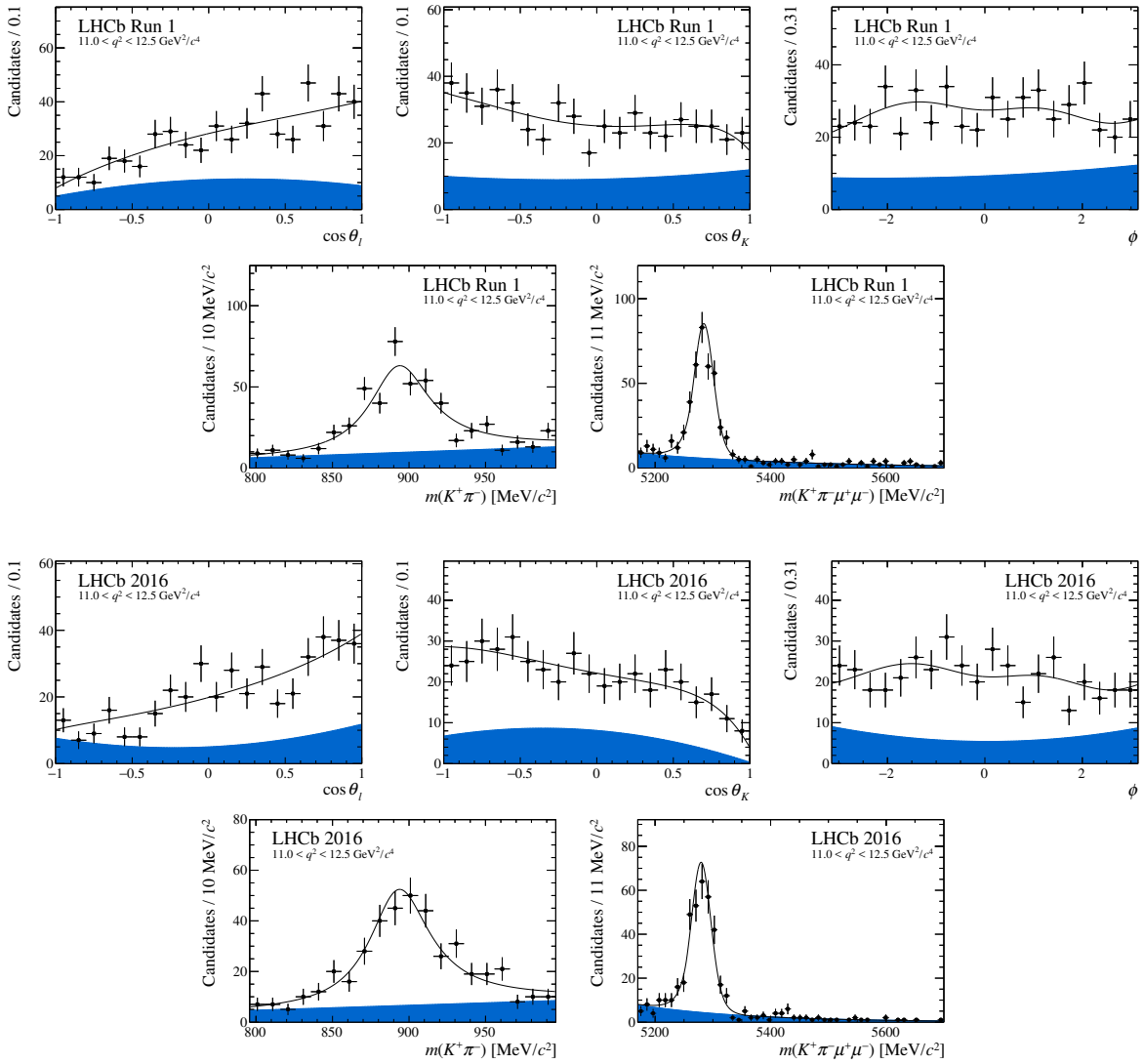


Figure F.5: Projections of the fitted probability density function on the decay angles, $m(K^+\pi^-)$ and $m(K^+\pi^-\mu^+\mu^-)$ for the bin $11.0 < q^2 < 12.5\,\mathrm{GeV}^2/c^4$. The blue shaded region indicates background. Figure taken from Ref. [1].

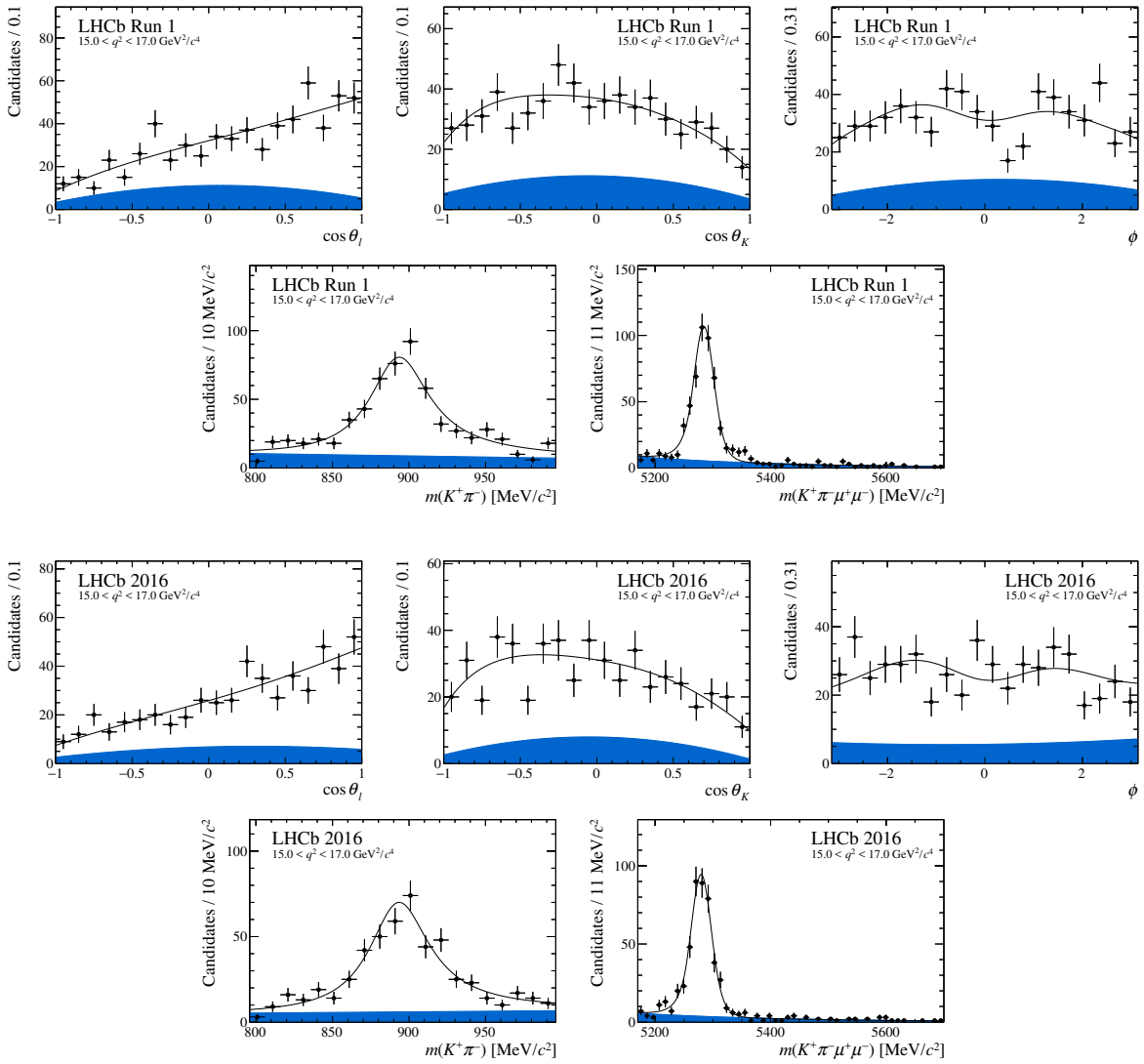


Figure F.6: Projections of the fitted probability density function on the decay angles, $m(K^+\pi^-)$ and $m(K^+\pi^-\mu^+\mu^-)$ for the bin $15.0 < q^2 < 17.0\,\mathrm{GeV}^2/c^4$. The blue shaded region indicates background. Figure taken from Ref. [1].

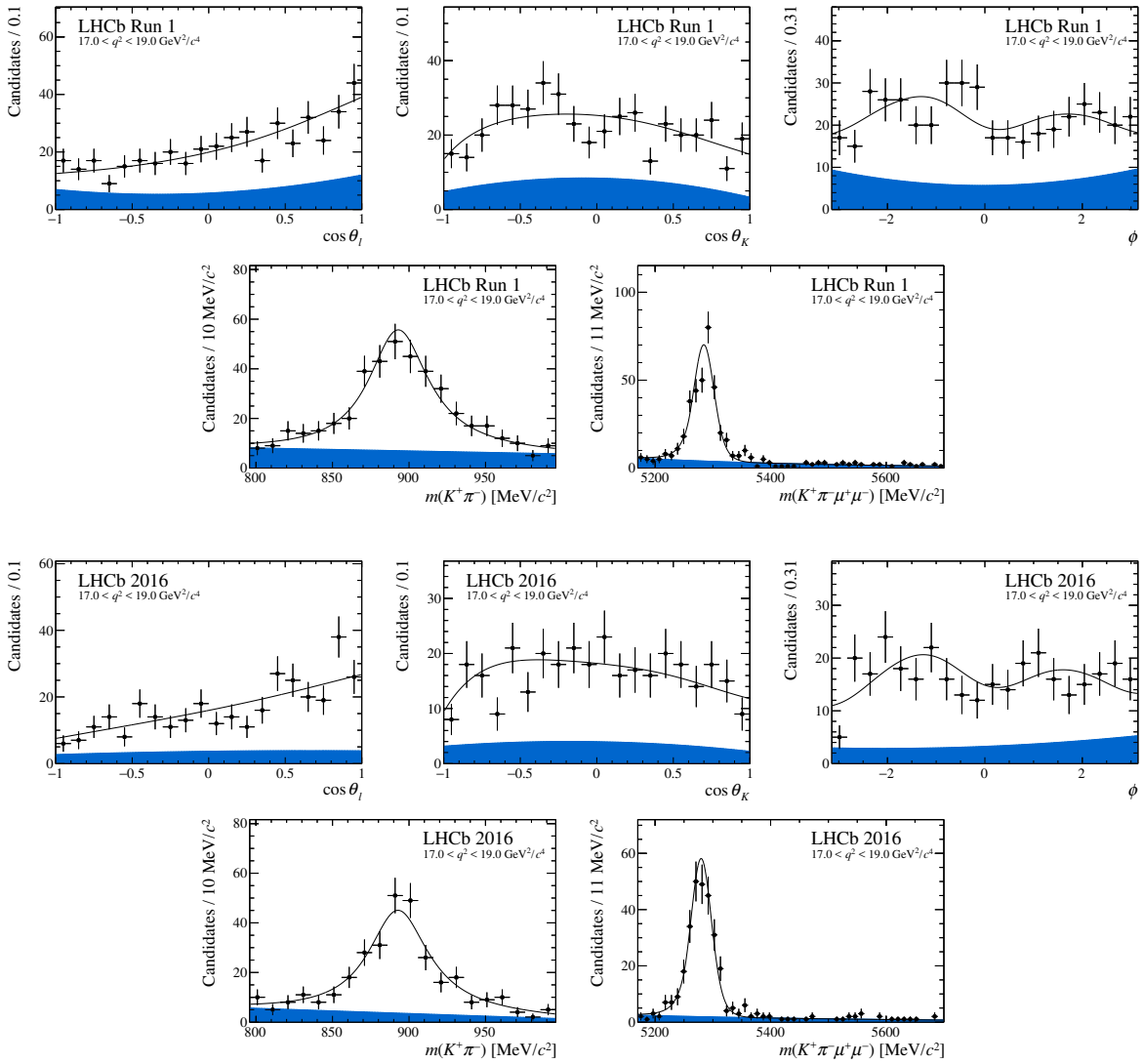


Figure F.7: Projections of the fitted probability density function on the decay angles, $m(K^+\pi^-)$ and $m(K^+\pi^-\mu^+\mu^-)$ for the bin $17.0 < q^2 < 19.0\,\mathrm{GeV}^2/c^4$. The blue shaded region indicates background. Figure taken from Ref. [1].

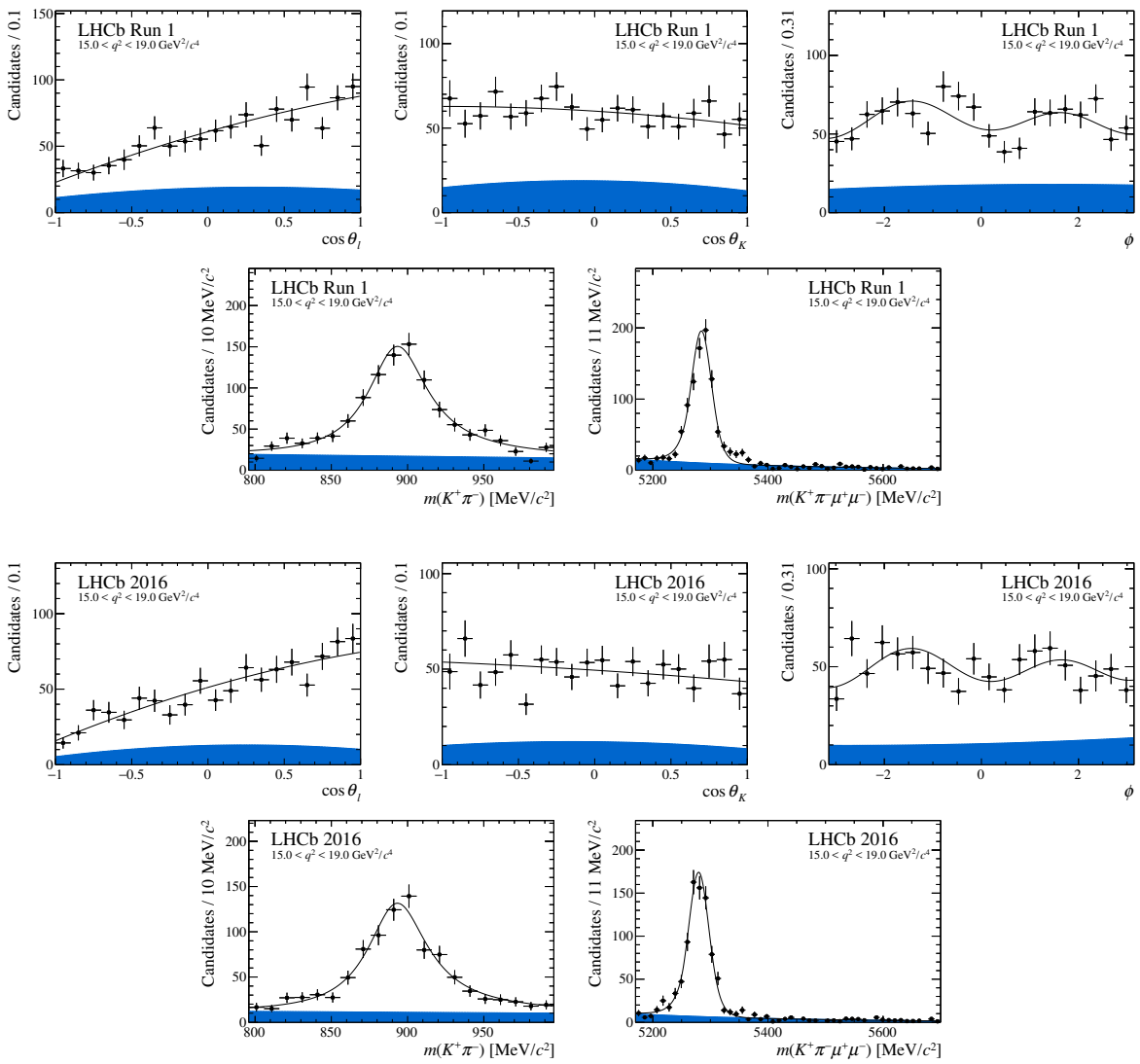


Figure F.8: Projections of the fitted probability density function on the decay angles, $m(K^+\pi^-)$ and $m(K^+\pi^-\mu^+\mu^-)$ for the bin $15.0 < q^2 < 19.0\,\mathrm{GeV}^2/c^4$. The blue shaded region indicates background. Figure taken from Ref. [1].

Appendix G

Correlation matrices

Table G.1: Correlation matrix for the *CP*-averaged observables from the maximum-likelihood fit in the bin $0.10 < q^2 < 0.98\,\mathrm{GeV}^2/c^4$.

	F_L	S_3	S_4	S_5	A_FB	S_7	S_8	S_9
F_L	1.00	−0.00	−0.03	0.09	0.03	−0.01	0.06	0.03
S_3		1.00	0.02	0.14	0.02	−0.06	0.01	−0.01
S_4			1.00	0.06	0.15	−0.03	0.06	0.00
S_5				1.00	0.04	−0.03	−0.01	0.00
A_FB					1.00	−0.02	−0.01	−0.02
S_7						1.00	−0.04	0.10
S_8							1.00	0.02
S_9								1.00

Table G.2: Correlation matrix for the *CP*-averaged observables from the maximum-likelihood fit in the bin $1.1 < q^2 < 2.5\,\mathrm{GeV}^2/c^4$.

	F_L	S_3	S_4	S_5	A_FB	S_7	S_8	S_9
F_L	1.00	0.05	0.04	0.16	0.11	−0.08	−0.06	0.05
S_3		1.00	0.00	0.04	0.05	0.08	0.08	0.18
S_4			1.00	−0.20	−0.01	0.02	−0.09	−0.07
S_5				1.00	−0.09	−0.11	−0.02	−0.12
A_FB					1.00	−0.03	0.08	−0.04
S_7						1.00	−0.16	0.14
S_8							1.00	−0.04
S_9								1.00

Table G.3: Correlation matrix for the *CP*-averaged observables from the maximum-likelihood fit in the bin $2.5 < q^2 < 4.0\,\mathrm{GeV}^2/c^4$.

	F_L	S_3	S_4	S_5	A_FB	S_7	S_8	S_9
F_L	1.00	−0.02	−0.03	−0.02	−0.03	−0.01	−0.08	0.06
S_3		1.00	−0.05	−0.03	0.05	0.02	−0.07	0.02
S_4			1.00	−0.13	−0.10	0.01	0.03	−0.03
S_5				1.00	−0.08	0.01	0.02	0.03
A_FB					1.00	0.06	−0.05	−0.08
S_7						1.00	0.01	0.03
S_8							1.00	−0.08
S_9								1.00

Table G.4: Correlation matrix for the *CP*-averaged observables from the maximum-likelihood fit in the bin $4.0 < q^2 < 6.0\,\mathrm{GeV}^2/c^4$.

	F_L	S_3	S_4	S_5	A_FB	S_7	S_8	S_9
F_L	1.00	−0.01	0.05	−0.02	−0.14	−0.10	0.09	0.04
S_3		1.00	−0.06	−0.10	0.06	−0.02	0.02	−0.08
S_4			1.00	0.01	−0.14	0.03	0.02	0.01
S_5				1.00	−0.08	0.07	0.02	−0.05
A_FB					1.00	−0.01	−0.03	0.01
S_7						1.00	0.03	−0.18
S_8							1.00	−0.00
S_9								1.00

Table G.5: Correlation matrix for the *CP*-averaged observables from the maximum-likelihood fit in the bin $6.0 < q^2 < 8.0\,\mathrm{GeV}^2/c^4$.

	F_L	S_3	S_4	S_5	A_FB	S_7	S_8	S_9
F_L	1.00	0.00	−0.01	−0.06	−0.20	−0.05	0.00	−0.06
S_3		1.00	−0.12	−0.24	0.01	0.05	0.04	−0.10
S_4			1.00	0.13	−0.10	0.02	−0.04	−0.04
S_5				1.00	−0.16	−0.01	0.02	−0.06
A_FB					1.00	−0.03	0.02	0.02
S_7						1.00	0.08	−0.09
S_8							1.00	−0.08
S_9								1.00

Table G.6: Correlation matrix for the *CP*-averaged observables from the maximum-likelihood fit in the bin $11.0 < q^2 < 12.5\,\mathrm{GeV}^2/c^4$.

	F_L	S_3	S_4	S_5	A_FB	S_7	S_8	S_9
F_L	1.00	0.14	0.02	−0.09	−0.56	0.02	0.01	0.01
S_3		1.00	0.08	−0.08	−0.15	0.02	0.06	−0.10
S_4			1.00	0.08	−0.12	0.03	−0.02	−0.02
S_5				1.00	−0.13	0.03	−0.00	−0.17
A_FB					1.00	−0.05	−0.10	0.12
S_7						1.00	0.27	−0.10
S_8							1.00	−0.01
S_9								1.00

Table G.7: Correlation matrix for the *CP*-averaged observables from the maximum-likelihood fit in the bin $15.0 < q^2 < 17.0\,\mathrm{GeV}^2/c^4$.

	F_L	S_3	S_4	S_5	A_FB	S_7	S_8	S_9
F_L	1.00	0.27	0.02	0.07	−0.53	0.00	−0.04	0.06
S_3		1.00	−0.05	0.01	−0.12	−0.02	−0.04	0.10
S_4			1.00	0.29	−0.15	0.02	0.06	0.03
S_5				1.00	−0.28	0.06	0.03	0.04
A_FB					1.00	0.01	−0.00	0.01
S_7						1.00	0.31	−0.23
S_8							1.00	−0.13
S_9								1.00

Table G.8: Correlation matrix for the *CP*-averaged observables from the maximum-likelihood fit in the bin $17.0 < q^2 < 19.0\,\mathrm{GeV}^2/c^4$.

	F_L	S_3	S_4	S_5	A_FB	S_7	S_8	S_9
F_L	1.00	0.14	0.06	0.00	−0.35	0.02	−0.02	0.08
S_3		1.00	−0.04	−0.15	−0.12	−0.04	0.03	−0.04
S_4			1.00	0.25	−0.14	−0.10	0.08	0.02
S_5				1.00	−0.25	−0.07	−0.08	0.05
A_FB					1.00	−0.00	−0.03	−0.09
S_7						1.00	0.33	−0.09
S_8							1.00	−0.13
S_9								1.00

Table G.9: Correlation matrix for the *CP*-averaged observables from the maximum-likelihood fit in the bin $1.1 < q^2 < 6.0\,\mathrm{GeV}^2/c^4$.

	F_L	S_3	S_4	S_5	A_FB	S_7	S_8	S_9
F_L	1.00	−0.01	−0.02	0.00	0.01	−0.08	0.02	0.03
S_3		1.00	−0.04	−0.01	0.04	0.03	0.00	−0.02
S_4			1.00	−0.07	−0.09	0.01	0.01	−0.03
S_5				1.00	−0.07	0.00	0.01	−0.04
A_FB					1.00	−0.01	−0.03	−0.03
S_7						1.00	−0.02	−0.04
S_8							1.00	−0.08
S_9								1.00

Table G.10: Correlation matrix for the *CP*-averaged observables from the maximum-likelihood fit in the bin $15.0 < q^2 < 19.0\,\mathrm{GeV}^2/c^4$.

	F_L	S_3	S_4	S_5	A_FB	S_7	S_8	S_9
F_L	1.00	0.18	−0.06	−0.07	−0.37	0.00	−0.03	0.07
S_3		1.00	−0.04	−0.03	−0.07	−0.00	−0.04	0.02
S_4			1.00	0.21	−0.13	−0.03	0.04	0.06
S_5				1.00	−0.23	0.02	−0.01	0.04
A_FB					1.00	0.03	−0.01	0.00
S_7						1.00	0.28	−0.18
S_8							1.00	−0.14
S_9								1.00

Table G.11: Correlation matrix for the optimised angular observables from the maximum-likelihood fit in the bin $0.10 < q^2 < 0.98\,\mathrm{GeV}^2/c^4$.

	F_L	P_1	P_2	P_3	P_4'	P_5'	P_6'	P_8'
F_L	1.00	0.03	0.02	0.03	−0.08	−0.13	−0.02	0.06
P_1		1.00	0.02	0.01	0.02	0.14	−0.06	0.01
P_2			1.00	0.02	0.14	0.03	−0.02	−0.01
P_3				1.00	−0.01	−0.00	−0.10	−0.02
P_4'					1.00	0.07	−0.03	0.06
P_5'						1.00	−0.03	−0.02
P_6'							1.00	−0.04
P_8'								1.00

Table G.12: Correlation matrix for the optimised angular observables from the maximum-likelihood fit in the bin $1.1 < q^2 < 2.5\,\mathrm{GeV}^2/c^4$.

	F_L	P_1	P_2	P_3	P_4'	P_5'	P_6'	P_8'
F_L	1.00	−0.23	−0.51	0.26	0.03	0.24	−0.13	−0.13
P_1		1.00	0.15	−0.23	−0.00	−0.02	0.11	0.11
P_2			1.00	−0.09	−0.03	−0.22	0.05	0.14
P_3				1.00	0.07	0.19	−0.17	−0.00
P_4'					1.00	−0.20	0.02	−0.09
P_5'						1.00	−0.12	−0.04
P_6'							1.00	−0.14
P_8'								1.00

Table G.13: Correlation matrix for the optimised angular observables from the maximum-likelihood fit in the bin $2.5 < q^2 < 4.0\,\mathrm{GeV}^2/c^4$.

	F_L	P_1	P_2	P_3	P_4'	P_5'	P_6'	P_8'
F_L	1.00	0.08	−0.34	0.01	−0.21	−0.09	−0.08	−0.06
P_1		1.00	0.02	−0.02	−0.07	−0.03	0.00	−0.08
P_2			1.00	0.07	−0.02	−0.05	0.08	−0.03
P_3				1.00	0.02	−0.04	−0.04	0.07
P_4'					1.00	−0.10	0.02	0.04
P_5'						1.00	0.01	0.02
P_6'							1.00	0.01
P_8'								1.00

Table G.14: Correlation matrix for the optimised angular observables from the maximum-likelihood fit in the bin $4.0 < q^2 < 6.0\,\mathrm{GeV}^2/c^4$.

	F_L	P_1	P_2	P_3	P_4'	P_5'	P_6'	P_8'
F_L	1.00	0.04	0.05	−0.10	−0.04	−0.14	−0.17	0.14
P_1		1.00	0.06	0.07	−0.06	−0.10	−0.03	0.02
P_2			1.00	−0.02	−0.14	−0.09	−0.03	−0.01
P_3				1.00	−0.01	0.07	0.19	−0.01
P_4'					1.00	0.02	0.04	0.01
P_5'						1.00	0.09	0.00
P_6'							1.00	0.02
P_8'								1.00

Table G.15: Correlation matrix for the optimised angular observables from the maximum-likelihood fit in the bin $6.0 < q^2 < 8.0\,\mathrm{GeV}^2/c^4$.

	F_L	P_1	P_2	P_3	P_4'	P_5'	P_6'	P_8'
F_L	1.00	−0.02	0.17	0.01	−0.14	−0.18	−0.08	−0.02
P_1		1.00	0.01	0.10	−0.12	−0.23	0.04	0.04
P_2			1.00	−0.00	−0.13	−0.21	−0.06	0.02
P_3				1.00	0.03	0.06	0.09	0.08
P_4'					1.00	0.15	0.03	−0.03
P_5'						1.00	0.00	0.02
P_6'							1.00	0.08
P_8'								1.00

Table G.16: Correlation matrix for the optimised angular observables from the maximum-likelihood fit in the bin $11.0 < q^2 < 12.5\,\mathrm{GeV}^2/c^4$.

	F_L	P_1	P_2	P_3	P_4'	P_5'	P_6'	P_8'
F_L	1.00	−0.07	0.13	−0.07	0.04	−0.07	0.03	0.00
P_1		1.00	−0.09	0.10	0.07	−0.06	0.01	0.05
P_2			1.00	−0.16	−0.12	−0.23	−0.05	−0.11
P_3				1.00	0.01	0.18	0.10	0.00
P_4'					1.00	0.08	0.03	−0.02
P_5'						1.00	0.03	0.00
P_6'							1.00	0.27
P_8'								1.00

Table G.17: Correlation matrix for the optimised angular observables from the maximum-likelihood fit in the bin $15.0 < q^2 < 17.0\,\mathrm{GeV}^2/c^4$.

	F_L	P_1	P_2	P_3	P_4'	P_5'	P_6'	P_8'
F_L	1.00	0.06	0.14	−0.06	0.18	0.23	−0.01	−0.04
P_1		1.00	0.03	−0.09	-0.04	0.00	−0.03	−0.04
P_2			1.00	−0.06	−0.13	−0.25	0.01	−0.03
P_3				1.00	−0.04	−0.05	0.23	0.13
P_4'					1.00	0.32	0.02	0.06
P_5'						1.00	0.06	0.03
P_6'							1.00	0.31
P_8'								1.00

Table G.18: Correlation matrix for the optimised angular observables from the maximum-likelihood fit in the bin $17.0 < q^2 < 19.0\,\mathrm{GeV}^2/c^4$.

	F_L	P_1	P_2	P_3	P_4'	P_5'	P_6'	P_8'
F_L	1.00	−0.10	0.16	−0.01	0.22	0.14	−0.01	−0.01
P_1		1.00	−0.10	0.05	−0.07	−0.16	−0.05	0.03
P_2			1.00	0.06	−0.09	−0.23	0.00	−0.05
P_3				1.00	−0.01	−0.06	0.09	0.14
P_4'					1.00	0.27	−0.09	0.08
P_5'						1.00	−0.07	−0.09
P_6'							1.00	0.34
P_8'								1.00

Table G.19: Correlation matrix for the optimised angular observables from the maximum-likelihood fit in the bin $1.1 < q^2 < 6.0\,\mathrm{GeV}^2/c^4$.

	F_L	P_1	P_2	P_3	P_4'	P_5'	P_6'	P_8'
F_L	1.00	−0.05	−0.33	0.09	−0.11	−0.03	−0.14	0.02
P_1		1.00	0.05	0.02	−0.04	−0.00	0.03	0.01
P_2			1.00	−0.00	−0.04	−0.06	0.03	−0.04
P_3				1.00	0.02	0.03	0.03	0.08
P_4'					1.00	−0.06	0.03	0.01
P_5'						1.00	0.01	0.00
P_6'							1.00	−0.02
P_8'								1.00

Table G.20: Correlation matrix for the optimised angular observables from the maximum-likelihood fit in the bin $15.0 < q^2 < 19.0\,\mathrm{GeV}^2/c^4$.

	F_L	P_1	P_2	P_3	P_4'	P_5'	P_6'	P_8'
F_L	1.00	−0.08	0.19	−0.02	0.11	0.09	−0.01	−0.04
P_1		1.00	−0.01	−0.00	−0.04	−0.02	0.00	−0.04
P_2			1.00	−0.04	−0.14	−0.25	0.03	−0.03
P_3				1.00	−0.06	−0.04	0.18	0.14
P_4'					1.00	0.21	−0.03	0.04
P_5'						1.00	0.02	−0.01
P_6'							1.00	0.28
P_8'								1.00